AN INVESTIGATION OF SURFACE SHAPE EFFECTS ON NEAR-FIELD RADIATIVE TRANSFER

A Dissertation
Presented to
The Academic Faculty

by

Keith F. Prussing

In Partial Fulfillment
of the Requirements for the Degree
Doctor of Philosophy in the
School of Physics

Georgia Institute of Technology
August 2015

AN INVESTIGATION OF SURFACE SHAPE EFFECTS ON NEAR-FIELD RADIATIVE TRANSFER

Approved by:

Dr. J. Michael Cathcart, Advisor
School of Physics
Georgia Institute of Technology

Dr. Zhuomin Zhang
School of Mechanical Engineering
Georgia Institute of Technology

Dr. Andrew Zangwill
School of Physics
Georgia Institute of Technology

Dr. A. Nepomuk Otte
School of Physics
Georgia Institute of Technology

Dr. Brian Kennedy
School of Physics
Georgia Institute of Technology

Date Approved: 30 April 2015

To my loving wife Yvette.

Without whose support and encouragement,

this would never have been completed.

ACKNOWLEDGEMENTS

This has been one long and challenging process filled with times of frustration and success. I hope that this work in some small way provides some insights to those who will follow in the ongoing exploration of radiative transport phenomena. This manuscript is the culmination of four years of work that has taught me many useful skills.

First and foremost, I want to thank my wonderful wife Yvette Pinnell-Prussing. Thank you for humoring me when I told you I wanted to drop everything and go back to school to get a PhD in physics. I know I frustrated you at various moments, but your constant support and kicks in the backside helped me get through this process. Thank you for all of the times you have let me decompress while we spent time with the dogs. And, thank you for helping me clarify my thoughts by making me strip out all of the jargon during our evening conversations.

I would also like to thank my advisor Mike Cathcart for his support and encouragement. I tend to learn best in a trial by fire manner, and you let me run with this thesis idea. You also kept me on track during the development phase by reminding me to look up every so often and keep an eye on the bigger picture. Thank you for also convincing me to do my research at GTRI instead of an academic lab. This gave me perspective on what it will be like to be a research scientist after graduation.

Thank you to my family Richard, Debbie, Patrick, Andrea, Eric, and Megan. Your encouragement and belief in me really helped push me to complete this process. You all keep telling me I am smart, and now maybe I will have to listen. Thank you Nigel Brett for the conversation that sparked this journey, and thank you Erika Plante for the conversations about anything other than physics. And finally, a thank you and an apology to I. V. Bray. Your physics class at Berkmar High School was what showed me that physics was an interesting subject, and I never really applied myself to the work.

I would like to acknowledge the Office of Naval Research for the support for this work

under contract N00014-11-C-0368.

TABLE OF CONTENTS

LIST OF TABLES

LIST OF FIGURES

SUMMARY

It has been shown that the energy exchange between two objects can be greatly enhanced when the separation between the objects is on the order of the wavelength of thermal emission. The earliest theoretical and computational work focused on simple planar and spherical geometries, or they resorted to approximations that separated the object to outside of the thermal wavelength $\lambda_T = hc/(k_B T)$. Since those original works, the study of near-field energy exchange has expanded to object shapes that can be described by a separable coordinate system using a spectral expansion of the dyadic Green function of the system. The boundary element method has also been used to study arbitrary shapes in thermal equilibrium. Application of these new expansion methods to general shapes out of thermal equilibrium will facilitate in the optimization of nanoscale structures.

A three step process is used to investigate the effects of object shape on the total and directionality of the energy exchange between objects. First, a general expression for the energy flux between the objects will be formulated. Second, a computational method to evaluate the expression will be implemented. Finally, the effects of varying the surface geometry will be explored.

The computational results demonstrate that the total energy exchange between two bodies is influenced by the surface shape of the objects even when the surface areas are held constant. While the primary increase over the classical blackbody energy exchange $\sigma T^4 A$ is primarily governed by separation of the surfaces, we show that the view factors from classical far-field radiative transfer can be used to predict the change in the total energy exchange from a reference configuration at the same separation when the surface area of the two objects is comparable. Additionally, we demonstrate that the spatial distribution of the energy exchange can be localized into small spatial region with a peak value increased over 30 % by using two objects with dramatically different projected areas.

CHAPTER I

INTRODUCTION

The well known result from the classical theory of radiative transfer states that the thermally emitted electromagnetic energy exchanged by two objects is governed by the blackbody radiation when the separation between the surfaces is large. However, when the separation between the two surfaces drops below the thermal wavelength $\lambda_T = hc/(k_B T)$, as derived from Wien's displacement law [3], we enter a region where the gap separating the surfaces is "small." For typical room temperatures, this separation is on the nanometer to micrometer scale. At these small separations, the energy exchange between the two surfaces is enhanced to exceed the classical blackbody limit. This near-field effect influences heat control in microprocessors [1], alternate energy sources [3], and even the evolution of interstellar gas-dust clouds [15]. By gaining a greater understanding of this enhanced energy exchange, we can devise new configurations to improve thermal control in small scale systems.

The study of objects separated by small gaps has been under investigation for over half a century. The bulk of the previous theoretical work has focused on simple geometries where closed form or semianalytic expressions are obtainable. In this work, we set out to investigate the effects of the shape of the objects on the energy exchange. To this end, we begin with an overview of the physical phenomena that forms the basis for this enhanced energy exchange. Next, we review previous work in this area to provide a basis for our starting point. The remainder of this thesis will delve into the effects of object shape on the total radiative exchange between two objects.

1.1 Physical Phenomena

All objects are surrounded by an electromagnetic field. The origin of this field is associated with quantum and thermal fluctuations of the charge carriers within the body [34]. The quantum fluctuations arise due to the uncertainty principle and persist at absolute zero; whereas, the thermal fluctuations are generated by random thermal motions which vanish

at absolute zero [73]. These random motions are simply microscopic currents that time average to zero [3]. These quantum and thermal currents, in turn, generate a fluctuating electromagnetic field that propagates as waves throughout the body according to the Maxwell equations.

As the waves propagate through the body, the magnitude of the waves is modulated according to the electromagnetic properties of the medium. As most materials are absorptive, this means the magnitude of the waves decrease. When a wave reaches the surface, two scenarios are possible. If the angle of incidence is below the critical angle, a portion of the energy in the wave is transmitted into the surrounding medium to radiate away. This is the classical blackbody radiation that is governed by the Stefan-Boltzmann law $H_{\mathrm{bb}} = \sigma T^4 A$. The remainder of the energy is reflected from the boundary to continue propagating throughout the body. On the other hand, if the angle of incidence is greater than the critical angle, total internal reflection occurs. A feature of total internal reflection is the generation of an evanescent wave along the interface that decays exponentially away from the boundary [26, 34]. These waves propagate along the surface of the materials, where it is possible for them to interact with the fundamental oscillations of the body's material.

As an evanescent wave propagates along a boundary, it can couple with the fundamental oscillations of the material of the object. This coupling of the electromagnetic wave and the material is called a surface-polariton [34]. In a metallic material, the wave couples to a charge density oscillation and is called a surface-plasmon-polariton; whereas, in a dielectric, the wave couples with an electromagnetic phonon and is termed a surface-phonon-polariton [34]. Although these polaritons can exist within the bulk material, it is specifically the surface-polaritons that influence the electromagnetic field surrounding the body [34]. Regardless of the particular kind, the surface polaritons are characterized by large energy densities that decay rapidly away from the surface [66]. These large energy densities are part of the reason that the near-field effects dominate the energy transfer between polar dielectric materials at separations small compared to the thermal wavelength [65] and are thought to be responsible for the enhanced transmission through nanostructures and Fabry-Perot style resonances [3].

The electromagnetic field surrounding objects is the mediator of the radiative interaction between the objects. When the separations of the surfaces are larger than the thermal wavelength, far-field effects are dominant. In the far-field regime, the energy exchange between objects is due solely to the propagating modes generated by the fluctuating currents in the objects [73]. In this regime, the results of geometric optics apply, and the Stefan-Boltzmann law correctly describes the energy transfer [3]. An equivalent view of this statement is that the blackbody radiation accounts for the propagating modes when the diffraction effects are unimportant [51]. In this approximation, the radiative transfer is under predicted when the separation between objects is on the order of or less than λ_T because of the neglect of near-field effects [65]. As the separation between two bodies decreases, these near-field effects must taken into account.

Once the separation between two objects reaches the order of the thermal wavelength, the wave nature of the electromagnetic field causes near-field effects. The first effects that must be taken into account as the objects approach each other are refraction, diffraction, reflection, and interference fields [3]. As the gap between the objects decreases further, the separation enters the decay range of the evanescent waves trapped on the surfaces. These evanescent waves can undergo multiple reflections between the surfaces which leads to a coupling of the evanescent waves between the two surfaces [3]. This results in a nonzero time averaged component of the Poynting vector normal to the surface that is interpreted as a photon tunneling across the gap [3]. This photon then couples with a surface-polaritan on the second surface creating an enhanced energy transfer between the surfaces which exceeds the classical blackbody transfer component.

These near-field effects are the driving force behind the enhanced energy transfer at small separations. When the two materials involved are capable of supporting surface polaritons, the radiative exchange is dominated by the evanescent contribution [73]. The frequencies that are near a resonance in the dielectric function of the materials contribute the most to the energy exchange [50]. This means that the largest transfer of energy occurs when the materials have resonances near the same frequency. Even though this near-field enhancement is dominant, the propagating modes cannot be neglected. The propagating

waves that are away from the resonant frequency in the dielectric function still traverse the regions of space where the near-field conditions are not met [65]. This means that the radiative properties of nanoscale objects are influenced by the shape of the object even if the volume is held constant [31]. This shape dependence forms the basis of the research presented in this thesis.

1.2 Literature Review

Before we get to the details of the thesis research, we provide a brief overview of the prior research on the subject of near-field radiative exchange. The history of the study of energy transfer at the microscale traces its roots back to the study of conduction properties of small objects. The initial work was aimed at understanding heat transfer on scales where macroscopic principles of heat transfer could be applied. The early computational work focused on finding the bulk properties of materials using molecular dynamics and Monte-Carlo simulations of either Fourier's law or the Boltzmann transport equation [1]. The molecular dynamics simulations of the phonons in the solids had all of the frequency modes excited; thus, the results were appropriate for solids above the Debye temperature [5]. Explicit incorporation of the phonon scattering had to be introduced into the governing equations to account for the effects of interfaces between materials in the region [5]. As the understanding of conduction at short scales expanded, interest in the radiative channel for energy exchange grew.

The specific interest in the radiative transfer over small scales dates back to the late 1950s. In 1959, Rytov introduced random current sources to describe the energy exchanged between two identical semi-infinite planes using the fluctuation-dissipation theorem [64]. In 1971, Polder and van Hove applied Rytov's formalism to a system of two planes of arbitrary electric properties [54]. More recently, Volokitin and Persson used a relativistic approach to study two planes in relative motion [74]. The two plane system is one of the few cases where a semianalytic expression can be obtained [73]. The two plane system remains a staple configuration of the literature because a semianalytic expression is available and all other formalism must reproduce these well known results.

The application of the fluctuation dissipation theorem has been used to study additional configurations. A great deal of effort has gone into the study of the sphere-sphere and the sphere-plane configurations using the dipole approximation. The dipole approximation requires the separations of the bodies to be much larger than the characteristic length scales of the bodies but does reproduce the blackbody result at large separations [18, 73]. An early application of the dipole approximation to the study of the sphere-sphere and sphere-plane configurations was given by Volokitin and Persson [72]. Dedkov and Kyasov developed a fully relativistic approach for the sphere-plane configuration using the local approximation for the dielectric and magnetic properties of the sphere [14, 38]. Dedkov and Kyasov also investigated the exchange of the objects with the background medium [16, 17]. Huth, Rütig, Biehs, and Holthaus used the dipole approximation to study a spheroidal particle near a plane to more closely match the shape of the tip of a near-field thermal microscope [31]. The results of the dipole approximation were also used by Prasher to investigate the exchange in a dense array of particles [57]. Recently, Messina, Tschikin, Biehs, and Ben-Abdallah considered the temperature evolution of three spherical dipoles in a heat bath [45].

The dipole approximation also plays a key role in the additive dipole approximation. The additive dipole approximation attempts to extend the results of the dipole approximation to finite sized objects. The dipole approximation is taken to hold for each volume element of an object. The total interaction between two bodies is then simply the integral over both volumes. According to Dedkov and Kyasov, this removes the restriction that the separation between objects is large compared to the size of the bodies [19]. The challenge with this assumption is that it directly opposes the dipole approximation. As the surfaces approach, there exist volume elements of the two bodies that do not satisfy the dipole approximation.

To overcome the size and separation restrictions imposed by the dipole approximation, the Green function of the system can be employed to compute the electromagnetic field. The basic premise behind this method is to expand the integral solution for the electromagnetic field using the method of moments [28]. Narayanaswamy and Chen used spherical basis functions to study the sphere-sphere system and created a regime map for the validity of common approximations [50]. Sasihithlu and Narayanaswamy investigated the truncation

parameters necessary in the sums for the sphere-sphere system using the spherical basis functions [65]. Carrillo and Bayazitoglu iteratively increased the size of one sphere to investigate the asymptotic approach to the sphere-plane system [7]. Carrillo and Bayazitoglu also used a cylindrical set of basis functions to study exchange between nanorods [8] and compared the results to approximating the rods as a line of spheres [9]. Otey and Fan also used a cylindrical basis but focused on the sphere-plane configuration directly [52], and McCauley, Reid, Krüger, and Johnson investigated the spatial distribution of the heat flux between a cone and a plane [44]. Mackowski and Mishchenko derived the interaction of a collection of spheres from the T-matrix scattering formalism and energy conservation principles [42]. Rodriguez, Reid, and Johnson used the boundary element method to study crossed cylinders and two cones [61]. Krüger, Bimonte, Emig, and Kardar presented a general trace formulation for the near-field radiative interaction in an arbitrary system of objects using the scattering operator [36]. Expanding the Green function uses the methodology of electromagnetic scattering routines supplemented by the fluctuation-dissipation theorem.

Underlying all of these solution methods is the validity of the fluctuation-dissipation theorem as applied to electromagnetic fields. The initial relation between the general dissipation of a system and the random fluctuations was presented by Callen and Welton [6]. Rytov was the first to apply the formalism to electromagnetic fields [64]. Landau and Lifshitz provided a general formulation of the fluctuation-dissipation theorem based on the linear response of a variable to a fluctuating force [39]. Agarwal used a quantum electrodynamics approach to apply the theorem but did not explicitly quantize the electromagnetic field [2]. Eckhardt compared two different semiclassical approaches to applying the fluctuation-dissipation theorem and detailed the limiting procedures necessary for each [21]. Janowicz, Reddig, and Holthaus explicitly quantized the electromagnetic field and demonstrated that the semiclassical approach to applying the fluctuation-dissipation theorem in electromagnetic problems is self-consistent [32]. With this level of scrutiny, the fluctuation-dissipation theorem has been placed on a firm footing for use in electromagnetic problems.

Although the theoretical predictions of an increased energy exchange were made over

50 years ago, measurements took a bit longer to occur. In 1969, Hargreaves reported an anomalous energy transfer between two closely space plates [27]. In 2009, Narayanaswamy, Shen, Hu, Chen, and Chen proposed an experimental setup to measure the energy transfer between a sphere and a plate [51]. Using this method, Shen, Narayanaswamy, and Chen reported the first measurement of an energy exchange in excess of the blackbody limit [66]. Later that same year, Rousseau, Siria, Jourdan, Volz, Comin, Chevrier, and Greffet also proposed a measurement process and reported an increased energy exchange [63]. These experiments demonstrate that the increased energy exchange is not simply a theoretical novelty but rather a physical reality.

1.3 Applications

The ability to tune the radiation properties has applications in a broad range of areas. For example, the ability to adjust the thermal conductivity is critical for the development of microscale structures such as processors where an increase in the thermal conductivity is necessary and solid-state refrigerators where a decrease in the thermal conductivity is necessary [5]. Radiation effects must be accounted for in multilayer, out-of-plane microelectronics and microheat pipes [1]. Optimization of these nanoscale structures requires an understanding of the near-field energy exchange [9]. Coupling the surface polaritons to the propagating electromagnetic waves through a grating has been used to make a tunable, highly directional emitter in the infrared with a narrow range of wavelengths [73]. These coherent emitters have been used in the detection of gases [55, 56], optimized to create an almost perfect blackbody absorber over a broad range of angles [20], and in energy conversion systems [3]. It has been proposed that the efficiencies and power densities of thermophotovoltaic systems can be further enhanced using the near-field emission properties of gratings [65]. By tuning the wavelength of the emitters to match the band gap of a photovoltaic cell, the efficiency of thermophotovoltaic systems can be increased [34]. Recently, the coupling the polaritons to the propagating electromagnetic field has been used with nanostructures to create a microlaser [67] and to influence the scattering of light through a dielectric [35].

Additionally, spectroscopic techniques rely on near-field radiative interaction. Raman

spectroscopy, near-field scanning optical microscopy, plasmonic optics, and subwavelength optics, and near-field thermal imaging all depend on near-field effects [65]. Managing the noncontact friction forces is important for detection of single spins by magnetic resonance force spectroscopy for three-dimensional atomic imaging [73]. Scanning thermal microscopes have used evanescent waves to image beyond the diffraction limit and do not require external light sources [3]. All of these methods require an understanding of the near electromagnetic field and the effect surface shape has on it.

Beyond the previous applications listed above, the near-field energy exchange can be used to direct energy through a system of objects. The focus of the project supporting this thesis was to further knowledge of counter directed energy techniques. To that end, this work focuses on the energy exchange as opposed to force generated by the electromagnetic field. The long term goal is to devise a matrix of objects that can quickly disperse high optical energy incident at a single location. Tailoring the object shapes and orientation, a preferential channel for energy transfer can be devised. By embedding this structure into a conducting medium, the thermal energy can be dispersed through the material to rapidly disperse the incident energy.

Until now, the study of radiative interaction between objects at small separations has focused on simple geometries. Only token studies of the effects of surface shape have been undertaken. In this thesis, we will take a closer look at effect of object shape on both the total and the spatial distribution of the near-field energy exchange between two objects. To do this, we derive the general formalism for the near-field energy exchange and discuss the implementation of a numerical method to compute the exchange. We will then turn our attention to systems of objects whose surface shapes have not been well studied in the literature.

The remainder of this thesis is organized as follows. In Chapter 2 we review the theoretical formalism and derive the equations necessary for our calculations. We discuss the implementation of the numerical method and verification process in Chapter 3. In Chapter 4, we begin the numerical investigation by considering a system of a sphere and a spheroid. Our second configuration of a disk and spheroid with aligned symmetry axes is

discussed in Chapter 5. Chapter 6 extends the discussion by considering a disk and spheroid without axially symmetry. Finally, in Chapter 7 we draw our conclusions.

CHAPTER II

THEORETICAL DEVELOPMENT

2.1 Introduction

In this chapter, we will review the theoretical formalism for computing the enhanced energy exchange between objects in a system. We begin by using the fluctuation-dissipation theorem to derive an expression for the electromagnetic energy exchanged within a system of objects. This will provide insights into the energy exchange that we will exploit later in this chapter. Our second step is to apply the boundary element method to establish our notation used in our analysis. We complete this chapter by combining the fluctuation-dissipation theorem and the boundary element method to establish the emission of an object in isolation followed by the interaction of multiple bodies. This final step provides the equations describing the energy exchange used in this research. Although most of the basic formalisms have been applied before, our analysis will discuss the necessary assumptions for establishing the final equations in the energy exchange formalism.

Before we get to the full theoretical development, we layout the conditions and our assumptions. Consider a system of N objects labeled by $\alpha \in [1, N]$ with temperature T_α and embedded in a background at temperature T_0. Each object occupies a region of space with a volume V_α and is bounded by the surface S_α. We assume that the electromagnetic properties of all objects are linear and described by relative dielectric permittivity $\overleftrightarrow{\boldsymbol{\varepsilon}}_\alpha(\boldsymbol{r}, \boldsymbol{r}', t)$ and relative magnetic permeability $\overleftrightarrow{\boldsymbol{\mu}}_\alpha(\boldsymbol{r}, \boldsymbol{r}', t)$. We assume the background material is linear, isotropic, and homogeneous in both permittivity $\overleftrightarrow{\boldsymbol{\varepsilon}}_0 = \varepsilon_0 \delta(\boldsymbol{r} - \boldsymbol{r}') \overleftrightarrow{\boldsymbol{I}}$ and permeability $\overleftrightarrow{\boldsymbol{\mu}}_0 = \mu_0 \delta(\boldsymbol{r} - \boldsymbol{r}') \overleftrightarrow{\boldsymbol{I}}$. The net effect of this last assumption is to establish the speed of light in the background. Our final assumption is that the system is in a thermally stationary state. To achieve this condition, we assume that there is a heat bath attached to each object that maintains the temperature of the object and does not disturb the other objects in the system or the radiative interaction.

2.2 Electromagnetic Energy Exchange

We seek to compute the power passing through one of the surfaces in the system S_α that separates the object α from the background. The power passing out of a closed surface is given by the integral of the Poynting vector over the surface

$$H(t) = \frac{c}{4\pi} \oint_{S_\alpha} \hat{\boldsymbol{n}} \cdot \langle \boldsymbol{E}(t) \times \boldsymbol{H}(t) \rangle \, dS \tag{1}$$

where $\langle \ldots \rangle$ indicates ensemble averaging and $\hat{\boldsymbol{n}}_\alpha$ is the normal so S_α pointing into the background. Written in terms of the Fourier transform, the power becomes

$$\begin{aligned} H(t) &= \frac{c}{4\pi} \int_{-\infty}^{\infty} \frac{d\omega}{2\pi} e^{-i\omega t} \int_{-\infty}^{\infty} dt' \oint_{S_\alpha} dS \, n_j \epsilon_{jkl} \left\langle E_k(t') H_l(t') \right\rangle e^{i\omega t'} \\ &= \frac{c}{4\pi} \int_{-\infty}^{\infty} \frac{d\omega}{2\pi} \int_{-\infty}^{\infty} \frac{d\omega'}{2\pi} \oint_{S_\alpha} dS \, n_j \epsilon_{jkl} \left\langle E_k(\omega') H_l(\omega - \omega') \right\rangle e^{-i\omega t} \\ &= \frac{c}{4\pi} \int_{-\infty}^{\infty} \frac{d\omega'}{2\pi} \int_{-\infty}^{\infty} \frac{d\omega''}{2\pi} \oint_{S_\alpha} dS \, n_j \epsilon_{jkl} \left\langle E_k(\omega') H_l(\omega'') \right\rangle e^{-i(\omega' + \omega'')t}. \end{aligned} \tag{2}$$

The Fourier components of the electromagnetic field satisfy the Maxwell equations

$$\boldsymbol{\nabla} \times \boldsymbol{E}(\boldsymbol{r}, \omega) = i \frac{\omega}{c} \boldsymbol{B}(\boldsymbol{r}, \omega) \tag{3a}$$

$$\boldsymbol{\nabla} \times \boldsymbol{H}(\boldsymbol{r}, \omega) = -i \frac{\omega}{c} \boldsymbol{D}(\boldsymbol{r}, \omega) + \frac{4\pi}{c} \boldsymbol{j}(\boldsymbol{r}, \omega) \tag{3b}$$

$$\boldsymbol{\nabla} \cdot \boldsymbol{D}(\boldsymbol{r}, \omega) = 4\pi\rho \tag{3c}$$

$$\boldsymbol{\nabla} \cdot \boldsymbol{B}(\boldsymbol{r}, \omega) = 0 \tag{3d}$$

subject to the boundary conditions

$$\hat{\boldsymbol{n}} \times \boldsymbol{E}(\boldsymbol{r}_1) = \hat{\boldsymbol{n}} \times \boldsymbol{E}(\boldsymbol{r}_2) \tag{4a}$$

$$\hat{\boldsymbol{n}} \times \boldsymbol{H}(\boldsymbol{r}_1) = \hat{\boldsymbol{n}} \times \boldsymbol{H}(\boldsymbol{r}_2), \tag{4b}$$

and supplemented by the constitutive relations

$$\boldsymbol{D}(\boldsymbol{r},\omega) = \int_{V_\alpha} \overleftrightarrow{\boldsymbol{\varepsilon}}_\alpha(\boldsymbol{r},\boldsymbol{r}',\omega)\cdot\boldsymbol{E}(\boldsymbol{r}',\omega)\,d\tau \qquad \equiv \overleftrightarrow{\boldsymbol{\varepsilon}}_\alpha * \boldsymbol{E} \tag{5a}$$

$$\boldsymbol{B}(\boldsymbol{r},\omega) = \int_{V_\alpha} \overleftrightarrow{\boldsymbol{\mu}}_\alpha(\boldsymbol{r},\boldsymbol{r}',\omega)\cdot\boldsymbol{H}(\boldsymbol{r}',\omega)\,d\tau \qquad \equiv \overleftrightarrow{\boldsymbol{\mu}}_\alpha * \boldsymbol{H} \tag{5b}$$

in a region α. The convolution introduced above is understood to be over the volume V_α and is used to simplify the notation. In the absence of external current sources, Faraday's and Amperè's laws can be written in the symmetrized form

$$\boldsymbol{\nabla}\times\boldsymbol{E} = i\frac{\omega}{c}\overleftrightarrow{\boldsymbol{\mu}}_\alpha * \boldsymbol{H} + 4\pi i\frac{\omega}{c}\boldsymbol{M} \tag{6a}$$

$$\boldsymbol{\nabla}\times\boldsymbol{H} = -i\frac{\omega}{c}\overleftrightarrow{\boldsymbol{\varepsilon}}_\alpha * \boldsymbol{E} - 4\pi i\frac{\omega}{c}\boldsymbol{P} \tag{6b}$$

where $\boldsymbol{P}$ and $\boldsymbol{M}$ are the polarization and magnetization fields respectively. Multiplying the symmetrized version of Faraday's law by $\overleftrightarrow{\boldsymbol{\mu}}_\alpha^{-1}$, integrating over the volume V_α, and taking the curl we find that the electric field satisfies the vector wave equation

$$\boldsymbol{\nabla}\times\overleftrightarrow{\boldsymbol{\mu}}_\alpha^{-1} * \boldsymbol{\nabla}\times\boldsymbol{E} = k_0^2\overleftrightarrow{\boldsymbol{\varepsilon}}_\alpha * \boldsymbol{E} + 4\pi k_0^2\boldsymbol{P} + 4\pi i k_0\boldsymbol{\nabla}\times\overleftrightarrow{\boldsymbol{\mu}}_\alpha^{-1} * \boldsymbol{M} \tag{7}$$

where $k_0 \equiv \omega/c$ is the angular wave number.

The vector wave equation has been well studied in the literature. Appendix A applies the methodology of Chew [11] to introduce the dyadic Green function for the system and derive the integral solution for Equation 7. After all of the manipulations are completed, the volume integral solution for the fields in terms of the dyadic Green function is

$$\begin{bmatrix}\boldsymbol{E}\\ \boldsymbol{H}\end{bmatrix} = \frac{4\pi}{c}\begin{bmatrix}\overleftrightarrow{\boldsymbol{G}}^{EE} & \overleftrightarrow{\boldsymbol{G}}^{EH}\\ \overleftrightarrow{\boldsymbol{G}}^{HE} & \overleftrightarrow{\boldsymbol{G}}^{HH}\end{bmatrix} * \begin{bmatrix}-i\omega\boldsymbol{P}\\ -i\omega\boldsymbol{M}\end{bmatrix} \tag{8}$$

where

$$\overleftrightarrow{\boldsymbol{G}}^{EE} = ik_0 \overleftrightarrow{\boldsymbol{\mu}}_0 * \overleftrightarrow{\boldsymbol{G}}_0 \tag{9a}$$

$$\overleftrightarrow{\boldsymbol{G}}^{EH} = -\overleftrightarrow{\boldsymbol{\mu}}_0 * \boldsymbol{\nabla} \times \overleftrightarrow{\boldsymbol{G}}_0 * \overleftrightarrow{\boldsymbol{\mu}}_0^{-1} \tag{9b}$$

$$\overleftrightarrow{\boldsymbol{G}}^{HE} = \overleftrightarrow{\boldsymbol{\mu}}_0^{-1} * \boldsymbol{\nabla} \times * \overleftrightarrow{\boldsymbol{\mu}}_0 * \overleftrightarrow{\boldsymbol{G}}_0 \tag{9c}$$

$$\overleftrightarrow{\boldsymbol{G}}^{HH} = ik_0 \overleftrightarrow{\boldsymbol{\mu}}_0 * \overleftrightarrow{\boldsymbol{\varepsilon}}_0 * \overleftrightarrow{\boldsymbol{G}}_0 * \overleftrightarrow{\boldsymbol{\mu}}_0^{-1}. \tag{9d}$$

To find the Poynting vector, we take the outer product of the fields and apply the fluctuation-dissipation theorem as shown in Appendix B. The total Poynting vector turns out to be the sum of the Poynting vectors due to each object independently:

$$\boldsymbol{S}(\boldsymbol{r}) = \int_0^\infty \sum_{\alpha=1}^{N} \boldsymbol{S}_\alpha(\boldsymbol{r}, \omega) \frac{d\omega}{2\pi} \tag{10a}$$

where each component of the vector $\boldsymbol{S}_\alpha$ is

$$S_{\alpha,j}(\omega) \equiv \epsilon_{jkl} k_0 \left[\Theta(\omega, T_\alpha) - \Theta(\omega, T_0)\right] \ldots \\ \Re \int d^3r' \int d^3r'' \left[\overleftrightarrow{\boldsymbol{G}}^{EE}(\boldsymbol{r}, \boldsymbol{r}') \cdot \Im \overleftrightarrow{\boldsymbol{\varepsilon}}_\alpha(\boldsymbol{r}', \boldsymbol{r}'') \cdot \overleftrightarrow{\boldsymbol{G}}^{HE,\dagger}(\boldsymbol{r}, \boldsymbol{r}'')\right]_{kl}. \tag{10b}$$

In this expression, we are using an effective permittivity to simplify the expression. In this expression, $\Theta(\omega, T) \equiv \hbar\omega/[\exp(\hbar\omega/k_B T) - 1]$ is the mean energy of an oscillator. It is straight forward to reintroduce the permeability as discussed in Appendix B.

To find the total power passing through a particular surface, we integrate the total Poynting vector across that surface. If we consider two specific bodies 1 and 2, the net power passing through the surface of 1 due to the presence of fluctuating currents in regions 1, 2, and the background is simply the sum of the two Poynting vectors; however, the direction of the normal will be flipped for contributions from region 2. The net result is that the contribution due to the background temperature vanishes and the temperature dependence is simply $\Theta(\omega, T_1) - \Theta(\omega, T_2)$. This means that the fluctuations of the background radiation are only important when we consider the emission of an object in isolation. Another result

of the fluctuation-dissipation theorem is that we are guaranteed to have a single frequency for the field. This means we do not need to worry about phase differences if we need to perform a time average [26]. The underlying challenge with applying the formalism we have just outlined involves the computation of the volume integrals. Using the equivalence principle, we can recast the formalism in terms of surface integrals.

2.3 Equivalence Principle and the Boundary Element Method

We have shown that the energy exchanged between two objects can be written in terms of the volume integral solution using the Green function. However, we can reduce the complexity of the integral solution by applying the equivalence principle to write the solution for the electromagnetic field in terms of surface integrals instead of volume integrals. In this section, we review the equivalence principle and the boundary element method. While the content of this section is not new [10, 61], it provides a review and introduces the notation used latter in this thesis.

In Appendix A, we considered a single electromagnetic field and single set of Green functions. This led to the vanishing of the surface integral when applying the boundary conditions at a surface between two regions. We know by the uniqueness principle, that any solution to the wave equation that satisfies the boundary conditions must be the correct solution. This encourages us to consider a piecewise continuous electromagnetic field and set of Green functions.

The effect of a piecewise continuous field is that the first volume integral encountered in Equation (72) in Appendix A does not vanish giving us

$$\underbrace{\begin{bmatrix} \boldsymbol{E}_\alpha \\ \boldsymbol{H}_\alpha \end{bmatrix}}_{|\phi_\alpha\rangle} = |\phi_\alpha^0\rangle - \oint_{S_\alpha} \underbrace{\begin{bmatrix} \overleftrightarrow{\boldsymbol{G}}^{EE} & \overleftrightarrow{\boldsymbol{G}}^{EH} \\ \overleftrightarrow{\boldsymbol{G}}^{HE} & \overleftrightarrow{\boldsymbol{G}}^{HH} \end{bmatrix}}_{\Gamma_\alpha} \cdot \underbrace{\begin{bmatrix} \hat{\boldsymbol{n}} \times \boldsymbol{H}_\alpha \\ \boldsymbol{E}_\alpha \times \boldsymbol{n} \end{bmatrix}}_{|\xi_\alpha\rangle} dS \tag{11}$$

where $\left|\phi_\alpha^0\right\rangle$ is the field due to sources embedded within the region

$$\left|\phi_\alpha^0\right\rangle \equiv \frac{4\pi}{c}\Gamma_\alpha * \underbrace{\begin{bmatrix} -i\omega \boldsymbol{P} \\ -i\omega \boldsymbol{M} \end{bmatrix}}_{\left|\sigma\right\rangle}. \tag{12}$$

We have introduced six component electromagnetic field vectors as kets to simplify the notation to follow. It is worth reminding the reader that the normal in the surface integral is the outward pointing normal with respect to region α to prevent confusion about the sign. This is essentially Huygen's principle for the electromagnetic field [62]. The above is often called the equivalence principle because it relates the field within a region to the field generated by an equivalent current $(\hat{\boldsymbol{n}}_j \times \boldsymbol{H}_j, \boldsymbol{E}_j \times \hat{\boldsymbol{n}}_j)^T$ on the boundary of the region [10, 11, 61]. The above equation is valid for any point within the region V_α. When the observation point is on the surface of the region, a factor of $1/2$ is acquired on the surface integral

$$\left|\phi_\alpha\right\rangle = \left|\phi_\alpha^0\right\rangle - \frac{1}{2}\oint_{S_\alpha} \Gamma_\alpha \cdot \left|\xi_\alpha\right\rangle dS, \quad \boldsymbol{r} \in S_\alpha. \tag{13}$$

This is due to isolating the singularity in the dyadic Green function when the observation and source point are the same [10, 40].

To find the field in a given region, we return to our original specification of the system. We reiterate that we are considering a system of N objects embedded in a background. This means that the field in each region can be written as

$$\left|\phi_0(\boldsymbol{r})\right\rangle = \left|\phi_0^0(\boldsymbol{r})\right\rangle + \sum_{\alpha=1}^{N} \oint_{S_\alpha} \Gamma_0(\boldsymbol{r}, \boldsymbol{x}) \cdot \left|\xi_\alpha(\boldsymbol{x})\right\rangle dS(\boldsymbol{x}) \tag{14a}$$

$$\left|\phi_\alpha(\boldsymbol{r})\right\rangle = \left|\phi_\alpha^0(\boldsymbol{r})\right\rangle - \oint_{S_\alpha} \Gamma_\alpha(\boldsymbol{r}, \boldsymbol{x}) \cdot \left|\xi_\alpha(\boldsymbol{x})\right\rangle dS(\boldsymbol{x}) \tag{14b}$$

where we have taken the normal at each surface to point from volume V_α into the background V_0. To further simplify notation, we define the operator over the surface as

$$\mathbb{G}_\alpha^\beta \left|\psi\right\rangle \equiv \oint_{S_\beta} \Gamma_\alpha(\boldsymbol{r}, \boldsymbol{x}) \cdot \left|\psi\right\rangle dS(\boldsymbol{x}). \tag{15}$$

In this equation, the notation on $\mathbb{G}$ is: the upper index β refers to the surface of integration and the lower index refers to the electromagnetic properties used in evaluating the Green function. In this new notation, the field in each region becomes

$$\big|\phi_0(\boldsymbol{r})\big\rangle = \big|\phi_0^0(\boldsymbol{r})\big\rangle + \sum_{\alpha=1}^{N} \mathbb{G}_0^\alpha \big|\xi_\alpha\big\rangle \tag{16}$$

$$\big|\phi_\alpha(\boldsymbol{r})\big\rangle = \big|\phi_\alpha^0(\boldsymbol{r})\big\rangle - \mathbb{G}_\alpha^\alpha \big|\xi_\alpha\big\rangle. \tag{17}$$

To complete the specification of the problem, we must introduce a suitable inner product [28]. For the problem at hand, we take

$$\big\langle\phi\big|\psi\big\rangle_{S_\alpha} \equiv \iint \begin{bmatrix}\boldsymbol{\phi}_e(\boldsymbol{r}), & \boldsymbol{\phi}_m(\boldsymbol{r})\end{bmatrix}^* \cdot \begin{bmatrix}\boldsymbol{\psi}_e(\boldsymbol{r}) \\ \boldsymbol{\psi}_m(\boldsymbol{r})\end{bmatrix} dS(\boldsymbol{r}). \tag{18}$$

We now use the method of moments to discretize the system [28, 62]. We introduce a set of basis functions $\{\big|f_\alpha^n\big\rangle\}$ on each surface. We then expand the unknown surface currents at surface α as $\big|\xi_\alpha\big\rangle \approx \sum_n x_\alpha^n \big|f_\alpha^n\big\rangle$. This, in turn, allows us to approximate the field as

$$\big|\phi_0(\boldsymbol{r})\big\rangle = \big|\phi_0^0(\boldsymbol{r})\big\rangle + \sum_{\alpha=1}^{N}\sum_n x_\alpha^n \mathbb{G}_0^\alpha \big|f_\alpha^n\big\rangle \tag{19}$$

$$\big|\phi_\alpha(\boldsymbol{r})\big\rangle = \big|\phi_\alpha^0(\boldsymbol{r})\big\rangle - \sum_n x_\alpha^n \mathbb{G}_\alpha^\alpha \big|f_\alpha^n\big\rangle. \tag{20}$$

The indexing convention used is: Greek letters indicate an object or the background and Roman letters indicate to a particular basis function defined on the surface α To find the unknown coefficients for the effective surface currents $\{x_\alpha^n\}$, we apply the boundary conditions $\hat{\boldsymbol{n}}_\alpha \times (\big|\phi_0\big\rangle - \big|\phi_\alpha\big\rangle) = 0$ at the surface of α and use a Galerkin set of testing functions [28]. Equating the tangential components of the field across the surface we find

$$\big\langle f_\alpha^m\big|\phi_\alpha^0\big\rangle_{S_\alpha} - \big\langle f_\alpha^m\big|\phi_0^0\big\rangle_{S_\alpha} = \sum_n x_\alpha^n \big\langle f_\alpha^m\big|\mathbb{G}_\alpha^\alpha\big|f_\alpha^n\big\rangle_{S_\alpha} + \sum_n\sum_\beta x_\beta^n \big\langle f_\alpha^m\big|\mathbb{G}_0^\beta\big|f_\beta^n\big\rangle_{S_\alpha}. \tag{21}$$

Taking the tangential projections of the incident field as $s_\alpha^m = \big\langle f_\alpha^m\big|\phi_\alpha^0\big\rangle_{S_\alpha} - \big\langle f_\alpha^m\big|\phi_0^0\big\rangle_{S_\alpha}$, we

can form the system of equations

$$\overline{\overline{\boldsymbol{W}}}^{-1}\overline{\boldsymbol{x}} = \overline{\boldsymbol{s}} \tag{22}$$

where $\overline{\boldsymbol{x}} = [\overline{\boldsymbol{x}}_1, \ldots, \overline{\boldsymbol{x}}_N]^T = [(x_1^1, \ldots, x_1^M)^T, \ldots, (x_N^1, \ldots, x_N^{M'})^T]^T$ is the concatenation of the expansion coefficients and $\overline{\boldsymbol{s}} = [\overline{\boldsymbol{s}}_1, \ldots, \overline{\boldsymbol{s}}_N]^T$ is the concatenation of the tangential projections. In the above, we have defined

$$\overline{\overline{\boldsymbol{W}}}^{-1} = \begin{pmatrix} \overline{\overline{\boldsymbol{G}}}_{0,11} & \overline{\overline{\boldsymbol{G}}}_{0,12} & \cdots \\ \overline{\overline{\boldsymbol{G}}}_{0,21} & \overline{\overline{\boldsymbol{G}}}_{0,22} & \\ \vdots & & \ddots \end{pmatrix} + \sum_{\alpha} \begin{pmatrix} 0 & 0 & 0 \\ 0 & \overline{\overline{\boldsymbol{G}}}_{\alpha,\alpha\alpha} & \cdots \\ 0 & \vdots & \ddots \end{pmatrix} \tag{23}$$

where the elements of the block matrices are $G^{nm}_{\alpha,\beta\gamma} \equiv \left\langle f^n_\beta \middle| \mathbb{G}^\gamma_\alpha \middle| f^m_\gamma \right\rangle_{S_\beta}$ [61]. The matrix under the summation is simply a diagonal block matrix with the (α, α) block corresponding to the interaction of the fields through the internal material of region α. This system of equations is well known from the study of electromagnetic scattering.

By appropriate choice of basis function to perform the expansion, a variety of methods can be reproduced. One of the most common choices for performing the expansion is solutions to the homogeneous wave equation in spherical coordinates [47, 53, 62, 71, 76]. This choice of basis functions is commonly known as Mie scattering, the T-matrix method, or the extended boundary condition method [11]. The first name derives from the fact that Mie applied this method to the study of spheres [46], and the last name derives from the fact that the method extends the boundary condition to the smallest nonoverlapping spherical surface that circumscribes the object. It is common practice to use a cylindrical or ellipsoidal basis set to exploit the geometry of the regions [58]. When the objects in the system have surfaces that align with a coordinate system, the matrix above becomes diagonal. When the objects do not align with the chosen coordinate system, the matrix is not diagonal. Additionally, each object in the system is restricted to exist within a region of constant radial component of the coordinate system that does not overlap the region of any other object. In spherical coordinates, this means that each object must be contained within the smallest sphere that circumscribes the object, and these sphere cannot overlap.

Two challenges arise with this method for closely space objects. The first is when the surfaces cannot be circumscribed by mutually exclusive surfaces of constant radial value. As mentioned above, this is a violation of the expansion. The second issue is when the regions are close compared with the wavelength. The extended boundary condition method relies on computing Hankel functions to transform between coordinate systems centered on the objects. The argument to the Hankel functions is proportional to d/λ where d is the separation between the object centers. When this value is small, the Bessel function of the second kind does not converge using standard computational methods so the Hankel function cannot be evaluated. This in turn restricts the interaction between two surfaces to a single scattering event [36, 42]. An alternative method is the boundary element method. In this approach, we segment the surfaces into meshes of triangular facets and define the basis functions over neighboring pairs of facets on the same surface [61]. This formally removes restrictions on the separation of the regions. In either case, libraries are available to assist in computing the elements of the matrices above. Later in this work we will use the boundary element method. Therefore, we will refer to $\overline{\overline{\boldsymbol{W}}}$ as the boundary element method matrix.

2.4 Energy Incident on an Isolated Object

A second advantage of this formalism is that we are able to adapt it to the computation of the energy passing into a surface. We now apply the formalism of Rodriguez, Reid, and Johnson to find the energy passing into a volume due to currents in the background [61]. The primary difference from Rodroguez, Reid, and Johnson's derivation is that we will correct a factor of 1/2 omitted in that prior work.

The power passing through the surface S_α is simply the Poynting vector integrated over

the surface. Adapting this to the bra-ket notation of the previous section we find

$$\begin{aligned} H_{0\to\alpha}(t) &= \frac{c}{4\pi}\oint_{S_\alpha} \hat{\boldsymbol{n}}\cdot\langle \boldsymbol{E}(t)\times\boldsymbol{H}(t)\rangle\, dS \\ &= \frac{c}{4\pi}\Re\int_0^\infty \frac{d\omega}{\pi}\int_{-\infty}^\infty \frac{d\omega'}{2\pi}\oint_{S_\alpha} -\left[\hat{\boldsymbol{n}}\times\boldsymbol{H}^*(-\omega')\right]\cdot\boldsymbol{E}(\omega)\, dS e^{-i(\omega+\omega')t} \\ &= -\frac{c}{8\pi}\Re\int_0^\infty \frac{d\omega}{\pi}\oint_{S_\alpha} \left[\hat{\boldsymbol{n}}\times\boldsymbol{H}^*(-\omega')\right]\cdot\boldsymbol{E}(\omega) - \left[\hat{\boldsymbol{n}}\times\boldsymbol{E}^*(-\omega')\right]\cdot\boldsymbol{H}(\omega)\, dS \\ &= -\int_0^\infty \frac{d\omega}{\pi}\frac{c}{16\pi}\Re\big\langle\xi_\alpha\big|\phi_0\big\rangle_{S_\alpha} \end{aligned} \tag{24}$$

where we have anticipated the fluctuation-dissipation theorem and introduced the $2\pi\delta(\omega+\omega')$ to remove one of the integrations in the second step and exploited the realness of the power in the last step. We introduced an additional factor of $1/2$ because we are evaluating the field on the surface [40]. For simplicity, we can work with the spectral components directly to write

$$H_{0\to\alpha}(t) = \int_0^\infty \Phi(\omega)d\omega \tag{25}$$

$$\begin{aligned} \Phi_{0\to\alpha}(\omega) &\equiv -\frac{c}{16\pi^2}\Re\big\langle\xi_\alpha\big|\phi_0\big\rangle_{S_\alpha} \\ &= \frac{c}{16\pi^2}\Re\big\langle\xi_\alpha\big|\phi_\alpha\big\rangle_{S_\alpha} \\ &= \frac{c}{16\pi^2}\Re\big\langle\xi_\alpha\big|\mathbb{G}_\alpha^\alpha\big|\xi_\alpha\big\rangle_{S_\alpha}. \end{aligned} \tag{26}$$

Next, we can expand the unknown currents on the surface in terms of the basis functions for the boundary element method matrix $\big|\xi_\alpha\big\rangle \approx \sum_n x_\alpha^n\big|f_\alpha^n\big\rangle$ to find

$$\begin{aligned} \Phi_{0\to\alpha}(\omega) &= \frac{c}{16\pi^2}\Re\sum_{n,m} x_\alpha^{n*}x_\alpha^m\big\langle f_\alpha^n\big|\mathbb{G}_\alpha^\alpha\big|f_\alpha^m\big\rangle \\ &= \frac{c}{32\pi^2}\sum_{n,m}(x_\alpha^{n*}x_\alpha^m G_{\alpha,\alpha\alpha}^{nm} + x_\alpha^n x_\alpha^{m*}G_{\alpha,\alpha\alpha}^{nm*}) \\ &= \frac{c}{16\pi^2}\sum_{n,m} x_\alpha^{n*}\frac{1}{2}(G_{\alpha,\alpha\alpha}^{nm} + G_{\alpha,\alpha\alpha}^{nm*})x_\alpha^m \\ &= \frac{c}{16\pi^2}\overline{\boldsymbol{x}}_\alpha^\dagger \mathrm{sym}\overline{\overline{\boldsymbol{G}}}_{\alpha,\alpha\alpha}\overline{\boldsymbol{x}}_\alpha. \end{aligned} \tag{27}$$

On the third line, we have simply swapped the summation indexes on the second term. We also introduce the Hermitian portion of the self-interaction matrix $\mathrm{sym}\overline{\overline{\boldsymbol{G}}}_{\alpha,\alpha\alpha} \equiv (\overline{\overline{\boldsymbol{G}}}_{\alpha,\alpha\alpha} + \overline{\overline{\boldsymbol{G}}}^{\dagger}_{\alpha,\alpha\alpha})/2$ to convert to matrix notation in the final step. We can use the boundary element method matrix to relate the power passing into the surface due to sources in the background as

$$\begin{aligned}\Phi_{0\to\alpha}(\omega) &= \frac{c}{16\pi^2}\overline{\boldsymbol{s}}^{\dagger}\overline{\overline{\boldsymbol{W}}}^{\dagger}\mathrm{sym}\overline{\overline{\boldsymbol{G}}}_{\alpha,\alpha\alpha}\overline{\overline{\boldsymbol{W}}}\,\overline{\boldsymbol{s}} \\ &= \frac{c}{16\pi^2}\mathrm{Tr}\left[\overline{\overline{\boldsymbol{W}}}^{\dagger}\mathrm{sym}\overline{\overline{\boldsymbol{G}}}_{\alpha,\alpha\alpha}\overline{\overline{\boldsymbol{W}}}\,\overline{\boldsymbol{s}}\,\overline{\boldsymbol{s}}^{\dagger}\right]. \end{aligned} \tag{28}$$

In this last expression, the sources are described by the Hermitian matrix $\overline{\boldsymbol{s}}\,\overline{\boldsymbol{s}}^{\dagger}$. If we take the sources to be fluctuating currents in the background, we can perform an ensemble average over all possible fluctuations to find

$$\left\langle \overline{\boldsymbol{s}}\,\overline{\boldsymbol{s}}^{\dagger}\right\rangle = \overline{\overline{\boldsymbol{C}}}_0 \tag{29a}$$

$$\begin{aligned} C_0^{nm} &= \left\langle \left\langle f_\alpha^n \middle| \phi_0^0\right\rangle\left\langle \phi_0^0 \middle| f_\alpha^m\right\rangle\right\rangle \\ &= \left(\frac{4\pi}{c}\right)^2 {}_{S_0}\!\left\langle f_\alpha^n\middle|\left\langle \middle|\Gamma_0 * \sigma\right\rangle\left\langle \Gamma_0 * \sigma\middle|\right\rangle\middle| f_\alpha^m\right\rangle_{S_0} \\ &= \left(\frac{4\pi}{c}\right)^2 {}_{S_0}\!\left\langle f_\alpha^n\middle|\Gamma_0 * \left\langle \middle|\sigma\right\rangle\left\langle \sigma\middle|\right\rangle * \Gamma_0^{\dagger}\middle| f_\alpha^m\right\rangle_{S_0}. \end{aligned} \tag{29b}$$

Simple inspection shows us that the source terms above are simply those we considered in the fluctuation-dissipation theorem in Appendix B

$$\begin{aligned}\left\langle \middle|\sigma\right\rangle\left\langle \sigma\middle|\right\rangle &= \omega^2\begin{pmatrix}\langle \boldsymbol{PP}\rangle & \langle \boldsymbol{PM}\rangle \\ \langle \boldsymbol{MP}\rangle & \langle \boldsymbol{MM}\rangle\end{pmatrix} \\ &= \frac{\hbar\omega^2}{4\pi}\coth\left(\frac{\hbar\omega}{2k_BT}\right)\Im\begin{pmatrix}\overleftrightarrow{\boldsymbol{\varepsilon}} & 0 \\ 0 & \overleftrightarrow{\boldsymbol{\mu}}\end{pmatrix}2\pi\delta(\omega+\omega'). \end{aligned} \tag{30}$$

This leaves us with

$$C_\alpha^{nm} = \frac{8\pi\omega}{c^2}\left[\Theta_0(\omega) + \Theta(\omega,T)\right]\left\langle f_\alpha^n\middle|\Gamma_0 * \Im\chi_0 * \Gamma_0^{\dagger}\middle| f_\alpha^m\right\rangle \tag{31}$$

where we omit the delta function because we have already anticipated its presence in Equation (24). We have also introduced the susceptibility tensor $\chi \equiv \begin{pmatrix} \overleftrightarrow{\varepsilon} & 0 \\ 0 & \overleftrightarrow{\mu} \end{pmatrix}$.

We now ask ourselves, what is the surface of integration over which the coefficients are defined? The answer is the surface bounding the background. Because we are considering an object isolation, this means the surface S_α and the boundary at infinity

$$s_0^n = \oint_{S_\alpha} \langle \sigma | * \Gamma_0 \cdot | f_\alpha^n \rangle \, dS + \oint_{S_\infty} \langle \sigma | * \Gamma_0 \cdot | f_\infty^n \rangle \, dS. \tag{32}$$

However, the Green function must satisfy the radiation condition at infinity. This means that the surface integral at infinity must vanish and we only need to consider the integral over surface S_α. This is equivalent to integrating over the background "dust" to determine the power radiated by an object in isolation [6, 36]. Thus, the power absorbed by a object in isolation is governed by the material properties of the region bounded by S_α and the matrix $\overline{\overline{C}}_0$.

To get a better understanding of the elements of $\overline{\overline{C}}_0$, let us consider the mechanical work done by the electromagnetic field on the background material due to electric currents in the background

$$\rho_0 C_{p,0} V_0 \frac{dT}{dt} = -\int_{V_0} \langle \boldsymbol{E}(t) \cdot \boldsymbol{J}(t) \rangle \, d^3 r \tag{33}$$

where ρ_0 is the density, $C_{p,0}$ is the specific heat capacity at constant pressure, and V_0 is the volume of the external region. Considering the Fourier components of the field and current and substituting in the Maxwell equations, we find

$$\begin{aligned}
\rho_0 C_{p,0} V_0 \frac{dT}{dt} &= -\int_{V_0} \frac{c}{4\pi} \int_{-\infty}^{\infty} \frac{d\omega}{2\pi} \int_{-\infty}^{\infty} \frac{d\omega'}{2\pi} \left\langle \boldsymbol{E}^*(-\omega) \cdot \Big(ik_0 \boldsymbol{D}(\omega) + \boldsymbol{\nabla} \times \boldsymbol{H}(\omega) \Big) \right\rangle d\tau \\
&= -\frac{c}{4\pi} \int_{-\infty}^{\infty} \frac{d\omega}{2\pi} \int_{-\infty}^{\infty} \frac{d\omega'}{2\pi} \int_{V_0} ik_0 \left\langle \boldsymbol{E}^* \cdot \overleftrightarrow{\varepsilon}_0 * \boldsymbol{E} \right\rangle \\
&\qquad + \langle \boldsymbol{H} \cdot \boldsymbol{\nabla} \times \boldsymbol{E}^* \rangle - \boldsymbol{\nabla} \cdot \langle \boldsymbol{E}^* \times \boldsymbol{H} \rangle \, d\tau \\
&= -\frac{c}{4\pi} \int_{V_0} \int_{-\infty}^{\infty} \frac{d\omega}{2\pi} \int_{-\infty}^{\infty} \frac{d\omega'}{2\pi} ik_0 \left\langle \boldsymbol{E}^* \cdot \overleftrightarrow{\varepsilon}_0 * \boldsymbol{E} \right\rangle \\
&\qquad + ik_0 \left\langle \boldsymbol{H}^* \cdot \overleftrightarrow{\mu}_0 * \boldsymbol{H} \right\rangle - \boldsymbol{\nabla} \cdot \langle \boldsymbol{E}^* \times \boldsymbol{H} \rangle \, d\tau.
\end{aligned} \tag{34}$$

Transforming to our bra-ket notation we get

$$\begin{aligned}\rho_0 C_{p,0} V_0 \frac{\Delta T}{\Delta t} &= \int_{-\infty}^{\infty} \frac{d\omega}{2\pi} \int_{-\infty}^{\infty} \frac{d\omega'}{2\pi} \Big[-\frac{1}{4\pi} \big\langle \phi_0^*(-\omega') \big| * (i\omega\chi_0) * \big| \phi_0(\omega) \big\rangle \\ &\qquad + \frac{c}{8\pi} \big\langle \xi_0^*(-\omega') \big| \phi_0(\omega) \big\rangle_{S_0} \Big] e^{-i(\omega+\omega')} \\ &= \int_0^{\infty} \frac{d\omega}{\pi} \frac{c}{8\pi} \Re \big\langle \xi_0 \big| \phi_0 \big\rangle_{S_0} - \frac{1}{4\pi} \Re \big\langle \phi_0 \big| * (i\omega\chi_0) * \big| \phi_0 \big\rangle \end{aligned} \tag{35}$$

where we have preemptively extracted the $2\pi\delta(\omega + \omega')$ from the fluctuation-dissipation theorem, and we have introduced the factor of $1/2$ necessary when evaluating the field on a boundary [40]. We have also used the realness of the work to consider only positive frequencies.

We already recognize the first term on the right-hand side as the Poynting vector integrated over the boundary of the external region. However, as we have already pointed out, the integral over infinity is zero. This means that we can simply consider the integral over the surface S_α. The second term on the right is the energy density associated with the electromagnetic field [26]. A bit of manipulation reveals

$$\begin{aligned} \Re \big\langle \phi_0 \big| * (i\omega\chi_0) * \big| \phi_0 \big\rangle &= -\Im \big\langle \phi_0 \big| * (\omega\chi_0) * \big| \phi_0 \big\rangle \\ &= -\frac{\omega}{2i} \Big(\big\langle \phi_0 \big| * \chi_0 * \big| \phi_0 \big\rangle - \big\langle \phi_0 \big| * \chi_0^\dagger * \big| \phi_0 \big\rangle \Big) \\ &= -\omega \big\langle \phi_0 \big| * \frac{\left(\chi_0 - \chi_0^\dagger \right)}{2i} * \big| \phi_0 \big\rangle \\ &= -\omega \big\langle \xi_0 \big| \mathbb{G}_0^{\alpha,\dagger} * \Im\chi_0 * \mathbb{G}_0^{\alpha} \big| \xi_0 \big\rangle \\ &= -\omega \, {}_{S_\alpha}\big\langle \xi_0 \big| \Gamma_0^\dagger * \Im\chi_0 * \Gamma_0 \big| \xi_0 \big\rangle_{S_\alpha} \end{aligned} \tag{36}$$

Inserting our expansion $\big|\xi_\alpha\big\rangle \approx \sum_n x_\alpha^n \big| f_\alpha^n \big\rangle$ we find

$$\begin{aligned} \Re \big\langle \phi_0 \big| * (i\omega\chi_0) * \big| \phi_0 \big\rangle &= -\omega \sum_{n,m} x_\alpha^{n*} x_\alpha^m \, {}_{S_0}\big\langle f_\alpha^n \big| \Gamma_0^\dagger * \Im\chi_0 * \Gamma_0 \big| f_\alpha^m \big\rangle_{S_0} \\ &= -\omega \frac{c^2}{8\pi\omega} \left[\Theta_0(\omega) + \Theta(\omega, T_0) \right]^{-1} \overline{\boldsymbol{x}}^\dagger \overline{\overline{\boldsymbol{C}}}_0^\dagger \overline{\boldsymbol{x}} \end{aligned} \tag{37}$$

where we have identified the $\overline{\overline{\boldsymbol{C}}}_0$ matrix from above. This allows us to write the power

dissipated by the fluctuating currents in the background as

$$\rho_0 C_{p,0} V_0 \frac{dT}{dt} = \frac{c}{8\pi} \int_0^\infty \frac{d\omega}{\pi} \overline{\boldsymbol{x}}^\dagger \left(\frac{c}{4\pi} \left[\Theta_0(\omega) + \Theta(\omega, T_0) \right]^{-1} \overline{\overline{\boldsymbol{C}}}_0^\dagger - \mathrm{sym} \overline{\overline{\boldsymbol{G}}}_{0,\alpha\alpha} \right) \overline{\boldsymbol{x}}. \tag{38}$$

Let us now pause to consider what we have just written down. The left-hand side is the mechanical energy lost by the material in the background due to radiation by the fluctuating currents within the material. The first term on the right-hand side derives from the energy stored in the electromagnetic field within the background region. This shows that the fluctuation-dissipation theorem relates the change in the mechanical energy to the change in the energy stored in the electromagnetic fields. We have already established that the last term on the right-hand side is the power passing through the surface S_α due to current sources in the background medium. The analysis of the thermally dynamic system requires consideration of all three terms of this expression. The common practice is to consider the time averaged value of the temperature change. The right-hand side remains the same, and the temperature dependence becomes $\frac{1}{\Delta t} \int_0^{\Delta t} \partial_t T dt = \Delta T / \Delta t$. There have been limited considerations of quasistatic changes [36], but the common practice is to assume a stationary state as we have. This simplification dictates that the temperature does not change. This provides us with the simple relationship between the elements of $\overline{\overline{\boldsymbol{C}}}_0$ and $\mathrm{sym}\overline{\overline{\boldsymbol{G}}}_{0,\alpha\alpha}$

$$\overline{\overline{\boldsymbol{C}}}_0 = \frac{4\pi}{c} \left[\Theta_0(\omega) + \Theta(\omega, T_0) \right] \mathrm{sym} \overline{\overline{\boldsymbol{G}}}_{0,\alpha\alpha}^\dagger \tag{39}$$

so long as they are under the Fourier integral.

Substituting this result into Equation (28), we find that the energy incident on the surface S_α due to current sources in the background is

$$\Phi_{0\to\alpha} = \frac{1}{4\pi} \left[\Theta_0(\omega) + \Theta(\omega, T_0) \right] \mathrm{Tr} \left[\overline{\overline{\boldsymbol{W}}}^\dagger \, \mathrm{sym} \overline{\overline{\boldsymbol{G}}}_{\alpha,\alpha\alpha} \, \overline{\overline{\boldsymbol{W}}} \, \mathrm{sym} \overline{\overline{\boldsymbol{G}}}_{0,\alpha\alpha} \right]. \tag{40}$$

2.5 Net Energy Exchange between Objects

In the previous section, we established the energy incident on the surface S_α due current sources in the background. To find the net energy passing through the surface, we also need

to know what the value of the Poynting vector is due to currents within the region bounded by S_α. Symmetry considerations allow us to derive this by simply exchanging the indices in the above analysis, $0 \leftrightarrow \alpha$. The net energy exchange between V_α and the background is simply the difference of the two results

$$\Phi_{0\to\alpha} = \frac{1}{4\pi}\left[\Theta(\omega, T_\alpha) - \Theta(\omega, T_0)\right] \mathrm{Tr}\left[\overline{\overline{\boldsymbol{W}}}^{\dagger}\, \mathrm{sym}\overline{\overline{\boldsymbol{G}}}_{\alpha,\alpha\alpha}\, \overline{\overline{\boldsymbol{W}}}\, \mathrm{sym}\overline{\overline{\boldsymbol{G}}}_{0,\alpha\alpha}\right]. \tag{41}$$

This result also allows us to derive the net exchange between two objects α and β. By simple extension of the logic used above, we can readily deduce that for two bodies embedded in a common background, the net exchange between them will be

$$\Phi_{\beta\to\alpha} = \frac{1}{4\pi}\left[\Theta(\omega, T_\alpha) - \Theta(\omega, T_\beta)\right] \mathrm{Tr}\left[\overline{\overline{\boldsymbol{W}}}^{\dagger}\, \mathrm{sym}\overline{\overline{\boldsymbol{G}}}_{\alpha,\alpha\alpha}\, \overline{\overline{\boldsymbol{W}}}\, \mathrm{sym}\overline{\overline{\boldsymbol{G}}}_{\beta,\beta\beta}\right]. \tag{42}$$

It is worth noting that this answer differs from a recently reported answer by a factor of 1/2 [61]. This appears to be due to a missed factor of 1/2 while applying the fluctuation-dissipation theorem in the prior work. Plugging this in, we find that the electromagnetic energy passing into volume V_α due to sources in volume V_β is

$$H_{\beta\to\alpha}(T_\alpha, T_\beta) = \int_0^\infty \left[\Theta(\omega, T_\beta) - \Theta(\omega T_\alpha)\right] \sum_n \left[\overline{\overline{\boldsymbol{W}}}^{\dagger}\, \mathrm{sym}\overline{\overline{\boldsymbol{G}}}_{\alpha,\alpha\alpha}\, \overline{\overline{\boldsymbol{W}}}\, \mathrm{sym}\overline{\overline{\boldsymbol{G}}}_{\beta,\beta\beta}\right]_{nn} \frac{d\omega}{4\pi}. \tag{43}$$

From the definition of the boundary element method matrix, $\overline{\overline{\boldsymbol{W}}}$, we see that the diagonal elements of the product matrix are simply the energy associated with each basis function use to discretize the problem

2.6 Conclusions

In this chapter we have reviewed the mathematical formalism necessary to evaluate the electromagnetic energy passing through a surface due to fluctuating currents in two configurations: an object in isolation interacting with the background and separate objects embedded in a common background. This flux is the source of the enhanced radiative energy exchange when the separation between the surfaces becomes small compared to the

thermal wavelength. We have also provided a detailed discussion for equating the elements of the correlation matrix, $\overline{\overline{\boldsymbol{C}}}$, and the Hermitian portion of the self-interaction matrix, $\mathrm{sym}\overline{\overline{\boldsymbol{G}}}_{\alpha,\alpha\alpha}$, Equation (39). We are able to equate the matrix elements only when the mechanical energy dissipated in the background vanishes. To achieve this, we consider a steady state configuration such that the temperatures of all objects and the background are fixed. With the formal solution in place, we can now select a set of basis functions to discretize the problem domain and implement a numerical method to evaluate the energy exchange in a steady state system.

CHAPTER III

NUMERICAL IMPLEMENTATION

3.1 Introduction

With the mathematical formalism in place, we turn our attention to the implementation of a numerical method to compute the energy exchange between two objects. Using an open source library as a back end, we implemented a package in Python to interface with the library and perform the basic calculations. We also implemented a script to handle the high level logic to compute the spectral distribution of the energy exchange across a single geometry and batching of multiple geometries. In this chapter, we review the structure of the software, discuss the verification process, and close with an investigation of the convergence properties of the routine.

3.2 Software Description

The energy exchanged between two objects is governed by the equation, as demonstrated in Chapter 2,

$$H_{\beta\to\alpha}(T_\alpha, T_\beta) = \int_0^\infty [\Theta(\omega, T_\beta) - \Theta(\omega T_\alpha)] \sum_n \left[\overline{\overline{\boldsymbol{W}}}^\dagger \, \mathrm{sym}\overline{\overline{\boldsymbol{G}}}_{\alpha,\alpha\alpha} \, \overline{\overline{\boldsymbol{W}}} \, \mathrm{sym}\overline{\overline{\boldsymbol{G}}}_{\beta,\beta\beta} \right]_{nn} \frac{d\omega}{4\pi}. \quad (44)$$

Evaluation of this expression is dependent on the choice of basis functions used to evaluate the matrix elements. When the surfaces are shapes that are compatible with a coordinate system that is separable, the matrices become diagonal and a semianalytic expression can be found. For general surfaces, the matrices are not diagonal and one must chose between the T-matrix approach and the boundary element method to populate the matrices. An early attempt was made to implement the T-matrix approach; however, we discovered this approach did not converge for the small separations due to the necessity to evaluate Bessel functions of small arguments. We then found the open source software SCUFF-EM which implements the boundary element method for solving electromagnetic problems [59, 60]

The software SCUFF-EM is a general purpose boundary element method solver for electromagnetic problems. It relies on the equivalence principle to solve for the value of the fields on a boundary as effective surface currents. The primary difference between the SCUFF-EM software and the T-matrix approach is the choice of basis functions. The T-matrix approach uses solutions to the homogeneous vector wave equation as basis functions; whereas, SCUFF-EM uses basis functions defined across the edges of a triangulated mesh of the surfaces in the configuration. An advantage to using basis functions defined by the edges of the faces is the diagonal entries in the matrix $\overline{\overline{\boldsymbol{W}}}^{\dagger}\,\mathrm{sym}\overline{\overline{\boldsymbol{G}}}_{\alpha,\alpha\alpha}\,\overline{\overline{\boldsymbol{W}}}\,\mathrm{sym}\overline{\overline{\boldsymbol{G}}}_{\beta,\beta\beta}$ can be easily mapped to the faces. This provides the power passing through a particular region of space on the surfaces

The software package is broken into two parts: various front ends that solve specific electromagnetic problems and the LIBSCUFF library. This library handles instantiating the geometry of the problem, assigning electromagnetic properties to the regions, and computing the elements of the interaction matrices $\overline{\overline{\boldsymbol{G}}}_{\alpha,\beta\gamma}$. By wrapping this with the native Python C interface, we were able to take advantage of the rapid development cycle and the scientific tools for Python to handle the matrix manipulation [33].

A small wrapper was written in C to handle instantiating a static copy of the native data structure of the library. We then implemented a package to handle the Python side of the interface and collect all of the tools to perform the calculations. This package provides a means to interact with the library in both a script and interactive environment. The API for the package is provided in Appendix D. The basic functionality in the package is: create the LIBSCUFF data structure and compute the elements of the matrix elements, populate the interaction block matrices and solve for the boundary element method matrix $\overline{\overline{\boldsymbol{W}}}$, and compute the energy exchange in the specified physical system. Tools were also developed for writing the flux associated with each basis function to file and reading the file back into memory.

We then implemented a script to handle the high level logic to compute the near-field flux between two objects. The core routine in the script assembles the interaction block matrices by calling methods in LIBSCUFF for a particular frequency. Then, the blocks are assembled into the whole matrix and inverted. Finally, the diagonal elements of the matrix

in Equation (44) are extracted and written to file. The script can also be flagged to create an archive of the source code at start time for reproducibility. The inputs to the script are modeled after the programs included in the SCUFF-EM suite of programs.

The primary input to the core routine is the specification of the scattering geometry. This is handled by the native geometry file for the LIBSCUFF library and is passed directly to the library. This file details the location and orientation of the surfaces in the system. The surface shape is specified by assigning a mesh file to each object. The mesh file specifies the vertexes and the triangular faces that discretize the surface. The format of the mesh file follows the output of the program GMSH which is designed to generate meshes for finite element analysis. In addition to the geometry, the electromagnetic properties of all regions are described in this input file. The secondary input to the program is the frequencies to use for computation in units of the angular wave number $k = 2\pi/\lambda$. The frequencies are specified either individually on the command line or as a list stored in a file.

The main script has two modes of operation: single and batch. In the single mode, the geometry file and frequencies are specified on the command line. This mode works on a single geometry file with potentially multiple frequencies. The batch mode was designed to operate on multiple geometries. In this mode, the frequency and geometry files are listed as pairs in a file that is input at the command line. In either mode, the desired outputs are specified as command line arguments.

While developing the numerical procedure, it was discovered that an issue with data caching exists in the LIBSCUFF library. When the same mesh file is used to define two surfaces, the second surface has self-interaction matrix entries that are twice the correct value. This showed that the library was adding the two results when computing the self-interaction matrix for the second surface $\overline{\overline{\boldsymbol{G}}}_{2,00}$ and not clearing the working storage matrix in the library data structure. The problem with this is that we are not guaranteed the order of the surfaces by the library. This means we could not be sure which of the two matrix blocks was the correct result.

To work around this, a fresh instance of the data structure is created in an isolated process using the MULTIPROCESSING module of Python. This procedure ensures that the

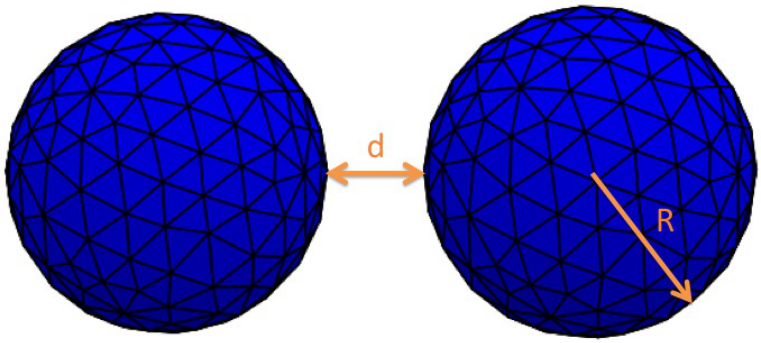

Figure 1: The annotated geometry for the sphere-sphere configuration used in the verification process.

calculation of all self-interaction matrices begin with a unique copy of the library data structure that is not shared across processes. Thus the matrix entries are correctly calculated. Although this introduces the additional overhead of creating and destroying the same data structure multiple times, we take advantage of multiple cores on a machine to offset this increase in computation time. With the software in place, we now turn our attention to verifying the numeric results and investigate the convergence behavior of the algorithm.

3.3 Verification

Before intensive numerical investigation of surface shape effects on near-field energy exchange, the verification of the above program was the first task undertaken with the implemented computation routine. For this task, we consider the standard sphere-sphere geometry used in several studies reported in the literature. The sphere-sphere configuration has been well studied, and published results are available against which we can compare our results. We took the recent results presented by Rodriguez, Reid, and Johnson to be the baseline against which we verified our computational routine [61]. To match their configuration, we constructed identical gold spheres each of radius R=0.200 µm set across a range of separations. Figure 1 presents the annotated geometry used in the verification process.

The electromagnetic properties of the spheres were determined based on the selection of gold as the material. A Drude model for the dielectric function $\varepsilon(\omega) = 1 - \omega_p^2/(\omega^2 + i\gamma\omega)$ with ω_p=$1.37 \times 10^{16}\,\mathrm{rad\,s^{-1}}$ and γ=$5.32 \times 10^{13}\,\mathrm{rad\,s^{-1}}$ was used for the permittivity. The permeability was set to one because gold is nonmagnetic in the frequency range considered. Both surfaces used the same mesh which was discretized using 510 edges.

3.3.1 Numerical Results

Figure 2 presents the initial computed results along with the data points presented by Rodriguez, Reid, and Johnson [61] for comparison. We first consider the inset which presents the spectral distribution of the emission by a sphere in isolation (blue) and the spectral distribution of flux between two spheres separated by one radius (green). The Φ' used here is the same from Chapter 2 but without the oscillator energy function

$$\Phi'(\omega) = \frac{1}{\pi}\mathrm{Tr}\left[\overline{\overline{\boldsymbol{W}}}^{\dagger}\,\mathrm{sym}\overline{\overline{\boldsymbol{G}}}_{1,11}\,\overline{\overline{\boldsymbol{W}}}\,\mathrm{sym}\overline{\overline{\boldsymbol{G}}}_{2,22}\right]. \tag{45}$$

We clearly see that the results are in excellent agreement for both emission and flux. Accounting for the imprecision in extracting the data points and numerical error, we can confidently state that the results are the same.

Now we turn out attention to the main figure. This presents the total heat exchange H with one sphere held at 300 K and the other at 0 K normalized by the classical blackbody results $\sigma A T^4$ where σ is the Stefan-Boltzmann constant and A is the surface area of one sphere. We see that our computed results under predict the total exchange compared with the reference. The discrepancy is largest for the smaller separations and decreases at larger separations. To gain a better understanding of this observation, we must examine the spectral distribution of the flux across the range of separations.

Figure 3 presents the spectral distribution of the flux Φ' between two gold spheres of radius 0.200 µm for all considered separations normalized by the surface area of one sphere. We clearly see a local maximum for longer wavelengths and this maximum becomes more pronounced for the smaller separations. Close examination of the numeric results shows that this maximum is present at the same wavelength of approximately 100 µm at

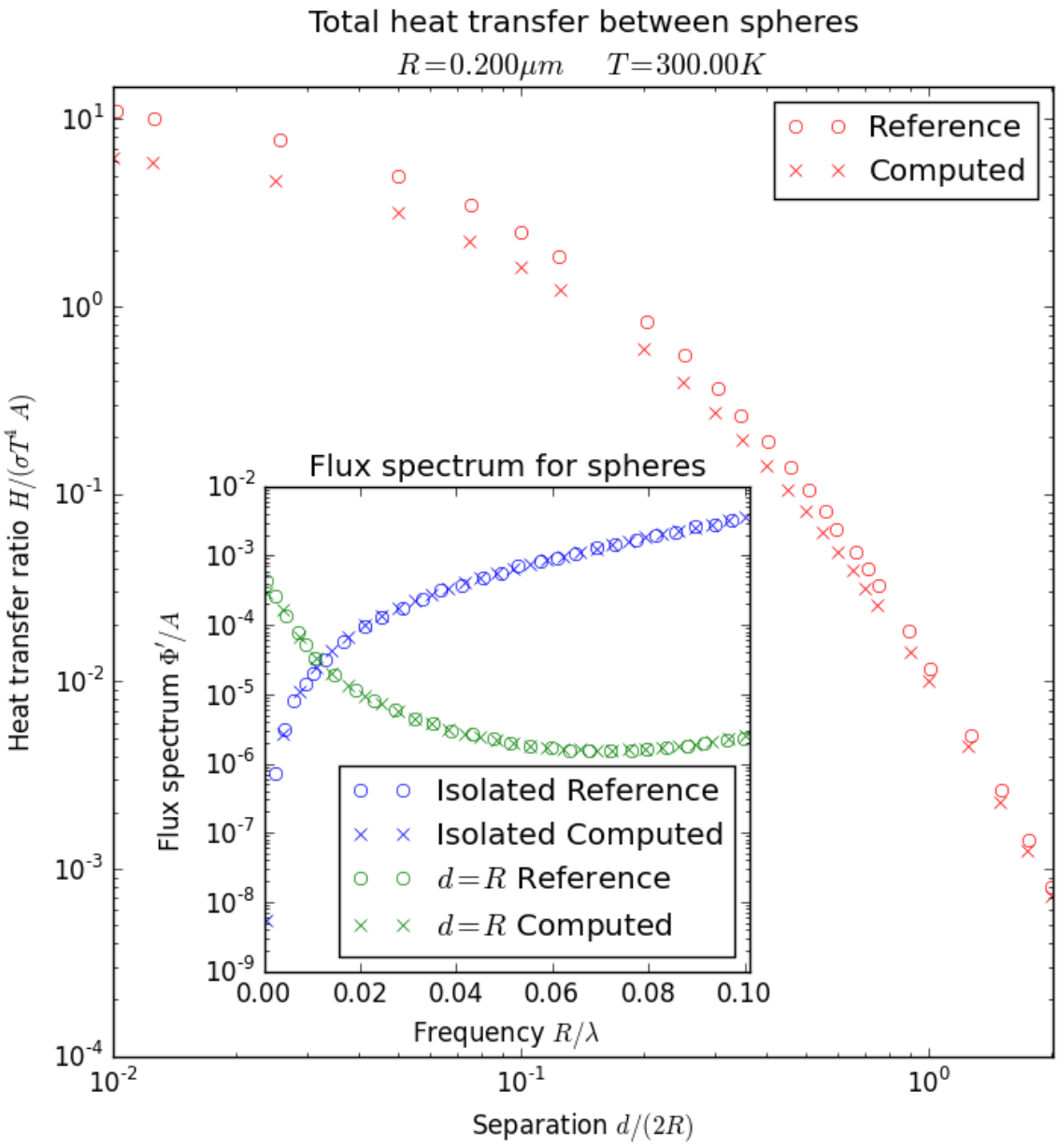

Figure 2: Comparison of calculated results (x) to reference values (o) [61].

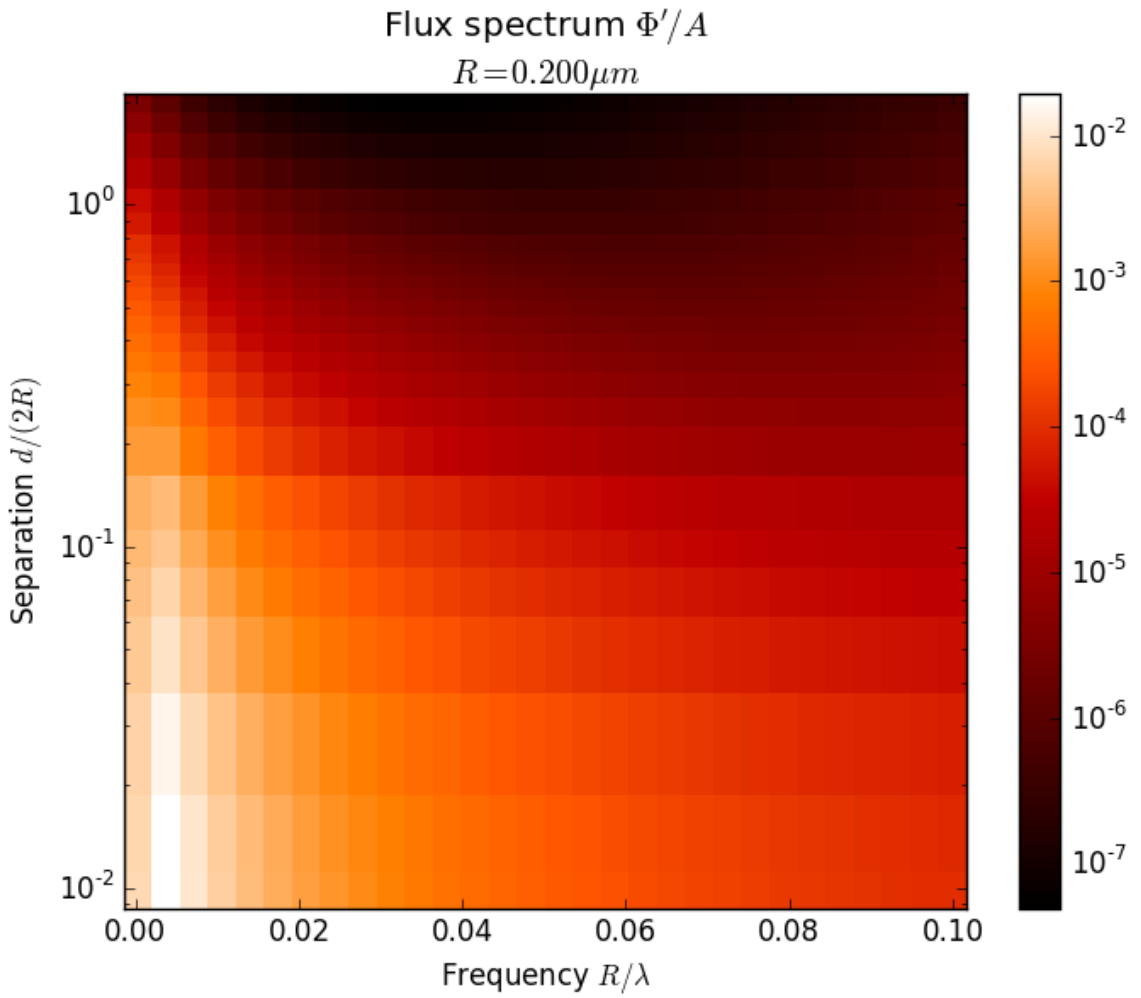

Figure 3: The spectral distribution of the flux between two gold spheres of radius 0.200 µm normalized by the surface area of one sphere.

all separations and is simply more pronounced at the smaller separations. Running the program with an over sampling of frequencies around the maximum reveals that the flux is a smooth function of the frequency at this point. This indicates that this turn over is not necessarily a numerical relic but rather shows a change to a decaying energy exchange at long wavelengths similar to other electromagnetic phenomena.

Considering the range of separations we have here, the linear extent of the sphere-sphere systems are on the order of 1 µm. This is two orders of magnitude smaller than the wavelength where the maximum occurs. Thus, the spatial configuration of the spheres resides in a long wavelength regime. This means we can use different approximations to probe the functional dependence of the flux on the wavelength in this regime. We begin by directly expanding the Poynting vector to get a rudimentary understanding of this functional dependence. After that, we will examine three approximations to test our prediction.

3.3.2 Long Wavelength Approximations

First, we expand the Poynting vector. From Chapter 2, we know that the Poynting vector is proportional to

$$\boldsymbol{S} \propto \Im\left[k^2\Theta(k,T)\overleftrightarrow{\boldsymbol{G}}\cdot\overleftrightarrow{\boldsymbol{\varepsilon}}''\cdot\boldsymbol{\nabla}\times\overleftrightarrow{\boldsymbol{G}}^{\dagger}\right] \tag{46}$$

where we have suppressed the volume integration for simplicity. The dyadic Green function of the system is related to the Green function of a homogeneous space by [41]

$$\overleftrightarrow{\boldsymbol{G}} = \overleftrightarrow{\boldsymbol{G}}_0 + \overleftrightarrow{\boldsymbol{G}}_0\cdot\overleftrightarrow{\boldsymbol{T}}\cdot\overleftrightarrow{\boldsymbol{G}}_0. \tag{47}$$

Inserting the known expression for the homogeneous dyadic Green function [62], we find a power series in k. Keeping the first two terms we find

$$\begin{aligned}
\boldsymbol{S} &\sim \Im\Big[\varepsilon'' \iiint \frac{ik^3}{|\boldsymbol{r}-\boldsymbol{r}'|^3} d^3r' \\
&\quad - \varepsilon'' \iiint \frac{1}{|\boldsymbol{r}-\boldsymbol{r}'|^5} d^3r'\Big] \\
\boldsymbol{S} &\sim \Im\Big[2\pi\varepsilon'' ik^3 r \int_0^{R/r} \frac{u}{2} \ln\frac{1+u}{1-u} du \\
&\quad + \frac{4\pi}{3r^2}\varepsilon'' \int_0^{R/r} \frac{3u^3+u^5}{(1-u^2)^3} du\Big].
\end{aligned} \tag{48}$$

It can be shown that the two integrals above are real finite constants independent of k. Thus, we find

$$\boldsymbol{S} \sim \varepsilon'' k^3 r. \tag{49}$$

If we integrate this over a sphere with a radius R_c that is the characteristic length of the system, we finally arrive at the expression

$$\Phi \sim \varepsilon'' k^3 R_c^3. \tag{50}$$

This tells us that we should predict a power law decay for the flux at long wavelength.

Now that we have our prediction of a power law decay at long wavelengths, we turn our attention to establishing three approximations to test this prediction. First, we note that a black sphere in isolation will radiate according to Planck's Law. The units of Planck's law are

$$\begin{aligned}
I(\omega,T) &= \frac{\omega^2}{4\pi^3 c^2} \frac{\hbar\omega}{e^{\hbar\omega/(k_B T)}-1} \\
&= \Psi(\omega)\Theta(\omega,T) && \text{(51a)} \\
&= \frac{[\text{Power}]}{[\text{Area}]\,[\text{Solid Angle}]\,[\text{Frequency}]} && \text{(51b)}
\end{aligned}$$

with $\Psi(\omega) \equiv [\omega/(2\pi c)]^2$ and $\Theta(\omega,T) \equiv (\hbar\omega)/\left\{\exp[\hbar\omega/(k_B T)]-1\right\}$. Noting the units of the

spectral Poynting vector are

$$\boldsymbol{S} = \frac{[\text{Power}]}{[\text{Area}]\,[\text{Frequency}]}, \tag{52}$$

we can deduce that the blackbody power passing through a sphere of radius r surrounding a black sphere is

$$\boldsymbol{S} \propto \Psi(\omega)\Theta(\omega, T)\frac{D}{r^2}\hat{\boldsymbol{r}} \tag{53}$$

where D/r^2 is a solid angle. Because the blackbody radiation is isotropic, we exploited the symmetry of the sphere to note that the direction of propagation of the Poynting vector must be radial.

Placing a second sphere a distance d away, the total power emitted by the first sphere incident on the second sphere is simply the Poynting vector integrated over the portion of the second spherical surface facing the emitter

$$\begin{aligned}
\Phi'_{a\to b}(\omega, T) &= \oint_{A_b} \boldsymbol{S}(\omega, T)\cdot d\boldsymbol{A} \\
&= \Theta(\omega, T)\Psi(\omega)\iint_{\hat{\boldsymbol{r}}\cdot\hat{\boldsymbol{n}}<1} \frac{D\hat{\boldsymbol{r}}\cdot\hat{\boldsymbol{n}}}{r^2}\, dA_b \\
&= \Theta(\omega, T)\Psi(\omega)C(\omega).
\end{aligned} \tag{54}$$

This surface integral equation establishes a starting point to find three approximations that will aid in our understanding of the local maximum in the flux.

A quick, back of the envelope approximation is to simply assume that all of the energy incident on the second sphere is absorbed; however, this does not account for reflections at the surface of the absorber. A simple means to incorporate reflections is to use the Fresnel transmission coefficients. Even though these are properly derived for a plane wave incident on a planar surface, it will provide us with a basic starting point to account for reflections. For unpolarized emission, the transmission into the absorber is a superposition of the transmission coefficients of the two possible polarizations $T = (T_\perp + T_\parallel)/\sqrt{2}$. To evaluate the surface integral, we note the azimuthal symmetry and consider the geometry depicted in Figure 4 to compute the polar angle integral. We note $\boldsymbol{a} = (R_a + R_b + d)\hat{\boldsymbol{z}}$ is the distance between the centers of the two spheres, $\gamma = \alpha + \theta$, $\hat{\boldsymbol{r}}\cdot\hat{\boldsymbol{n}} = (R_b - a\cos\alpha)/r$, and

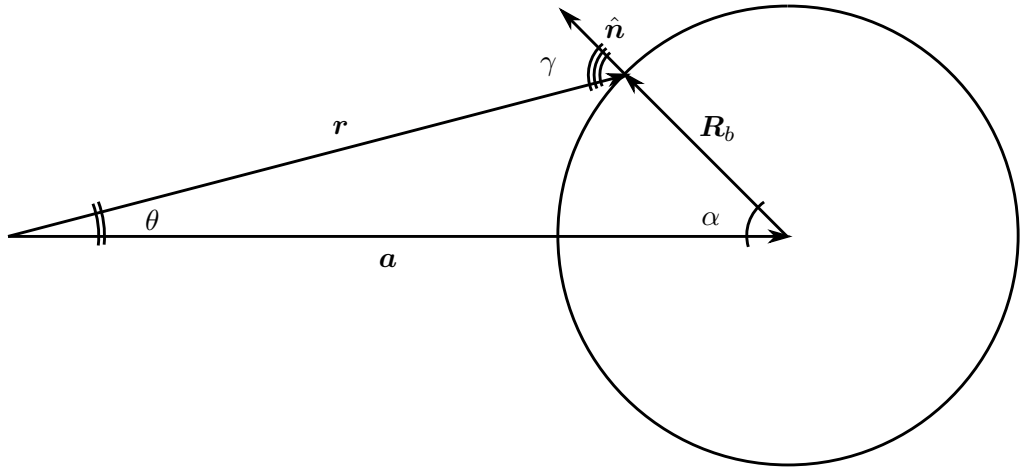

Figure 4: The annotated geometry used to compute the solid angle subtended by a sphere centered a distance a along the $\hat{\boldsymbol{z}}$ axis.

the upper limit of integration is $\gamma = \pi/2$ or $\cos\alpha = R_b/a$. Assuming that all of the energy that passes into the sphere is absorbed we find

$$C_{\mathrm{F}} \approx 2\pi A_a \int_{-1}^{R/a} T(\cos\theta) \frac{\hat{\boldsymbol{r}} \cdot \hat{\boldsymbol{n}}}{r^2} \, d(\cos\theta). \tag{55}$$

The general form of this expression does not yield a closed form solution so numerical methods must be employed.

The two other approximations come from the literature. Mackowski and Mishchenko derived an expression for the energy exchange using the scattering matrix formalism with one reflection for a vanishing separation [42]. Due to the fact that the separation only appears in their expression as a product with the wave number kd, we can use their approximation for long wavelengths as well

$$\Psi(\omega) C_{\mathrm{mm}} \approx \left[\frac{\varepsilon''}{(\varepsilon' + 1)^2 + \varepsilon''^2} \right]^2 \frac{R_a}{d}. \tag{56}$$

The dipole approximation is a third common approximation found in the literature. Although the separation of the spheres considered precludes the use of the dipole approximation in its entirety, the wavelengths of interest in the this analysis are large enough to satisfy

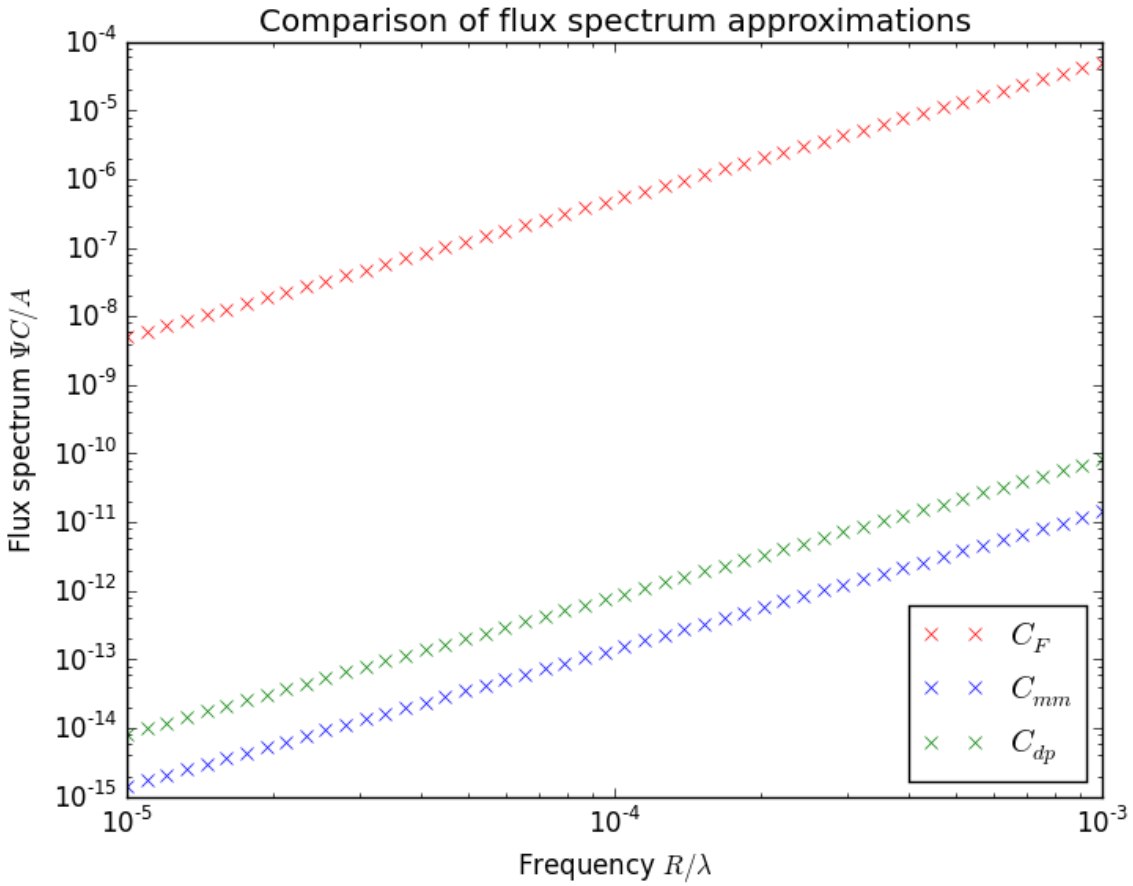

Figure 5: A comparison of the approximations in the long wavelength regime.

the necessary conditions for the dipole approximation. We can use the dipole approximation with the goal to understand the functional dependence of the flux on the wavelength at long wavelengths. Adapting the expression for the heat exchange presented by Volokitin and Persson, the cross-section in the dipole approximation is [73]

$$\Psi(\omega)C_{\mathrm{dp}} \approx \frac{2}{\pi}\frac{\alpha_1''\alpha_2''(8/d^3)^2}{|1-(8/d^3)^2\alpha_1\alpha_2|^2}. \tag{57}$$

The polarizability of a sphere is simply $\alpha = (\varepsilon-1)/(\varepsilon+2)R^3$ [23]. With these three approximations, Equations (55), (56), and (57), we now investigate the long wavelength region of the spectrum.

To investigate the nature of the exchange, we consider two gold spheres of radius 0.200 µm separated by 0.200 µm. Figure 5 presents the product $\Psi C/A$ plotted as a function

of R/λ. This is the same presentation as the inset of Figure 2. The first thing we see is: The magnitudes of the approximations are different. This is due to the fact that our derivation of the approximations was not strict about the constant coefficients. This is acceptable because our goal in this section is to simply understand the functional relationship between thermally generated electromagnetic flux and wavelength at long wavelengths and not to get a quantitative answer. Casual inspection of these three approximations initially leads us to think that the flux is proportional to the square of the angular wave number through Ψ; whereas Equation (50) shows $\Phi' \propto \lambda^{-3}$. Fitting the curves in Figure 5 reveals that the flux decays as λ^{-4} for all three approximations. This discrepancy is resolved by noting that the wavelength dependence also enters Equations (50), (55), (56), and (57) through the dispersion relation of the dielectric function.

To further understand this behavior, we consider that at λ =100 µm we have a ratio of $R/\lambda = 0.002$. The extent of the system is on the order of 1 µm. This means the wavelength is 100 times the size of the entire two sphere system. The low energy is distributed over a large distance and the system experiences a field that is closer to static rather than dynamic. It is well known that static fields do not radiate, and, therefore, the flux *must* decay to zero at long wavelengths. Although the trend in these approximations is for the energy exchange to increase with decreasing wavelength, we know these long wavelength approximations will rapidly break down and become invalid as shorter wavelengths. On the other end of the spectrum, when the wavelength becomes small compared to the objects and separation, the system appears more like a far-field system so the energy exchange will exponentially decay according to the Planck blackbody curve.

3.3.3 Conclusions

In this section, we have used results for the sphere-sphere configuration from the literature to verify the results produced by the implemented numerical method. Our initial results predicted a lower total energy exchange between the spheres than that predicted in the reference results. Looking at the spectral distribution of the flux, we noticed that the numerical results indicated a decaying nature at long wavelengths. We then used three

different long wavelength approximations to determine if the decay we observed was a numerical relic or if it was physical in nature. All three approximations indicated that the flux must decay at these long wavelengths. With these observations, we can confidently state that the decaying nature displayed in our results is due to the physics of the system and not simply numerical error. Thus we may have confidence in the numeric results we are obtaining from the routine.

3.4 Convergence Analysis

Now that we have confidence in our base result, let us consider how the answer changes when we adjust the resolution of the mesh used in the computation. The boundary element method converges to the exact answer as the number of edges used to discretize the surface increases [61]. We need to compute the total energy exchange with a range of discretization levels and see how the answer varies. While we are establishing the change in the final result, we can also profile the routine and determine where the computational effort is being expended.

To perform the analysis we again consider our two gold spheres of radius 0.200 µm. Figure 6 presents the discretized geometries used in the analysis. The meshes were generated using the GMSH computer program [25]. We take the 510 edge count mesh as our baseline for comparison because we know from the previous section it produces reasonable results at a modest computational investment. The numerical routine was run for a selection of separations, and the spectrum used is that from the verification process.

Figure 7 presents the relative change in the total heat transfer between two gold spheres of radius 0.200 µm with a separation d. The total heat exchange is scaled to the reference discretization of 510 edges. As in the verification process, one of the spheres is held at 300 K and the other is at 0 K. We see that for a separation of 0.200 µm or larger, the change in the total heat levels off above 2000 edges. On the other hand, we do not observe this for the smaller 0.005 µm separation until over 2500 edges. This indicates that a smaller separation requires a higher spatial discretization to achieve quantitatively correct results. Before we decide on the minimum number of edges necessary to use in our calculations for

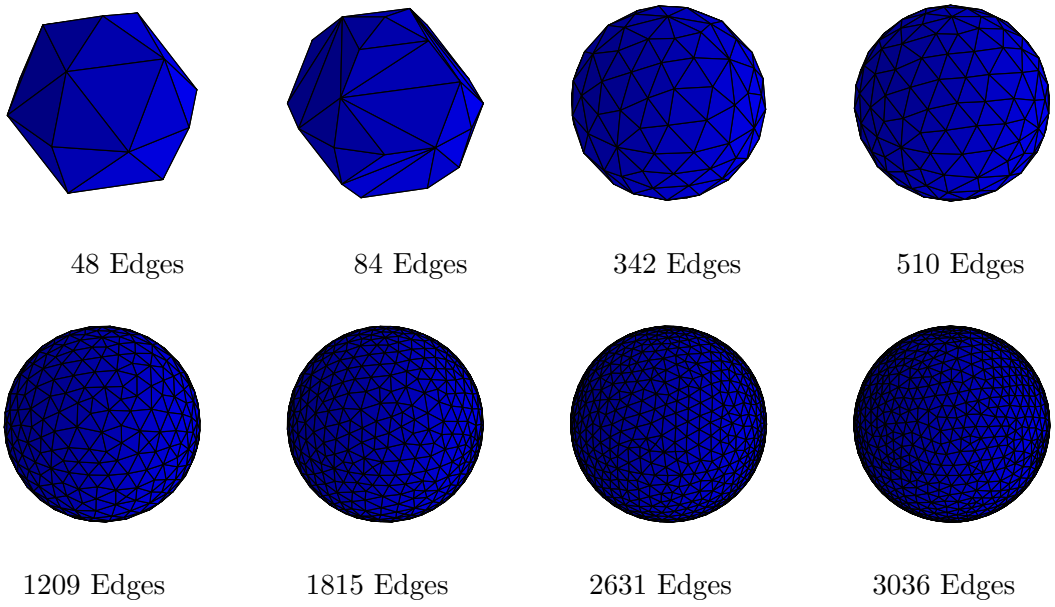

Figure 6: The discretized geometry of a sphere used in the convergence analysis. The increasing edge count produces shorter edges thus a better approximation to a sphere.

quantitatively accurate results, we need to investigate the computational time requirement for each discretization level.

Figure 8 presents the time needed to compute the heat exchange between the two spheres. These timing results were obtained by running the routine on an Apple Mac Pro (Early 2008) with two 2.8 GHz Quad-Core Intel Xeon Processors and 16 GB RAM. The script was executed with Python 3.3.3 from MacPorts using NumPy 1.8.0 and SciPy 0.13.2. The first observation is that the difference in computation time for different separations is within 0.01 % which is trivial. On the other hand, we see that the computation time is quadratic in the number of edges. This is because the algorithm spends the most time assembling the interaction matrix $\overline{\overline{\boldsymbol{W}}}^{-1}$ which requires visiting each pair of edges in the system. We can use these results to estimate the amount of time needed to run a calculation. For two surfaces meshed with 3036 edges each, a single wavelength/separation combination takes a little more than 1 h; whereas, meshes with 510 edges only require 2 min. We can use our base 510 edge mesh to do a high level parameter space exploration to save a significant amount of time. Through this process, we can identify regions of interest in parameter

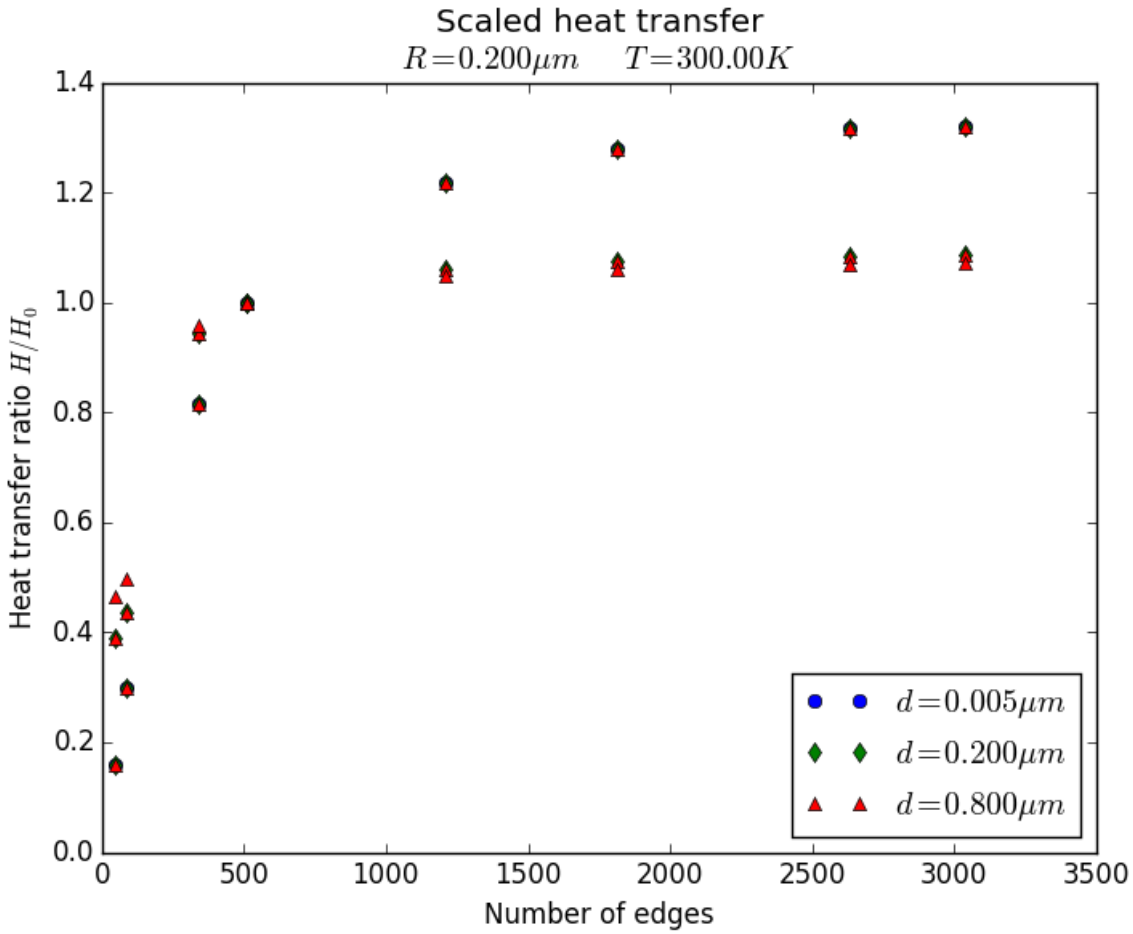

Figure 7: The relative change in the total heat transfer between two gold spheres scaled by the reference 510 edge discretization.

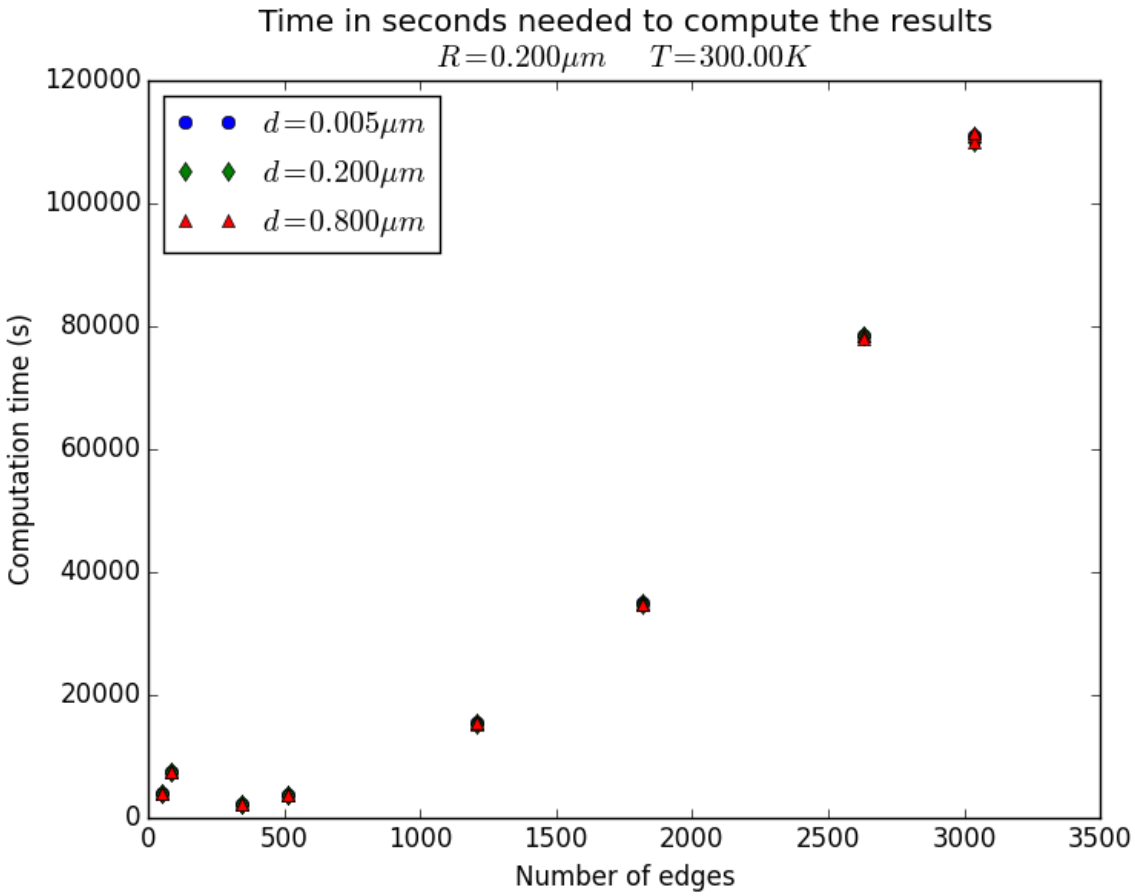

Figure 8: The computation time in seconds for a range of spatial discretization at a selection of separations.

space in a short amount of time. Then we can use a higher resolution mesh and dedicate focused computation time to obtain higher accuracy values for the smaller separations.

In the process of profiling the timing of the routine, it was found that 4000 edges per surface is the practical upper limit on the discretization. The routine utilizes NumPy arrays for storing the complex valued matrix elements and must pass the blocks between processes. Each edge has a both an electric and a magnetic basis function associated with it. This means that the size of the blocks when the surface has 4000 edges is 8000 by 8000. The version of Python used in these computations is not able to pass arrays larger than 8000 by 8000 between processes. The exact limit on the surface size has not been completely explored; however, when the blocks of the boundary element method become large, the total memory usage will also become a limiting element during execution.

Having considered the convergence behavior of routine, we are now ready to move on to investigating the effect of surface shape on the radiative energy exchange. We are able to perform a high level parameter space exploration using a 510 edge discretization in a modest amount of time. Once we have identified regions of the parameter space that need higher accuracy results, we can use a higher resolution mesh to dedicate additional computational resources.

3.5 Conclusion

In this chapter, we have discussed the implementation, verification, and convergence of the computational routine. The program is implemented in Python and the subtle issue of data caching in the LIBSCUFF library was discovered, addressed, and solved. Following this, we turned our attention to the verification process. The numerical results have been compared to results from the literature. Our initial results were lower than that found in the literature at small separations, but we have shown that the physical nature of the flux is to decay at longer wavelengths and small separations. This tells us that we are receiving physically reasonable results. Our last task for this chapter was to investigate the convergence of the routine. We found that qualitative results can be found using a coarse mesh, and increasing the resolution of the mesh brings our numerical results in agreement with the literature.

This means a coarse mesh can be used to investigate parameter space, and, onces a region of interest in parameter space is identified, we can dedicate computational resources to obtain higher accuracy results with a higher resolution mesh. These results give us confidence in the routine; thus, we now begin the investigation of the effect of shape on the radiative exchange between two objects.

CHAPTER IV

SPHERE-SPHEROID EXCHANGE ANALYSIS

4.1 Introduction

The numeric investigation of novel nanoscale object configurations begins with a consideration of the interaction of a sphere and a spheroid with an aligned symmetry axis which is a natural extension of the sphere-sphere system. We begin with a sphere and a spheroid because it is a natural extension of the well known sphere-sphere system that has not been thoroughly studied before. Figure 9 presents a selection of configurations we will consider in this chapter. We begin this chapter with an overview of the geometric configuration. Next, we investigate the total heat exchange between these objects as a function of eccentricity and separation. Then, we briefly consider the spatial distribution of the electromagnetic flux across the surfaces. We close this chapter with a general discussion.

A spheroid is simply the surface traced out by rotating an ellipse about either the semimajor or semiminor axis for an oblate or prolate spheroid respectively. The surface of a spheroid is defined by the equation

$$\frac{x^2+y^2}{a^2}+\frac{z^2}{c^2}=1. \tag{58}$$

The oblate and prolate cases are differentiated based on whether $a > c$ or $a < c$ respectively. A sphere is simply the special case of a spheroid with $a = c$ and is the transition between oblate and prolate spheroids. An oblate spheroid can be pictured as a "flattened" sphere and a prolate spheroid is a sphere that has been "stretched" along the symmetry axis. These mental images allow for quick visualization of the change in the projected area between the sphere and spheroid. Looking down the symmetry axis, an oblate spheroid will subtend a larger solid angle than a sphere and a prolate spheroid will subtend a smaller solid angle as viewed from the surface of the other object. We know that the projection of the surface area governs the classical blackbody radiation exchange between objects. This implies that the

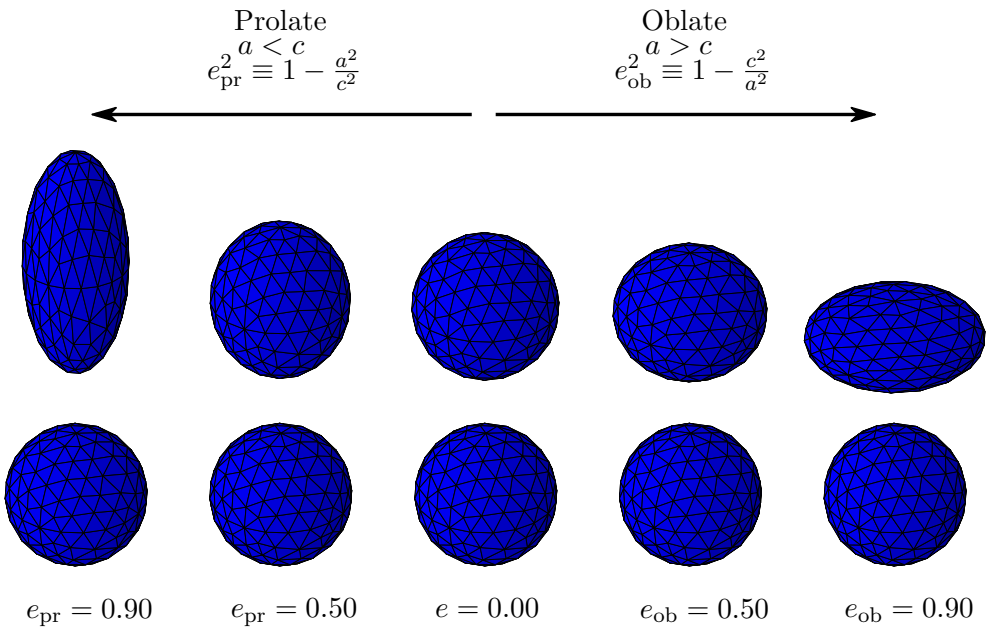

Figure 9: A sample of the geometric configurations considered. The sphere and the spheroid have equal surface area. The presented configurations have a separation equal to the radius of the sphere.

energy exchanged between an oblate spheroid and a sphere will be larger than the reference sphere-sphere case. Conversely, the system of a prolate spheroid and a sphere will have a reduced energy exchange from the reference sphere-sphere case. We can study the projected area of the spheroid to quantify the change in total energy exchange from the sphere-sphere configuration.

In the classical formalism, the blackbody exchange is computed by limited by the viewable area of the objects $H_{12} = \sigma A_1 F_{12} \left(T_1^4 - T_2^2\right)$ [24, 29, 68]. The value F_{12} is the fraction of the area of object 2 viewable by object 1 and is referred to in the literature as the view factor [13, 29], the angle factor [29, 68], and the configuration factor [22]. The value of the view factor is given by the double surface integral

$$F_{12} = \frac{1}{A_1} \iint_{A_1} \iint_{A_2} \frac{\cos\theta_1 \cos\theta_2}{\pi r_{12}^2} \, dA_1 dA_2 \tag{59}$$

where θ_i is the angle between the normal vector $\boldsymbol{n}_i$ of surface i and the vector connecting the integration point in the surfaces $\boldsymbol{r}_{12}$ with $\|\boldsymbol{r}_{12}\| = r_{12}$. The geometry to evaluate the kernel of the view factor double integral is shown in Figure 10. Methods to evaluate the

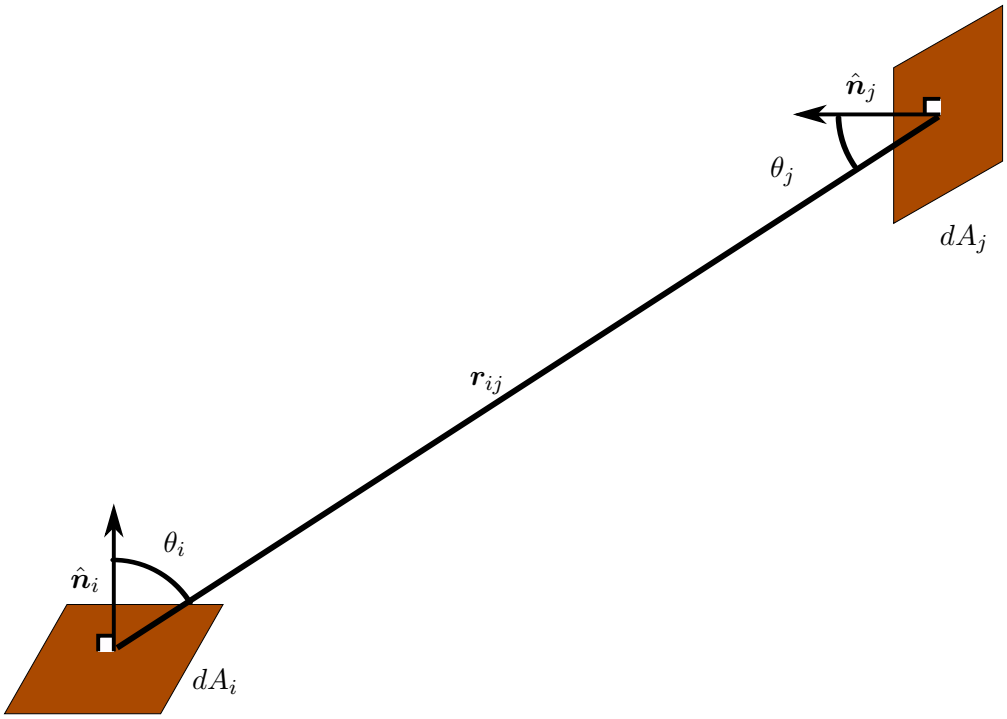

Figure 10: The geometry to evaluate the differential view factor.

double surface integral have been under investigation for over half a century with great focus on the handling of shadowing because of intervening objects [4, 29, 75]. Catalogs of standard configurations are available [30]; however, the precision is not high. For axially symmetric cases, semianalytic expressions exist [12, 48]. For more complex configurations where the symmetry is broken, numerical methods such as VSWEEP can be used [4].

For the results presented in this thesis, we used the VSWEEP code to compute the view factors for the different configurations investigated. To use VSWEEP, we exploit the scale invariance of the double integral to perform the calculation for nanoscale objects. Passing a surface description with units smaller than millimeter scale to the program is not possible because the input file does not allow for values that small. However, by simply scaling up to the meter size, we get the correct value for the view factor F_{12} which we can then multiply by the correct nanoscale area for further calculations. We must average the two area-weighted view factors because the symmetry of the view factors is lost due to memory limitations in VSWEEP. The relative error in doing this is less than 0.7 % and is largest at higher separations. Running VSWEEP on the sphere-sphere system and performing

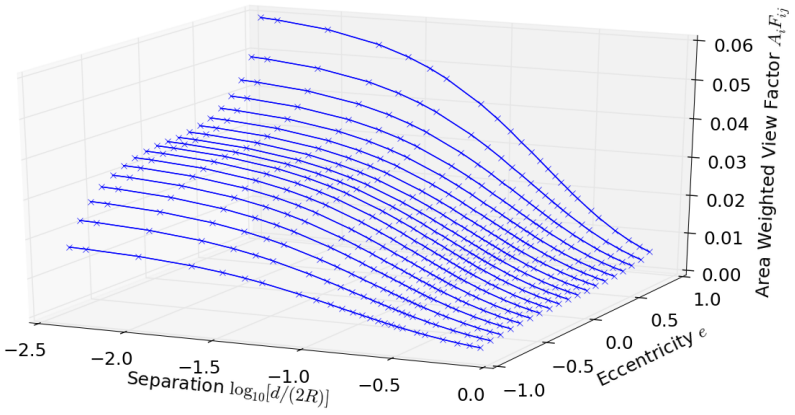

Figure 11: The area weighted view factors between a sphere and a spheroid where R is the radius of the sphere. Positive eccentricities denote oblate spheroids, and negative eccentricities denote prolate spheroids.

the area-weighted average yields the same result as the semianalytic expression and the cataloged value within numerical precision. Although the semianalytic expression is easier to evaluate in symmetric configurations, we use VSWEEP to ensure a consistent approach is used when comparing results from asymmetric systems to symmetric systems.

Running VSWEEP on a range of separations and spheroid eccentricities, we can get a quantitative prediction for the change in the total energy exchange due to the change in surface shape. Figure 11 presents the area weighted view factors as computed by VSWEEP. We can clearly see that the energy exchange increases in the oblate spheroid over the sphere; whereas, the energy exchange decreases in the prolate spheroid. This change should be most pronounced at the smallest separations and becomes less obvious as the separation increases. At the smallest separations depicted, we see that the total energy exchanged between the most prolate spheroid, $e_{\mathrm{pr}} = 0.9$, and a sphere is half that of a sphere and a sphere. Further, the most oblate spheroid, $e_{\mathrm{ob}} = 0.9$, and sphere exchange energy at twice the rate as the two sphere system. When the separation is above $\sim 2R$, the difference between in the energy exchange between a sphere and a spheroid should be negligible.

To establish the desired parameter space, we consider a sphere and a spheroid with

equal surface areas. The choice of surface area as a fixed parameter rests on the fact that blackbody radiation is governed by the surface area of the objects as opposed to the volume as was investigated previously [31]. Integrating the surface function, Equation (58), the surface areas for the two types of spheroids are

$$A_{\text{ob}} = 2\pi a^2 \left(1 + \frac{1 - e_{\text{ob}}^2}{e_{\text{ob}}} \operatorname{artanh} e_{\text{ob}}\right) \text{ with} \qquad e_{\text{ob}}^2 = 1 - \frac{c^2}{a^2}, \text{ and} \tag{60a}$$

$$A_{\text{pr}} = 2\pi a^2 \left(1 + \frac{\arcsin e_{\text{pr}}}{e_{\text{pr}}\sqrt{1 - e_{\text{pr}}^2}}\right) \text{ with} \qquad e_{\text{pr}}^2 = 1 - \frac{a^2}{c^2}. \tag{60b}$$

Given the radius of an equal surface area sphere and the desired eccentricity, these equations can be solved for the equatorial radius a and the polar distance c. These factors are then used to generate a spheroidal surface.

The default method to generate a spheroidal mesh is to directly use the equatorial radius and polar distance with the GMSH program to specify an ellipse to rotate about an axis. However, we found that it is not possible to fix the number of edges using the GMSH program. This is due to the internal logic used by the program to dynamically generate a mesh. The intent of the GMSH software is to automate the process of generating a mesh for use with finite element methods. The concept of controlling the number of edges is not included as an option in the program. Analytically, the surfaces are simply related, but the program logic does not know this.

The convergence analysis in Chapter 3 established that the numeric results for the exchange is highly sensitive to the number of edges in the meshes at small separations. Thus, *the same number of edges in the meshes must be used to make comparisons among different eccentricities.* To ensure the number of edges remains the same, the equatorial radius and polar distance for a spheroid with surface area equal to the unit sphere, 4π, are computed. These factors are then used as scaling factors for the Cartesian coordinates of a reference sphere mesh. Multiplying the $\hat{\boldsymbol{x}}$ and $\hat{\boldsymbol{y}}$ coordinates by the equatorial radius a and the $\hat{\boldsymbol{z}}$ by the polar distance c generates a spheroid mesh with surface area formally equal to the reference sphere and the same number of edges and numerically equal to 1×10^{-4}.

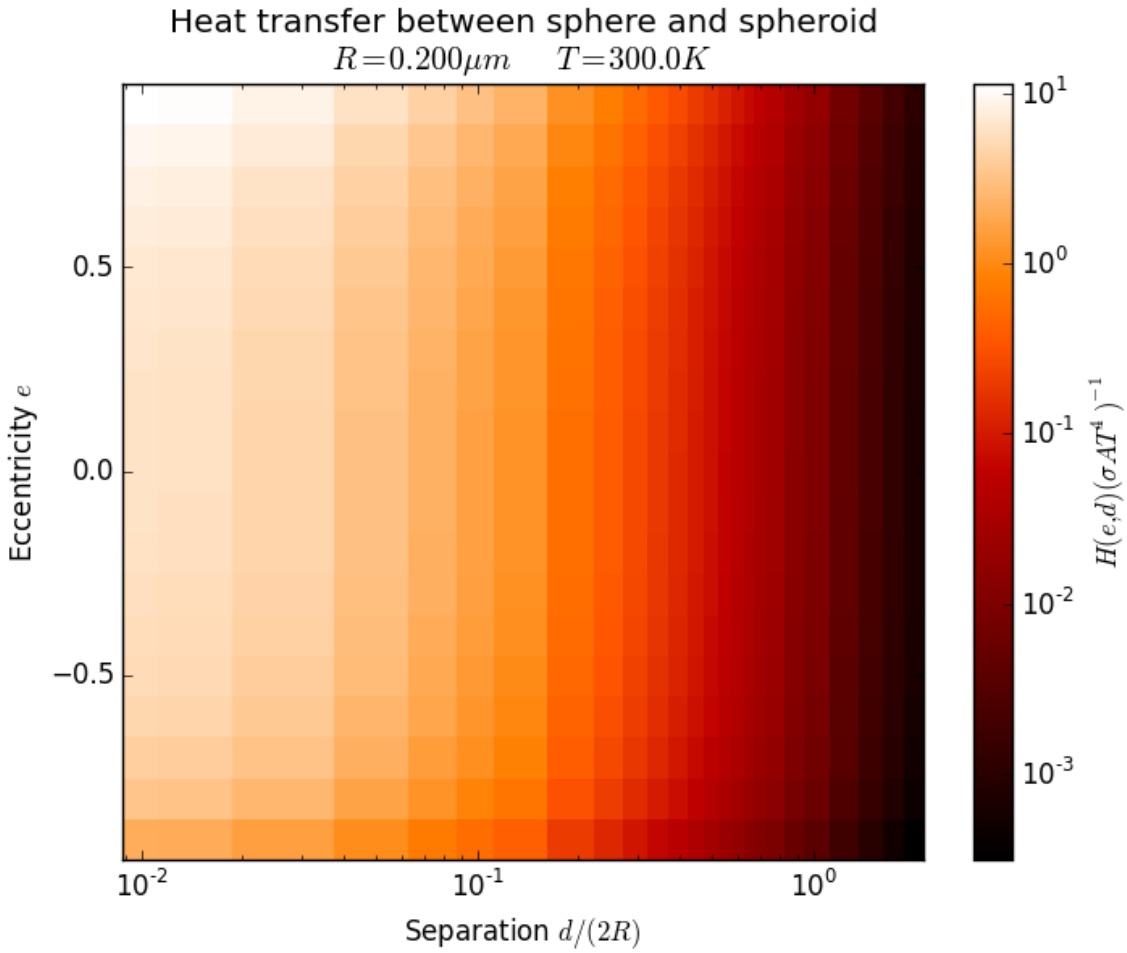

Figure 12: The scaled heat exchange between a sphere and a spheroid. Both objects are gold and have equal surface area.

This final scaling establishes the nanoscale geometry for the radiative energy exchange computations. With the geometry set, the parameter space established, and the meshes generated, let us turn our attention to the numerical results.

4.2 Numeric Results

First, consider the total energy exchange normalized by the blackbody value without the view factor σAT^4. Figure 12 presents the total heat exchange between a gold sphere of radius 0.200 µm at temperature 0 K and a gold spheroid of equal surface area at temperature 300 K. This presentation of the data is analogous to the presentation of the main figure in Figure 2 from the verification procedure in Chapter 3. We have simply added a second axis indicating eccentricity with the sphere-sphere configuration the $e = 0$ line. We indicate

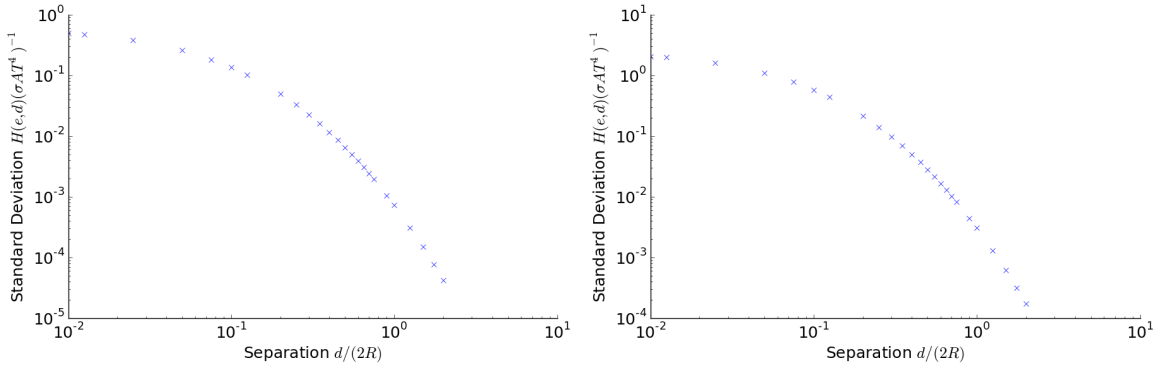

(a) $e \leq 0.5$ **(b)** All eccentricities

Figure 13: The standard deviation from the sphere-sphere results without accounting for the view factor.

the prolate spheroid systems with negative eccentricities to differentiate the two types of spheroids. The most prominent feature we see is that the increase in the exchange due to small separations is much stronger than the shape effects.

We see a significant change from the sphere-sphere interaction for larger eccentricities of both the oblate and prolate spheroids; however, small eccentricities, $e \leq 0.5$, are close to the reference sphere-sphere system. Figure 13a shows that variance from the sphere-sphere case for small eccentricities is less than 1 at all separations; however, when the larger eccentricities are included, Figure 13b, the variance at a particular separation increases by an order of magnitude. This large variance from the sphere-sphere results can be understood by noting the change in the face orientations. Looking back to Figure 9, we see that the large eccentricities cause a dramatic change in the orientations of the faces nearest the gap compared to a sphere. This change in orientation moves faces into the decay range of evanescent waves on the surface of the sphere in the oblate spheroid-sphere system and out of the decay range in the prolate spheroid-sphere system. According to the near-field formalism discussed in Chapters 1 and 2, the enhanced energy exchange is highly dependent on the proximity of the surfaces. The two figures also show that the variance is largest at the small separations and decays smoothly as the separation increases.

Considering the change in the total energy exchange as a function of separation, as shown in Figure 14a, we see the decay profile of sphere-sphere system is still present. This

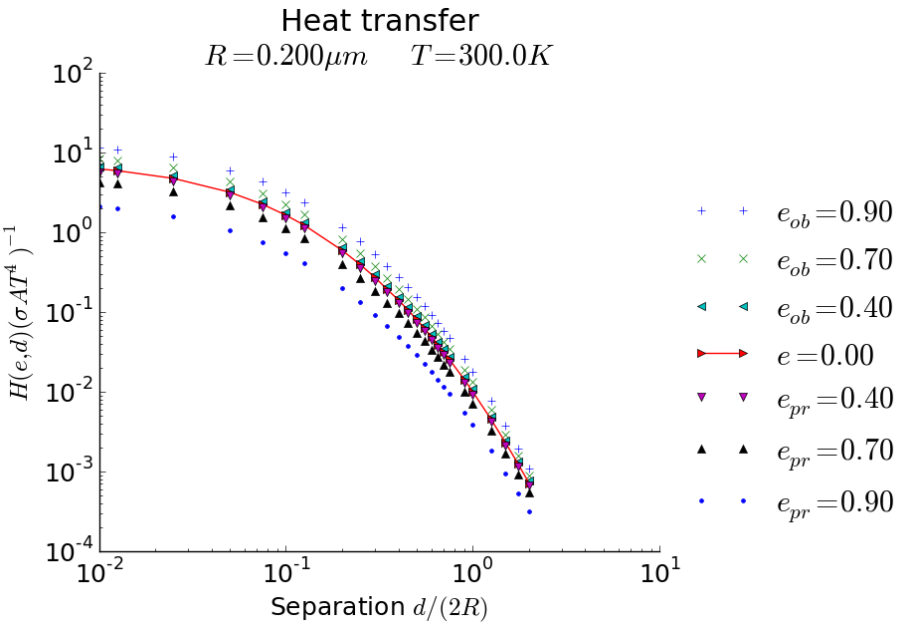

(a) Heat transfer for a subset of eccentricities as a function of separation.

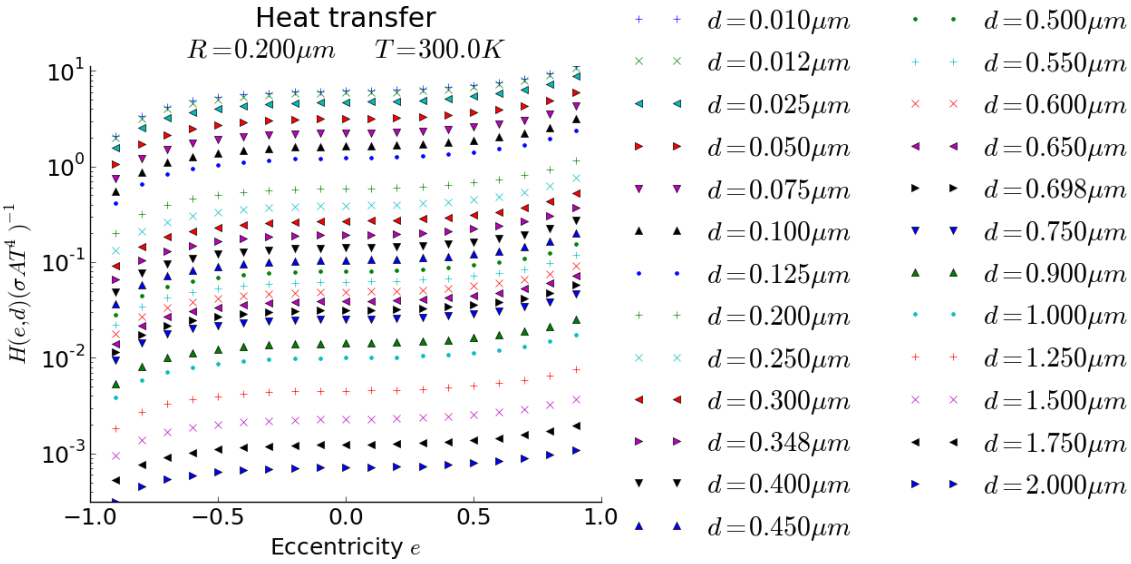

(b) Heat transfer as a function of eccentricity.

Figure 14: The results from Figure 12 as a function of separation and eccentricity.

presentation also reveals that the largest difference in the decay profile occurs at the smallest separation. At this small separation, the total energy exchanged between the $e_{\text{ob}} = 0.9$ oblate spheroid and the sphere is 10 times higher than the sphere-sphere system; whereas, the total energy exchange in the e_{pr} prolate spheroid-sphere system is 0.5 that in the sphere-sphere system. For all eccentricities, the change across the eccentricity spectrum is less than two orders of magnitude. Figure 14b shows that the increase in the heat transfer is a monotonic function of the eccentricity. The energy transfer increases with eccentricity for the oblate case and decreases with increasing eccentricity for the prolate case as predicted. Combining Figures 14a and 14b, we see that the energy transfer is monotonic in both eccentricity and separation.

So far we have used a normalization based on simply the classical blackbody result without considering the shape effects. Close inspection of the results shows that the exchange between the sphere and the prolate spheroid is decreasing more rapidly than the oblate exchange is increasing. The functional shape of the dependence appears to be cubic. Referring back to Equation (60), we see that the surface area functions of the spheroids are defined by the arcsin and artanh functions. Both of these functions are odd which means the first two terms in the Maclaurin series for both are the linear and cubic terms. This indicates that we must indeed account for the true shape of the spheroidal surfaces in evaluating the total energy exchange.

Figure 15 incorporates the view factor into the numeric results presented in Figure 12 by including it in the blackbody value $\sigma A F(e, d) T^4$. As before, both the sphere and spheroid are gold with one held at 300 K and the other at 0 K. Both objects have equal surface area and the sphere has a radius 0.200 µm. We note the separation remains the dominant contribution to the increased heat exchange, and the prolate spheroid retains a noticeable decrease from the sphere-sphere configuration at small separations.

The strong dependence on the eccentricity for the prolate spheroid can easily be explained through proximity effects. The prolate spheroid is sharp which means only a small amount of the surface is within a close proximity to the sphere. A small change in the eccentricity will dramatically alter the amount of the surface within the decay range of

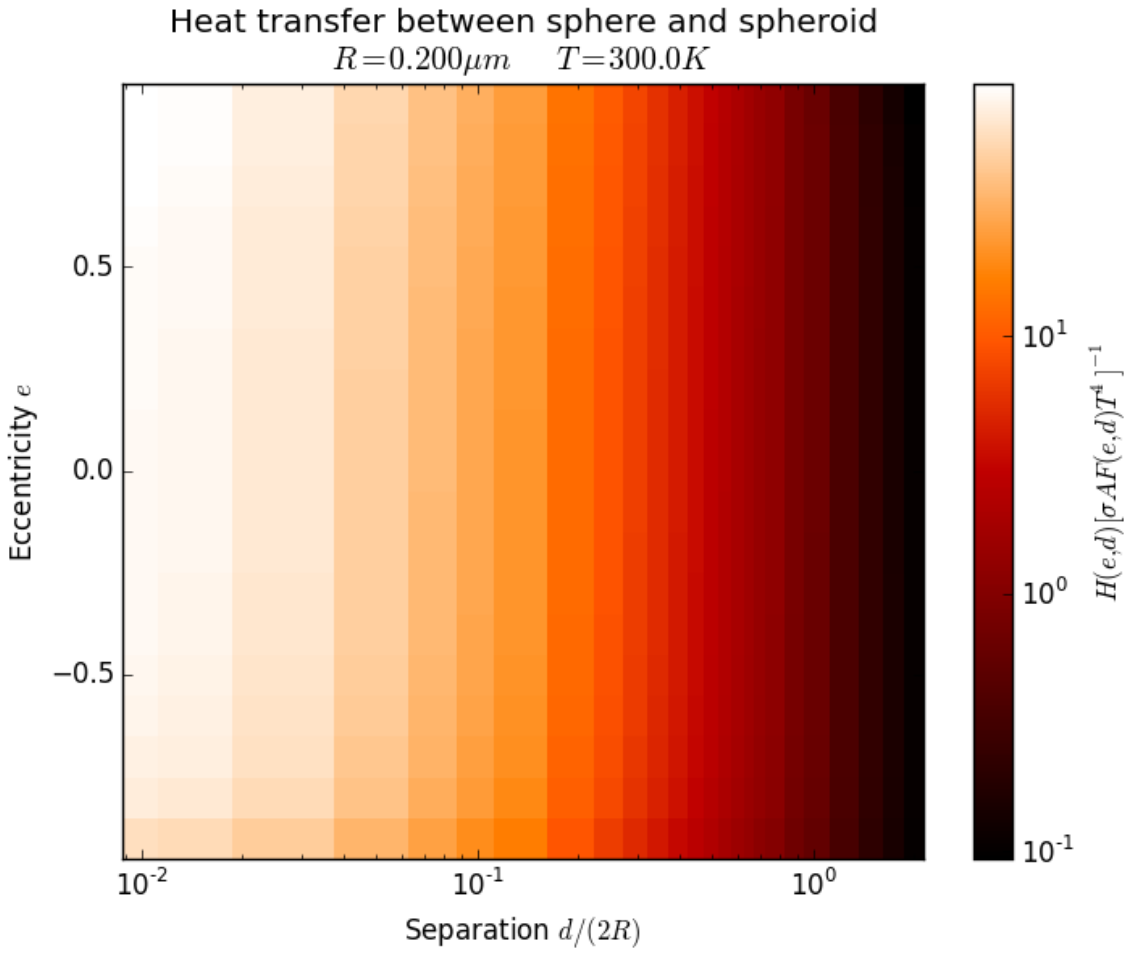

Figure 15: The scaled heat exchange between a sphere and a spheroid normalized by the blackbody results including the view factor. Both objects are gold and have equal surface area.

the evanescent waves on the sphere. Because the decay range of the evanescent wave is exponential, a small change in separation of the faces on each surface will cause a dramatic change in the coupling of the evanescent waves on the surfaces. Conversely, the energy exchange in the oblate spheroid-sphere system does not show this strong variation because it is limited by the curvature of the sphere which limits the number of faces on the sphere that can be within the decay range of evanescent waves on the spheroid.

Figure 16b provides a clearer picture of the separation dependence. Here we have reproduced the Figure 14a for comparison. This view reveals that the numeric results are packed more closely around the sphere-sphere decay curve when the view factor is included. We clearly see that the results converge to the sphere-sphere curve faster with the view factor included compared to neglecting the view factor. In Figure 14a, the numeric results have not converged to the sphere-sphere results at a separation of $4R$; whereas, in Figure 16b, the results have converged when the separation is $R/2$. This indicates that the view factor is a good description for the change in the energy exchange from the reference sphere-sphere system at separations greater than $R/2$.

To put a more quantitative value on this, we can look at the average value of the relative difference between the sphere-sphere results and the sphere-spheroid results

$$1.0 - \frac{H(e,d)}{F(e,d)} \frac{F(0,d)}{H(0,d)}. \tag{61}$$

Figure 17 presents the mean relative difference. We can clearly see that the largest errors occur at the smallest separations. We see the error in using the view factor to predict the change in the energy exchange between a sphere and a spheroid from the sphere-sphere system is less than 2 %. This means that the view factor correctly describes the change in the energy exchange from the sphere-sphere system with three significant figures of accuracy.

Figure 18 shows the energy exchange as a function of the eccentricity. We clearly see that the variance for a particular separation as a function of eccentricity is reduced by including the view factor. At the smallest separation, the relative variance from the reference sphere-sphere configuration without the view factor across all eccentricities is 2.06. When

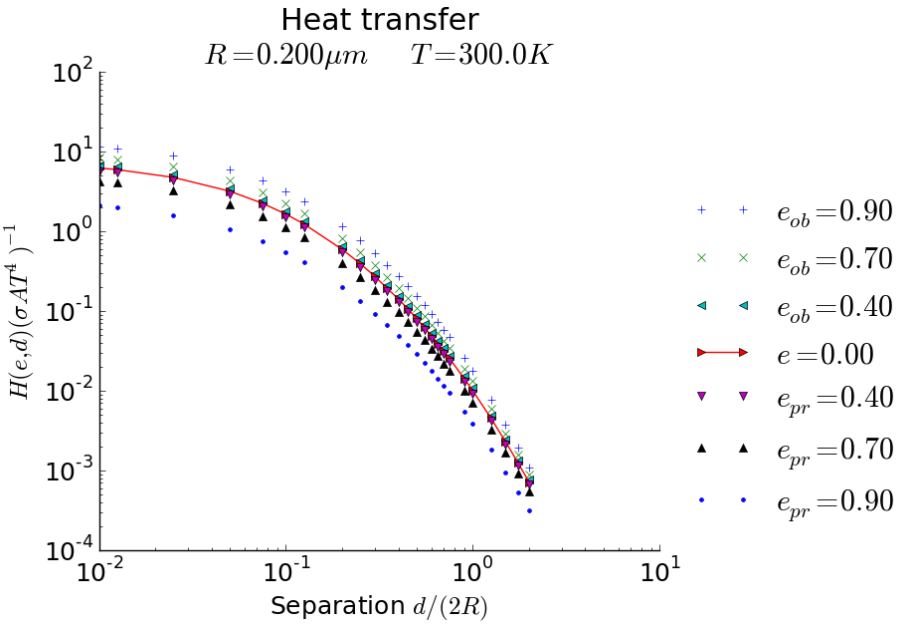

(a) Energy exchange *without* the view factors (Figure 14a).

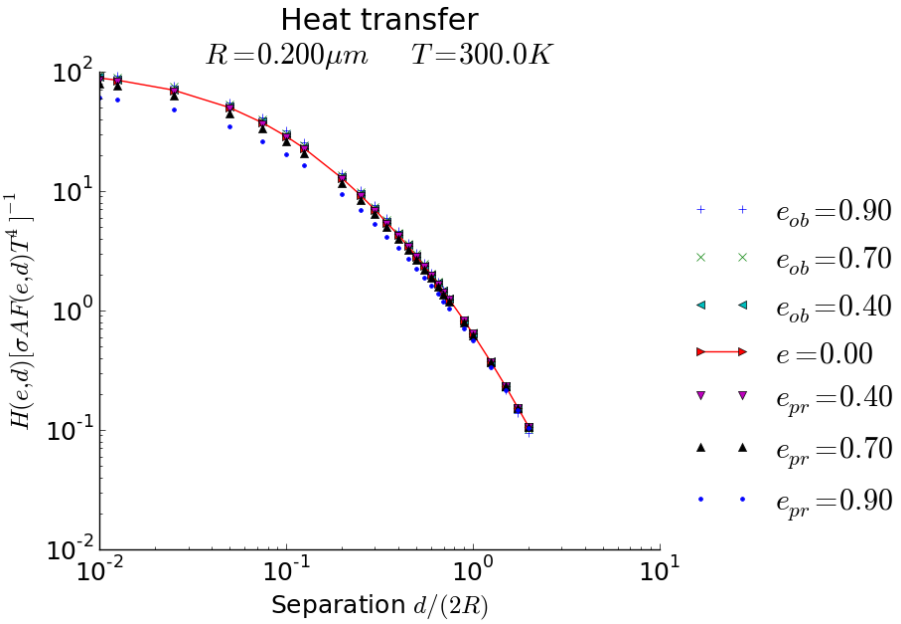

(b) Energy exchange *with* the view factors.

Figure 16: Comparison of the heat exchange as a function of the separation both with and without the view factors taken into account.

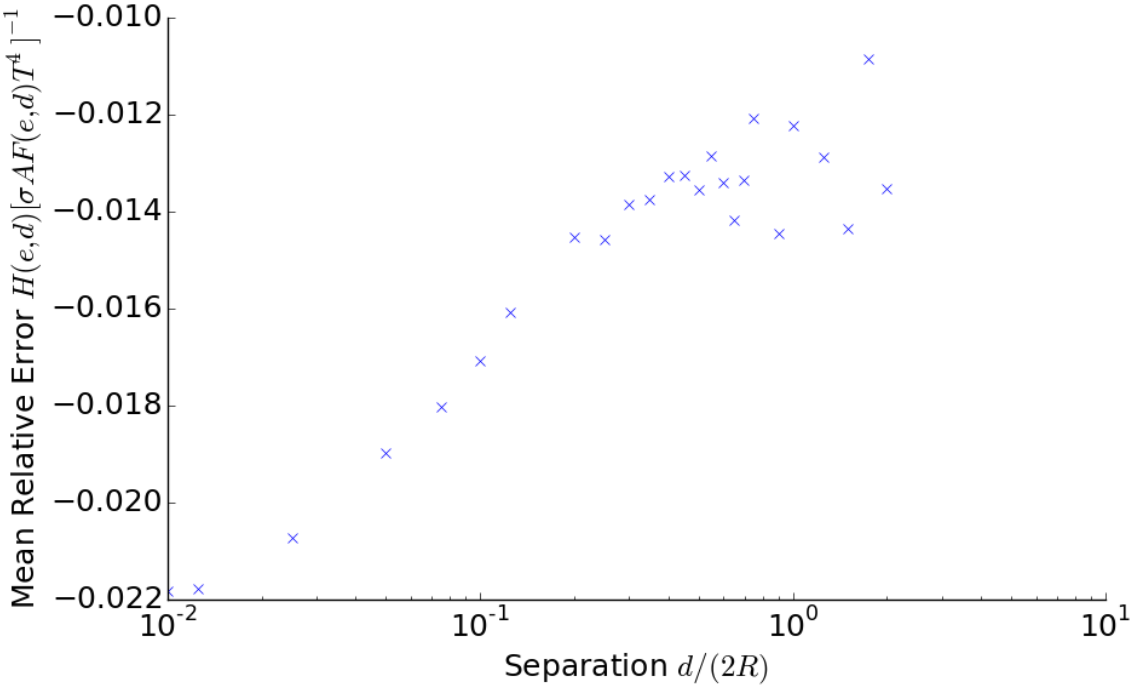

Figure 17: Average relative difference in energy exchange across eccentricities.

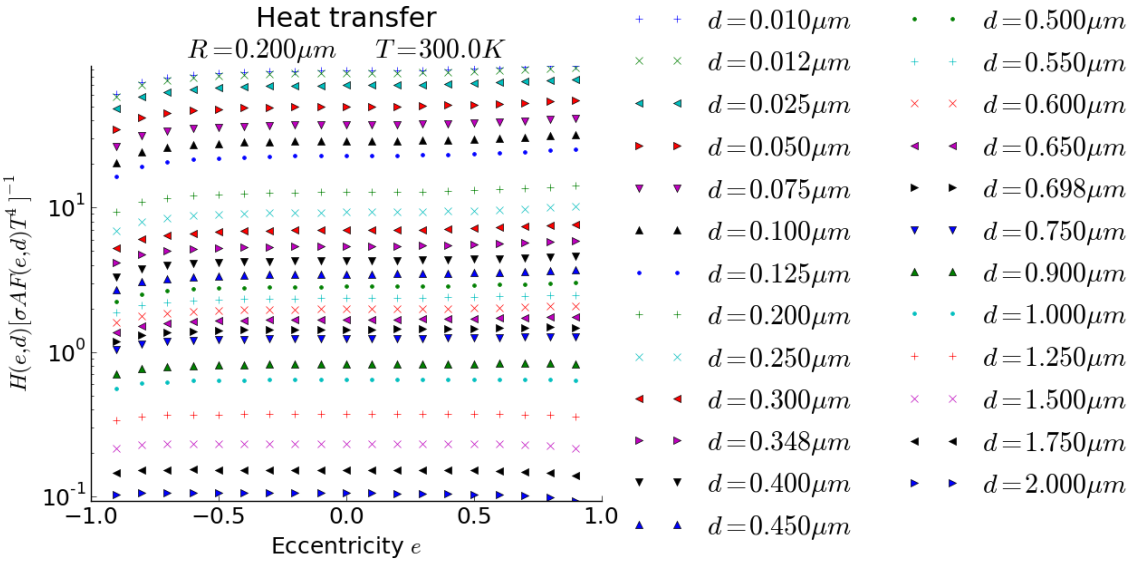

Figure 18: The heat exchange as a function of eccentricity with the view factors taken into account.

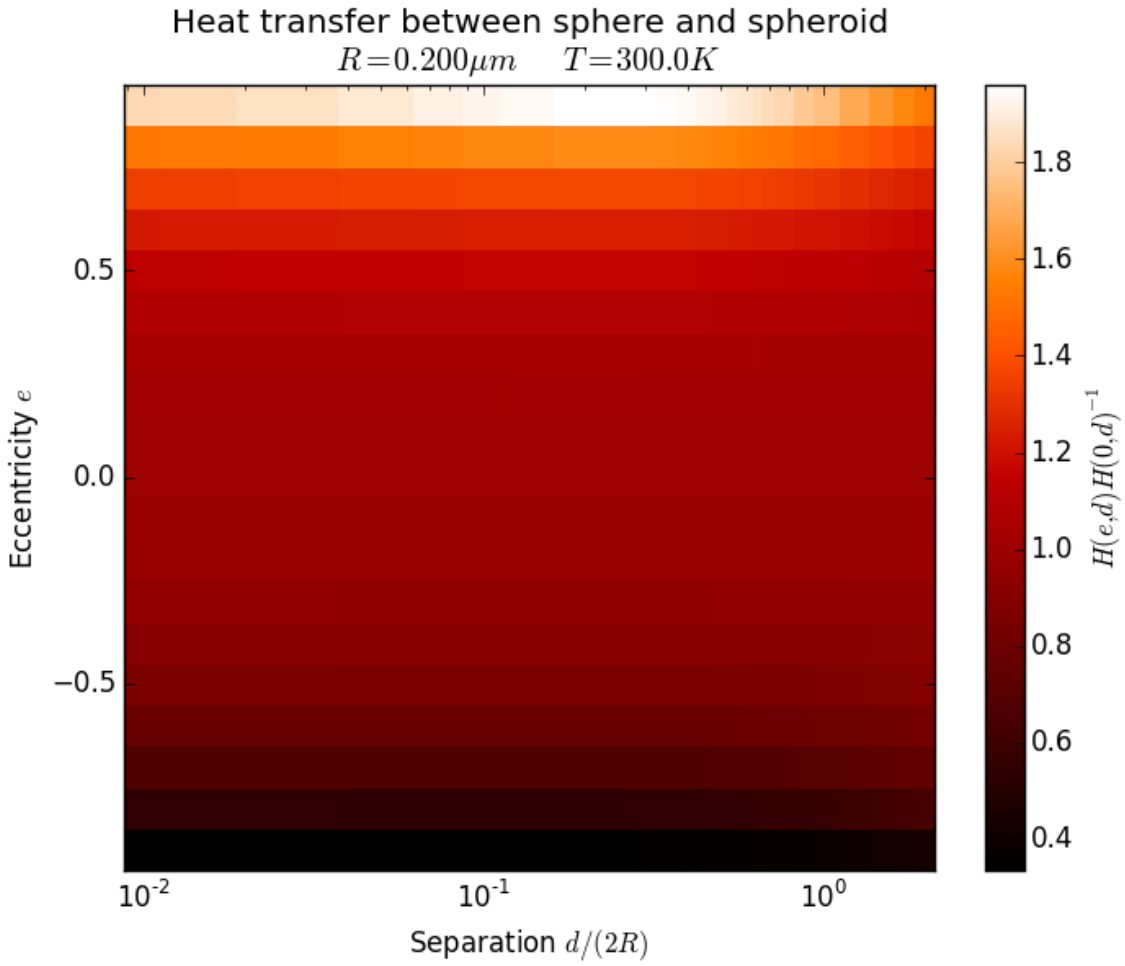

Figure 19: Scaled heat exchange between a sphere and a spheroid normalized by the numeric results for the sphere-sphere system at the same separation.

the view factor is taken into account, the relative variance drops to 0.093. This means that the sphere-sphere configuration predicts the dominant increase in the total energy exchanged between a sphere and a spheroid due to the small separation. The view factor for a sphere-spheroid system can be used to get the change in the total energy exchange between sphere and a spheroid from a sphere-sphere configuration at the same separation as predicted earlier in this thesis. The variation remains largest at the small separations; however, this is attributable to the under sampling of the surfaces because the interaction is strongest at the small separations. Use of a finer mesh to investigate this region of parameter space should verify this prediction.

Another informative way to look at the data is to directly compare the change in the

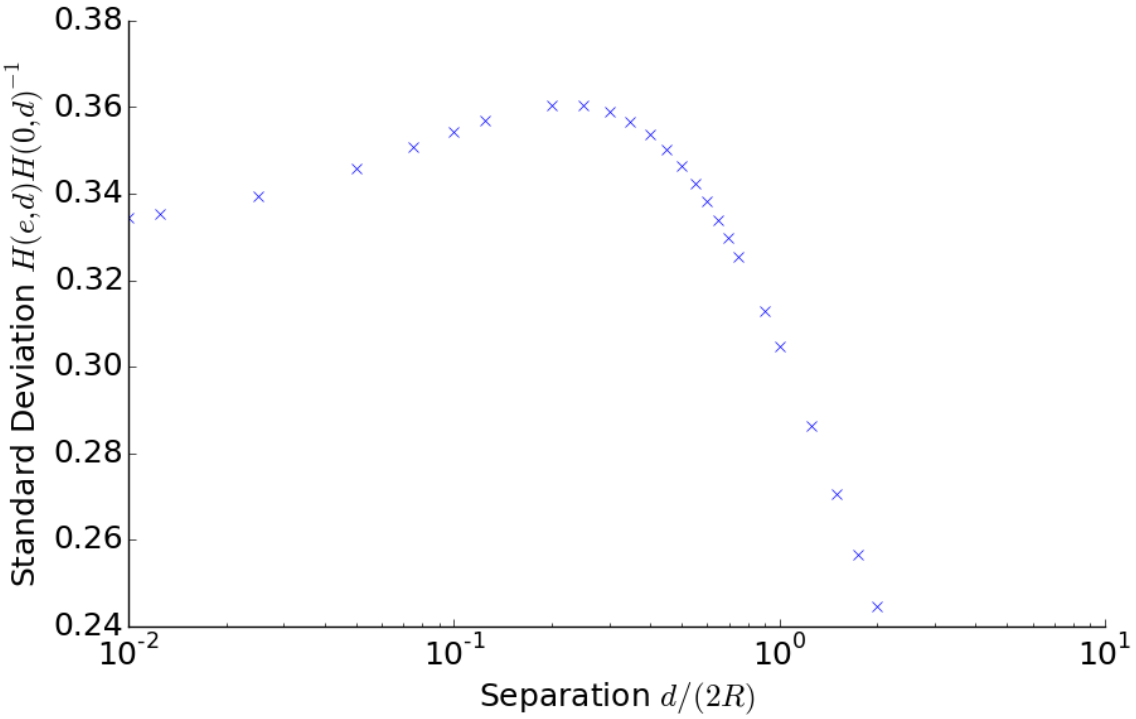

Figure 20: Standard deviation across eccentricities of Figure 19.

heat exchange to the sphere-sphere system. This reveals how the exchange is modulated by changing the surface shape compared directly to the same separation sphere-sphere system. Figure 19 presents the numeric results for the energy exchange divided by the sphere-sphere system result at the same separation. As noted above, the deviation from the sphere-sphere system is not evident in both the oblate and prolate case for eccentricities below $e \sim 0.5$. Physically, spheroids with this small of an eccentricity do not geometrically vary significantly from a sphere; thus the total energy exchange does not vary significantly from the sphere-sphere value. This observation confirms the intuitive prediction that a spheroid of small eccentricity is well approximated by a sphere.

A striking feature shown in Figure 19 is that the largest variance from the sphere-sphere system is not at the smallest separation. What we find is that the largest relative increase over the sphere-sphere configuration is 96 % for an oblate spheroid with $e_{\text{ob}} = 0.9$ at a separation of $d = R/2$. On the other hand, the largest relative decrease in the exchange for the prolate spheroid is 66 % for $e_{\text{pr}} = 0.9$ at $d = 0.15R$. Figure 20 confirms this observation showing the largest variance at $d = 0.2R$. The appearance of a local maximum in the

variance away from the smallest separation implies that there exists intermediate length scales that can be used to tailor the total energy exchange for maximal increase. To check this prediction, additional configurations need to be investigated.

4.3 Spatial Distribution of the Flux

The final characteristic considered for the interaction of a sphere and a spheroid is the spatial distribution of the flux across the two surfaces. The boundary element method formalism of the near-field radiative energy exchange establishes the heat associated with each edge of the mesh. To map the energy from the edges to the faces, we simply use an area weighting technique. The total area associated with edge I is the sum of the two faces it joins $A_I = A_i + A_j$ where we are using capital letters to denote the edge and lower case for the faces. The portion of the energy H_I associated with face i is then simply the area weighted value $H_{i,I} = H_I * A_i / A_I$. The total energy passing through a particular face is then just the sum of the contributions of the edges defining the face $H_i = \sum_I H_{i,I}$. Summing over all faces, it can be shown that the total energy exchange is conserved in this mapping scheme.

Figure 21 presents the flux through each face for a selection of eccentricities and separations. The flux through a given face is simply the total energy passing through the face divided by the area of the face. The numeric values are for a gold sphere of radius 0.200 µm at 0 K and a gold spheroid of equal surface areas at temperature 300 K in units of the blackbody flux σT^4. The surfaces have been rotated away so that the distribution around the gap is evident.

At small separations, the energy exchange is highly concentrated on the faces nearest the gap. This is due to the exponential decay of the evanescent waves limiting the photon tunneling to only the small gaps. The faces away from the gap exist farther out in the decay range and, therefore, do not contribute strongly to the exchange. As the surfaces separate, the distribution of the exchange expands away from the axis of symmetry and a local minimum forms at the center of the gap. This change in the flux distribution is due to faces moving out of the decay range of the evanescent waves.

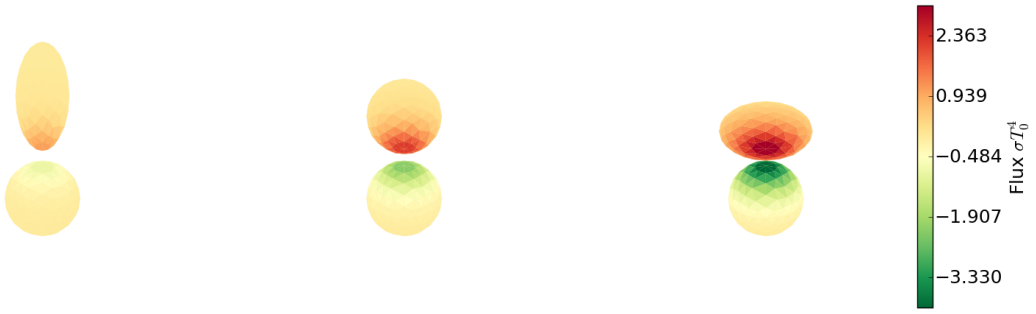

(a) $d = 0.5R$

(b) $d = R$

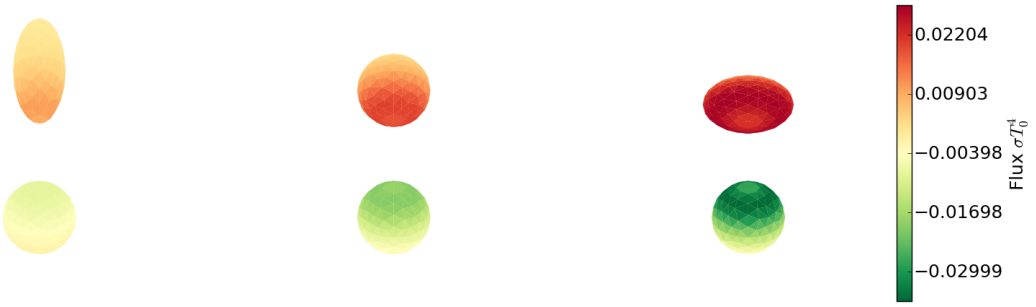

(c) $d = 2R$

Figure 21: The spatial distribution of the heat passing through each facet normalized by the facet area.

At large separations, the faces away from the center line of the gap begin to show increased participation in the energy exchange. This is due to two parts: First, as mentioned before, the surfaces are moving out of the decay range of the evanescent waves lowering the near-field contribution and decreasing the total exchange. Second, the propagating modes continue to mediate the far-field energy exchange. The local minimum at the center of the gap is simply a manifestation of destructive interference due to the wave nature of the fields.

Focusing on the concentration, we see that a hot spot forms on the object with a larger radius of curvature at small separations. This means the sphere in the prolate system and the spheroid in the oblate system. This increase in local flux demonstrates that the spatial distribution of the flux is influenced by the surface shape; however, the curvature of both surfaces hides the details of the relation between the distance from the symmetry axis and the flux. To further investigate the radial dependence of the flux, we need to consider a surface with faces in a common plane.

4.4 Conclusions

In this chapter, we applied the boundary element method to investigate the interaction of a sphere and a spheroid at nanoscale sizes and separations. Our areas of investigation covered the total energy exchanged between the two surfaces and the spatial distribution of the flux across the surfaces.

In the process of investigating the total energy exchange, we compared the numeric results to the classical blackbody value both with and without the view factor from classical radiative transfer theory. We found that the separation between the surfaces is the dominant contribution to the enhanced energy exchange, but the view factors describe the change in the energy transfer from a reference configuration within a few percent. This means that a computationally simpler system such as the sphere-sphere can be used to get the separation dependence, and the view factors can be used to predict the modified near-field energy exchange for a spheroid near a sphere.

The second feature we discovered while investigating the total energy exchange is that the largest variation from the sphere-sphere configuration is not at the smallest separation.

We found the largest increase in an oblate spheroid-sphere system over a sphere-sphere system to be at a separation of $0.5R$, and the largest decrease in a prolate spheroid-sphere system below the sphere-sphere system is at $0.15R$ separation where R is the radius of the sphere. We also established that the largest variance is at $0.2R$. The appearance of the extrema at intermediate separations instead of the smallest show that the shape effect appears to be strongest at intermediate separations. This could be due to destructive interference as the back sides of the objects become involved in the near-field energy exchange; however, more configurations need to be investigated to establish this claim.

Our third observation comes from the investigation of the distribution of the flux across the surfaces. We found that a sharper object concentrates the flux through a small region on the flatter object at small separations and creates a local minimum at the center line of the gap at larger separations. This means there exists a separation where the flux across the surface of the flatter object is uniform. Coupling this fact with our previous observation about the largest change in the exchange from the sphere-sphere system, we can deduce that the appropriate choice of separation and object shape will produce a distinct total and spatial distribution of the flux in a system. Specifically, at large separations, we predict a local minimum on the surfaces on the symmetry axis due to destructive interference and a local maximum at small separations due to coupling of the evanescent and propagating waves on the surfaces.

To continue the investigation of the shape effects, we turn our attention to a spheroid and a disk. This is a configuration that resembles a scanning tunneling microscope tip and sample disk. By considering this new system, we will further test the validity of the view factors in describing the change in the total energy exchange compared to a reference system. This will also allow us to probe the radial distribution of the flux across a flat surface and provide insight on how to create flux patterns.

The results presented in this chapter used the basic mesh of 510 edges from the convergence analysis in Chapter 3. This allowed for the high level overview of the shape effects discussed above. Further investigation of the spatial distribution across the surfaces will

benefit from the use of finer meshes. This would provide additional insight to pattern formation on surfaces. However, the time needed to compute the high fidelity results must be taken into account. For two meshes with 2,600 edges each, the time needed to evaluate all 30 wavelength for 25 separations and 19 eccentricities is 10,336 computer hours or 430 computer days. This time estimate is based on the timing results from the convergence analysis is Chapter 3. The workstations available are comparable, but the scaling of the sphere mesh to a spheroid changes the separation between the edges within the mesh. Specifically, the spatial separation between two edges in a given mesh are, on average, decreased. This decrease causes the LIBSCUFF library to use a more computationally demanding algorithm to compute the interaction. This results in an increase int the computational requirement at larger eccentricities.

CHAPTER V

DISK-SPHEROID EXCHANGE ANALYSIS

5.1 Introduction

In this chapter, we extend the results of the sphere-spheroid analysis to a system of a spheroid and a circular disk. As in the previous chapter, the spheroid-disk system has only received cursory analysis in the literature, and we will provide a more complete analysis of this system. Previously, we considered the total energy exchange as a function of the eccentricity of the spheroid and the separation between the surfaces. In that investigation, we discovered that the total energy exchange is governed by the mutually projected areas of the objects, and established that the view factors of classical far-field radiative transport theory describe the modulation observed in the near-field heat transfer from the reference sphere-sphere interaction curves (Figures 16b and 18). We also considered the spatial distribution of the flux across the surfaces of the objects and observed that the peak of the exchange does not stay focused at the center of the objects but rather spreads out to the edges as the separation increases. This spreading of the flux created a local minimum on both surfaces at the point where the surfaces are closest due to destructive interference. These observations led us to two predictions: The separation is the dominant contributor to the enhanced energy exchange with the view factors describing the modulation from a sphere-sphere configuration, and a ring should form on both surface as the separation between two surfaces increases.

In addition to testing our predictions, changing from a sphere-spheroid system to a circular disk-spheroid system provides a clearer way to investigate the radial distribution of the flux. The definition of the disk places all of the faces on one of the circular faces in a common plane. When we considered the flux through a sphere previously, the curvature of the sphere introduced an additional displacement and rotation from the orientation of a face at the center of the gap. With the top of the disk in one plane, only one variable

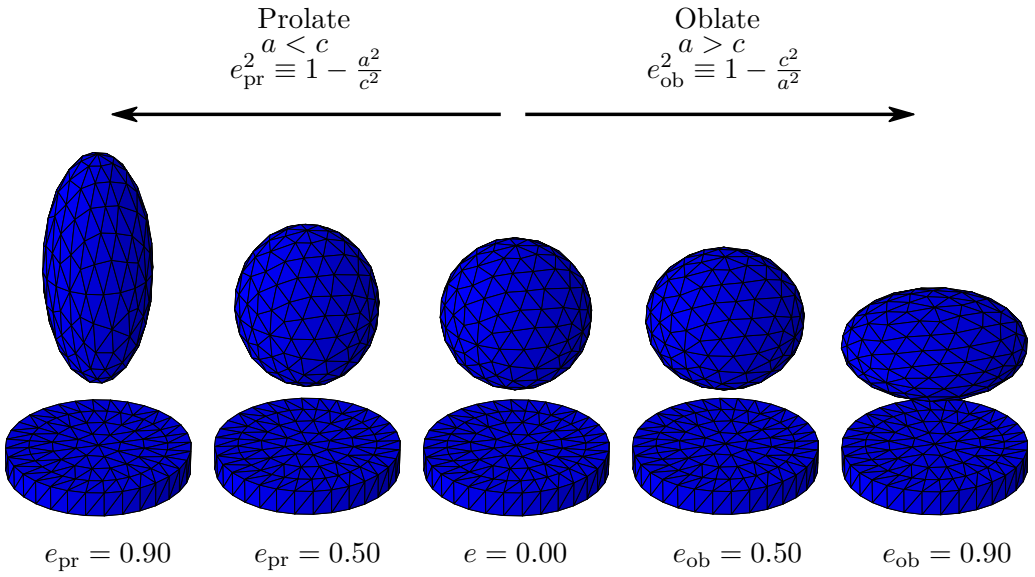

Figure 22: A sample of the geometric configurations considered.

remains in the transformation from the center of the disk: the radial displacement from the symmetry axis of the system.

To test these predictions, we consider the case of a spheroid above a circular disk. We take the symmetry axes of the spheroid and disk to be aligned as depicted in Figure 22. This choice maintains the cylindrical symmetry of the system. We also continue with the same assumptions used in the previously studied systems; specifically, the disk and spheroid are both made of gold with one held at 300 K and the other at 0 K. We continue to use gold for the systems under consideration for two reasons: First, it makes our system is a simple extension of the verification system, and second, gold is a common material for constructing nanostructures. Other materials that have been considered in the literature are SiC [73] and SiO_2 [50]. Both of these materials support polaritons in the visible and infrared region of the electromagnetic spectrum. The specification of which object is at which temperature is postponed until later because the temperatures only enters through the difference of the oscillator energy functions $\Theta(\omega, T_s) - \Theta(\omega, T_p)$. We use the spheroid geometry used in the previous chapter and create a new mesh for the disk with 528 edges. Our initial analysis begins with a disk of equal surface area to that of the spheroid.

5.2 Spheroid Above an Equal Surface Area Disk

As in the sphere-spheroid system, we begin by examining the total energy exchanged between the disk and the spheroid. We take a spheroid with surface area equal to a sphere of radius 0.200 µm and a disk with radius 0.250 µm and height 0.070 µm. These dimensions generate a disk with surface area equal to the spheroid. Figure 23a presents the total radiative energy exchange between the axially aligned spheroid and disk with one held at 300 K and the other at 0 K normalized by the classical blackbody value without the view factor σAT^4, and Figure 23b presents the results normalized with the view factor.

The purpose of considering the normalization without the view factor in addition to the normalization with the view factor is to set a standard for our prediction. The common normalization in the literature is to neglect the view factor; whereas, we have predicted that the view factor of classical radiative far-field transfer is appropriate for the near-field as well to describe the modulation about a reference configuration. In order to properly evaluate our prediction, we must continue to test it by investigating the total energy exchange both with and without the view factor included in the normalization. Our first observation is that the separation is the dominant contribution to the enhanced energy exchange. This is consistent with our observation in Chapter 4 that the enhanced energy exchange is primarily governed by the separation of the surfaces. Both with and without the view factor, we see a variation in the energy exchange as a function of eccentricity at each separation. We can clearly see the increased energy exchange for the oblate spheroid-disk systems and the decreased energy exchange for the prolate spheroid-disk systems as predicted. The variance is evident at all separations in Figure 23a, and it is always seen at the small separations in Figure 23b.

To take a closer look at this variance as a function of eccentricity, let us consider the value

$$\log_{10}\left[\frac{H(e,d)}{\sigma AF(e,d)T^4}\right] - \log_{10}\left[\frac{H(0,d)}{\sigma AF(0,d)T^4}\right] \tag{62}$$

both with and without the view factor $F(e,d)$ included. Our prediction states that including the view factor for a spheroid-disk system will describe the change in the total energy

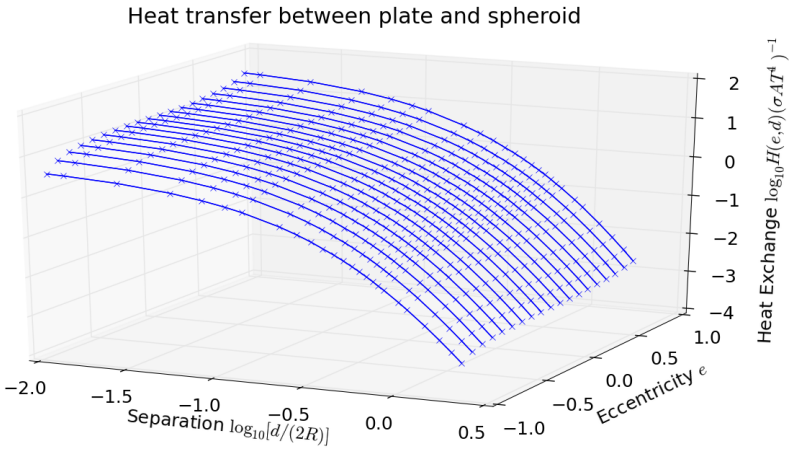

(a) Total heat exchange without accounting for the view factors σAT^4.

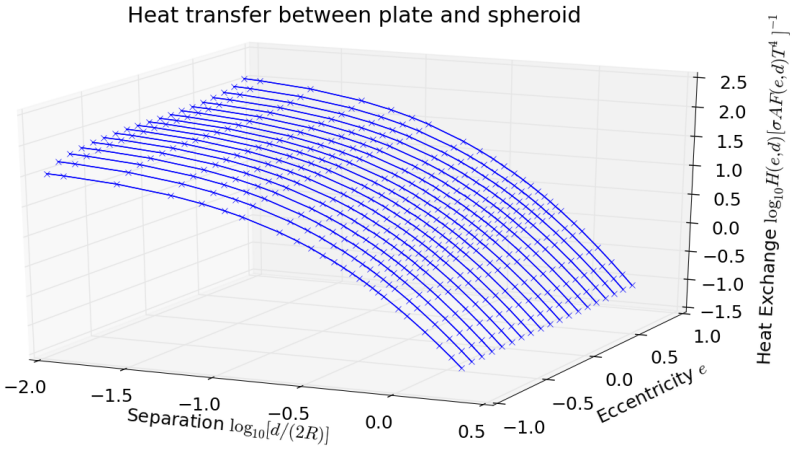

(b) Total heat exchange accounting for the view factors $\sigma AF(e,d)T^4$.

Figure 23: The total heat exchange between a spheroid and a disk with equal surface areas normalized by the blackbody value.

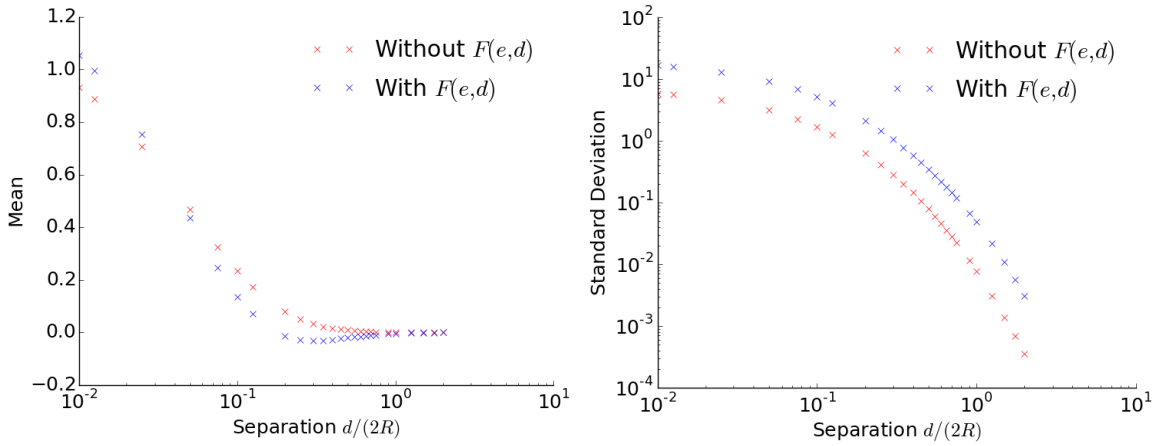

(a) Average across eccentricities.

(b) Standard deviation across eccentricities.

Figure 24: Mean and standard deviation across eccentricities of Figures 23a and 23b minus the sphere-disk ($e = 0$) result.

exchange from a reference sphere-disk system. If our prediction is correct, then this value will tend to zero; thus, we can use it as an estimate of the error. Figure 24a presents the average of this value at each separation, and Figure 24b presents the corresponding standard deviation at each separation.

Looking at Figure 24a, we immediately see that the raw magnitude of the mean of the error is higher when we include the view factors at small separation. The error when including the view factor drops below the error without the view factor at a separation of $d \approx 0.08R$ where R is the radius of a sphere with surface area equal to the spheroid. As the separation further increases, both errors tend to zero at a separation of $d \approx 2R$. At first glance, it would appear that using the view factors does not provide a better description of the heat exchange at the small separations; however, looking at Figure 24b reveals that the error with the view factors included varies over an order of magnitude larger than the error without the view factors because the raw values are an order of magnitude higher than the results without the view factors. Thus, we need to look at the relative error.

Defining the relative error as

$$1.0 - \log_{10}\left[\frac{H(e,d)}{\sigma A F(e,d) T^4}\right] / \log_{10}\left[\frac{H(0,d)}{\sigma A F(0,d) T^4}\right], \tag{63}$$

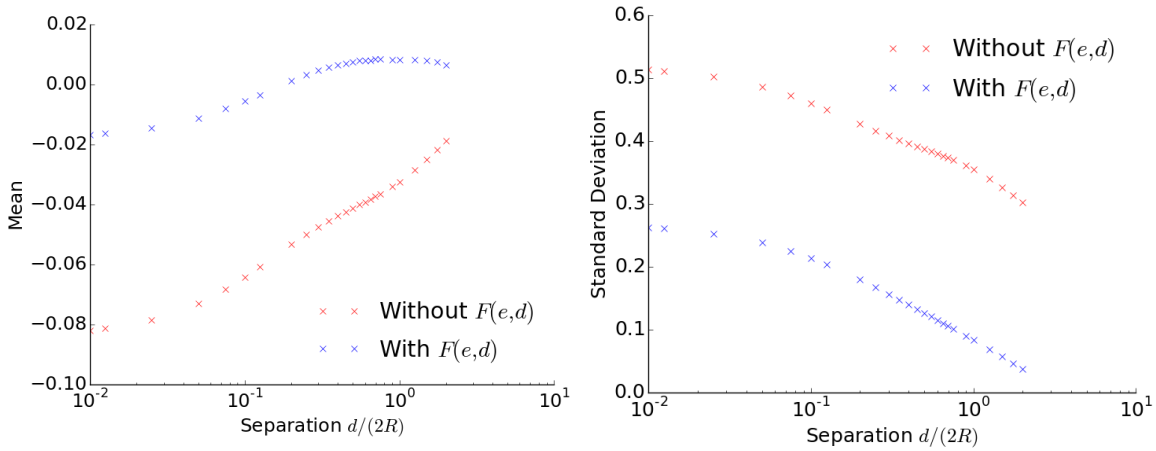

(a) Average across eccentricities.

(b) Standard deviation across eccentricities.

Figure 25: Mean and standard deviation across eccentricities of the relative error in Figures 23a and 23b minus the sphere-disk ($e = 0$) result.

we can get a better estimate how well the view factor describes the change of the enhanced total exchange from a sphere-disk system due to increased eccentricity of a spheroid. Figure 25a presents the average relative error at each separation as a function of eccentricity both including and excluding the view factor. We clearly see that the relative error using the view factor is dramatically lower than excluding the view factor. For separations below $d \lesssim 0.1R$, the relative error without the view factor is roughly 5 times higher than the error including the view factor. For separations above $d \gtrsim .1R$, the relative error in neglecting the view factor is an order of magnitude larger than the error including the view factor. These results confirm our prediction that the view factors from classical radiative transfer can be used to predict the modulation of enhanced near-field radiative energy exchange from a reference configuration.

Considering Figure 25b, we see that although the view factor does indeed account for most of the modulation of the enhanced energy exchange from a sphere-disk system, the standard deviation in the error as a function of eccentricity is still appreciable at small separations. We can understand this large variation by considering the separation of the faces on the surfaces. In the sphere-spheroid case, the curvature of the sphere moves additional faces outside of the decay range of the evanescent waves on the surface of the spheroid. In the case of a circular disk and a spheroid, the inclusion of more faces in the same plane

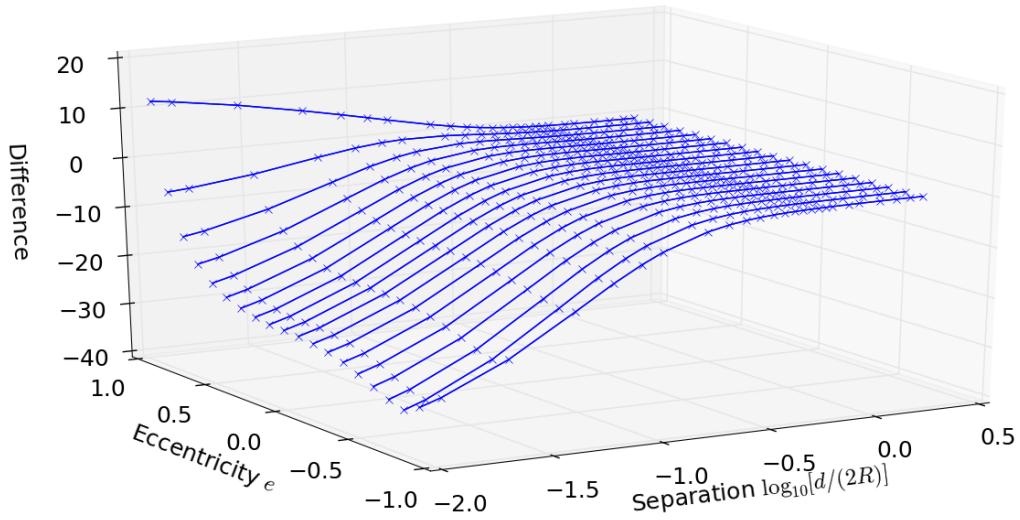

Figure 26: Difference between sphere-spheroid results and disk-spheroid results.

means that a larger portion of the faces on the disk remain within the decay range of the evanescent waves on the spheroidal surface. As we keep seeing, this increase in the amount of the surface in the decay range of the evanescent waves increases not only the total energy transfer but also the sensitivity of the energy transfer to the separation.

We know that the view factor describes the change in the enhanced energy exchange for a spheroid-disk system from a sphere-disk system, but how far can we distort the shape? Let us compare these spheroid-disk results with the spheroid-sphere results from Chapter 4. This will demonstrate how far we can distort the reference system and still use the view factors do describe the change in the energy exchange. Figure 26 presents

$$\frac{H_{\text{sphere-spheroid}}(e,d)}{\sigma A F_{\text{sphere-spheroid}}(e,d)T^4} - \frac{H_{\text{disk-spheroid}}(0,d)}{\sigma A F_{\text{disk-spheroid}}(0,d)T^4} \tag{64}$$

where $H_{\text{sphere-spheroid}}$ are the results presented in Figure 15. We see that at large separations, $d \gtrsim 2R$, the view factor approach can correctly predict the change in the enhanced energy exchange when the sphere in a sphere-spheroid system is swapped out for an equal surface area disk.

On the other hand, at smaller separations, we see an increasing difference between the

two systems. We see that the spheroid-disk system predicts a larger interaction for all but the most oblate spheroid-disk systems compared to the spheroid-sphere system with the same eccentricity and separation. Inspecting Figures 15 and 23b, we see that the results for the energy exchange in a disk-spheroid system and a sphere-spheroid system lie within an order of magnitude of each other. If we look at the relative error using the view factor to convert from the sphere-sphere configuration to a disk-sphere, we find that the relative errors are on the order of 0.2. This means that the view factor is well suited to describe incremental changes in one surface shape; however, when one of the surfaces dramatically changes, like from a sphere to a disk, the view factor does not describe the change at small separations.

Now we compare the numeric results for the disk-spheroid systems at each separation to the disk-sphere system at the same separation. Figure 27 presents the total energy exchange between the disk and the spheroid normalized by the disk-sphere configuration at the same separation both with and without the view factor. As in the sphere-spheroid case, these plots provide a direct means to investigate how the eccentricity of the spheroid modulates the total energy exchange which is dominated by the separation of the objects.

Unlike the sphere-spheroid case, we see that the largest variation in the enhanced energy transfer is at the smallest separation. This is due to the disk having faces closer to the sphere. As discussed above, the curvature of a sphere simultaneously draws faces away from the spheroid while the curvature of the spheroid draws faces away from the sphere in the sphere-spheroid system. In a disk-spheroid system, the increase in separation between individual faces is due solely to the curvature of the spheroid as the eccentricity changes. This means more faces are within the decay range of the evanescent waves on the surfaces of the disk spheroid system leading to additional energy exchange at small separations.

At large separations, the view factor in the oblate spheroid-disk system accounts for all but 4.6 % of the variation in the enhanced energy exchange from the sphere-disk configuration. This can be understood by considering the projected area. For an oblate spheroid with eccentricity $e_{\mathrm{ob}} = 0.9$, the equatorial radius is very close to the radius of a circular disk with the same surface area. In our specific case, the surface area of both the disk

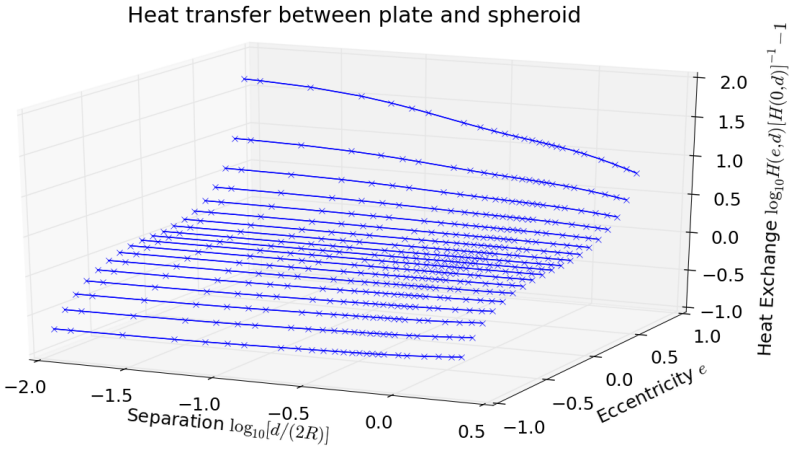

(a) Without the view factors.

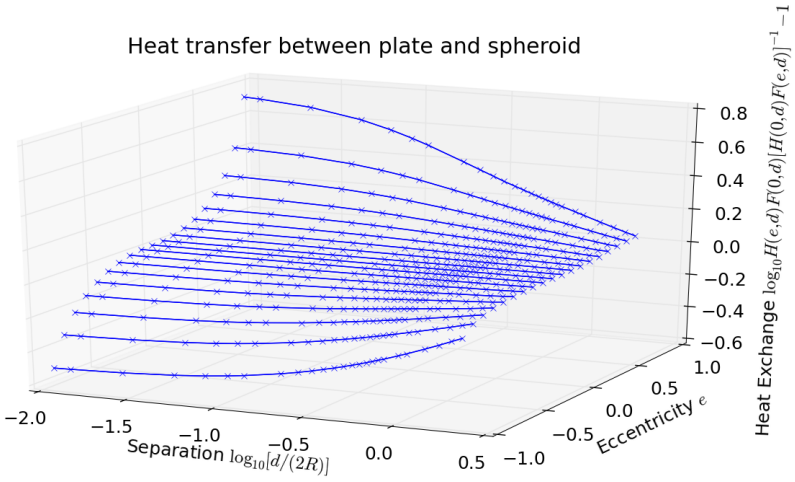

(b) With the view factors.

Figure 27: Total energy exchange normalized by the sphere-disk result at the same separation.

and the spheroid is $4\pi 0.200^2$ which give an equatorial radius of 0.247 µm for the spheroid, and we defined the radius of the disk to be 0.250 µm. This has two consequences: First, more faces on the spheroid are oriented toward the disk which increases the efficiency of the energy exchange; thus, the view factors produce a more accurate description of the energy exchange. Second, the interaction of the sides of the disk become nontrivial and cannot be ignored. Specifically, the system is approaching the point where the surface of the spheroid is within the decay range of the faces on the sides of the disk. To investigate the effect of the sides of the disk, we will need to investigate the spatial distribution of the energy exchange across the surfaces.

Our final observation before we move onto considering the spatial distribution of the flux is that the heat exchange remains a smooth monotonic function of the both eccentricity and separation. This means that we can inspect a subset of these two parameters and use an interpolation scheme to find intermediate values if necessary. By reducing the number of unique parameters calculated, the raw computational effort is reduced. This provides additional time that can be applied to additional configurations or to using higher resolution meshes to analyze known systems.

Now that we have considered the total enhanced energy exchange between a spheroid and a disk with equal surface area, we consider the distribution of the flux across the surfaces. As discussed in Chapter 4, we use an area weighting scheme to map the flux from the edges to individual faces on the surfaces. The results presented below are for a gold spheroid with surface area equal to a sphere of radius 0.200 µm and a circular disk with radius 0.250 µm and height 0.070 µm. We set the disk to be at a temperature 300 K and the spheroid to have a temperature of 0 K. Figure 28 presents an example of the distribution of the fluxes across the surfaces at a separation of 0.100 µm. The rotational symmetry of the system is reflected in the flux distribution and is evident at all separations. To simplify the plots, we can consider the flux through each face as a function of the distance of the face midpoint from the center of the top of the disk.

Figures 29 through 34 present the flux through each face normalized by σT_0^4, where $T_0 = 300\,\mathrm{K}$, as a function of the distance from the center of the top of the disk for six

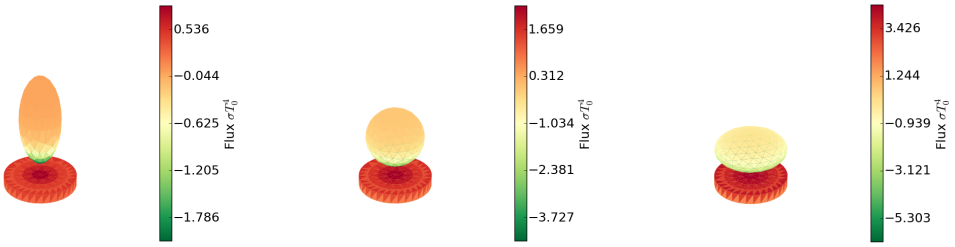

(a) Prolate spheroid $e_{\text{pr}} = 0.9$ **(b)** Sphere $e = 0.0$ **(c)** Oblate spheroid $e_{\text{ob}} = 0.9$

Figure 28: Surface distribution of the flux for three eccentricities at a separation of 0.100 µm.

separations. The results for the prolate spheroid with $e_{\text{pr}} = 0.9$ (red), sphere (green), and oblate spheroid with $e_{\text{ob}} = 0.9$ (blue) are plotted along with the disk in each system. We have taken the disk to be the hot object; however, as mentioned above, simply swapping the temperatures would cause the graphs to be mirrored across the x-axis. The first thing we see in Figures 29 and 30 is that the exchange is highly focused around the point of smallest separation for both objects at these small separations just as we saw in the sphere-spheroid analysis. We also see that the curvature of the spheroid concentrates the flux on the disk underneath the tip of the spheroid. In addition, the flux is distributed across a larger area of the disk than that of the spheroid. This is because the faces of the disk reside in a common plane and, therefore, are in closer proximity to the spheroid than would be the case had we used a sphere. The curvature of the spheroid pulls more faces away from the center of the gap reducing the number of interacting faces and increasing the flux through an individual face.

Considering Figures 31 and 32, we see there is a transition from a local maximum in the flux to a local minimum passing through the top of the disk. The formation of the local minimum as the separation increases from 0.100 µm to 0.200 µm is most pronounced for the oblate spheroid-disk system, but it also exists for the sphere-disk system. This means that there exists a separation where the spatial distribution across the disk is uniform. Looking closely at Figure 32a, we see that the prolate spheroid is indeed close to uniform. However, this uniform distribution is marred by the increased contribution along the edges of the disk which begins to become evident at a separation of 0.100 µm. We can also see the formation of a local minimum on the spheroid between these two separations. In

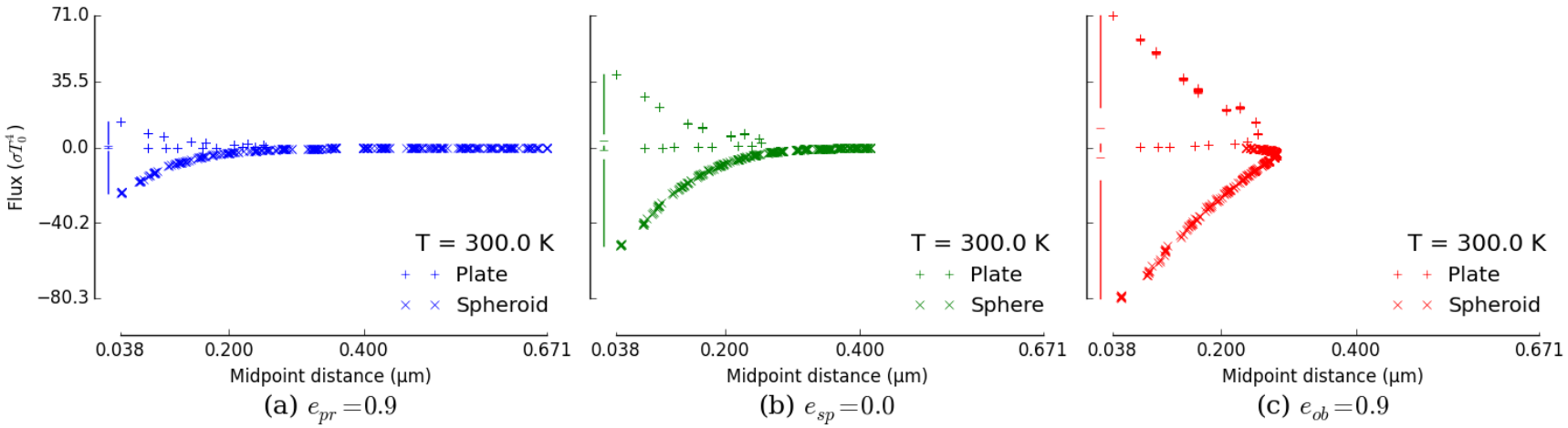

Figure 29: Radial distirbution of the flux in a circular disk-spheroid system (prolate $e_{\rm pr} = 0.9$ (a), sphere $e_{\rm sp} = 0.0$ (b), and oblate $e_{\rm ob} = 0.9$ (c)) normailzed by the classical blackbody flux value σT_0^4 where T_0 is 300 K and the surfaces are separated by a gap of 0.020 μm.

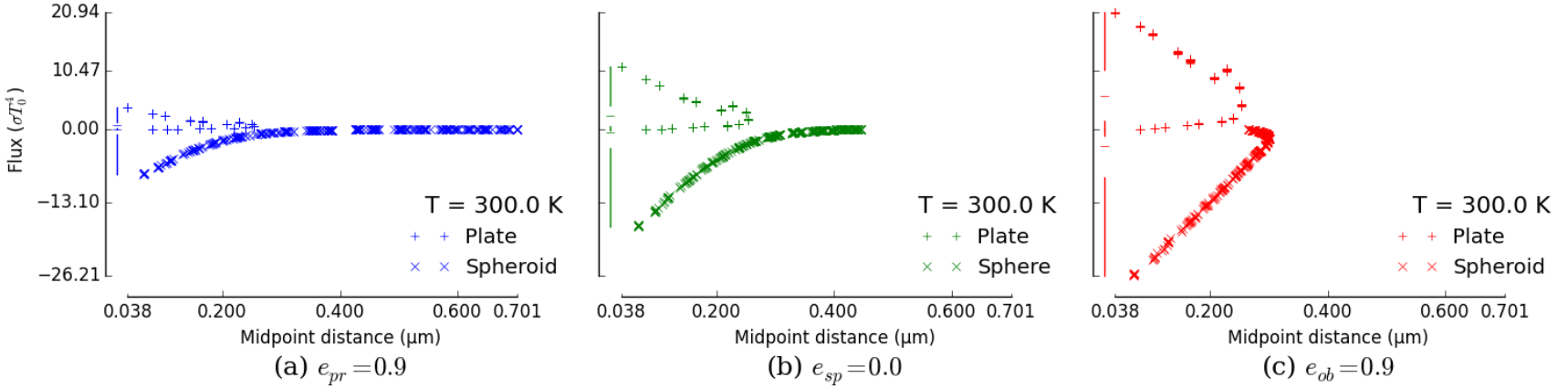

Figure 30: Radial distirbution of the flux in a circular disk-spheroid system (prolate $e_{\rm pr} = 0.9$ (a), sphere $e_{\rm sp} = 0.0$ (b), and oblate $e_{\rm ob} = 0.9$ (c)) normailzed by the classical blackbody flux value σT_0^4 where T_0 is 300 K and the surfaces are separated by a gap of 0.050 μm.

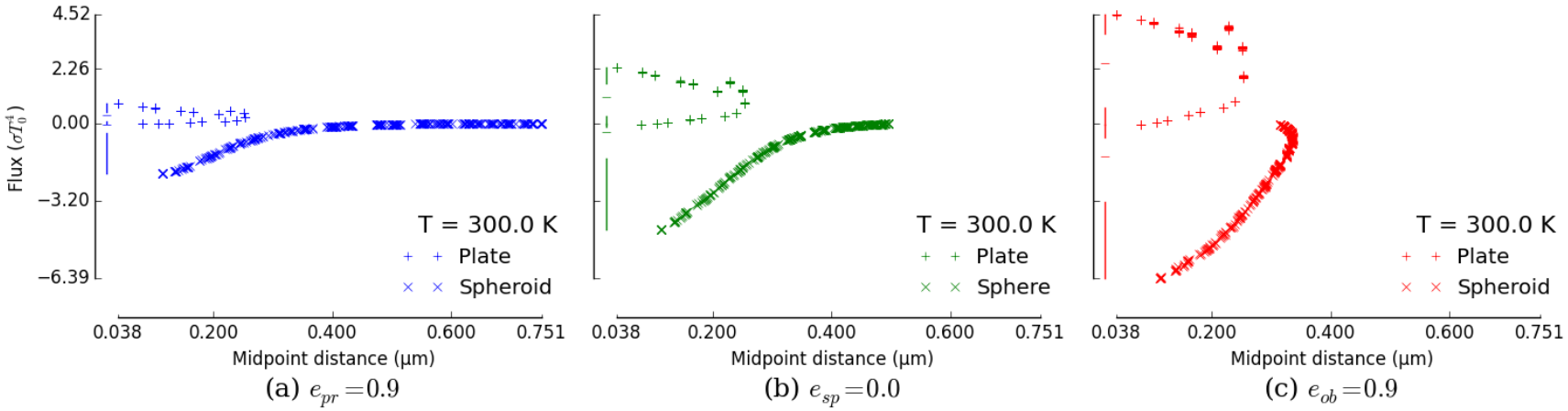

Figure 31: Radial distirbution of the flux in a circular disk-spheroid system (prolate $e_{\rm pr} = 0.9$ (a), sphere $e_{\rm sp} = 0.0$ (b), and oblate $e_{\rm ob} = 0.9$ (c)) normailzed by the classical blackbody flux value σT_0^4 where T_0 is 300 K and the surfaces are separated by a gap of 0.100 μm.

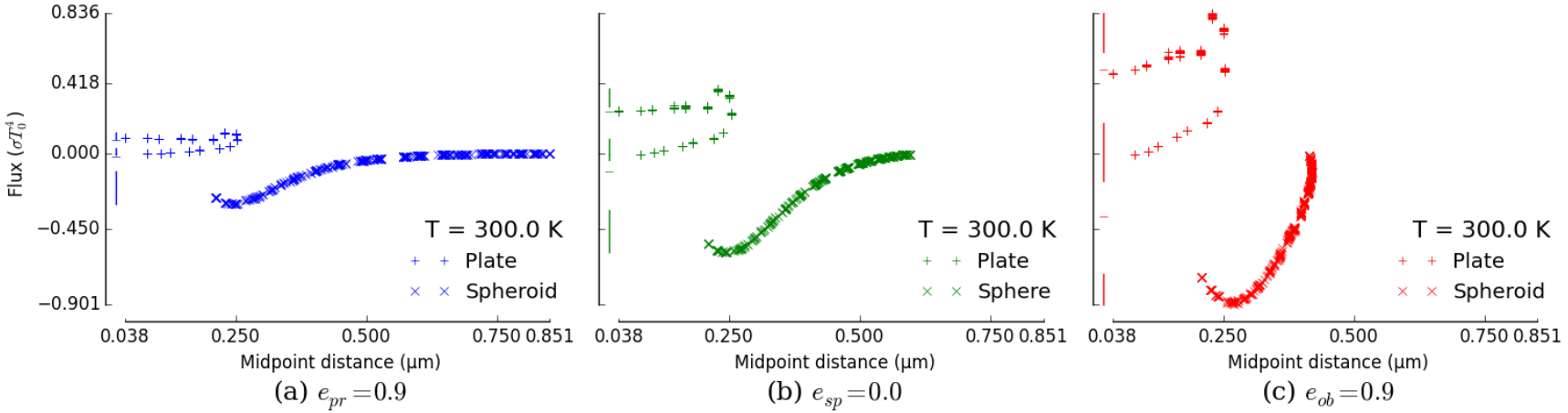

Figure 32: Radial distirbution of the flux in a circular disk-spheroid system (prolate $e_{\rm pr} = 0.9$ (a), sphere $e_{\rm sp} = 0.0$ (b), and oblate $e_{\rm ob} = 0.9$ (c)) normailzed by the classical blackbody flux value σT_0^4 where T_0 is 300 K and the surfaces are separated by a gap of 0.200 μm.

the sphere-spheroid analysis, we did not see the formation of the local minimum on either surface until separations between 0.200 µm and 0.400 µm. This demonstrates the destructive interference caused by the edges of the disk.

At the smaller separation of 0.050 µm, Figure 30 shows that the hot spot of the flux in the center of the disk is approximately three times higher than the flux through the faces at the edge of the disk across all eccentricities. Figure 33 reveals that at the larger separation of 0.400 µm, the flux through faces on the edge of the disk are three time higher than the flux through the center of the disk in the disk-sphere system. As the separation further increases to 0.800 µm, as depicted in Figure 34, the interaction of the edge of the disk is the dominant contribution to the energy exchange and is most pronounced in the oblate spheroid-disk system. As mentioned before, the equatorial radius of the oblate spheroid is comparable to the radius of the disk. This means that more faces on the disk are within the decay range of the evanescent waves on the oblate spheroid as compared to the prolate spheroid. This increase in interacting faces means that there will be a larger fraction of the spheroidal surface interacting with the faces on the edge of the disk than for the other systems. Close inspection of the fractional contribution of the faces to the exchange reveals that the edge of the disk is holding at a constant fraction of the interaction as a function of separation and becomes the dominant contribution at separations above 0.400 µm. The edge of the disk is the point on the mesh where the basis functions are defined over faces with dramatically different orientations because the surface is discontinuous. If we look at the case of an oblate spheroid in the sphere-spheroid analysis, we see a smooth distribution of the flux at a similar distance to where the spheroid-disk system has a peak in the flux at the edge.

To ensure that the peak at the edge is not simply a numerical relic of the computation method, we need to consider a circular disk with a larger radial extent. If we find the radial distribution remains the same, we will know that the dramatic edge effects are not due to a simple numeric issue. Before moving on to the larger disk analysis, let us take a moment to consider the interaction of the back of the disk. Looking back to Figures 29, 30, and 31, we see that the magnitudes of the interaction of the faces on the back of the

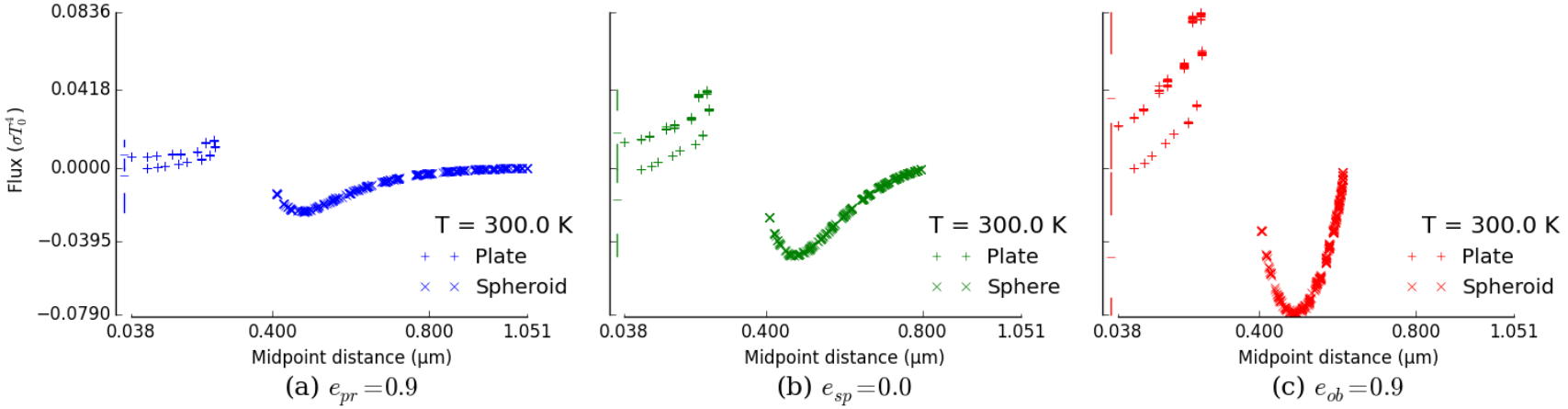

Figure 33: Radial distirbution of the flux in a circular disk-spheroid system (prolate $e_{\rm pr} = 0.9$ (a), sphere $e_{\rm sp} = 0.0$ (b), and oblate $e_{\rm ob} = 0.9$ (c)) normailzed by the classical blackbody flux value σT_0^4 where T_0 is 300 K and the surfaces are separated by a gap of 0.400 μm.

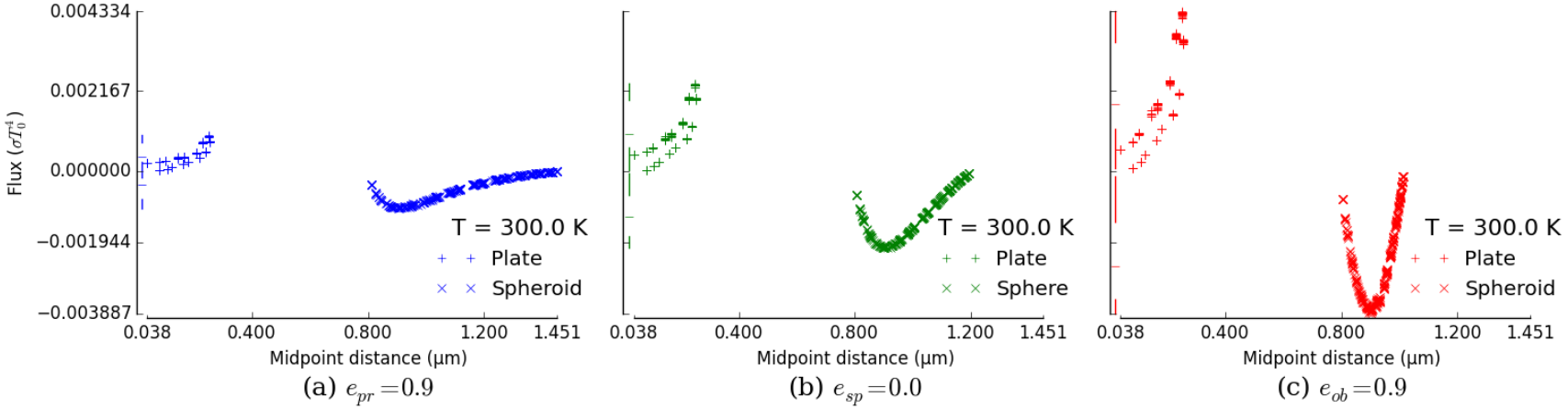

Figure 34: Radial distirbution of the flux in a circular disk-spheroid system (prolate $e_{\rm pr} = 0.9$ (a), sphere $e_{\rm sp} = 0.0$ (b), and oblate $e_{\rm ob} = 0.9$ (c)) normailzed by the classical blackbody flux value σT_0^4 where T_0 is 300 K and the surfaces are separated by a gap of 0.800 μm.

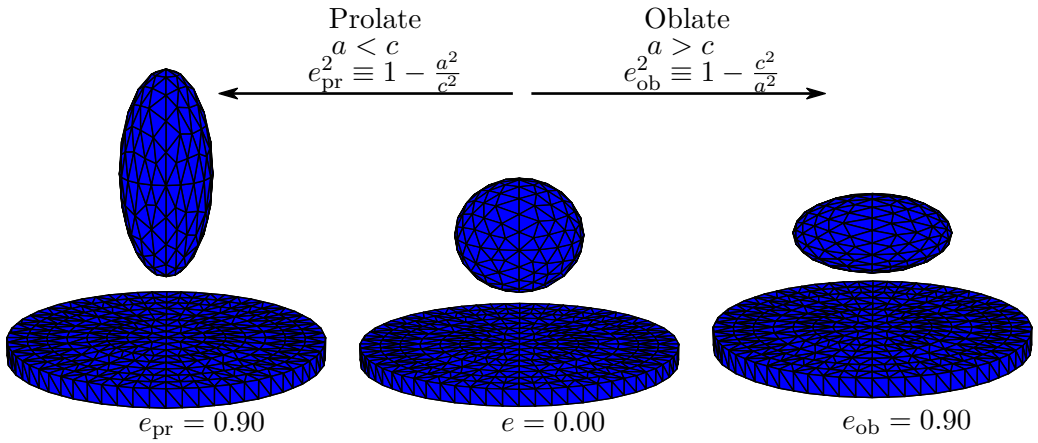

Figure 35: A sample of the geometric configurations considered.

disk are trivial compared to the interaction of faces on the top and sides. As the separation increases, we see that the faces at the center of the back of the disk remain close to zero; however, the faces closer to the edge of the disk produce a significant contribution to the interaction. This is due to not only the wave nature of the exchange, which can traverse the internal medium of the disk, but also the decreased total exchange between the disk and the spheroid. The net result of this is that we cannot simply neglect the back of the disk in an attempt to reduce the number of edges used to generate the mesh for the disk; the back of the disk must also be modeled.

5.3 Spheroid Above a Large Disk

To further probe the nature of the edge effects on the disk, we consider a disk larger than the one in the previous section. For this case, we double the radius of the top and bottom of the disk to 0.500 µm and take the total surface area to be 3.5 times the surface area of the spheroid. We also consider a reduced number of eccentricities and separations. The smooth nature of the radiative energy exchange as a function of these two parameters allows us to consider this reduced parameter space and we can use interpolation to find intermediate values. This reduced parameter space reduces the total computational time while providing a basic understanding of the radiative energy exchange. We also continue to use gold as the material of the bodies.

Figure 35 depicts some of the geometries considered with the larger disk. Looking at

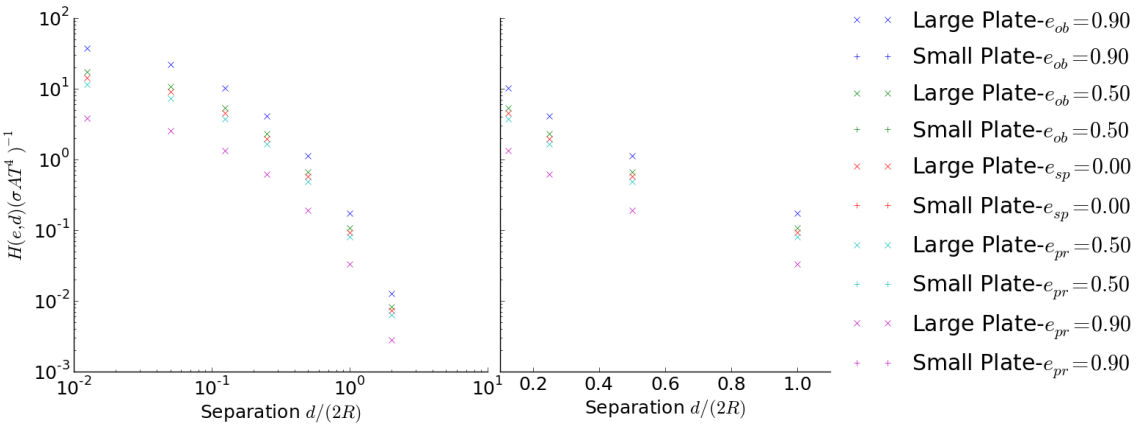

Figure 36: Total energy exchange in a small (+) and large (x) disk spheroid system in units of the basic blackbody exchange σAT^4.

the prolate spheroid in this figure, we see that a practical ramification of this larger disk configuration is that the prolate spheroid-disk system begins to more closely resemble a tip used in scanning probe microscopy. This provides a means by which the numerical results presented in this thesis can be investigated experimentally. For example, a scanning tunneling microscope with a cantilever can be used to measure the temperature distribution across a thin film and thus directly measure the spatial distribution of the radiative exchange.

Figure 36 presents the total energy exchange in both a large disk-spheroid system (x) and a small disk-spheroid system (+). In all of the systems presented, the disk is held at 300 K and the spheroid is at 0 K. The results are normalized by the classical blackbody value without the view factor σAT_0^4 where A is the surface area of the spheroid and $T_0 = 300\,\mathrm{K}$. This normalization simply presents the raw value of the exchange in a common unit and does not account for shape effects. At the smallest separation, the large disk system exchanges radiative energy at a rate 1.31 times higher than the small disk. On the other hand, at the larger separations the large disk system exchanges energy at a rate 6.01 times higher than the small disk.

By construction, the surface area of the disk is 3.5 times that of the smaller disk. Knowing that the surface area governs the interaction, we would have initially expected the increased interaction due to the larger disk to be closer to this factor of 3.5. However, this assumption does not account for the viewable area. At the smallest separations, only

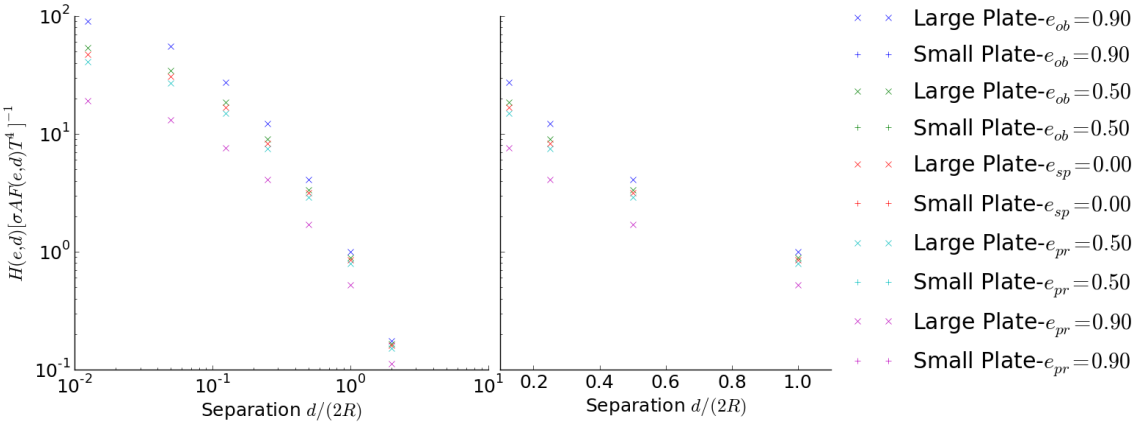

Figure 37: Total energy exchange in a small (+) and large (x) disk spheroid system in units of the basic blackbody exchange including the view factor $\sigma AF(e,d)T^4$.

the top circular surface is truly viewable by the spheroid. Taking the parameters used to generate the large disk, the fraction of the total surface area of one circular side of the disk f_l is 1.14 times larger than the fraction of the circular side on the small disk $f_l = \pi r_l^2/A_l = 4\pi r_s^2/(3.5A_s) = (4/3.5)f_s$. This demonstrates that the faces closest to the center of the disk dominate the interaction at the small separations because they are outside of the decay range of the evanescent waves. The additional faces away from the center do participate in the interaction, but their contribution is not as large. As the separation increases, the contributions of faces closer to the edge of the disk and on the back become more in line with those faces at the center as the propagating modes become the dominant channel of interaction which accounts for the larger increase in the energy exchange at the larger separations.

Taking a look at the radiative exchange results with the view factor incorporated, Figure 37, we see the view factor is a slightly better fit for the smaller disk because the results are closer to the sphere-disk curve. This is more pronounced for the prolate than the oblate systems. The small disk has a higher exchange at small separations compared with the larger disk. The prolate spheroid-small disk system has an interaction 1.5 times larger than the large disk counterpart while the oblate system is only 0.12 times larger. At the larger separations, we see that all of the small disk results are between 7×10^{-2} and 9×10^{-2}; whereas, the large disk results are between 10^{-1} and 2×10^{-1}. This means we have inverted

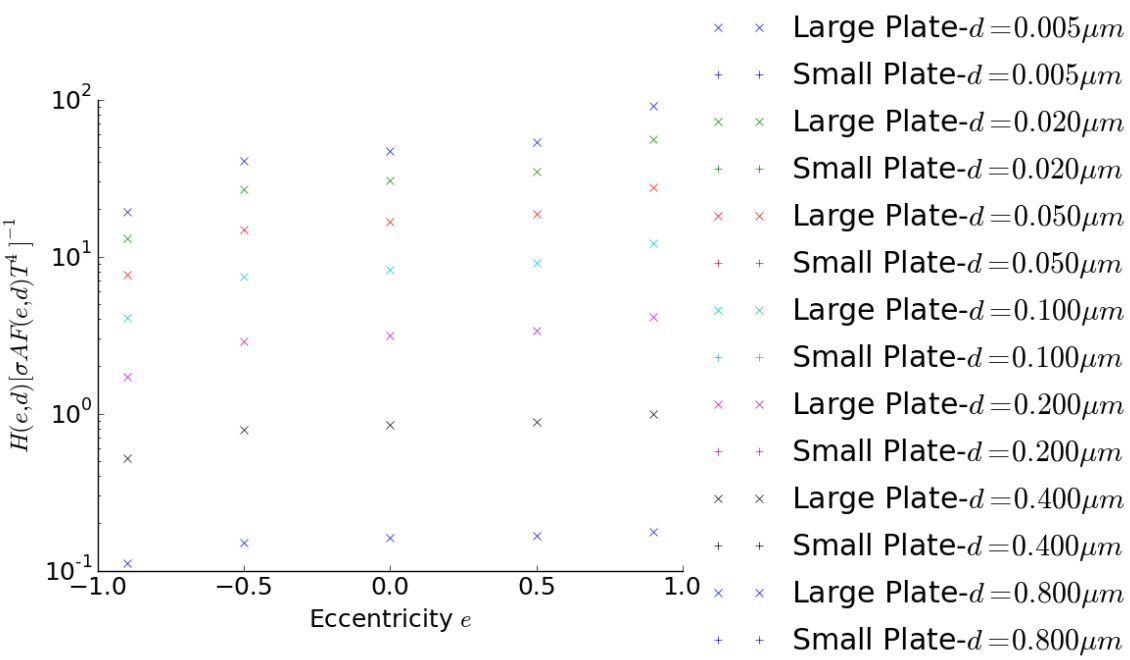

Figure 38: Total energy exchange in a small (+) and large (x) disk spheroid system in units of the basic blackbody exchange including the view factor $\sigma AF(e,d)T^4$.

the situation compared with the small separations. Here, the large disk systems have an interaction 1.5 to 2 times larger than the small disk systems.

Figure 38, presents the same results as Figure 37 plotted as a function of eccentricity instead of separation. Looking at the data in this way, we see that the separation where the energy exchange in the small disk-spheroid system drops below the large disk-spheroid system is between 0.100 µm and 0.200 µm. To put these values into context of the system, the radius R of a sphere with surface area equal to the spheroid is 0.200 µm. We can also see that at large separations, the energy exchange in the prolate spheroid-large disk system is decreasing with increased eccentricity faster than the same separation oblate spheroid-large disk system increases.

The increased exchange in the large disk-spheroid at large separations is easily explained by the increased area of the disk. As the separation increases, the view factor tends to the simple solid angle subtended by the top of the disk. The large disk subtends a larger solid angle. In the current system, the large disk must be 1.5 times farther away from the spheroid for the top of the disk to subtend the same solid angle as the small disk. The increase in

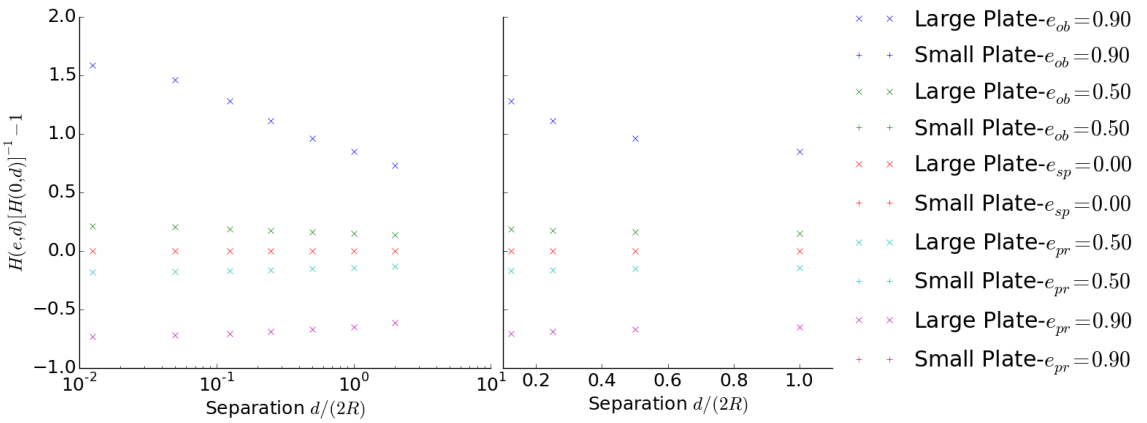

Figure 39: Total energy exchange in a small (+) and large (x) disk spheroid system scaled by the sphere-disk result at the same separation without the view factors.

the energy exchange for the small disk at the small separation is a bit trickier. At these small separations, essentially all of the surface of the small disk is in the decay range of the evanescent waves on the surface of the spheroid. This means all faces are participating in the exchange. For the large disk, the faces on the side of the disk are farther out in the decay range of the evanescent waves and can only contribute to the energy exchange via propagating waves which provide a dramatically lower contribution to the total exchange. These propagating waves then destructively interfere to reduce the energy exchange.

A second point to consider is what we are actually measuring in these plots. Figure 36 provides an absolute scale in units of σAT^4 and shows that for any pair of eccentricity and separation, the large disk-spheroid system always exchanges more energy than the small disk-spheroid system. On the other hand, in both Figure 37 and Figure 38 we are measuring the energy exchange in units that include the fractional viewable area. The net result is that the large disk-spheroid results decay slower than the small disk-spheroid results. This means that the view factors are accounting for more of the separation dependence in the large disk systems than the small disk systems.

To take a close look at how the view factor description of the energy exchange changes as we use a larger disk, we can compare the results at a single separation to the sphere-disk system at the same separation. Figure 39 presents the numeric results scaled by the sphere-disk results at the same separation. A quick glance at Figure 39 readily reveals that the

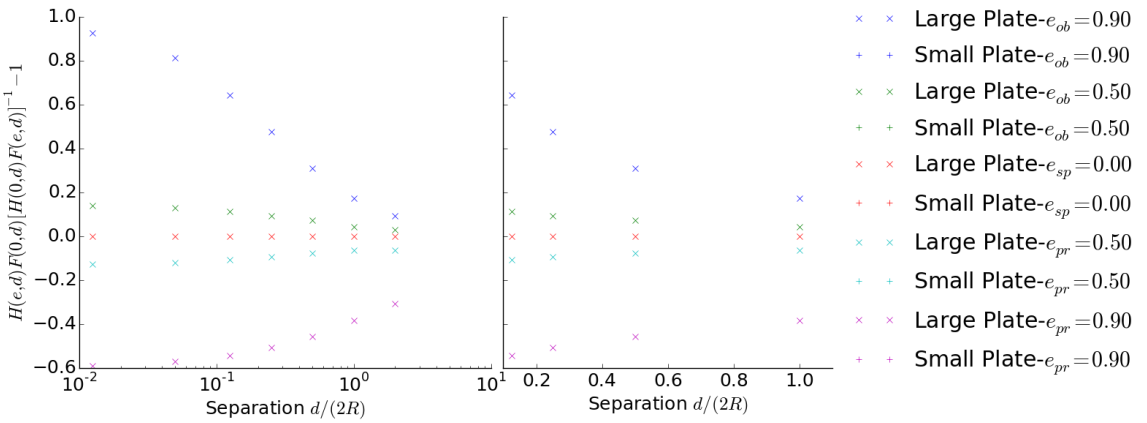

Figure 40: Total energy exchange in a small (+) and large (x) disk spheroid system scaled by the sphere-disk result at the same separation with the view factors.

same scaling factor describes the change from a sphere-disk to a spheroid-disk system when the view factor is not included for all the prolate and the slightly oblate spheroids. This scaling factor is independent of the disk size in these configurations. The oblate spheroid-disk system has more variance in this scaling factor, but that can be attributed to the increase in the projected area. For the small eccentricities, $e \lesssim 0.5$, the variation of this scaling factor is within a few percent of constant as a function of separation. This result supports the previous observation that slightly spheroidal objects can be treated as spheres without introducing too large of an error. Specifically, we now know that the upper bound on the error associated with this treatment is roughly 1 %.

Now we turn our attention to Figure 40 which incorporates the view factor into the results of Figure 39. We can clearly see that the scaling factors for the small eccentricities vary considerably. We also see that the scale factors for the larger eccentricities vary significantly between the two size disks. This large variation is due to double counting of the surface shape. In Figure 40 we are plotting

$$\frac{H(e,d)}{H(0,d)}\frac{\sigma AF(0,d)T^4}{\sigma AF(e,d)T^4}. \tag{65}$$

As we have discussed previously, the view factors account for the shape effects; however, in forming this ratio we have inadvertently included the shape effects twice. The calculation of the energy exchange H uses electromagnetic wave scattering techniques to populate the

matrices. These scattering algorithms automatically include the shape of the surfaces. When we include the view factors in this ratio, we include the shape twice.

To establish the modulation of the enhanced energy exchange from a sphere-disk system to a spheroid-disk system as a function of eccentricity, we cannot include the view factor. Instead, we must consider the ratio $H(e,d)/H(0,d)$ as presented in Figure 39. To compare the numeric results to the blackbody result, the view factor is necessary to account for the shape effects because that is how the shape enters into the classical blackbody exchange. This explains the large variance we observed in the sphere-spheroid analysis. In short, the view factors are necessary to account for the shape effects when one is comparing the simulated results to the classical blackbody result. However, when comparing simulated results for a spheroid-disk system to simulated results for a sphere-disk system, the view factors must not be included to prevent double counting.

We now turn our attention to the spatial distribution of the flux across the surfaces. We can normalize the scales on the spatial distribution by considering the temperature necessary for the spheroid-disk systems to exchange energy at the same rate as a sphere-disk system. This normalization method provides two primary benefits: First, it allows us to make direct comparisons among the distributions, across the surfaces. Second, the equivalent temperature provides a measure of the total energy exchanged between the surfaces. It is possible to do this because the temperature only enters the energy exchange through the oscillator energy distribution $\Theta(\omega, T)$. A tertiary benefit of finding the equivalent temperature is that the power exchanged between a body at finite temperature and a body at 0 K is proportional to the radiative conductance of the system [50]

$$G(T,\omega) = \lim_{\Delta T \to 0} \frac{H(T, T+\Delta T, \omega)}{\Delta T} = \frac{\hbar\omega}{k_B T^2} \frac{e^{(\hbar\omega/k_B T)}}{e^{(\hbar\omega/K_B T)} - 1} H(T,\omega). \tag{66}$$

The design of thermal control systems or energy transfer systems, as mentioned in Chapter 1, requires an understanding of this radiative conductance. Table 1 presents the equivalent temperature used for each spheroid in the subsequent surface distribution plots.

Figures 41 through 46 present the spatial distribution of the flux across the surface of

Table 1: Equivalent temperature in Kelvin

$d/(2R)$	$e_{\mathrm{pr}} = 0.9$	$e_{\mathrm{pr}} = 0.5$	$e_{\mathrm{sp}} = 0.0$	$e_{\mathrm{ob}} = 0.5$	$e_{\mathrm{ob}} = 0.9$
0.0125	743	342	300	266	171
0.0500	742	343	300	265	171
0.1250	738	343	300	265	173
0.2500	730	342	300	266	176
0.5000	712	341	300	267	180
1.0000	678	339	300	269	186
2.0000	622	335	300	271	195

the large disk and spheroid normalized by the blackbody flux σT_0^4 where $T_0 = 300\,\mathrm{K}$. The disk is held at the temperature listed in Table 1 and the spheroid is held at $0\,\mathrm{K}$. The flux is plotted as a function of the distance of the midpoint of each face from the center of the top of the disk just as in the small disk-spheroid presentation.

The first thing we notice is that the radial distribution of the flux across the large disk is much smoother than that for the smaller disk. The general shape of the flux distribution is consistent with all of the smaller disk radiative exchange results. Close inspection of the distribution of the flux across the disk in the sphere-disk systems for both large and small disk shows that the flux is generally lower at all points in the small disk system compared with the large disk. The only discrepancy is along the edge of the small disk where the face that is on the top of the disk suddenly jumps above the flux in the large disk system. Looking at the larger separations, Figures 45 and 46, we see that this anomalous increase at the edge of the disk exists in the large disk system as well. This tells us that the jump we saw in the small disk results is simply numerical noise.

At all separations, the flux through the faces at the center of the top of the disk in the sphere-large disk systems are larger than the smaller disk. At first glance, one might think that a particular face should contribute the same amount of flux if the face area remains the same. However, this does not take into account the increased surface area of the disk.

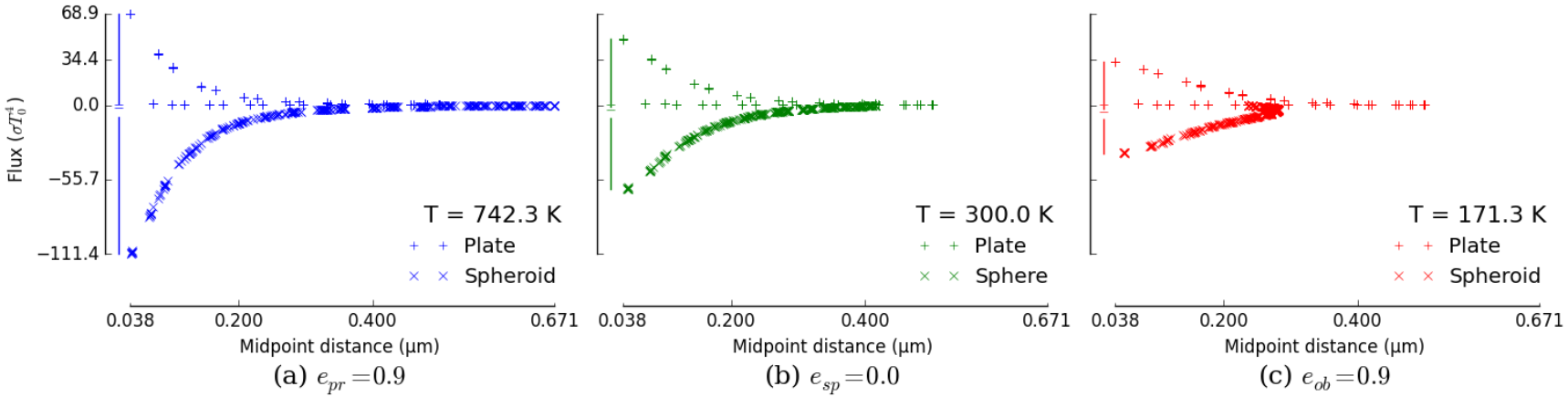

Figure 41: Radial distirbution of the flux in a circular disk-spheroid system (prolate $e_{\mathrm{pr}} = 0.9$ (a), sphere $e_{\mathrm{sp}} = 0.0$ (b), and oblate $e_{\mathrm{ob}} = 0.9$ (c)) normailzed by the classical blackbody flux value σT_0^4 where T_0 is 300 K and the surfaces are separated by a gap of 0.020 μm.

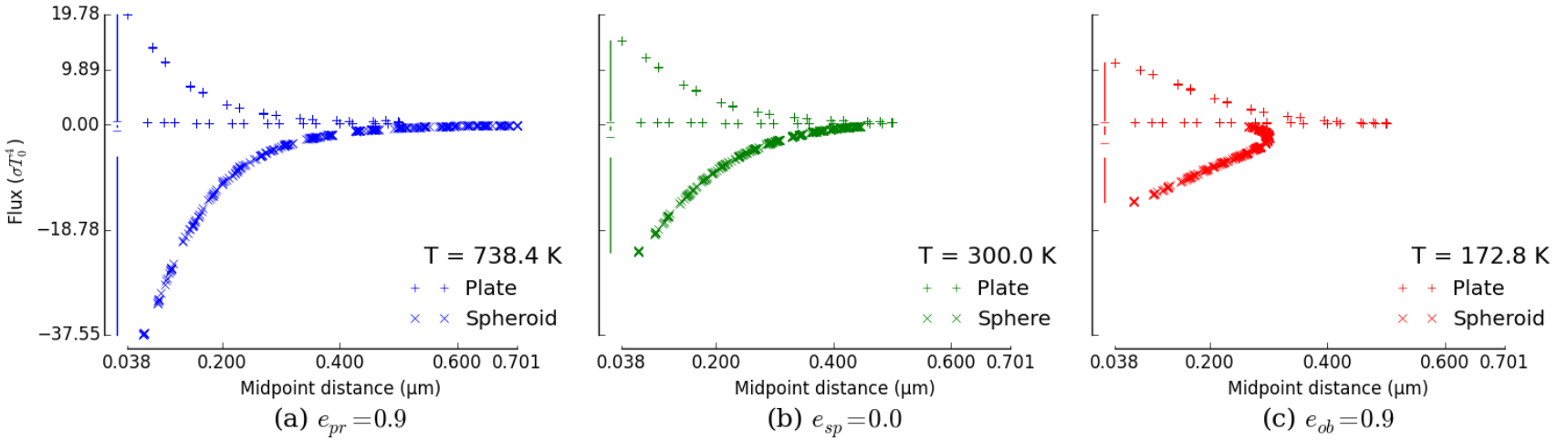

Figure 42: Radial distirbution of the flux in a circular disk-spheroid system (prolate $e_{\mathrm{pr}} = 0.9$ (a), sphere $e_{\mathrm{sp}} = 0.0$ (b), and oblate $e_{\mathrm{ob}} = 0.9$ (c)) normailzed by the classical blackbody flux value σT_0^4 where T_0 is 300 K and the surfaces are separated by a gap of 0.050 μm.

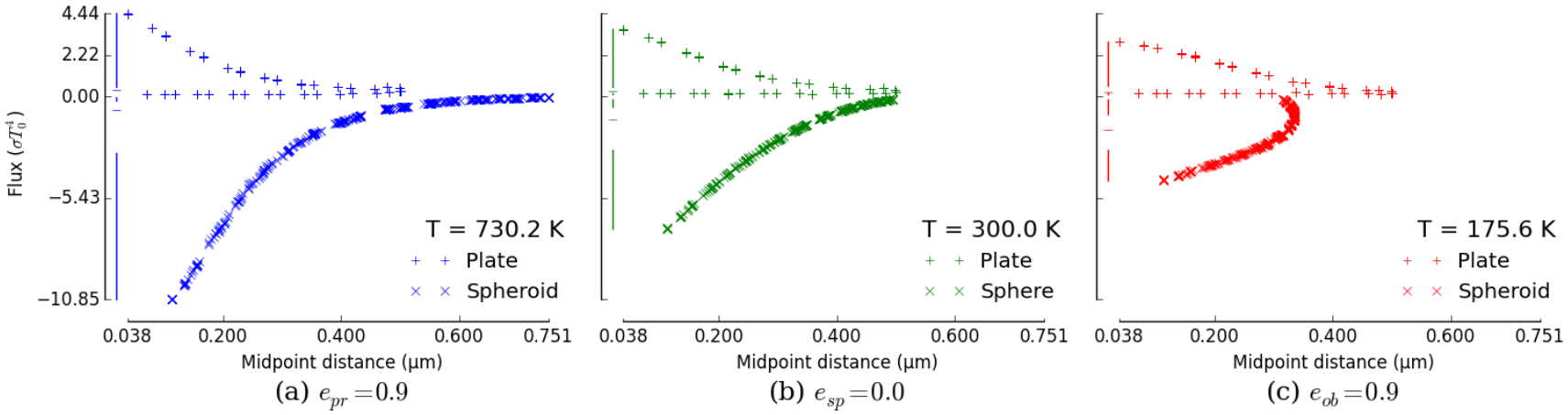

Figure 43: Radial distirbution of the flux in a circular disk-spheroid system (prolate $e_{\rm pr} = 0.9$ (a), sphere $e_{\rm sp} = 0.0$ (b), and oblate $e_{\rm ob} = 0.9$ (c)) normailzed by the classical blackbody flux value σT_0^4 where T_0 is 300 K and the surfaces are separated by a gap of 0.100 μm.

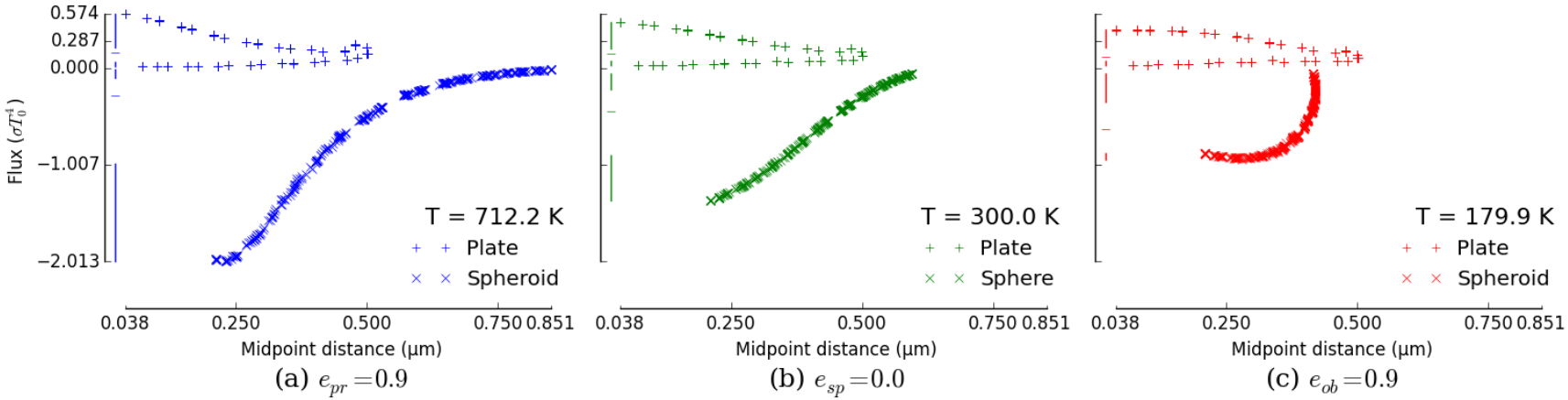

Figure 44: Radial distirbution of the flux in a circular disk-spheroid system (prolate $e_{\rm pr} = 0.9$ (a), sphere $e_{\rm sp} = 0.0$ (b), and oblate $e_{\rm ob} = 0.9$ (c)) normailzed by the classical blackbody flux value σT_0^4 where T_0 is 300 K and the surfaces are separated by a gap of 0.200 μm.

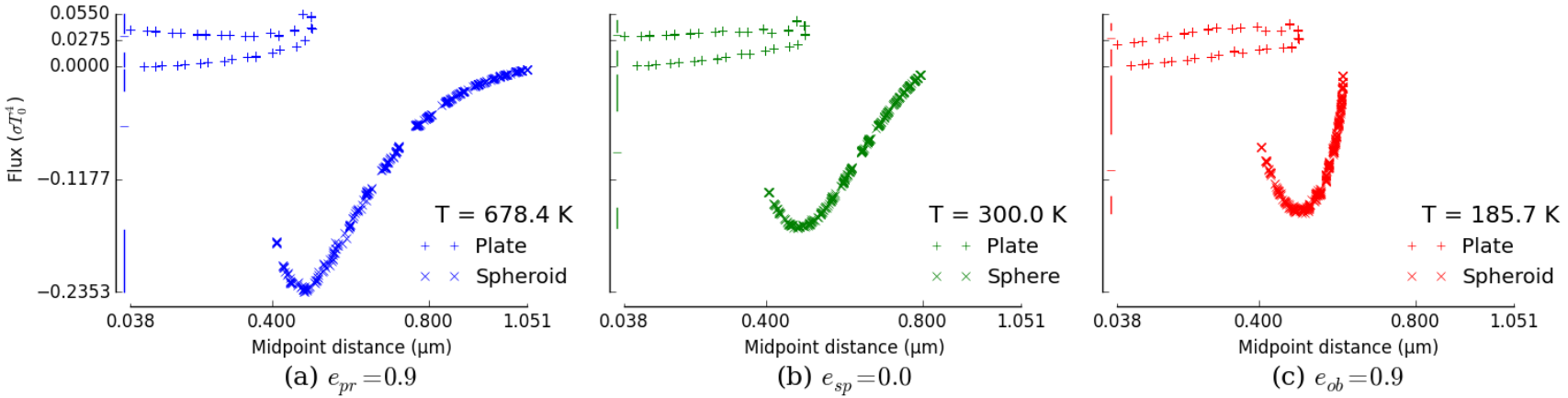

Figure 45: Radial distirbution of the flux in a circular disk-spheroid system (prolate $e_{\rm pr} = 0.9$ (a), sphere $e_{\rm sp} = 0.0$ (b), and oblate $e_{\rm ob} = 0.9$ (c)) normailzed by the classical blackbody flux value σT_0^4 where T_0 is 300 K and the surfaces are separated by a gap of 0.400 µm.

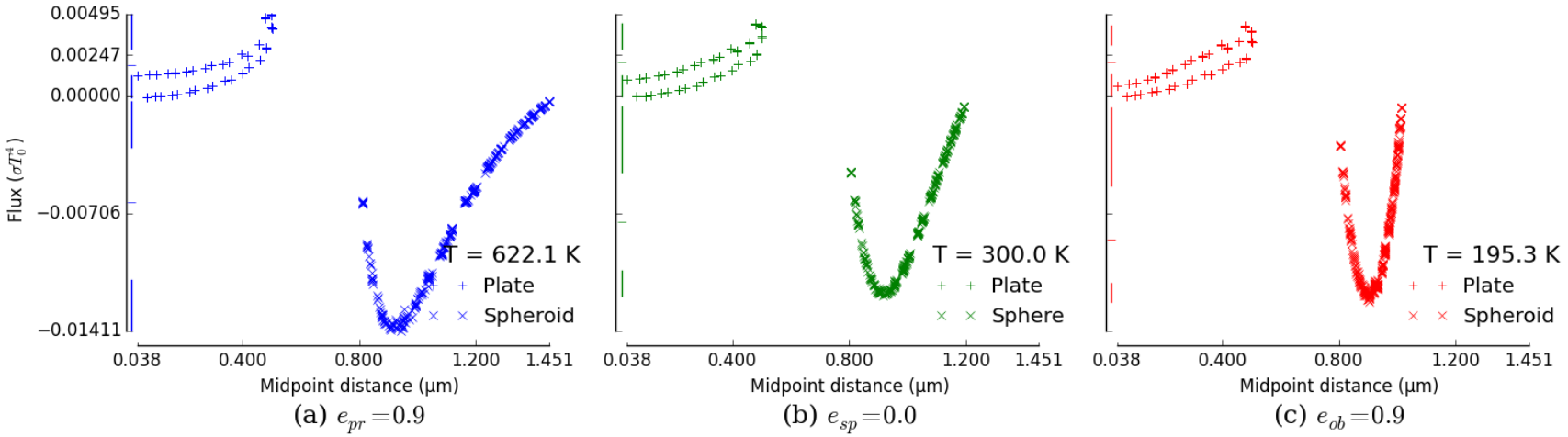

Figure 46: Radial distirbution of the flux in a circular disk-spheroid system (prolate $e_{\rm pr} = 0.9$ (a), sphere $e_{\rm sp} = 0.0$ (b), and oblate $e_{\rm ob} = 0.9$ (c)) normailzed by the classical blackbody flux value σT_0^4 where T_0 is 300 K and the surfaces are separated by a gap of 0.800 µm.

According to the formalism laid out in Chapter 2, the flux through a particular face is dependent on the flux passing through the closed surfaces in the system regardless of where the face exists. By increasing the surface area of the disk, the flux through the faces at the center of the disk must increase. Physically, this is because increasing the surface area increases the volume of the region that is emitting the energy. By increasing the volume, more fluctuations of the charge carries in the internal material contribute to the energy exchange.

We clearly see the exponential decay across the disk in the prolate spheroid systems. This was to be anticipated from the formalism because the evanescent waves decay exponentially away from the surface. The shape of the prolate spheroid places only a small region of its surface area within the decay range of the evanescent waves on the disk. This highly concentrates the flux when the separation between the surfaces is small. At the separation of 0.020 µm, the peak flux through the center of the disk is 39 % higher than the sphere-disk system and 210 % higher than the oblate spheroid-disk system. Considering a face with a midpoint 0.100 µm away from the center of the top of the disk, this enhancement decreases to 3.8 % more than the sphere and 18 % more than the oblate spheroid at the same separation. Doubling the separation drops the peak flux by an order of magnitude and begins to demonstrate the wave nature of the interaction. This shows us that to focus the flux, we must increase the difference in size of the objects.

Investigating the local extrema on the surfaces, we see that the prolate system has a local maximum at all separations except for the largest. On the other hand, we see that a local minimum forms in both the sphere-disk and oblate spheroid-disk systems between separations of 0.200 µm and 0.400 µm. In the small disk-spheroid and sphere-spheroid systems, the local minimum appeared above a separation of 0.100 µm. As we discussed above, the local increase in the flux through a face is easily attributed to the increase in the surface area of the disk because more fluctuations in the internal material are included. Thus, the formation of the local minimum on the disk must occur at a larger separation. When we look at the spheroid, we see that the local minimum begins to form above the separation of 0.100 µm just as with the small disk.

Finally, the interaction of the faces on the back and sides of the disk remain nontrivial at the larger separations. At a separation of 0.200 µm, we see that the back of the disk near the edge is beginning to develop a non-negligible contribution to the energy exchange. At the largest separation of 0.800 µm, we see that the difference in the spatial distribution across the disks among the spheroids is becoming trivial, and the flux through the back of the disk near the edge is larger than the flux through the top of the disk. However, we also know that this separation is reaching the point where the total energy exchange is below the blackbody result. This shows that at this large separation, we are reaching the limits of the approximations used to establish the formalism in Chapter 2.

5.4 Conclusions

In this chapter we have considered the interaction of spheroid above a disk. We have seen that the proximity of the disk and spheroid remains the dominant contribution to the total exchange. In our investigation, we established that the view factor describes the variation of the total energy exchange from a reference sphere-disk system at the same separation when the separation is above twice the radius of a sphere with surface area equal to the spheroid. At these separations, the evanescent modes become small and the propagating modes are dominant which is the regime of the classical blackbody result. When the separation is smaller than twice the radius of the equal surface area sphere, or investigation demonstrated that the error in using the view factor is less than 2 % when the disk and spheroid have the same surface area. On the other hand, our investigation revealed that the view factor is inappropriate to describe the change when one of the surfaces dramatically changes shape. This means we cannot use the view factor to describe the sphere-disk interaction based on the results of the sphere-sphere configuration.

The errors associated with using the view factor to compute the modulation in the total exchange derived from the fundamental differences in the approximations used to compute the view factors compared with the near-field approximations used in Chapter 2. Due to the wave nature of the electromagnetic fields, the interaction of faces on one object that point away from the second object are nonzero and contribute measurably to the radiative energy

exchange. The propagating modes traverse through the objects and around the edges to add to the interaction. The classical calculation of the view factors is based on geometric optics; thus, these faces do not contribute because the normals of the two surfaces point away from each other at these points. This means that we should expect the view factors to under predict the total energy exchange at nanoscale separations; however, we have seen that the error in using the view factor is only a few percent.

Additionally, we have shown that a large disparity between the projected area of the two objects facilitates the concentration of the energy flux. In the classical radiative transfer exchange, the scale of this modulation is governed by the view factor; however, at nanoscale separations, we have demonstrated that this focusing is greatly enhanced. A mutually large projected area as in the oblate spheroid-disk system, is capable of increasing the total energy exchange; however, the spatial distribution of the flux is over a larger area of the disk. By decreasing the projected area from a sphere to a prolate spheroid, the flux is concentrated into a region of half the radius of a sphere with equal surface area as the spheroid, and the magnitude of the peak flux is increased by over 30 %. The trade off is that the total flux is necessarily reduced. By selecting an appropriate combination of temperature difference, spheroid eccentricity, and separation, a desired flux concentration through the center of the disk can be achieved.

CHAPTER VI

ASYMMETRIC DISK-SPHEROID EXCHANGE ANALYSIS

6.1 Introduction

Thus far, we have exclusively considered systems with a cylindrical symmetry in this thesis. This symmetry has allowed us to verify our numerical routine and to investigate the spatial distribution of the energy exchange between two surfaces with an aligned symmetry axis. This investigation produced three main results. First, we have seen that the total energy exchange between two bodies is primarily governed by the separation and the shape effects modulate the energy exchange. Second, we have shown that the view factors from classical blackbody radiation describe the change in the total exchange from a reference sphere system due to the eccentricity of the spheroid when the separation is large. Third, we have seen that a large discrepancy in the projected areas of the surfaces tightly focuses the flux into a small region.

Due to the rotational symmetry of the systems considered, the distribution of the flux across the surfaces has also displayed the rotational symmetry. A subsequent question is then: What effect does the orientation of the spheroid above a disk have on the energy exchange? We have already established that the flux is governed by the projected area of the spheroid, and rotating the spheroid will alter the projected area. To answer this question, we turn out attention to systems without a symmetry axis. An asymmetric system can be generated by simply rotating the spheroid from the previous chapter. In this chapter, we venture into new territory. This will provide the first analysis of a rotated spheroid above a disk. We begin this chapter with a discussion of the system configuration. Next, we present the numerical results, and, finally, we complete this chapter with a discussion of our conclusions.

When the axial symmetry of the system of a disk and spheroid is broken, new spatial distribution patterns of the irradiance will form on the disk. Based on our previous discovery

(a-i) Rotated 0.0 ˚ (a-ii) Rotated 30.0 ˚ (a-iii) Rotated 60.0 ˚ (a-iv) Rotated 90.0 ˚

(a) Prolate spheroid $e_{\text{pr}} = 0.9$

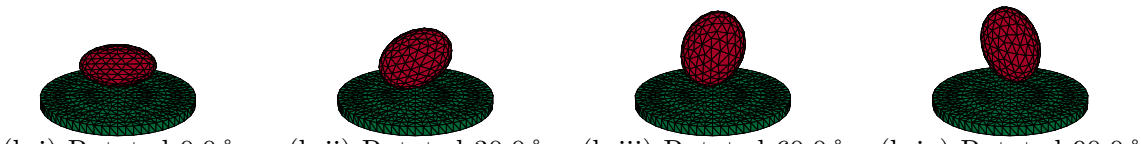

(b-i) Rotated 0.0 ˚ (b-ii) Rotated 30.0 ˚ (b-iii) Rotated 60.0 ˚ (b-iv) Rotated 90.0 ˚

(b) Oblate spheroid $e_{\text{ob}} = 0.9$

Figure 47: Sample geometries displaying the rotation of the spheroid.

of the focusing of the flux in the prolate spheroid case, we predict that the energy flux will be guided along the symmetry axis of the spheroid. To investigate this prediction, we consider our previous system of a large disk and spheroid and rotate the spheroid about an axis in the equatorial plane of the spheroid. We continue to work with the reduced separation and eccentricity selection used in the preceding chapter; however, we do not have to include the sphere-disk system, $e_{\text{sp}} = 0$, because the sphere is invariant under rotations of the sphere. This reduces the eccentricity portion of parameter to 0.5 and 0.9 space for both oblate and prolate spheroids. As before, this sparse sampling provides a high level overview of the parameter space.

Now that we have established the parameter space for the eccentricities and separations, we turn our attention to the selection of rotation angles. Figure 47 presents a selection of rotations for both the prolate and oblate spheroid-disk systems. We immediately see that a polar rotation of 0° is unnecessary simply because these calculations we presented in the second half of Chapter 5. Similarly, we do not need to consider rotations greater than 90 degrees due to the mirror symmetry of the spheroid across its equatorial plane. A rotation about an axis in the equatorial plane by an angle θ greater than 90 degrees is isomorphic to a rotation by $90 - \theta$ about the same axis followed by a rotation of 180 degrees about

the original symmetry axis perpendicular to the equatorial plane. Thus, we only need to consider rotations in the range (0°,90°].

To decide how finely we can sample angle space, we review the timing logs for the axially aligned calculations in Chapter 5. At the current discretization level, the disk has 1872 edges with an average face area of $1.40 \times 10^{-3}\,\mu m^2$ and the spheroids have 510 edges with an average face area of $1.45 \times 10^{-3}\,\mu m^2$. The calculation for a single eccentricity-separation-wavelength combination required an average of 30 minutes in the axially aligned calculations. With the knowledge that 30 wavelengths are required to get an integrated exchange, we will need 420 computer hours or 17 computer days to calculate a single angle. With this knowledge, we select the angles of 30°, 60°, and 90° to sample the entire rotational space. Due to computational time constraints, this sampling was of necessity coarse. Based on this knowledge, these computations will take approximately 51 computer days.

6.2 Numeric Results

In this section, we present the numeric results for the energy exchange between a rotated spheroid and a circular disk. As in previous analysis, we take both disk and spheroid to be gold. The surface area of the spheroid is equal to a sphere of radius $R = 0.200\,\mu m$. The disk has a radius of $2.5R$ and the surface area is 3.5 times the spheroid surface area. In these calculations, the spheroid was shifted so that the center of the spheroid remained on the symmetry axis of the disk and the surface to surface separation d is the same across eccentricities. The computational load was distributed across ten workstations configured as listed in Table 2.

We begin our study of the numeric results by considering the total integrated energy exchange between a disk and a spheroid rotated away from the symmetry axis. Figure 48 presents the base 10 logarithm of this exchange with the disk held at 300 K and the spheroid at 0 K normalized by the blackbody value $\sigma A F(e,d) T^4$ where A is the surface area of the spheroid and T is 300 K for each indicated rotation angle. We see that as the rotation angle increases, the prolate and oblate systems swap behavior. At 0° rotation, the oblate spheroid-disk system exchanges more energy than the prolate; whereas, at 90° rotation, the

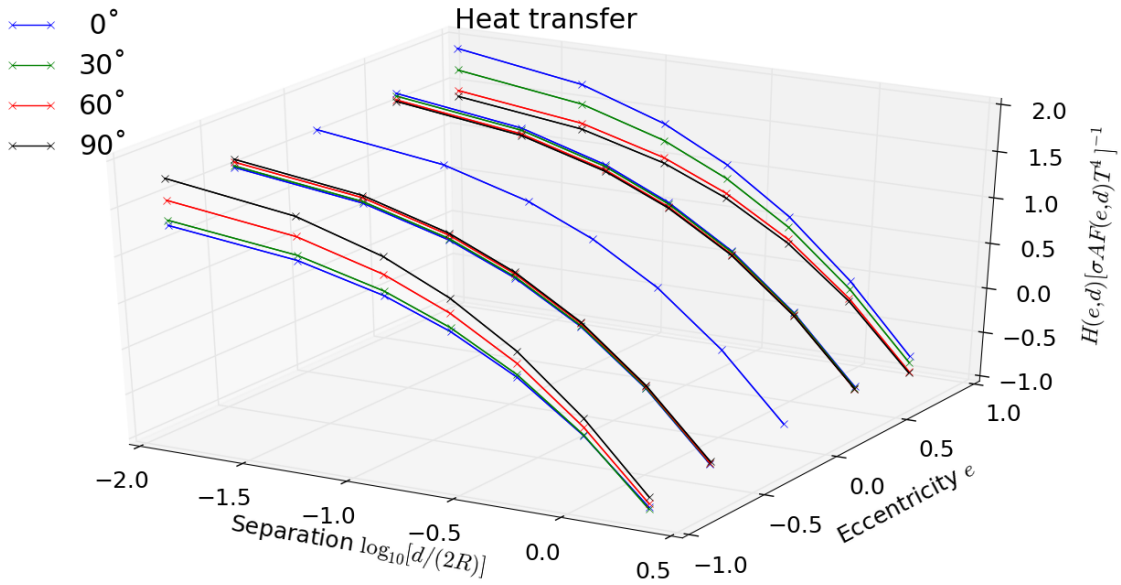

Figure 48: The total integrated heat exchange between a disk and a spheroid normalized by the blackbody value $\sigma A_1 F_{12} T^4$.

prolate spheroid system exchanges more energy than the oblate spheroid system rotated by 90°. By rotating the spheroid, we are transitioning from a projected area that is circular to one that is elliptical. This behavior is reflected in Figure 48 where the total energy exchange increases for the prolate system and decreases for the oblate as the rotation angle increases. At first glance, we might expect the projected area of the ellipses to be the same; however, this does not take into account the method used to generate the spheroids which will alter the projected area.

To understand the projected area of the spheroids when they have been rotated by 90°,

Table 2: Specifications of the workstations used in performing the calculations.

Count and CPUs	Memory	Python	NumPy	SciPy
1 Dual Intel Xeon E-2609	16 GB	3.3.3	1.8.0	0.13.3
2 Dual Intel Xeon E5645	12 GB	3.3.2	1.8.0-dev069e9b0	0.13.0-cc09a77
2 Dual Intel Xeon E5-2650	64 GB	3.3.2	1.8.0-dev069e9b0	0.13.0-cc09a77
2 Dual Intel Xeon L5520	12 GB	3.3.3	1.8.0	0.13.3
3 Dual Intel Xeon X5650	24 GB	3.3.2	1.8.0-dev069e9b0	0.13.0-cc09a77

we must consider the constraints on the generating ellipses. In selecting the computational domain, we employed equal surface area spheroids. To compute the surface area, we must calculate the arc length of half an ellipse based on which axis will be the axis of revolution. For an eccentricity of 0.9, the area of the ellipse used to generate the prolate spheroid is 1.79 times that used to generate the oblate spheroid. This means the projected area of the prolate spheroid is similarly scaled at a rotation of 90°. However, due to the double surface integral in the view factor calculation, the scaling factor is not as large.

This difference in projected area is directly reflected in the difference in the total energy exchanged between the disk and the spheroids. When we look at the energy exchange normalized by the blackbody in Figure 48, the prolate spheroid-disk system is 2.21 times the oblate-disk of eccentricity 0.9 at 90° rotation at a separation of 0.005 µm. At a separation of 0.050 µm, this ratio drops to 1.93 and further to 1.56 at 0.200 µm. This shows that at small separations, the total energy exchange is strongly influenced by the shape of the surfaces even when the surface area is held constant.

We can also see that the change from a circular projected area to an elliptical projected area alters the large separation behavior. At first glance, it appears that all of the values are below the reference sphere at the 0.800 µm separation. Close investigation of the values shows that the prolate spheroid with eccentricity 0.5 is 1.3 % higher than the sphere-disk system, but the rest of the values are less than the sphere-disk system. This inconsistency can be attributed to numerical errors in calculating the view factors.

The program VSWEEP used to compute the view factors generates a result for both the disk to spheroid and the reverse spheroid to disk direction. The area weighted view factors are formally symmetric as discussed in Chapter 4. We can establish the relative error in the view factors by dividing the absolute value of the difference between the results by the average of the results. Figure 49 presents the relative error as a function of separation. The colors denote the same rotations as in Figure 48 and the shapes are listed in the legend. The dash indicates the median at each separation, and the vertical lines mark the minimum, first quartile, third quartile, and maximum. From this, we can clearly see the error is growing exponentially above separations of 0.200 µm. Below this separation, the relative

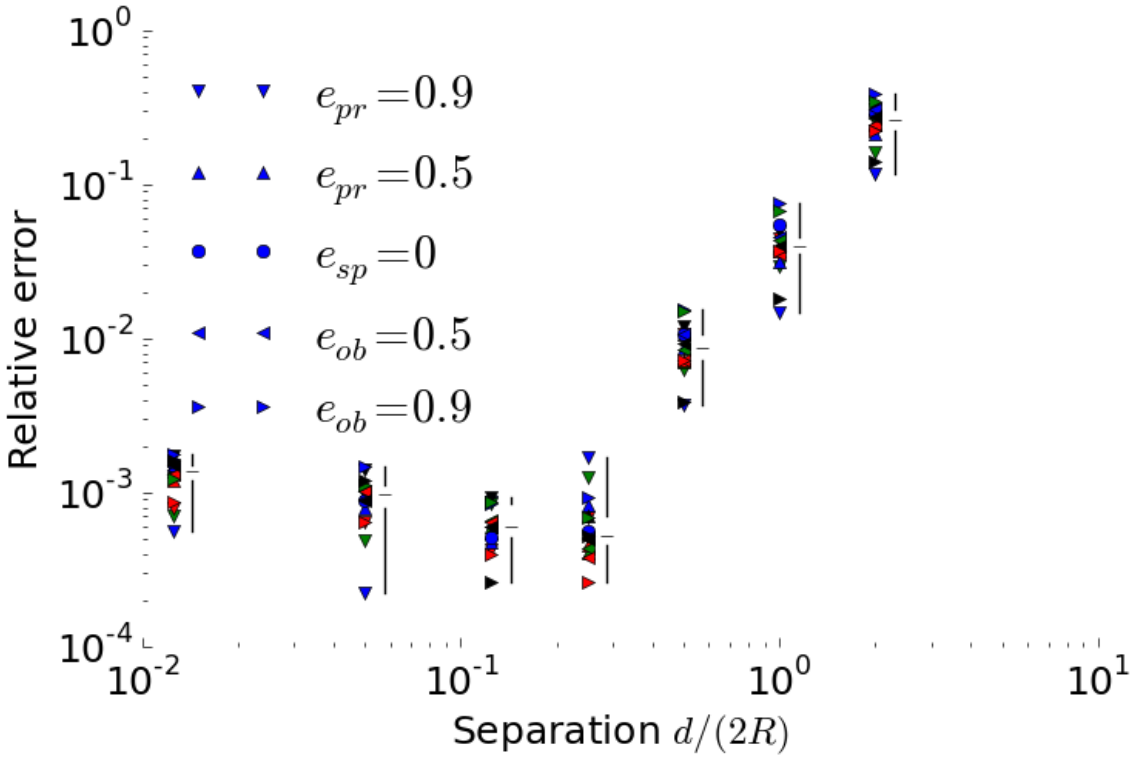

Figure 49: The relative error in the view factor calculation.

error between the two values is 0.1 %.

This tells us that VSWEEP is not ideal for the calculation of the rotated spheroid. In both Chapters 4 and 5 we found that the relative error in the view factor was under 0.7 % when the total surface areas of the two objects were the same. In our current configuration, one surface is much larger than the other. Reflecting back on the original intent of VSWEEP, it was designed to compute the view factors between planar surfaces of comparable size. The large difference in size are not well matched for the algorithm logic, and the curvature of the spheroid is not helping. Additionally, the implementation of the program limits the accuracy with which it can operate. This means that the values for the separations larger than 0.200 µm in Figure 48 are qualitative in nature. At the smaller separations, we retain the three significant figure accuracy from the prior configurations.

Now that we have considered the total exchange, let us investigate the spatial distribution of the exchange. Figure 50 presents the spatial distribution of the flux between a spheroid with surface area equal to a sphere of radius 0.200 µm and a circular disk with

radius 0.500 µm and surface area equal to 3.5 times the spheroid separated by 0.400 µm. The spheroid is held at 0 K and the disk is held at the temperature listed above each plot. This temperature is the equivalent temperature necessary for the system to exchange energy at the same rate as a sphere-disk system at the same separation with the disk held at 300 K and the sphere at 0 K. Figure 51 presents the same data plotted as a function of the distance of the face midpoint from the center of the top of the disk. The marks below zero are the fluxes through each face on the spheroid. The marks above zero denote the quartiles of the flux through the faces on the disk with a common radial distance from the origin. We exclude the 0.5 eccentricities because they simply follow the same trends as the 0.9 counterparts, but the variation of the flux as a function of rotation angle is less than 1 %.

As the spheroid is rotated, we can see that the flux across the disk shifts to the point of closest approach between the surfaces; although, the average value passing through the top of the disk is independent of the rotation angle of the spheroid. This simply means the flux is passing through different faces on the disk, but the total flux remains constant. We see that the point of the peak flux shifts away from the center of the disk as the major axis of the generating ellipse rotates toward the disk and trails the major axis. This is expected because the center of the spheroid remains on the symmetry axis of the disk. This means that the point where the separation is smallest moves away from the center of the disk for rotation angle below 45° and then returns to the center above 45°.

Taking a close look at Figure 51b-iii, we see that the minimum flux through the spheroid is at a rotation of 60°. Similarly, the maximum flux through the disk occurs on the edge of the disk in this system. The appearance of the extremum on the edge of the disk might seem, at first glance, indicate directionality in the flux. However, we see the magnitude of the maxima on the disk in all eight combination of spheroid and angle are very close and the maxima are more than twice as large as the flux through the center of the disk. We can see that in all eight configurations presented the flux is at a maximum on the edge of the disk. If the disk were larger, we would expect to see the flux remain a smooth function of the distance from the center of the disk and these edge effects would vanish. Referring back

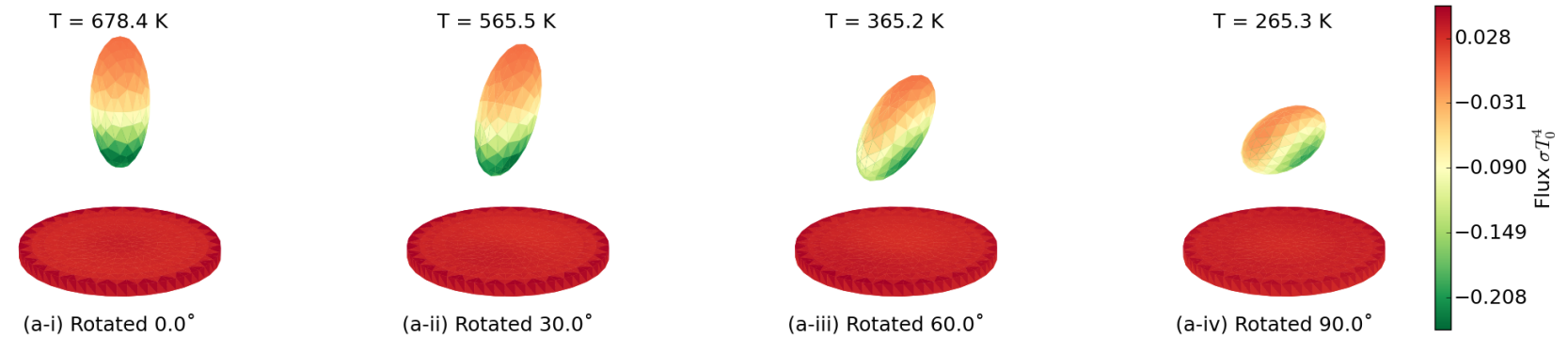

(a) $e_{\mathrm{pr}} = 0.9$

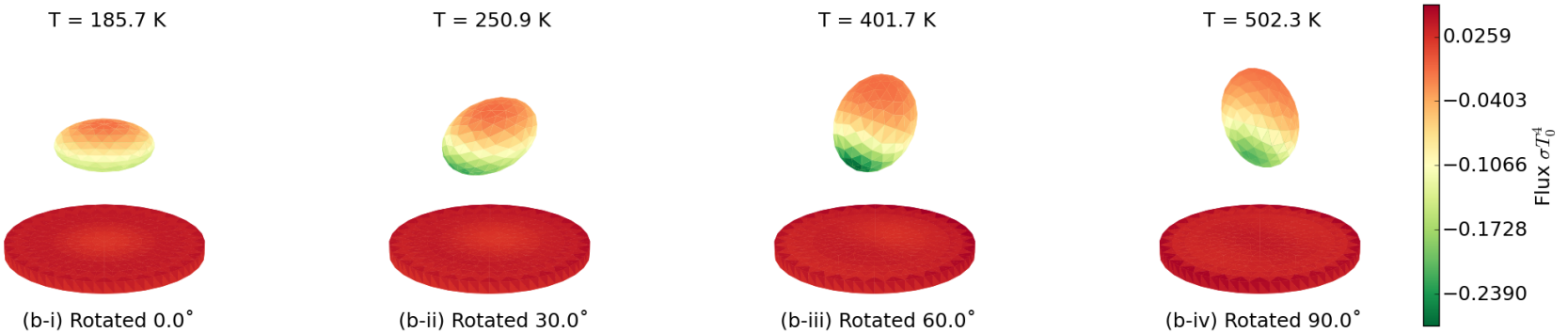

(b) $e_{\mathrm{pr}} = 0.9$

Figure 50: Spatial distribution of the flux in the spheroid-disk systems normalized by the blackbody value σT_0^4 where T_0 is 300 K and the surfaces are separated by a gap of 0.400 µm.

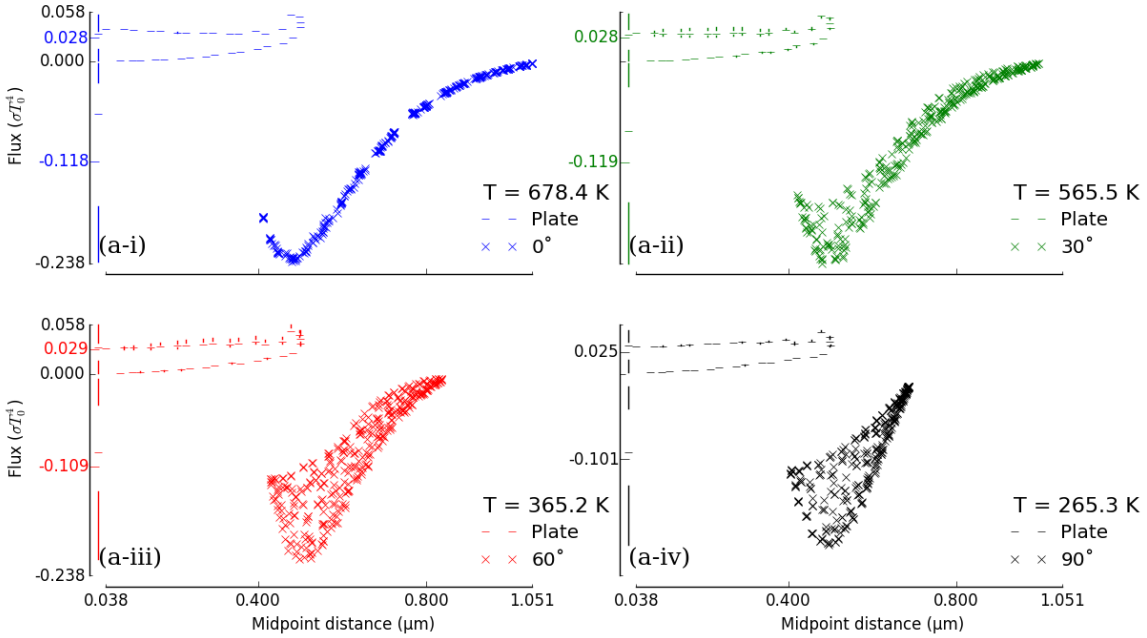

(a) $e_{\mathrm{pr}} = 0.9$

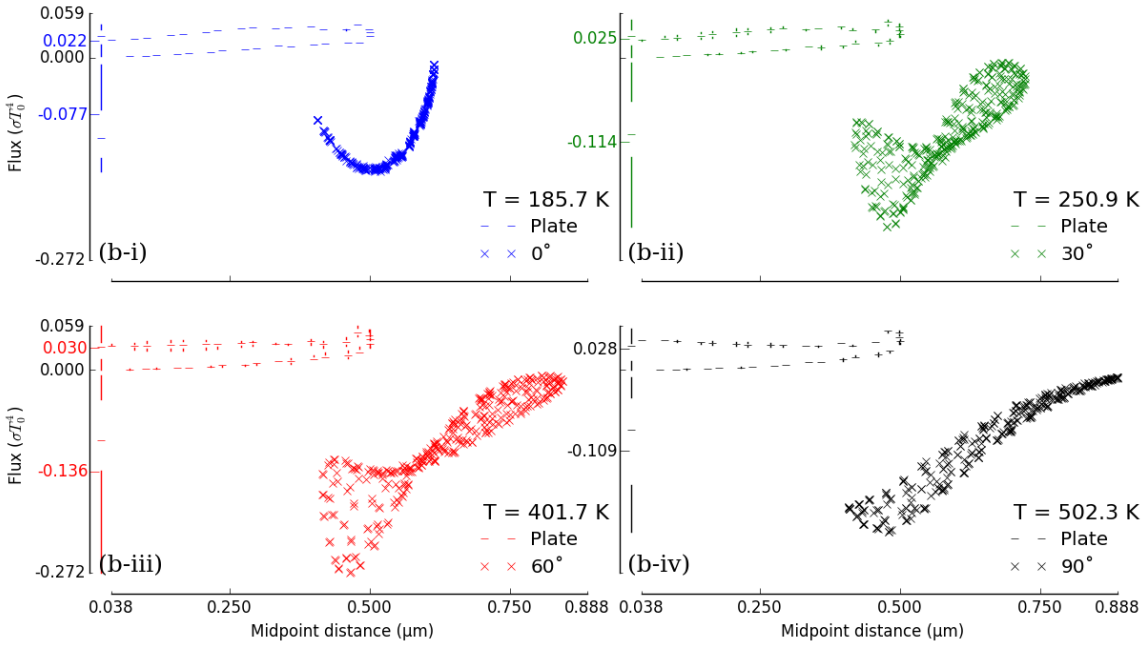

(b) $e_{\mathrm{ob}} = 0.9$

Figure 51: Radial distribution of the flux in the spheroid-disk systems normalized by the blackbody value σT_0^4 where T_0 is 300 K and the surfaces are separated by a gap of 0.400 μm. The half maximum value and the quartiles are noted for each orientation

to Figure 48, we see that at a separation of $d = 2R$, where R is the radius of the sphere with equal surface area as the spheroid, the total energy exchange is just below the classical blackbody prediction. This indicates that we cannot definitively state that these results are significant, and we are in a regime where the current algorithm is inappropriate. For these reasons, we discontinue our investigation of separations larger than 0.200 µm.

Dropping the separation down to 0.200 µm, as depicted in Figure 52, we see that the numerical errors induced by the edge effects are minimal. We do see the edge effects beginning to creep into our results; however, these are not the dominant feature. Figure 53 presents the companion surface distribution of the flux to Figure 52. At this separation, the oblate spheroid with eccentricity 0.9 at 90° rotation has the highest value of 0.587 σT_0^4 at the center of the disk. In Figure 52b-iv, we clearly see the ellipse formed by projecting the generating ellipse of the spheroid onto the disk. This further demonstrates the localization of the flux into a specified region when the difference in the projected areas of the surfaces are dramatically different. Looking at the prolate spheroid, we see that the ellipse is present; however, it is not as distinct as the oblate spheroid configuration.

Comparing the eight configurations in Figure 53, we can clearly see there exists an angle between 30° and 60° where the projected area of the spheroids changes between the prolate and oblate spheroids. An initial estimate for this angle is the obvious one of 45° as this is the point where the major and minor axes of the generating ellipse are at the same angle to the normal of the top of the disk. When the major axis of the generating ellipse is pointing towards the disk, the flux is focused into a smaller region of the disk. When the minor axis is pointing toward the disk, the flux is distributed over a larger area of the disk. Comparing the equivalent temperatures of the systems, we see that the increased spatial distribution of the flux also results in a higher total energy exchange between the surfaces.

Considering the distribution of the flux across the spheroid, we see that the peak flux out of the spheroid is comparable when the major axis of the spheroid is at an intermediate angle of 30° or 60° to the surface of the disk. When the major axis of the spheroid is directed toward the disk in both the oblate and prolate spheroid systems, we get a larger peak radiant emittance near the tip of the spheroid. This maximum is three times higher

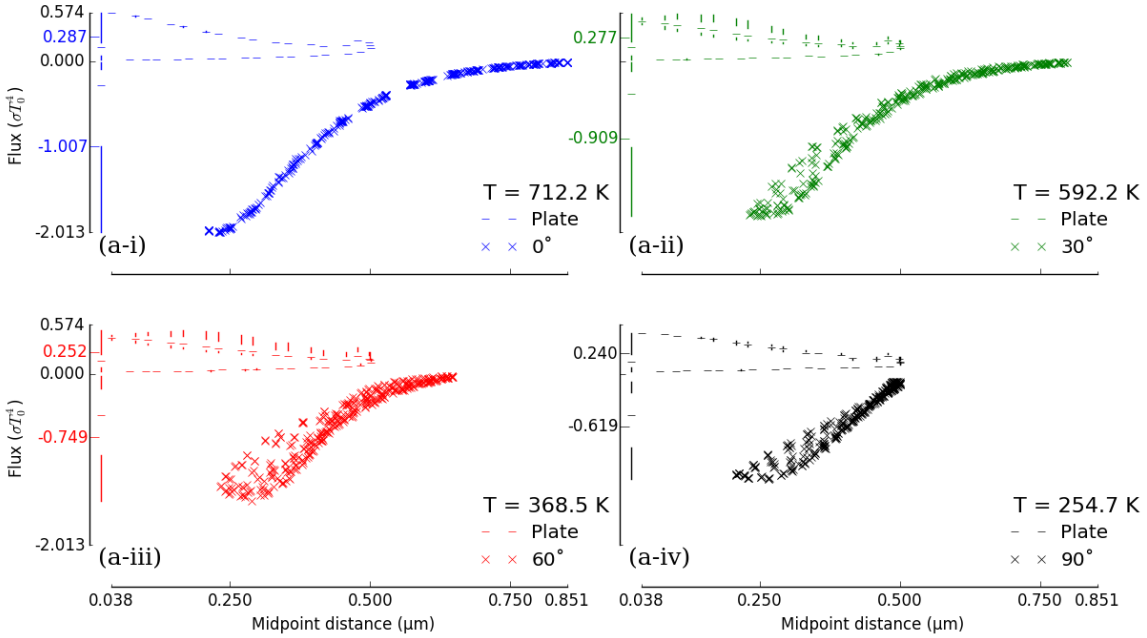

(a) $e_{\mathrm{pr}} = 0.9$

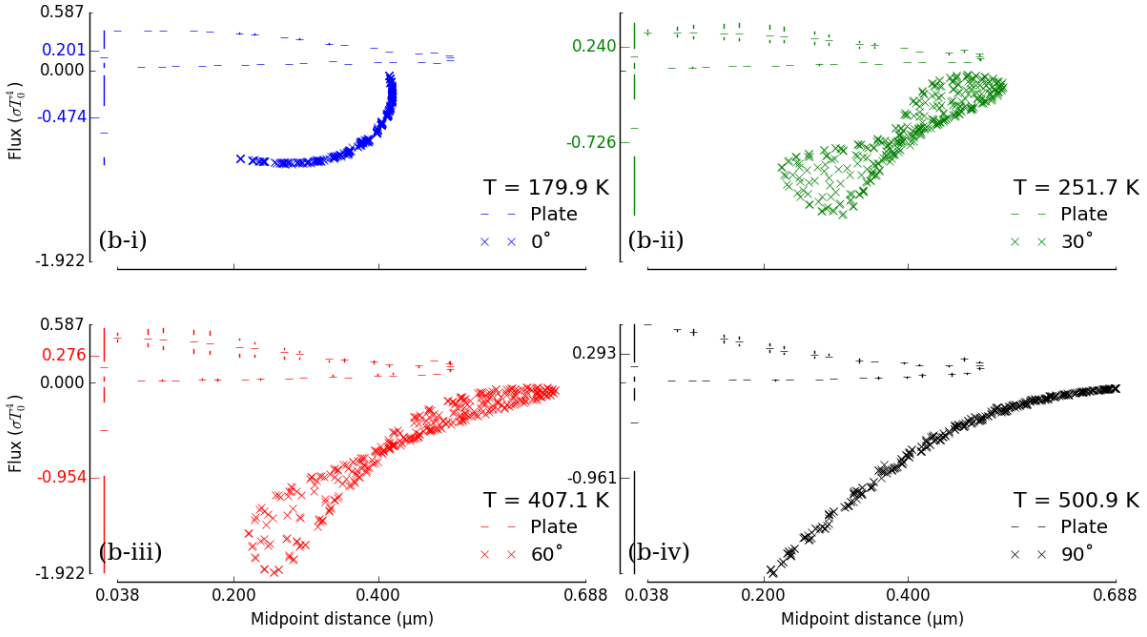

(b) $e_{\mathrm{ob}} = 0.9$

Figure 52: Radial distribution of the flux in the spheroid-disk systems normalized by the blackbody value σT_0^4 where T_0 is 300 K and the surfaces are separated by a gap of 0.200 µm. The half maximum value and the quartiles are noted for each orientation

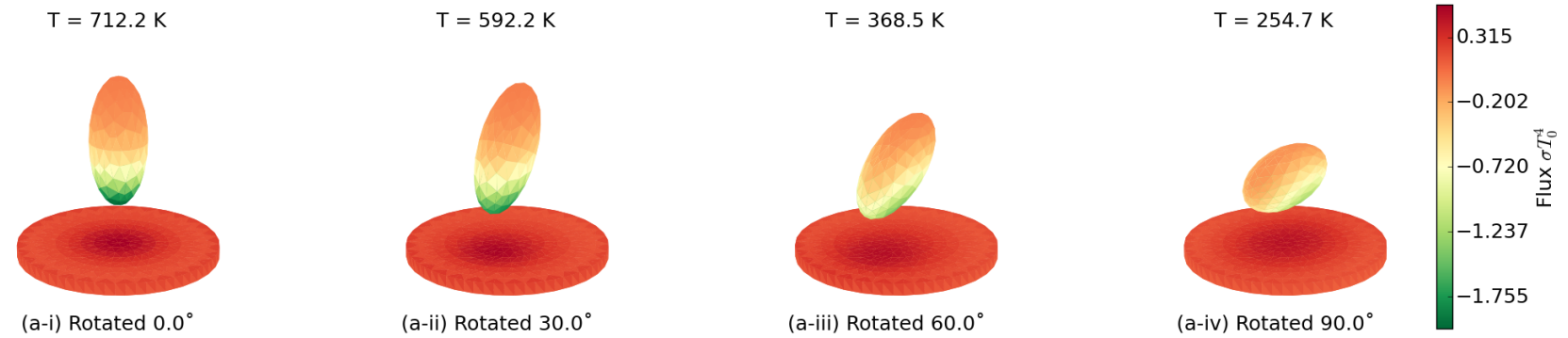

(a) $e_{\mathrm{pr}} = 0.9$

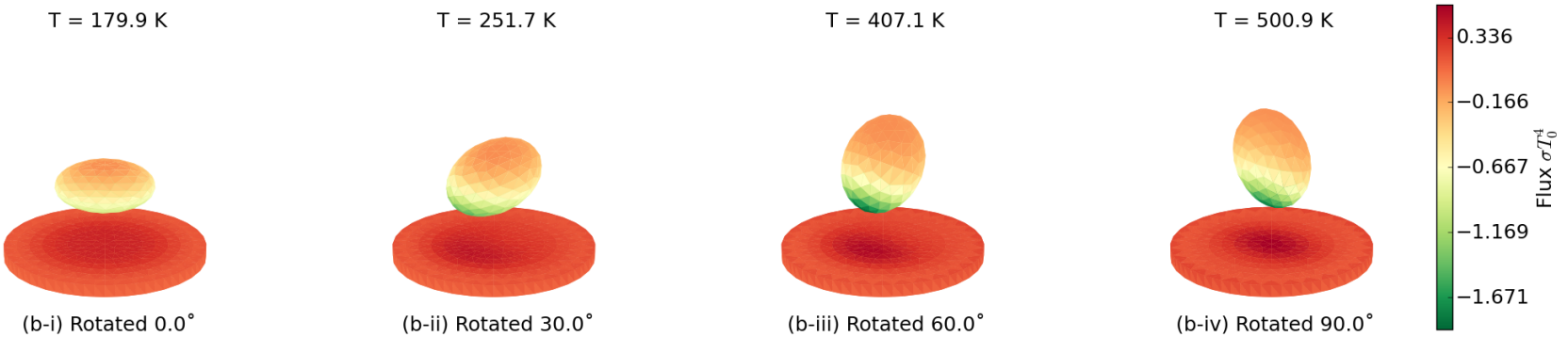

(b) $e_{\mathrm{pr}} = 0.9$

Figure 53: Spatial distribution of the flux in the spheroid-disk systems normalized by the blackbody value σT_0^4 where T_0 is 300 K and the surfaces are separated by a gap of 0.200 µm.

than the corresponding maximum on the disk.

We can also see that the flux decays along the surface of the spheroid until the point furthest from the disk is reached, and the flux approaches zero. The rate at which the flux decays is comparable between the oblate and prolate spheroids when the major axis of the generating ellipse is pointed toward the disk. We clearly see that the flux does not reach zero at the faces furthest from the disk when the minor axis of the spheroid is directed toward the disk for both oblate and prolate spheroids. That the flux does not go to zero is most pronounced in the prolate spheroid rotated 90° system, but this is seen in all orientations.

The fact that the flux does not reach zero regardless of the spheroid shape or orientation demonstrates the wave nature of the interaction. Reflecting on the orientations shown in Figure 53, we see that the electromagnetic wave originating on the surface of the disk can easily propagate around the surface of the spheroid to interact with faces on the back of the spheroid. The reason this is most pronounced in the 90° rotated prolate spheroid system is because the faces on the back of the spheroid are well within the decay range of the evanescent waves on the surface of the disk. Additionally, the small equatorial radius of the prolate spheroid establishes a configuration where the evanescent waves on opposing sides of the spheroid can establish a constructive interference pattern. These observations are consistent with the knowledge that the energy exchange is dominated by the proximity of the two surfaces even if the surfaces are simply the opposite sides of the same object.

If we consider the 60° rotation of the prolate spheroid, we see a marked increase in the flux along the edge of the disk. The maximum relative increase in the flux from the nonrotated configuration along the edge is 5.4 % and the maximum relative increase across the entire disk is 31 %. Due to symmetry, the 30° rotation of the oblate spheroid is the similar projection to the 60° rotation of the prolate spheroid. In the oblate spheroid rotated 30°, the maximum relative increase along the edge is 6.5 %, and the maximum relative increase across the entire disk is 21 %. In both oblate and prolate cases, the maximum relative change from the nonrotated system occurs through the faces directly under the gap contrary to our prediction that the flux should be guided along the major axis of the spheroid. In the oblate system, we see that the angular expanse of the flux distribution

is larger than the prolate system. The large relative change in the flux at the edge of the disk clearly demonstrates that we are within but near the limit of validity for the current approximations at this surface separation.

Our initial prediction at the beginning of this chapter was that the flux between the surfaces would be directed along the major axis of the spheroid. So far, we have seen that the flux remains at the point of smallest separation between the surfaces. However, we have also seen that our current separation is near the limit of the validity of the approximations. This means that we have not definitively shown that the flux is not guided along the major axis of the spheroid. Furthermore, we know decreasing the separation will increase the interaction of the surfaces. For this reason, we decrease the separation to further investigate the effect of surface shape on the spatial distribution of the flux.

Halving the separation between the spheroid and the disk to 0.100 µm increases the flux by an order of magnitude as depicted in the spatial distribution in Figure 54 and the radial distribution in Figure 55. Inspecting the maximum relative change in the flux on the edge of the disk, we find an average change of 2.3 %, but the average relative change across entire disk is 28 %. This reveals that the interaction of the edges when we considered the 0.200 µm separation above was not simply numerical noise. Only 4 % of the change in the edge interactions is due to numerical noise. The remainder reflects the true change in the flux through the edge of the disk as the spheroid is rotated. As the distance from the edge of the disk to the spheroid increases, we expect the relative change to continue to decrease. This means if we increase the size of the disk or decrease the separation between the disk and spheroid, we expect the relative change in the flux through the edge of the disk as a function of spheroid orientation to decrease.

Focusing on the spatial distribution of the flux in Figure 54, we can see that the peak flux across the spheroid is at the point of closest approach between the surfaces. The maximum flux through the disk is also at the point of closest approach regardless of orientation. This is contrary to our original prediction that the flux projects predominantly from the major axis of the spheroid. We do see the asymmetric distribution across both surfaces as opposed to that found in the axially aligned systems. Although the flux is concentrated on

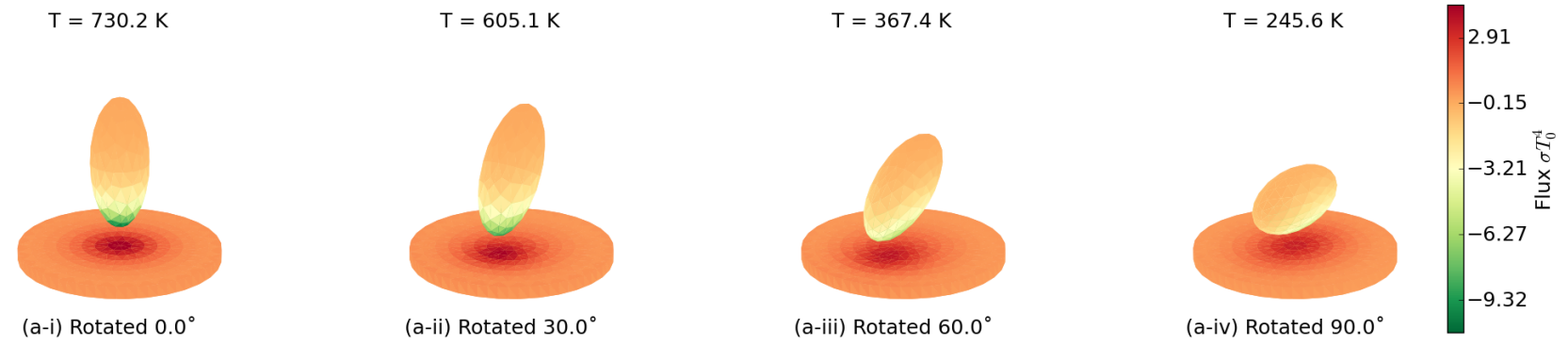

(a) $e_{\mathrm{pr}} = 0.9$

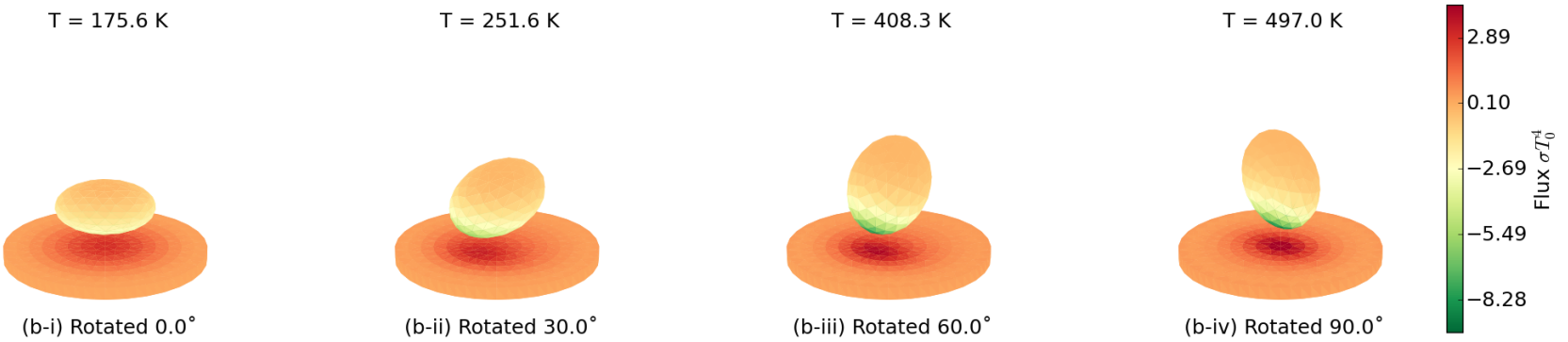

(b) $e_{\mathrm{pr}} = 0.9$

Figure 54: Spatial distribution of the flux in the spheroid-disk systems normalized by the blackbody value σT_0^4 where T_0 is 300 K and the surfaces are separated by a gap of 0.100 µm.

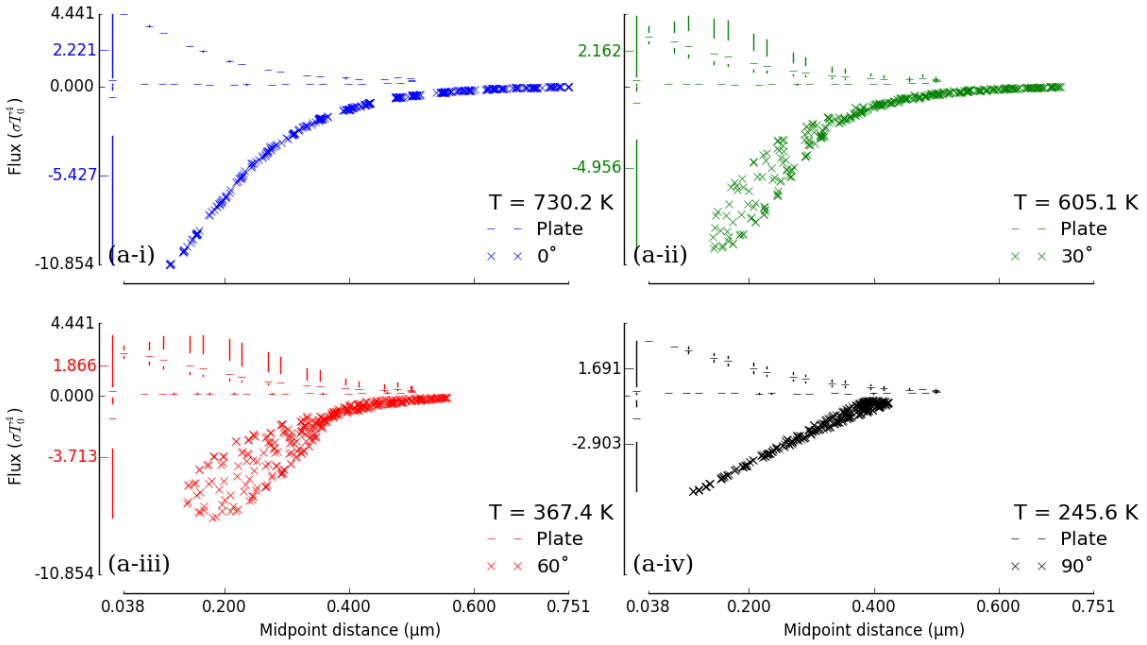

(a) $e_{\mathrm{pr}} = 0.9$

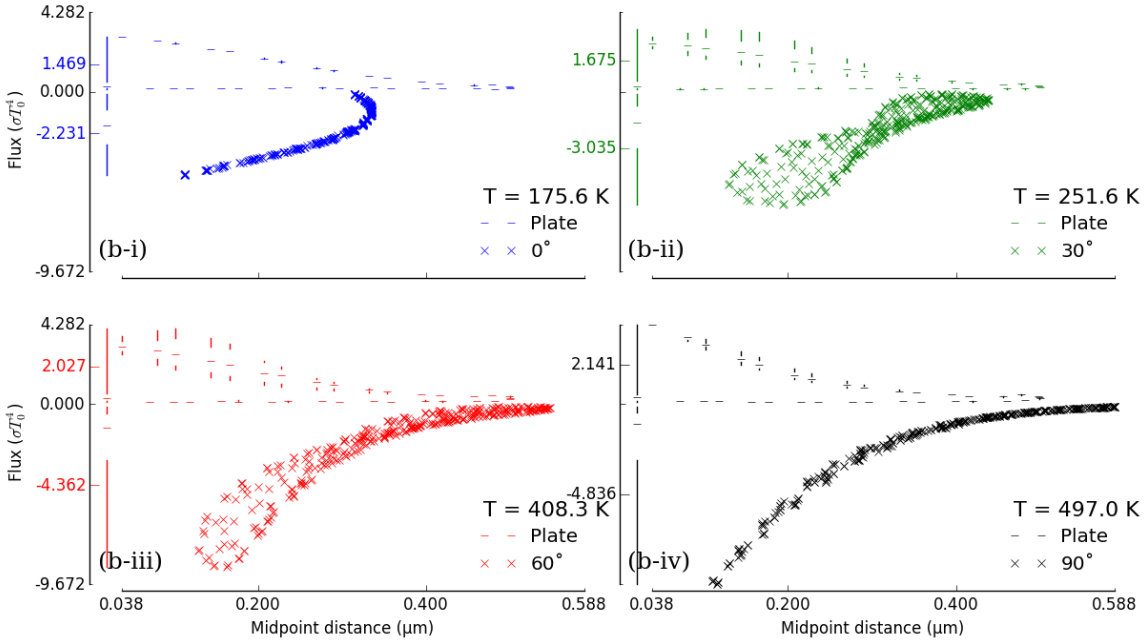

(b) $e_{\mathrm{ob}} = 0.9$

Figure 55: Radial distribution of the flux in the spheroid-disk systems normalized by the blackbody value σT_0^4 where T_0 is 300 K and the surfaces are separated by a gap of 0.100 μm. The half maximum value and the quartiles are noted for each orientation

the disk more around the major axis of the spheroid, Figures 54a-i and 54b-iv, than the minor axis, Figures 54a-iv and 54b-i, the proximity of the faces near the gap overwhelms the directionality of the flux.

Comparing the 30° rotated prolate spheroid, Figure 55a-ii, and the 60° rotated oblate spheroid, Figure 55b-iii, we see that the prolate spheroid is focusing the flux on the disk better. The half maximum value of the flux across the disk is 2.16 σT_0^4 with a spatial halfwidth of 0.228 µm in the prolate spheroid-disk system; however, the half maximum value in the oblate spheroid-disk system is 2.03 σT_0^4 with a halfwidth of 0.207 µm. Reviewing the surface distribution plots in Figures 54a-ii and 54b-iii, we see that the oblate spheroid increase is spread over a larger number of faces on the disk. We can see this on the radial plots as well by noticing that the median and first quartile at each midpoint distance are lower for the prolate spheroid than the oblate spheroid. This means that the oblate spheroid generates an increase farther along the disk.

In the swapped rotation case with the prolate spheroid rotated by 60°, Figure 55a-iii, and the oblate spheroid rotated by 30°, Figure 55b-ii, the faces near the center of the disk are comparable in value with the flux in the prolate system being slightly higher than the oblate system. Looking at the other faces on the disk, we see that when a change in the flux through a face is present, the prolate spheroid causes a larger change from the nonrotated system than the oblate spheroid. The general pattern of the flux distribution across the disk is the same for both the prolate and oblate spheroid systems. At these rotations, we clearly see that the flux through the faces on the disk in the oblate system have a smaller variance. This is due to the larger projected area the oblate spheroid provides to the disk. The large variance in the prolate spheroid-disk system is due to the focusing of the flux along the major axis of the spheroid. The oblate spheroid has more of a circular projection at this rotation and the prolate is more elliptical.

Halving the separation again to 0.050 µm we get the results presented in Figures 56 and 57. We again see the increase in flux by an order of magnitude. We now see that the edge effects are no longer evident. Although the numerical error is still there, it is much less than the magnitude of the flux through the center of the disk. We can see the exponential

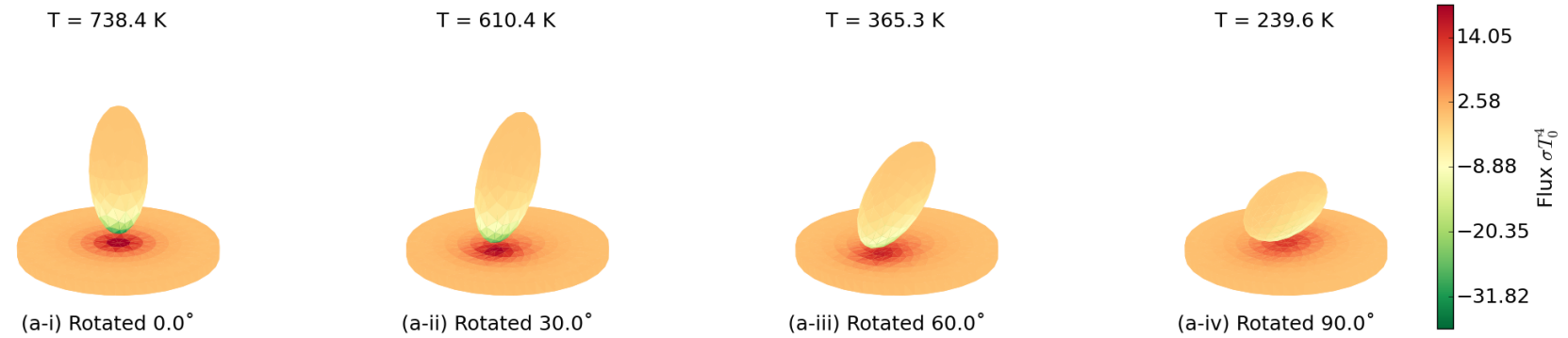

(a) $e_{\mathrm{pr}} = 0.9$

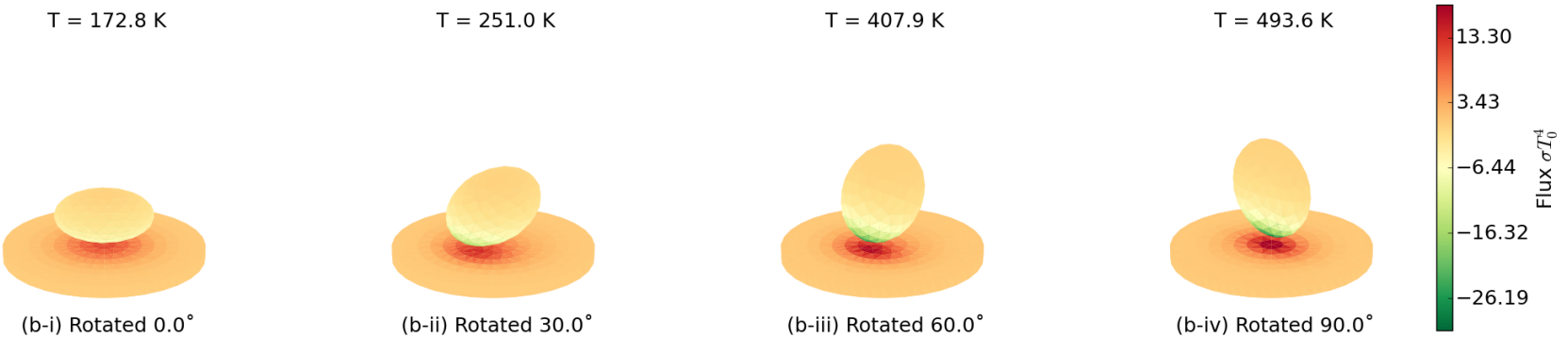

(b) $e_{\mathrm{pr}} = 0.9$

Figure 56: Spatial distribution of the flux in the spheroid-disk systems normalized by the blackbody value σT_0^4 where T_0 is 300 K and the surfaces are separated by a gap of 0.050 µm.

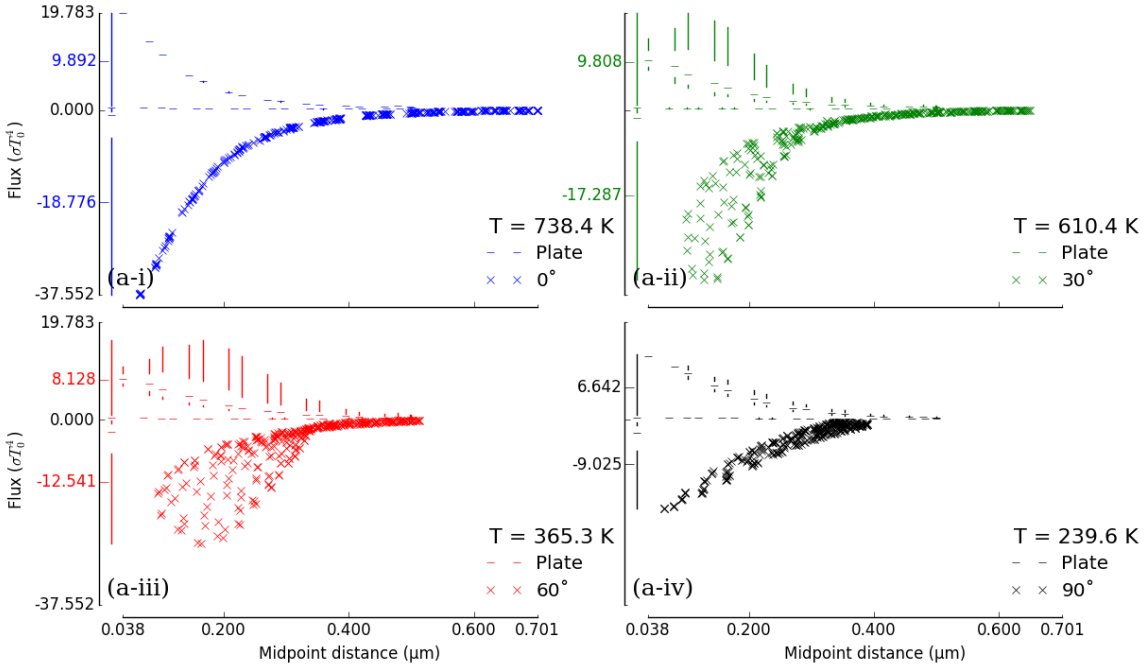

(a) $e_{\mathrm{pr}} = 0.9$

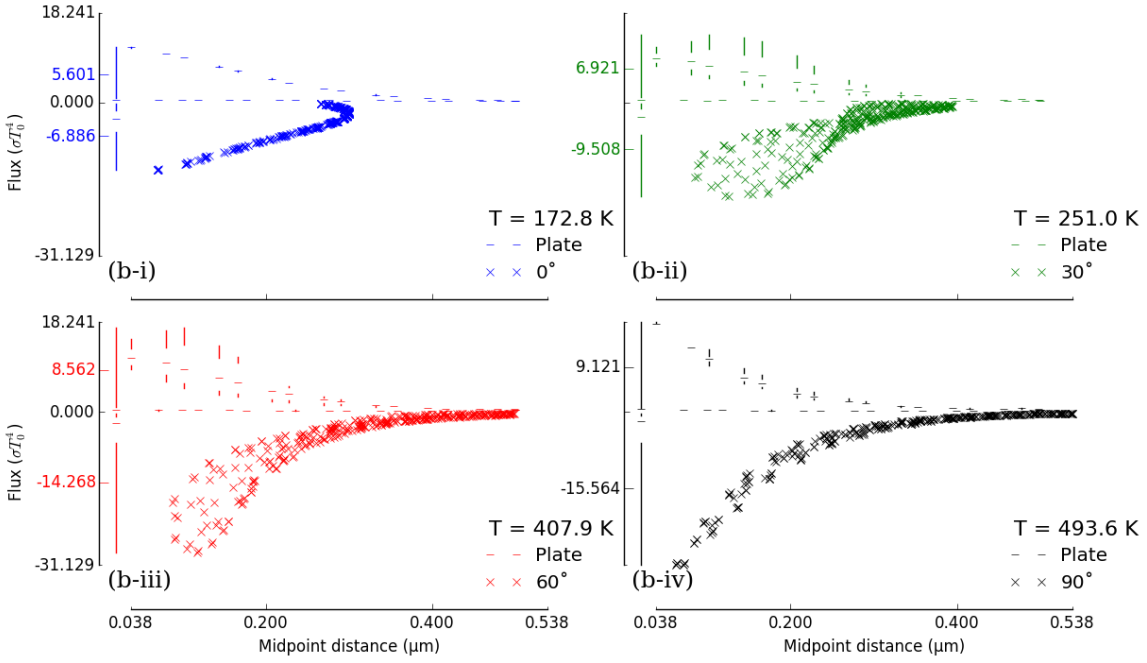

(b) $e_{\mathrm{ob}} = 0.9$

Figure 57: Radial distribution of the flux in the spheroid-disk systems normalized by the blackbody value σT_0^4 where T_0 is 300 K and the surfaces are separated by a gap of 0.050 μm. The half maximum value and the quartiles are noted for each orientation

decay across the disk in the 0° rotation prolate spheroid-disk system. Due to this rapid decay, we see that the flux remains under the closest point. We see that the flux is still directed ahead of the spheroid; however, the close proximity of the surfaces confines the flux to the small region near the gap. This trend of increasing flux through a smaller region continues as the separation between the surfaces decreases.

The ramification of this extreme focusing is that the flux will always remain at the point of closest approach for small separations. Thus, a configuration to concentrate the flux into a small region must use separations of 0.050 µm. However, the ability to direct the energy in any direction other than that of the closest surface is lost. By increasing the separation to 0.100 µm, the focusing of the flux is reduced, but the directionality of the flux can be tailored by adjusting the orientation of the spheroid. To devise a configuration to direct the energy in the system, optimal results will be found for separation of 0.100 µm.

6.3 Conclusions

In this chapter, we continued our investigation of shape effects on near-field radiative energy exchange by altering the symmetry of the disk-spheroid system. To break the symmetry of the system, we rotated the spheroid about an axis in its equatorial disk to create a different projected area on the disk. We have seen that the flux remains focused around the point of closest proximity. This point shifts along the top of the disk because the spheroid is shifted to keep the center of mass on the symmetry axis of the disk. This result is contrary to the initial prediction that the flux will be preferentially guided along the major axis of the spheroid.

Reviewing the physical situation outlined earlier in this manuscript, this was a poor prediction. This prediction did not consider the proximity effects that we know dominate near-field radiative transfer. At small separations, the evanescent modes of energy exchange at the gap will overwhelm the effects of spheroid orientation. At moderate separations, 0.100 µm to 0.400 µm, the contribution of the propagating modes will become evident which will increase the spatial distribution of the flux. However, the dominant contribution to the radiative energy exchange will always remain with the evanescent modes.

The second thing we learned is that the numerical method is not well suited to the larger separations with a small disk. We clearly see the effects of the restricted disk size at these large separations. This is due to two limitations. One is embedded in the library in the way the integrals are computed. We already know that the library has limitations and needs to be reevaluated for further use. The other point is the total integrated flux is below the blackbody value. At a separation of 0.400 µm, the exchange is below the classically predicted value. At a separation of 0.200 µm, the total energy exchange curves are decaying as d^{-2} as expected by electrodynamics. These two points indicate that we have considered regimes where the formalism and numerical method are not appropriate.

The final conclusion we can extract from this chapter is about directing the flux. The larger projected area of the oblate spheroid increases not only the efficiency of the energy exchange but also the interaction range in the system. The increased efficiency at exchanging energy means that the radiative conductance of a oblate spheroid-disk system will be higher than a sphere-disk system at a given temperature. The increased interaction range indicates that the oblate spheroids can be used to guide energy through a system of spheroids. On the other hand, the lower projected area of the prolate spheroid is better suited to focusing the flux into a small region which can be used to design an energy sink.

CHAPTER VII

CONCLUSIONS

This thesis set out to investigate the effect of surface shape on the near-field energy exchange. Specifically, the goal was to enhance the understanding of the effect of surface shape on the total and spatial distribution of the near-field energy exchanged between two objects. In this work, we have presented the first detailed analysis of the total and spatial distribution of the energy exchange in both a sphere-spheroid and a disk-spheroid system. Neither of these systems has been previously studied in detail. A detailed knowledge of the spatial distribution informs us how the energy is passing through the system. This provides a means to investigate configurations that can be used to tailor the temperature field and the radiative flux directionality.

To probe the nature of the shape dependence of the near-field radiative exchange, we undertook a three part investigation. First, we reviewed the theoretical formalism behind the exchange. Next, we implemented and verified a numerical routine to compute the total and spatial distribution of the energy exchange. Finally, we applied the numerical model to study three new classes configurations that had not been previously studies using the Green function expansion method or computing near-field radiative exchange. The new configurations investigated were a spheroid near a sphere, a spheroid near a disk, and a rotated spheroid near a disk. In all three classes, we considered both a prolate and an oblate spheroid at a range of eccentricities for the generating ellipse.

The first step to the investigation into the effect of surface shape was to review the formalism of the exchange. We derived the distribution of the energy exchange for an arbitrary number of objects embedded in a common background based on the formalism presented by Rodriguez, Reid, and Johnson [61]. In the process of deriving the formula for the exchange, we corrected an erroneous factor of 1/2 that was lost in applying the fluctuation-dissipation theorem by the previous authors. We also provided an in-depth

discussion of the approximations necessary to equate the source correlation matrix from the fluctuation-dissipation theorem $\langle \overline{\boldsymbol{s}}\, \overline{\boldsymbol{s}}^{\dagger} \rangle$ and the Hermitian portion of the self interaction matrix $\mathrm{sym}\overline{\overline{\boldsymbol{G}}}_{j,jj}$. The ability to relate the values requires that the mechanical work done on the materials time average to zero. The common method in the literature is to work in a thermally steady state configuration without explicit statement of this fact. This research laid out this approximation and explicitly illustrated its impact.

After we had the formalism in place, we were able to implement a numerical routine to compute the interaction between two objects. The computational routine hinges on the choice of basis function used to discretize the problem domain. The first choice of basis functions we attempted were the solutions to the homogeneous vector wave equation as is done in T-matrix scattering programs. During the verification process for that implementation, we rediscovered the issue with this choice of basis function: the summation does not converge for multiple scattering events. This is due to the need to evaluate Bessel functions of the second kind with small arguments. In fact, we found that the published literature simply truncates the expansion of the dyadic Green function to avoid this issue and thus ignore the convergence problem.

The alternative basis set that was ultimately used is defined over triangular facets on a surface. The primary advantage with this second choice of basis functions is that the expansion will converge. A secondary advantage is that a library was available to compute the matrix elements. The library was wrapped in the native C interface to Python, and the logic to assemble the necessary matrices and compute the near-field energy exchange was implemented in Python. With the numerical routine in place, we were able to verify the calculations against theoretical results published in the literature. During the final verification process, we considered a long wavelength expansion for the flux and demonstrated that the energy exchange decays according to a power law at the long wavelengths as expected.

After the verification process, we were able to turn the research to configurations of object shapes that have not been well investigated in the literature: spheroids near spheres and circular disks. We found that the total energy exchange is predominantly governed by the separation of the surfaces. We found that replacing the spheroid with an equal

surface area sphere at the same separation provides a first approximation to the total energy exchange. When the surface areas of the two objects are close, we demonstrated that the geometric view factors from far-field radiative exchange can be used to predict the modulation of the total energy exchange from the reference sphere system to within 2 %. This is the first time the view factors from far-field radiative energy transfer have been shown to apply to near-field phenomena. Additionally, we demonstrated that the total energy exchange is a monotonic function of not only the separation but is also a monotonic function of the spheroid eccentricity independently of the separation.

We observed that a separation of $2R$, where R is the radius of a sphere with surface area equal to the spheroid, is where the near-field effects become negligible. This is the separation where the total energy exchange drops below the blackbody value in all of the axially aligned systems. This observation is consistent with the literature in indicating a separation smaller than the decay length of the evanescent wave is necessary for the enhanced energy transfer. Above this separation, the near-field effects are small and classical far-field formalism properly describes the energy exchange. This is evident from the fact that the numeric results for all of the configurations studied here are below the classical blackbody value above this separation.

We also demonstrated that it is possible to create a desired pattern on a surface by fine tuning the separation between and orientations of the surfaces. In the axially aligned systems we considered, we saw the energy can be focused into a small region on the larger surface. This is evident from the 50 % increase in the peak energy flux through the disk in the prolate spheroid-large disk system considered in Chapter 5 compared to the sphere-disk system at the same separation. Additionally, we saw the development of a local minimum on the surfaces beginning at a separation of $\sim R/2$ in the sphere-spheroid systems and $\sim R$ in the disk-spheroid systems. The development of this local minimum is a result of the coupling of the near and far-field effects and means that there are intermediate separations where the flux across the surfaces are uniform.

Considering the asymmetric system of a rotated spheroid and a disk in Chapter 6, we demonstrated that the flux is always concentrated under the point of closets separation.

However, we saw that the projected shape of the spheroid onto the disk will govern the distribution across the disk. We saw that a larger projected area will increase the efficiency of the energy exchange at a larger separation. This means that an object with a larger projected area, like an oblate spheroid, will guide energy through a system better than one with a small projected area, like a prolate spheroid. However, an object with a smaller projected area can greatly localize the energy.

All of these points demonstrate that the radiative properties of a system are influenced by the surface shape at constant surface area. Although this result is well known in classical far-field radiative transfer, we have shown that it also applies to near-field radiative transfer. The key distinction is that the near-field radiative properties are more sensitive to the surface shape than the far-field properties. This supplements the known fact that the surface shape is also important at constant volume [31]. By selecting an appropriate combination of temperature difference, spheroid eccentricity, and surface separation, a desired flux concentration through a region of the disk can be achieved.

The results presented in the preceding chapters demonstrate that the radiation is indeed influenced by the shape of the interacting objects; however, these results are limited in precision to three significant figures by two key factors. The first is that the view factor calculation used is an older program that is not capable of high precision results. This means we have not established a rigorous correlation between the view factors and the near-field radiative heat exchange. The second limitation to our results is the use of a coarse mesh with a sparse sampling of the relevant parameter space. This approach enabled us to produce results within the time constraints and computational power available. To establish a stronger relationship between the surface shape and the energy exchange, we need to use a high resolution mesh in addition to using a higher precision routine to compute the view factors.

Before moving onto investigation of higher resolution meshes, a few items need to be addressed. First, the numeric method used in this work needs to be reevaluated. Three basic components comprise the numeric analysis developed in this thesis: populating the matrices, solving the linear system of equations, and computing the view factors. The

method used to compute the elements of the matrices is a brute force approach. The blatant parallelism in the calculation of the 2 by 2 blocks that represent the edge-edge interactions is not exploited. Additionally, the symmetry of the matrix can be used to reduce the shear number of blocks that must be calculated to $N(2N+1)$ from $4N^2$ where N is the number of edges in the system. After the matrix is populated, the LU-factorization of the full matrix is performed. The matrices that arise in the formalism are block matrices. Formal methods for inverting block matrices exist; however, resource constrains prevented the allocation of time to perform a literature review and to implement one of these methods. The third part of the puzzle is the view factor calculation. Due to the limited precision available in the program used, we were not able to get high precision values for this work. Efficient calculation of these factors is an open problem that has applications from both near-field and far-field radiative exchange to image rendering, and a program that is high precision and well validated and verified was not readily available.

In addition to the higher level algorithmic work, the underlying library used to compute the matrix elements needs review. The current implementation is memory limited. Because of memory caching in the library, each block of the $\overline{\overline{\boldsymbol{W}}}^{-1}$ matrix must be computed in an isolated process during runtime. The step of collecting these blocks together limits the size of the individual meshes to less than 4000 edges each because the matrix becomes too large to pass between processes. The net result is that we cannot use geometries with high resolution meshes with the current implementation. A second issue with the library is the portability. The current version of the source code available on the web does not readily compile on any of the operating systems available. This issue is exacerbated by the fact that the version of the code available on the web has the same version number as the code that was downloaded and used in this thesis. For long term usability, a different implementation of the boundary element method needs to be investigated. Once the routine has been updated, new configurations can be investigated as well as high resolution meshes for the systems presented in the previous chapters.

An extension to the theoretical investigation performed in this thesis is to consider a spheroid with a different generating ellipse. This work focused on spheroids with equal

surface area. This meant that the generating ellipses for the two types of spheroids had different axes; which, in turn, means that the projected areas of the spheroids rotated by 90° were very different. If the same ellipse was used as the generating function for both the prolate and oblate spheroids, the projected areas would be closer in value. This, would provide additional insight into the interaction. Additionally, systems with more surfaces could be investigated. This would provide an opportunity to investigate long range order and tailoring flux patterns using multiple objects in a cluster. Another possible avenue of investigation is the thermally dynamic problem. The current formalism depends on a thermally steady state system. As of the time of writing, no one has presented a fully time dependent solution to the problem of near-field radiative transport. The current formalism relies on the use of time averaging to equate the flux through the surface to the fluctuations of the charge carriers. Recent attempts have been made to investigate the thermally dynamic problem; however, the studies rely on a quasistatic approach [36] or neglect the field energy density [45]. The solution to the thermally dynamic problem remains an open question.

To perform the research for this thesis, a few new subjects were learned and applied to the research. First was electromagnetic wave scattering off nonspherical objects. The basic formalism is straight forward; however, the breadth of applications and subtlety of learning to ask the correct questions leaves a rich area to continue exploration. While learning about electromagnetic wave scatter, the dyadic Green function was introduced. This led directly to an introduction to dyadic analysis which provides a rich set of tools to analyze higher dimensional problems. Finally, the fluctuation-dissipation theorem was investigated. Although we could have blindly applied the known formalism, the basic understanding of this theorem allowed us to not only better understand the connection between the random fluctuations and the electromagnetic field but also correctly apply the theorem and get the correct prefactor in our final equation.

In addition to the theoretical skills, we also got practice in translating the theory to a working computer program. The translation of the formal equations to computer code provided ample practice working with linear algebra and specifically matrix manipulation. Once the matrix formulation was at hand, we were able to gain exposure to the major

programming languages for scientific computing (FORTRAN 77, Fortran 2003, C/C++, and Python). The understanding of these languages was needed in order to stitch together the pieces of software used to compute the raw interaction from the formalism and to analyse the computed results. Finally, the analysis of the results provided ample opportunity to study data visualization techniques. This was an chance to generate and compare data presentation forms such as heat maps versus 3D scatter plots, 3D surface distribution plots versus radial scatter plots, and how to display statistical distribution information along with the raw data on the same plot.

Several cautionary tales do stand out from the experience of performing the research. The first is to write papers faster. The general formalism for the interaction among an arbitrary number of objects embedded in a common background had been worked out in 2011; however, an attempt to publish the formalism was not made. The attempt to save that work for this thesis resulted in others getting to publication first [36]. The second lesson is to read the literature very carefully. The information about the convergence behavior of the T-matrix approach was there [42], but it was not heeded. This resulted in a year and a half spent on a program that did not further our knowledge of the problem. That may have simply been one of the things that had to be learned the hard way by trying to reinvent the wheel. A corollary to this is the third lesson: always check for previously implemented libraries to perform calculations. Time could have been spent more efficiently had a T-matrix library been used in the initial implementation. The initial program would have been completed faster, and, thus, lesson two hammered home quicker.

Finally, the problem domain needs to be properly parameterized. In the process of collecting results, we considered the integrated exchange between the surfaces. This means we computed 30 frequencies for each configuration. This was unnecessary. In the process of analyzing the flux distribution, we found that the spectral components follow the same general trends as the integrated result. This means we could have taken a strategy from electromagnetic scattering problems and worked with a scaled wavelength. The common practice in that field is to take the electromagnetic properties as free parameters and parameterize all lengths in terms of d/λ [42]. This choice would have reduced the computation

overhead and provided additional time to consider higher resolution meshes, more configurations, or simply improve the implementation of the routine. Regardless of where the future work in this field takes us, these are four key points to always remember.

APPENDIX A

VOLUME INTEGRAL SOLUTION FOR THE FIELDS

In this appendix, we establish the volume integral solution for the Fourier components of the electromagnetic field. The general procedure is adapted from that presented by Chew to account for arbitrary linear anisotropic media [11]. To begin, we introduce the dyadic Green function associated with the electric field. To do this, we follow Tai's example and elevate the Maxwell equations to dyadics

$$\boldsymbol{\nabla} \times \overleftrightarrow{\boldsymbol{G}} = \overleftrightarrow{\boldsymbol{\mu}}_\alpha * \overleftrightarrow{\boldsymbol{G}}_m \tag{67a}$$

$$\boldsymbol{\nabla} \times \overleftrightarrow{\boldsymbol{G}}_m = k_0^2 \overleftrightarrow{\boldsymbol{\varepsilon}}_\alpha * \overleftrightarrow{\boldsymbol{G}} + \overleftrightarrow{\boldsymbol{\mu}}_\alpha^{-1} \delta(\boldsymbol{r} - \boldsymbol{r}') \tag{67b}$$

where $\overleftrightarrow{\boldsymbol{E}} \rightarrow \overleftrightarrow{\boldsymbol{G}}$, $ik_0 \overleftrightarrow{\boldsymbol{H}} \rightarrow \overleftrightarrow{\boldsymbol{G}}_m$, and $ik_0 4\pi \overleftrightarrow{\boldsymbol{\mu}}_\alpha \overleftrightarrow{\boldsymbol{J}}/c = \overleftrightarrow{\mathbf{1}}$ [69]. A bit of manipulation reveals that the dyadic Green function satisfies the wave equation

$$\boldsymbol{\nabla} \times \overleftrightarrow{\boldsymbol{\mu}}_\alpha^{-1} * \boldsymbol{\nabla} \times \overleftrightarrow{\boldsymbol{G}}(\boldsymbol{r}, \boldsymbol{r}') = k_0^2 \overleftrightarrow{\boldsymbol{\varepsilon}}_\alpha * \overleftrightarrow{\boldsymbol{G}}(\boldsymbol{r}, \boldsymbol{r}') + \overleftrightarrow{\boldsymbol{\mu}}_\alpha^{-1} \delta(\boldsymbol{r} - \boldsymbol{r}') \tag{68}$$

in region V_α subject to the boundary conditions

$$\hat{\boldsymbol{n}} \times \overleftrightarrow{\boldsymbol{G}}(\boldsymbol{r}_1, \boldsymbol{r}') = \hat{\boldsymbol{n}} \times \overleftrightarrow{\boldsymbol{G}}(\boldsymbol{r}_2, \boldsymbol{r}') \tag{69a}$$

$$\hat{\boldsymbol{n}} \times \left[\overleftrightarrow{\boldsymbol{\mu}}_1^{-1} * \boldsymbol{\nabla} \times \overleftrightarrow{\boldsymbol{G}}(\boldsymbol{r}_1, \boldsymbol{r}') \right] = \hat{\boldsymbol{n}} \times \left[\overleftrightarrow{\boldsymbol{\mu}}_2^{-1} * \boldsymbol{\nabla} \times \overleftrightarrow{\boldsymbol{G}}(\boldsymbol{r}_2, \boldsymbol{r}') \right] \tag{69b}$$

where $\boldsymbol{r}_1$ and $\boldsymbol{r}_2$ are on opposite sides of the surface bounding the specific region [69]. The Green function is also subject to the radiation condition in the external medium that extends to infinity [62].

Next, we consider the vector-dyadic product

$$\boldsymbol{\nabla} \times \overleftrightarrow{\boldsymbol{\mu}}_\alpha^{-1} * \boldsymbol{\nabla} \times \boldsymbol{E} * \overleftrightarrow{\boldsymbol{G}} - \boldsymbol{E} * \boldsymbol{\nabla} \times \mu_\alpha^{-1} \boldsymbol{\nabla} \times \overleftrightarrow{\boldsymbol{G}} \tag{70}$$

where the integration is over volume V_α bounded by surface S_α [11]. Substituting in the wave equations for the electric field, Equation (7), and the Green function, Equation (68), we find

$$\begin{aligned}
&\boldsymbol{\nabla}\times\overleftrightarrow{\boldsymbol{\mu}}_\alpha^{-1}*\boldsymbol{\nabla}\times\boldsymbol{E}*\overleftrightarrow{\boldsymbol{G}}-\boldsymbol{E}*\boldsymbol{\nabla}\times\mu_\alpha^{-1}\boldsymbol{\nabla}\times\overleftrightarrow{\boldsymbol{G}}\\
&\qquad=k_0^2\overleftrightarrow{\boldsymbol{\varepsilon}}_\alpha*\boldsymbol{E}*\overleftrightarrow{\boldsymbol{G}}+ik_0\frac{4\pi}{c}\boldsymbol{j}*\overleftrightarrow{\boldsymbol{G}}-k_0^2\boldsymbol{E}*\overleftrightarrow{\boldsymbol{\varepsilon}}_\alpha*\overleftrightarrow{\boldsymbol{G}}-\boldsymbol{E}*\overleftrightarrow{\boldsymbol{\mu}}_\alpha^{-1}\\
&\qquad=4\pi k_0^2\boldsymbol{P}*\overleftrightarrow{\boldsymbol{G}}+4\pi ik_0\boldsymbol{\nabla}\times\overleftrightarrow{\boldsymbol{\mu}}_\alpha^{-1}*\boldsymbol{M}*\overleftrightarrow{\boldsymbol{G}}-\boldsymbol{E}*\overleftrightarrow{\boldsymbol{\mu}}_\alpha^{-1}
\end{aligned}\tag{71}$$

where we have used the dyadic identity $\boldsymbol{a}\cdot\overleftrightarrow{\boldsymbol{b}}=\overleftrightarrow{\boldsymbol{b}}^T\cdot\overleftrightarrow{\boldsymbol{a}}$ [70] and the symmetry property of the permittivity $\overleftrightarrow{\boldsymbol{\varepsilon}}^T(\boldsymbol{r},\boldsymbol{r}')=\overleftrightarrow{\boldsymbol{\varepsilon}}(\boldsymbol{r}',\boldsymbol{r})$ [21]. On the other hand, if we use the chain rule $\boldsymbol{\nabla}\cdot(\boldsymbol{a}\times\overleftrightarrow{\boldsymbol{b}})=(\boldsymbol{\nabla}\times\boldsymbol{a}\cdot\overleftrightarrow{\boldsymbol{b}})-\boldsymbol{a}\cdot(\boldsymbol{\nabla}\times\overleftrightarrow{\boldsymbol{b}})$ [70] we find

$$\begin{aligned}
&\boldsymbol{\nabla}\times\overleftrightarrow{\boldsymbol{\mu}}_\alpha^{-1}*\boldsymbol{\nabla}\times\boldsymbol{E}*\overleftrightarrow{\boldsymbol{G}}-\boldsymbol{E}*\boldsymbol{\nabla}\times\mu_\alpha^{-1}\boldsymbol{\nabla}\times\overleftrightarrow{\boldsymbol{G}}\\
&\quad=\boldsymbol{\nabla}\cdot(\overleftrightarrow{\boldsymbol{\mu}}_\alpha^{-1}*\boldsymbol{\nabla}\times\boldsymbol{E}\times\overleftrightarrow{\boldsymbol{G}})+\overleftrightarrow{\boldsymbol{\mu}}_\alpha^{-1}*\boldsymbol{\nabla}\times\boldsymbol{E}*\boldsymbol{\nabla}\times\overleftrightarrow{\boldsymbol{G}}\\
&\qquad+\boldsymbol{\nabla}\cdot(\boldsymbol{E}\times\overleftrightarrow{\boldsymbol{\mu}}_\alpha^{-1}*\boldsymbol{\nabla}\times\overleftrightarrow{\boldsymbol{G}})-\boldsymbol{\nabla}\times\boldsymbol{E}*\overleftrightarrow{\boldsymbol{\mu}}_\alpha^{-1}*\boldsymbol{\nabla}\times\overleftrightarrow{\boldsymbol{G}}.
\end{aligned}$$

Using the symmetry of the permeability [21] this becomes

$$=\boldsymbol{\nabla}\cdot(\overleftrightarrow{\boldsymbol{\mu}}_\alpha^{-1}*\boldsymbol{\nabla}\times\boldsymbol{E}\times\overleftrightarrow{\boldsymbol{G}})+\boldsymbol{\nabla}\cdot(\boldsymbol{E}\times\overleftrightarrow{\boldsymbol{\mu}}_\alpha^{-1}*\boldsymbol{\nabla}\times\overleftrightarrow{\boldsymbol{G}}),$$

and using the Maxwell equations this reduces to

$$=\boldsymbol{\nabla}\cdot(ik_0\boldsymbol{H}\times\overleftrightarrow{\boldsymbol{G}}+\boldsymbol{E}\times\overleftrightarrow{\boldsymbol{\mu}}_\alpha^{-1}*\boldsymbol{\nabla}\times\overleftrightarrow{\boldsymbol{G}})+\boldsymbol{\nabla}\cdot(4\pi ik_0\overleftrightarrow{\boldsymbol{\mu}}_\alpha^{-1}*\boldsymbol{M}\times\overleftrightarrow{\boldsymbol{G}}).\tag{72}$$

We can use the divergence theorem to convert the first volume integral to a surface

integral

$$\begin{aligned}
&\int_{V_\alpha} \boldsymbol{\nabla} \cdot \left[ik_0 \boldsymbol{H}(\boldsymbol{r}) \times \overleftrightarrow{\boldsymbol{G}}(\boldsymbol{r}, \boldsymbol{r}') + \boldsymbol{E}(\vec{r}) \times \overleftrightarrow{\boldsymbol{\mu}}_\alpha^{-1}(\boldsymbol{r}, \boldsymbol{r}'') * \boldsymbol{\nabla} \times'' \overleftrightarrow{\boldsymbol{G}}(\boldsymbol{r}'', \boldsymbol{r}) \right] d^3\boldsymbol{r} \\
&\quad = \oint_{S_\alpha} \hat{\boldsymbol{n}}_\alpha \cdot \left[ik_0 \boldsymbol{H}(\boldsymbol{r}) \times \overleftrightarrow{\boldsymbol{G}}(\boldsymbol{r}, \boldsymbol{r}') + \boldsymbol{E}(\vec{r}) \times \overleftrightarrow{\boldsymbol{\mu}}_\alpha^{-1} * \boldsymbol{\nabla}_{r''} \times \overleftrightarrow{\boldsymbol{G}}(\boldsymbol{r}'', \boldsymbol{r}) \right] dS(\boldsymbol{r}) \\
&\quad = \oint_{S_\alpha} ik_0 \left[\hat{\boldsymbol{n}}_\alpha \times \boldsymbol{H}(\boldsymbol{r}) \right] \cdot \overleftrightarrow{\boldsymbol{G}}(\boldsymbol{r}, \boldsymbol{r}') + \left[\hat{\boldsymbol{n}}_\alpha \times \boldsymbol{E}(\boldsymbol{r}) \right] \cdot \overleftrightarrow{\boldsymbol{\mu}}_\alpha^{-1} * \boldsymbol{\nabla}_{r''} \times \overleftrightarrow{\boldsymbol{G}}(\boldsymbol{r}'', \boldsymbol{r}') dS(\boldsymbol{r}) \quad (73)
\end{aligned}$$

where $\hat{\boldsymbol{n}}_\alpha$ point out of V_α and we have used the identity $\boldsymbol{a} \cdot (\boldsymbol{b} \times \overleftrightarrow{\boldsymbol{c}}) = -\boldsymbol{b} \cdot (\boldsymbol{a} \times \overleftrightarrow{\boldsymbol{c}}) = (\boldsymbol{a} \times \boldsymbol{b}) \cdot \overleftrightarrow{\boldsymbol{c}}$ [70]. We now apply the boundary conditions, Equation (4) and Equation (69), on the integrand and find

$$\begin{aligned}
&\oint_{S_\alpha} ik_0 \left[\hat{\boldsymbol{n}}_\alpha \times \boldsymbol{H}(\boldsymbol{r}) \right] \cdot \overleftrightarrow{\boldsymbol{G}}(\boldsymbol{r}, \boldsymbol{r}') + \left[\hat{\boldsymbol{n}}_\alpha \times \boldsymbol{E}(\boldsymbol{r}) \right] \cdot \overleftrightarrow{\boldsymbol{\mu}}_\alpha^{-1} * \boldsymbol{\nabla}_{r''} \times \overleftrightarrow{\boldsymbol{G}}(\boldsymbol{r}'', \boldsymbol{r}') dS(\boldsymbol{r}) \\
&\quad = -\oint_{S_\alpha} ik_0 \left[\hat{\boldsymbol{n}}_0 \times \boldsymbol{H}(\boldsymbol{r}) \right] \cdot \overleftrightarrow{\boldsymbol{G}}(\boldsymbol{r}, \boldsymbol{r}') + \left[\hat{\boldsymbol{n}}_0 \times \boldsymbol{E}(\boldsymbol{r}) \right] \cdot \overleftrightarrow{\boldsymbol{\mu}}_0^{-1} * \boldsymbol{\nabla}_{r''} \times \overleftrightarrow{\boldsymbol{G}}(\boldsymbol{r}'', \boldsymbol{r}') dS(\boldsymbol{r}).
\end{aligned} \quad (74a)$$

We can include the boundary at infinity because the Green function must obey the radiation condition to convert the surface integral to a volume integral to find

$$= \int_{V_0} \boldsymbol{\nabla} \cdot \left[ik_0 \boldsymbol{H}(\boldsymbol{r}) \times \overleftrightarrow{\boldsymbol{G}}(\boldsymbol{r}, \boldsymbol{r}' + \boldsymbol{E}(\vec{r}) \times \overleftrightarrow{\boldsymbol{\mu}}_0^{-1}(\boldsymbol{r}, \boldsymbol{r}'') * \boldsymbol{\nabla}_{r''} \times \overleftrightarrow{\boldsymbol{G}}(\boldsymbol{r}'', \boldsymbol{r}) \right] d^3\boldsymbol{r} \quad (74b)$$

using the chain rule and

$$\begin{aligned}
&= -\boldsymbol{\nabla} \times \overleftrightarrow{\boldsymbol{\mu}}_0^{-1} * \boldsymbol{\nabla} \times \boldsymbol{E} * \overleftrightarrow{\boldsymbol{G}} + \boldsymbol{E} * \boldsymbol{\nabla} \times \mu_0^{-1} \boldsymbol{\nabla} \times \overleftrightarrow{\boldsymbol{G}} \\
&= -4\pi k_0^2 \boldsymbol{P} * \overleftrightarrow{\boldsymbol{G}} - 4\pi i k_0 \boldsymbol{\nabla} \times \overleftrightarrow{\boldsymbol{\mu}}_0^{-1} * \boldsymbol{M} * \overleftrightarrow{\boldsymbol{G}} \ldots \\
&\qquad + \iint \boldsymbol{E}(\boldsymbol{r}) \cdot \overleftrightarrow{\boldsymbol{\mu}}_0^{-1}(\boldsymbol{r}, \boldsymbol{r}'') \delta(\boldsymbol{r}'' - \boldsymbol{r}') \, d^3r \, d^3r''
\end{aligned} \quad (74c)$$

using the Maxwell equations. When the observation point is not in the background region, the final integral above vanishes. If source fields, $\boldsymbol{P}$ and $\boldsymbol{M}$, are present in the background, we can simply collect those regions into a single piecewise continuous term in the background. The net effect is that the surface integral in Equation 72 vanishes. This means we

can write the solution to the electric field as

$$\boldsymbol{E} = 4\pi k_0^2 \overleftrightarrow{\boldsymbol{\mu}}_0 * \overleftrightarrow{\boldsymbol{G}} * \boldsymbol{P} + 4\pi i k_0 \overleftrightarrow{\boldsymbol{\mu}}_0 \boldsymbol{\nabla} \times \overleftrightarrow{\boldsymbol{G}} * \overleftrightarrow{\boldsymbol{\mu}}_0^{-1} * \boldsymbol{M} \tag{75}$$

and we have invoked the symmetry property of the dyadic Green function $\overleftrightarrow{\boldsymbol{G}}(\boldsymbol{r}, \boldsymbol{r}') = \overleftrightarrow{\boldsymbol{G}}^T(\boldsymbol{r}', \boldsymbol{r})$ [69].

Finding the magnetic field takes a bit of care. First, we invoke Faraday's law to find

$$\begin{aligned}\boldsymbol{H} &= \frac{1}{ik_0} \overleftrightarrow{\boldsymbol{\mu}}_0^{-1} * \boldsymbol{\nabla} \times \boldsymbol{E} - 4\pi \overleftrightarrow{\boldsymbol{\mu}}_0^{-1} * \boldsymbol{M} \\ &= -4\pi i k_0 \overleftrightarrow{\boldsymbol{\mu}}_0^{-1} \boldsymbol{\nabla} \times * \overleftrightarrow{\boldsymbol{\mu}}_0 * \overleftrightarrow{\boldsymbol{G}} * \boldsymbol{P} - 4\pi \overleftrightarrow{\boldsymbol{\mu}}_0^{-1} * \boldsymbol{M} \ldots \\ &\quad + 4\pi \overleftrightarrow{\boldsymbol{\mu}}_0^{-1} * \boldsymbol{\nabla} \times \overleftrightarrow{\boldsymbol{\mu}}_0 * \boldsymbol{\nabla} \times \overleftrightarrow{\boldsymbol{G}} * \overleftrightarrow{\boldsymbol{\mu}}_0^{-1} * \boldsymbol{M}. \end{aligned} \tag{76}$$

To understand the final term, we must consider $\overleftrightarrow{\boldsymbol{\mu}}^{-1} \cdot \boldsymbol{\nabla}_{r'} \times \overleftrightarrow{\boldsymbol{\mu}}$. We use the identity demonstrated in Appendix C to write $\boldsymbol{\nabla} \cdot (\overleftrightarrow{\boldsymbol{\mu}}^{-1} \times \overleftrightarrow{\boldsymbol{\mu}}) = \overleftrightarrow{\boldsymbol{\mu}} \cdot \boldsymbol{\nabla} \times \overleftrightarrow{\boldsymbol{\mu}}^{-1} - \overleftrightarrow{\boldsymbol{\mu}}^{-1} \cdot \boldsymbol{\nabla} \times \overleftrightarrow{\boldsymbol{\mu}}$. This means we can swap the order of positions of $\overleftrightarrow{\boldsymbol{\mu}}$ and $\overleftrightarrow{\boldsymbol{\mu}}^{-1}$ at the expense of the boundary term. However, upon closer inspection we find $(\overleftrightarrow{\boldsymbol{\mu}}^{-1} \times \overleftrightarrow{\boldsymbol{\mu}})_{ijk} = 0$. This means the last term can be written as

$$\begin{aligned} &4\pi \overleftrightarrow{\boldsymbol{\mu}}_0^{-1} * \boldsymbol{\nabla} \times \overleftrightarrow{\boldsymbol{\mu}}_0 * \boldsymbol{\nabla} \times \overleftrightarrow{\boldsymbol{G}} * \overleftrightarrow{\boldsymbol{\mu}}_0^{-1} * \boldsymbol{M} \\ &\quad = 4\pi \overleftrightarrow{\boldsymbol{\mu}}_0 * \boldsymbol{\nabla} \times \overleftrightarrow{\boldsymbol{\mu}}_0^{-1} * \boldsymbol{\nabla} \times \overleftrightarrow{\boldsymbol{G}} * \overleftrightarrow{\boldsymbol{\mu}}_0^{-1} * \boldsymbol{M} \\ &\quad = 4\pi k_0^2 \overleftrightarrow{\boldsymbol{\mu}}_0 * \overleftrightarrow{\boldsymbol{\varepsilon}}_0 * \overleftrightarrow{\boldsymbol{G}} * \overleftrightarrow{\boldsymbol{\mu}}_0^{-1} * \boldsymbol{M} + 4\pi \overleftrightarrow{\boldsymbol{\mu}}_0 * \overleftrightarrow{\boldsymbol{\mu}}_0^{-1} * \overleftrightarrow{\boldsymbol{\mu}}_0^{-1} * \boldsymbol{M} \end{aligned} \tag{77}$$

where the last term reduces to the second term in Equation (76). This reveals that the electromagnetic field in a region due to polarization and magnetization sources is

$$\boldsymbol{E} = 4\pi k_0^2 \overleftrightarrow{\boldsymbol{\mu}}_0 * \overleftrightarrow{\boldsymbol{G}} * \boldsymbol{P} + 4\pi i k_0 \overleftrightarrow{\boldsymbol{\mu}}_0 \boldsymbol{\nabla} \times \overleftrightarrow{\boldsymbol{G}} * \overleftrightarrow{\boldsymbol{\mu}}_0^{-1} * \boldsymbol{M} \tag{78a}$$

$$\boldsymbol{H} = -4\pi i k_0 \overleftrightarrow{\boldsymbol{\mu}}_0^{-1} * \boldsymbol{\nabla} \times \overleftrightarrow{\boldsymbol{\mu}}_0 * \overleftrightarrow{\boldsymbol{G}} * \boldsymbol{P} + 4\pi k_0^2 \overleftrightarrow{\boldsymbol{\mu}}_0 * \overleftrightarrow{\boldsymbol{\varepsilon}}_0 * \overleftrightarrow{\boldsymbol{G}} * \overleftrightarrow{\boldsymbol{\mu}}_0^{-1} * \boldsymbol{M} \tag{78b}$$

or in a unified form

$$\begin{bmatrix} \boldsymbol{E} \\ \boldsymbol{H} \end{bmatrix} = \frac{4\pi}{c} \begin{bmatrix} \overleftrightarrow{\boldsymbol{G}}^{EE} & \overleftrightarrow{\boldsymbol{G}}^{EH} \\ \overleftrightarrow{\boldsymbol{G}}^{HE} & \overleftrightarrow{\boldsymbol{G}}^{HH} \end{bmatrix} * \begin{bmatrix} -i\omega \boldsymbol{P} \\ -i\omega \boldsymbol{M} \end{bmatrix} \tag{79}$$

where

$$\overleftrightarrow{\boldsymbol{G}}^{EE} = ik_0 \overleftrightarrow{\boldsymbol{\mu}}_0 * \overleftrightarrow{\boldsymbol{G}}_0 \tag{80a}$$

$$\overleftrightarrow{\boldsymbol{G}}^{EH} = -\overleftrightarrow{\boldsymbol{\mu}}_0 * \boldsymbol{\nabla} \times \overleftrightarrow{\boldsymbol{G}}_0 * \overleftrightarrow{\boldsymbol{\mu}}_0^{-1} \tag{80b}$$

$$\overleftrightarrow{\boldsymbol{G}}^{HE} = \overleftrightarrow{\boldsymbol{\mu}}_0^{-1} * \boldsymbol{\nabla} \times * \overleftrightarrow{\boldsymbol{\mu}}_0 * \overleftrightarrow{\boldsymbol{G}}_0 \tag{80c}$$

$$\overleftrightarrow{\boldsymbol{G}}^{HH} = ik_0 \overleftrightarrow{\boldsymbol{\mu}}_0 * \overleftrightarrow{\boldsymbol{\varepsilon}}_0 * \overleftrightarrow{\boldsymbol{G}}_0 * \overleftrightarrow{\boldsymbol{\mu}}_0^{-1}. \tag{80d}$$

For simple materials, we have $\overleftrightarrow{\boldsymbol{\varepsilon}} = \varepsilon \overleftrightarrow{\boldsymbol{I}} \delta(\boldsymbol{r} - \boldsymbol{r}')$ $\overleftrightarrow{\boldsymbol{\mu}} = \mu \overleftrightarrow{\boldsymbol{I}} \delta(\boldsymbol{r} - \boldsymbol{r}')$ and the integral equations for the fields reduce to the more common form

$$\boldsymbol{E} = 4\pi k_0^2 \mu_0 \overleftrightarrow{\boldsymbol{G}}_0 * \boldsymbol{P} + 4\pi i k_0 \boldsymbol{\nabla} \times \overleftrightarrow{\boldsymbol{G}}_0 * \boldsymbol{M} \tag{81a}$$

$$\boldsymbol{H} = -4\pi i k_0 \boldsymbol{\nabla} \times \overleftrightarrow{\boldsymbol{G}} * \boldsymbol{P} + 4\pi k_0^2 \varepsilon_0 \overleftrightarrow{\boldsymbol{G}} * \boldsymbol{M}. \tag{81b}$$

To the best of our knowledge, this the first time Equation (78) has been rigorously demonstrated for arbitrary linear, dispersive, anisotropic materials.

APPENDIX B

FLUCTUATION-DISSIPATION THEOREM

In this appendix, we apply the fluctuation-dissipation theorem to establish the cross-spectral density of the electromagnetic field. Consider a system of N objects labeled $\alpha \in [1, N]$ embedded in a common background labeled $\alpha = 0$. Object α has temperature T_α and electromagnetic properties $\overleftrightarrow{\boldsymbol{\varepsilon}}_\alpha$ and $\overleftrightarrow{\boldsymbol{\mu}}_\alpha$. Taking the outer product of the fields gives us, in summation notation,

$$E_l H_o = -\left(\frac{4\pi}{c}\right)^2 \omega\omega' \Big[G^{EE}_{lm} * P_m P_p * G^{HE}_{op} + G^{EE}_{lm} * P_m M_p * G^{HH}_{op} \ldots + G^{EH}_{lm} * M_m P_p * G^{HE}_{op} + G^{EH}_{lm} * M_m M_p * G^{HH}_{op} \Big]. \tag{82}$$

Performing an ensemble average results in the cross-spectral density

$$\langle E_l H_o \rangle = -\left(\frac{4\pi}{c}\right)^2 \omega\omega' \Big[G^{EE}_{lm} * \langle P_m P_p \rangle * G^{HE}_{op} + G^{EE}_{lm} * \langle P_m M_p \rangle * G^{HH}_{op} \ldots + G^{EH}_{lm} * \langle M_m P_p \rangle * G^{HE}_{op} + G^{EH}_{lm} * \langle M_m M_p \rangle * G^{HH}_{op} \Big]. \tag{83}$$

The correlations and cross-correlations between the polarization and magnetization fields and the electromagnetic field is determined by the fluctuation-dissipation theorem.

To apply the fluctuation-dissipation theorem to an electromagnetic problem, we follow the basic steps Rytov introduced [64]. We introduce lateral microscopic electric and magnetic fields of strength $\boldsymbol{K}_e$ and $\boldsymbol{K}_h$ as a computation tool that act on the microscopic currents in the materials. The lateral fields are added to the macroscopic fields and average to zero $\langle \boldsymbol{K}_e \rangle = \langle \boldsymbol{K}_h \rangle = 0$ in the absence of external sources. Fluctuations of these lateral

fields drive the polarization and magnetization fields according to the relations

$$\boldsymbol{P} = \frac{1}{4\pi} \int \left[\overleftrightarrow{\boldsymbol{\varepsilon}}(\boldsymbol{r}, \boldsymbol{r}') - \overleftrightarrow{\boldsymbol{I}} \delta(\boldsymbol{r} - \boldsymbol{r}') \right] \cdot \boldsymbol{K}_e(\boldsymbol{r}') \, d^3 r' \tag{84a}$$

$$\boldsymbol{M} = \frac{1}{4\pi} \int \left[\overleftrightarrow{\boldsymbol{\mu}}(\boldsymbol{r}, \boldsymbol{r}') - \overleftrightarrow{\boldsymbol{I}} \delta(\boldsymbol{r} - \boldsymbol{r}') \right] \cdot \boldsymbol{K}_h(\boldsymbol{r}') \, d^3 r'. \tag{84b}$$

From these relations, we can immediately write down the time averages of the polarization and magnetization as $\langle \boldsymbol{P} \rangle = \langle \boldsymbol{M} \rangle = 0$. According to the fluctuation-dissipation theorem, given a variable x_β and a force f_γ related through a linear response

$$x_\beta(\boldsymbol{r}) = \int_V \alpha_{\beta\gamma}(\boldsymbol{r}, \boldsymbol{r}') f_\gamma(\boldsymbol{r}') d^3 r', \tag{85}$$

the cross-spectral density of the fluctuating variable due to the random force is [39]

$$\left\langle x_\beta(\boldsymbol{r}) x_\gamma(\boldsymbol{r}') \right\rangle = \frac{\hbar}{2i} \coth\left(\frac{\hbar\omega}{2k_B T} \right) \left[\alpha_{\beta\gamma}(\boldsymbol{r}, \boldsymbol{r}') - \alpha^*_{\gamma\beta}(\boldsymbol{r}', \boldsymbol{r}) \right] 2\pi\delta(\omega + \omega'). \tag{86}$$

By simple inspection of Equation (84), we see that the variable fields are related through the linear response of the electromagnetic properties to the lateral fields. This allows us to use Equation (85) and Equation (86) to write the cross-spectral densities of the polarization and magnetization fields as

$$\left\langle P_l(\boldsymbol{r}) P_k(\boldsymbol{r}') \right\rangle = \frac{\hbar}{4\pi} \coth\left(\frac{\hbar\omega}{2k_B T} \right) \Im\varepsilon_{lk}(\boldsymbol{r}, \boldsymbol{r}') 2\pi\delta(\omega + \omega') \tag{87a}$$

$$\left\langle M_l(\boldsymbol{r}) M_k(\boldsymbol{r}') \right\rangle = \frac{\hbar}{4\pi} \coth\left(\frac{\hbar\omega}{2k_B T} \right) \Im\mu_{lk}(\boldsymbol{r}, \boldsymbol{r}') 2\pi\delta(\omega + \omega') \tag{87b}$$

$$\left\langle P_l(\boldsymbol{r}) M_k(\boldsymbol{r}') \right\rangle = 0. \tag{87c}$$

where we have exploited the symmetry of the permeability $\overleftrightarrow{\boldsymbol{\varepsilon}}(\boldsymbol{r}, \boldsymbol{r}', \omega) = \overleftrightarrow{\boldsymbol{\varepsilon}}^\dagger(\boldsymbol{r}', \boldsymbol{r}, -\omega)$ and permeability $\overleftrightarrow{\boldsymbol{\mu}}(\boldsymbol{r}, \boldsymbol{r}', \omega) = \overleftrightarrow{\boldsymbol{\mu}}^\dagger(\boldsymbol{r}', \boldsymbol{r}, -\omega)$ [21]. The last equation follows from the assumption that the electrical and magnetic properties are independent.

Using these equations, the cross-spectral density of the electromagnetic fields becomes

$$\begin{aligned}\left\langle E_k(\boldsymbol{r},\omega)H_l^*(\boldsymbol{r},\omega')\right\rangle =& \frac{4\pi}{c}\hbar\omega k_0 \coth\left(\frac{\hbar\omega}{2k_BT}\right)\ldots \\ &\times\left[\overleftrightarrow{\boldsymbol{G}}^{EE} * \Im\overleftrightarrow{\boldsymbol{\varepsilon}} * \overleftrightarrow{\boldsymbol{G}}^{HE\dagger} + \overleftrightarrow{\boldsymbol{G}}^{EH} * \Im\overleftrightarrow{\boldsymbol{\mu}} * \overleftrightarrow{\boldsymbol{G}}^{HH\dagger}\right]_{kl}\end{aligned} \tag{88}$$

where we have used the time symmetry of the Green function $\overleftrightarrow{\boldsymbol{G}}^*(\omega) = \overleftrightarrow{\boldsymbol{G}}(-\omega)$ to write the $\boldsymbol{H}$ field in terms of the complex conjugate [21]. It is also understood that the temperature dependence is to be taken under the volume integral indicated by the convolutions. We see that the electromagnetic properties, $\overleftrightarrow{\boldsymbol{\varepsilon}}$ and $\overleftrightarrow{\boldsymbol{\mu}}$, appear symmetrically between the corresponding Green functions. For non-magnetic materials, we have $\mu = 1$ and the second term vanishes to reveal the well know result from the literature.

We are able to simplify our expression by considering a few points from the literature. Narayanaswamy and Chen point out that when dispersion is considered, the permeability and permittivity are not independent quantities [49]. This result is consistent with the quantum electrodynamics formulation of the fluctuation-dissipation theorem which allows for the dielectric function to be phenomenological in nature or a more fundamental description [32]. The two facts allow us to simplify our expression by omitting the permeability [21]. It is possible to reintroduce the magnetic properties to subsequent expressions by adding the final term back into the final equation.

We can insert this result into the equation for the Poynting vector and simplify by applying our local temperature distribution

$$T(\boldsymbol{r}) = \begin{cases} T_\alpha & \boldsymbol{r}\in V_\alpha \\ \\ T_0 & \boldsymbol{r}\in V_0 \end{cases}, \quad \alpha\in[1,N]. \tag{89}$$

Dividing the volume integral into individual regions we find

$$S_j = \epsilon_{jkl}\int_0^\infty \frac{d\omega}{2\pi}\left[\overleftrightarrow{\boldsymbol{M}}_{0,kl}(\omega) + \sum_{\alpha=1}^{N}\overleftrightarrow{\boldsymbol{M}}_{\alpha,kl}(\omega)\right] \tag{90a}$$

where

$$\overleftrightarrow{\boldsymbol{M}}_{\alpha}(\omega) \equiv k_0 \Re \int_{V_\alpha} d^3r' \int_{V_\alpha} d^3r'' \left[\Theta_0(\omega) + \Theta(\omega, T_\alpha)\right] \ldots \\ \times \overleftrightarrow{\boldsymbol{G}}^{EE}(\boldsymbol{r}, \boldsymbol{r}') \cdot \Im \overleftrightarrow{\boldsymbol{\varepsilon}}_{\alpha}(\boldsymbol{r}', \boldsymbol{r}'') \cdot \overleftrightarrow{\boldsymbol{G}}^{HE,\dagger}(\boldsymbol{r}, \boldsymbol{r}'') \tag{90b}$$

and we have used the relationship $\coth(x) = 2[\frac{1}{2} + \frac{1}{e^{2x}-1}]$ to separate the zero point energy $\Theta_0(\omega) \equiv \hbar\omega/2$ from the mean energy of an oscillator above the zero point $\Theta(\omega, T) \equiv \hbar\omega/[\exp(\hbar\omega/k_B T) - 1]$ [43]. We consider only the real part because we know the Poynting vector is real, and, therefore, we only need to consider the positive frequencies in the Fourier transform.

For global thermal equilibrium, the real part of the integral over the background volume must equal the real part of the sum of the integral over each object region with opposite sign because no net energy exchange is possible [21]. This means the volume integral over the background above, the first term under the integral $\overleftrightarrow{\boldsymbol{M}}_{0,kl}(\omega)$, is equal to the volume integral over the embedded objects with each object held at the background temperature. This allows us to substitute the sum over each object volume held at the background temperature for the integral over the background

$$\boldsymbol{S}(\boldsymbol{r}) = \int_0^\infty \sum_{\alpha=1}^{N} \boldsymbol{S}_\alpha(\boldsymbol{r}, \omega) \frac{d\omega}{2\pi} \tag{91a}$$

where each component of the vector $\boldsymbol{S}_\alpha$ is

$$S_{\alpha,j}(\omega) \equiv \epsilon_{jkl} k_0 \left[\Theta(\omega, T_\alpha) - \Theta(\omega, T_0)\right] \ldots \\ \Re \int d^3r' \int d^3r'' \left[\overleftrightarrow{\boldsymbol{G}}^{EE}(\boldsymbol{r}, \boldsymbol{r}') \cdot \Im \overleftrightarrow{\boldsymbol{\varepsilon}}_{\alpha}(\boldsymbol{r}', \boldsymbol{r}'') \cdot \overleftrightarrow{\boldsymbol{G}}^{HE,\dagger}(\boldsymbol{r}, \boldsymbol{r}'')\right]_{kl}. \tag{91b}$$

We note that in the above equations, each object is treated as an independent emitter of an electromagnetic field. The only dependence on other objects enters through the Green function. This is consistent with the observation of Krüger, Emig, and Kardar [37] that each object can be treated as an independent emitter at temperature T_α with all other

regions at temperature T_b and only the geometry of the objects must be considered.

APPENDIX C

DIVERGENCE OF THE CROSS PRODUCT

In this appendix, we establish the divergence of the cross product of two dyadics. We begin with the identity [70]

$$\boldsymbol{\nabla} \cdot \left(\boldsymbol{a} \times \overleftrightarrow{\boldsymbol{b}} \right) = (\boldsymbol{\nabla} \times \boldsymbol{a}) \cdot \overleftrightarrow{\boldsymbol{b}} - \boldsymbol{a} \cdot \boldsymbol{\nabla} \times \overleftrightarrow{\boldsymbol{b}}.$$

Now we consider three distinct vectors $\boldsymbol{a}_i$. We can juxtapose a constant unit vector $\hat{\boldsymbol{x}}_i$ to the front of each and sum to find

$$\sum_i \hat{\boldsymbol{x}}_i \boldsymbol{\nabla} \cdot \left(\boldsymbol{a}_i \times \overleftrightarrow{\boldsymbol{b}} \right) = \sum_i \hat{\boldsymbol{x}}_i \left(\boldsymbol{\nabla} \times \boldsymbol{a}_i \right) \cdot \overleftrightarrow{\boldsymbol{b}} - \sum_i \hat{\boldsymbol{x}}_i \boldsymbol{a}_i \cdot \boldsymbol{\nabla} \times \overleftrightarrow{\boldsymbol{b}}.$$

We have passed the unit vectors through the divergence because they are constant. Next, we define the dyadic $\overleftrightarrow{\boldsymbol{a}} = \sum_i \boldsymbol{a}_i \hat{\boldsymbol{x}}_i$ and find

$$\begin{aligned} \boldsymbol{\nabla} \cdot \left(\sum_i \hat{\boldsymbol{x}}_i \boldsymbol{a}_i \times \overleftrightarrow{\boldsymbol{b}} \right) &= \sum_i \hat{\boldsymbol{x}}_i \left(\boldsymbol{\nabla} \times \boldsymbol{a}_i \right) \cdot \overleftrightarrow{\boldsymbol{b}} - \sum_i \hat{\boldsymbol{x}}_i \boldsymbol{a}_i \cdot \boldsymbol{\nabla} \times \overleftrightarrow{\boldsymbol{b}} \\ \boldsymbol{\nabla} \cdot \left(\overleftrightarrow{\boldsymbol{a}}^T \times \overleftrightarrow{\boldsymbol{b}} \right) &= \left(\boldsymbol{\nabla} \times \overleftrightarrow{\boldsymbol{a}} \right)^T \cdot \overleftrightarrow{\boldsymbol{b}} - \overleftrightarrow{\boldsymbol{a}}^T \cdot \boldsymbol{\nabla} \times \overleftrightarrow{\boldsymbol{b}}. \end{aligned}$$

Because the differential operators are invariant with respect to coordinate system [70], we find the identity

$$\boldsymbol{\nabla} \cdot \left(\overleftrightarrow{\boldsymbol{a}}^T \times \overleftrightarrow{\boldsymbol{b}} \right) = \left(\boldsymbol{\nabla} \times \overleftrightarrow{\boldsymbol{a}} \right)^T \cdot \overleftrightarrow{\boldsymbol{b}} - \overleftrightarrow{\boldsymbol{a}}^T \cdot \boldsymbol{\nabla} \times \overleftrightarrow{\boldsymbol{b}}.$$

APPENDIX D

APPLICATION PROGRAMMING INTERFACE

D.1 nanotools

The package of tools to compute the near-field exchange.

This is the collection of tools developed to compute the enhanced near-field energy exchange between two surfaces that are separated by a gap smaller than the thermal wavelength. This package was developed in support of [prussing_investigation_2015]. The primary tools assemble the boundary element method matrix using the geometry structure of LIBSCUFF [reid_surface_2011] and compute the flux. There are also additional tools for plotting, computing the far-field radiative exchange view factors, and manipulating meshes.

D.1.1 Subpackages

bemmatrix Find and operate on the boundary element method matrix.

emission Find the emission of an object in isolation.

flux Find the flux between closely spaced surfaces.

geometry Interact with the geometry structure.

plotting Generate surface plots.

scuffem The Python interface to LIBSCUFF.

sphere2spheroid Tools to convert a sphere mesh to a spheroid mesh.

sphereplots Tools for generating the sphere-sphere plots.

spheroidplots Tools for generating the sphere-spheroid plots.

viewfactors Tools to compute the view factors between surfaces.

D.1.2 Constants

SIGMA Stefan-Boltzmann constant $\mathrm{W\,\mu m^{-2}\,K^{-4}}$.

KB Boltzmann constant $\mathrm{J\,K^{-1}}$.

C Speed of light in vacuum $\mathrm{\mu m\,s^{-1}}$.

HBAR Reduced Planck constant J s.

D.1.3 References

- [prussing_investigation_2015] K. F. Prussing *An investigation of surface shape effects on near-field radiative transfer*. Thesis, Georgia Institute of Technology, 2015.
- [reid_surface_2011] M. T. H. Reid, *Surface current/field fluctuation of electromagnetism* (2011), URL http://homerreid.com/scuff-em.

D.1.4 oscillator_energy(omega, T)

Compute the average oscillator energy.

Compute the average energy of an oscillator with frequency omega at temperature T

$$E = \frac{\hbar\omega}{\exp(\hbar\omega/k_B T) - 1}.$$

D.1.4.1 Parameters

- omega : [*array_like*] NumPy array compatible object with containing angular wave numbers in $\mathrm{rad\,s^{-1}}$ with a shape member.
- T : [*scalar*] Temperature in K.

D.1.4.2 Returns

- out : [*array_like*] NumPy Array with the same shape as omega with the average oscillator energy in units of J rad.

D.2 nanotools.bemmatrix

Routines to operate on the boundary element method (BEM) matrix.

The BEM matrix is the matrix of coefficients that describe the transformation from the source terms in a scattering problem to the unknown coefficients for the surface currents at a boundary

$$\overline{\overline{\boldsymbol{W}}}^{-1} = \overline{\overline{\boldsymbol{G}}}_0 + \sum_{\alpha} \overline{\overline{\boldsymbol{G}}}_{\alpha,\alpha\alpha}.$$

The inverted BEM matrix $\overline{\overline{\boldsymbol{G}}}$ is represented by a *BEM dictionary*.

BEM dictionary A nested dictionary structure. The top level keys are integer indicating the surface number in the SCUFF-EM geometry with 0 indicating the homogeneous background. The values of the top level dictionary are dictionaries with keys 'Label' and 'Matrix' where the value for the 'Matrix' is the self interaction block. Additionally, the input geometry file and the frequency are stored in the top level of the dictionary under the keys 'geometry' and 'omega' respectively.

The assumed logic in these routines is for isolated objects embedded in a common background. The inversion method will add the individual blocks for the objects to the 'diagonal' block of the background. A consequence of the structure used here, each edge i in a surface is associated with the $[2i, 2i+1]$ elements of the diagonal in the corresponding surface block.

D.2.1 Example

```
>>> import bemmatrix
>>> G = bemmatrix.assemble("Test.scuffgeo", 3.14)
>>> G0 = G[0]["Matrix"] # Background matrix
>>> L0 = G[0]["Label"]  # Background
>>> G1 = G[1]["Matrix"] # Guaranteed square
>>> L1 = G[1]["Label"]  # SphereA or some such
>>> n1 = G1.shape[0] /2 # Number of edges is half of a dimension
>>> G["geometry"]
'Test.scuffgeo'
>>> G["omega"]
```

```
(3.140000+0j)
```

D.2.2 assemble(geomfile, omega, njobs=None)

Assemble the interaction matrix $\overline{\overline{\boldsymbol{G}}}$.

This routine assembles the blocks of the inverted BEM matrix into the full form using the geometry file geomfile at frequency omega. matrix is returned as a BEM dictionary. The njobs variable is used to tune the number of processes.

D.2.2.1 Parameters

- geomfile : [*string*] The SCUFF-EM geometry file to use.
- omega : [*scalar*] The angular wavenumber k to use in the calculations in $\mathrm{rad}\,\mu\mathrm{m}^{-1}$.
- njobs : [*scalar, optional*] The number of process to use. Default is to let the `multiprocessing` module handle this.

D.2.2.2 Returns

- G : [*dict*] The BEM dictionary.

D.2.3 initialize(geomfile, background=True)

Initialize a BEM dictionary.

Read the geometry file geomfile and create the BEM dictionary. We extract the labels and place them in the appropriate dictionaries and initialize all arrays to $0+i0$ of the correct size.

D.2.3.1 Parameters

- geomfile : [*string*] The SCUFF-EM geometry file to analyze to initialize the dictionary.
- background : [*boolean, optional*] Initialize the matrix for the background. Default is True, but set to False for high edge count meshes.

D.2.3.2 Returns

- G : [*dict*] The initialized BEM dictionary.

D.2.4 invert(G)

Invert the BEM matrix.

Add the block matrices together and compute the inverse

$$\overline{\overline{\boldsymbol{W}}}^{-1} = \overline{\overline{\boldsymbol{G}}}_0 + \sum_{\alpha} \overline{\overline{\boldsymbol{G}}}_{\alpha,\alpha\alpha}$$

to return the BEM matrix $\overline{\overline{\boldsymbol{W}}}$.

D.2.4.1 Parameters

- G : [*dict*] A BEM dictionary.

D.2.4.2 Returns

- W : [*array_like*] The fully inverted BEM matrix $\overline{\overline{\boldsymbol{W}}}$.

D.2.5 lu_factor(G)

LU-factorize the BEM matrix.

Add the block matrices together and compute the LU-factorization of the BEM matrix $\overline{\overline{\boldsymbol{W}}}$.

D.2.5.1 Parameters

- G : [*dict*] A BEM dictionary.

D.2.5.2 Returns

- W : [*tuple*] The LU-factorization parameters returned by `scipy.linalg.lu_solve` to pass to `scipy.linalg.lu_solve`.

D.2.6 number_of_regions(G)

Get the number of surfaces in the BEM dictionary.

This is simply a method to return the number of surface in the dictionary. This is really just the number of integer keys, but we write it as a method so that we don't have to copy the code in multiple places. We could simply take the length and subtract the known

number of keys that are added, but that means we have to rewrite the code if we add or remove data with noninteger keys. The for loop prevents that. Note that we are actually returning 1+ the number of surfaces because of the background. This facilitates the use in `for` loops as a happy side effect.

D.2.6.1 Parameters

- G : [*dict*] A boundary element method matrix dictionary.

D.2.6.2 Returns

- nsurf : [*scalar*] The number of surface in the system.

D.2.7 stamp(I, J, interior, block, G)

Place the computed block into the BEM dictionary.

Place the computed block into the (I,J) section of the BEM dictionary G taking into account the interior flag when I == J. The first four inputs are simply the return values of the .scuffem.get_block method. The last is the BEM dictionary and is used for input and output. If the background has not been initialized, it will be so on return with the (I,J) block in place.

D.2.7.1 Parameters

- I : [*scalar*] Index of the first surface.
- J : [*scalar*] Index of the second surface.
- interior : [*boolean*] If I == J, place in the self interaction matrix.
- block : [*array_like*] The computed (I,J) block to insert in the dictionary.
- G : [*dict*] The BEM dictionary. Updated in place.

D.2.7.2 Returns

- success : [*boolean*] Returns False on an error and True success.

D.3 nanotools.emission

Routines to operate on the emission into the background

The emission of an object in isolation is simply the flux into the background. These are routines to compute the emission, handle reading and writing of the results, and make a simple plot of the data. These routine operate on an *emission dictionary*.

Emission dictionary A dictionary whose keys are the angular wavenumbers k and the values are nested dictionaries. The nested dictionary keys are the surface labels and the values are NumPy arrays with length equal to twice the number of edges in the surface and the entries are the emission associated with each edges.

D.3.1 compute(G, emis=None)

Compute the emission from each object into the background.

We compute the of the emission as if each object was in isolation. We place the results in the given emission dictionary emis using the frequency stored in the BEM dictionary G as the key. If the emission dictionary is not provided, we create and return a new dictionary.

D.3.1.1 Parameters

- G : [*dict*] The BEM dictionary from the .bemmatrix module.
- emis : [*dict*] The emission dictionary. It this is None, the dictionary is initialized.

D.3.1.2 Returns

- emis : [*dict*] The emission dictionary with the updated frequency value.

D.3.2 plot(emissions, R, show=True)

Plot the emissions data in the emission dictionary.

We create a plot of the spectral distribution of the total emission Φ from each object. The given radius will be used to plot the scaled values $kR/(2\pi)$ and $\Phi/(4\pi R^2)$. The show flag is useful for inspecting the plot interactively.

D.3.2.1 Parameters

- emissions : [*dict*] An emission dictionary.
- R : [*scalar*] The radius used for normalization.
- show : [*boolean, optional*] Show the plot on exit. Default is True.

D.3.2.2 Returns

- fig : [*matplotlib.figure.Figure*] The figure containing the plot.

D.3.3 read(fname)

Parse the given emission file.

The routine will parse the given file and return an emission dictionary that was written to the file. The goal is to reproduce the emission structure as computed by the compute routine and written to the file using the write routine.

D.3.3.1 Parameters

- fname : [*string*] The file to parse for the emission data.

D.3.3.2 Returns

- emis : [*dict*] An emission dictionary.

D.3.4 write(fname, emissions)

Write the given emission dictionary to the given file.

We append the data to the given file. Each line shall correspond to a unique frequency and label combination. The remainder of the line will be the distribution of the emission among the edges.

D.3.4.1 Parameters

- fname : [*string*] The file to which to write the emission dictionary.
- fluxes : [*dict*] The emission dictionary

D.4 nanotools.flux

Routines to operate on the energy exchange between objects.

The energy exchange from object β into object α embedded in a common background is computed using first using a "flux"

$$\Phi_n = \left[\overline{\overline{\boldsymbol{W}}}^{\dagger} \, \mathrm{sym}\overline{\overline{\boldsymbol{G}}}_{\alpha,\alpha\alpha} \, \overline{\overline{\boldsymbol{W}}} \, \mathrm{sym}\overline{\overline{\boldsymbol{G}}}_{\beta,\beta\beta} \right]_{nn}$$

and the integrated heat exchange

$$H_n = \int_0^\infty \left[\Theta(\omega, T_\beta) - \Theta(\omega, T_\alpha)\right] \Phi_n \frac{d\omega}{4\pi}.$$

These are routines to compute the flux and heat and operate with the results. These routines operate on a *flux dictionary* or *heat dictionary*.

Flux dictionary A dictionary whose keys are the angular wave numbers k and the values are nested dictionaries. The nested dictionary keys are the tuple (INTO, DUE TO) and the values are a NumPy arrays whose length is twice the number of edges in the (INTO) surface and the entries are the flux associated with each edge.

Heat dictionary A dictionary whose keys are the (INTO, DUE TO) tuples from a *flux dictionary* and the values are NumPy arrays. The length of the NumPy is twice the number of edges in the (INTO) surface and the entries are the integrated heat associated with each edge.

The "INTO" and "DUE TO" denote the flux (heat) INTO an object DUE TO fluctuating currents in another object.

D.4.1 compute(G, W, flux=None)

Compute the flux between each pair of objects.

We compute the edge distribution between each pair of objects assuming that they exist within a single background. The current logic requires that the objects are distinct. We place the results in the given flux dictionary flux using the frequency stored as the key in G. If the dictionary is not provided, we create and return a new dictionary.

The current version demands that W is the LU-factorization of the BEM matrix returned by .bemmatrix.lu_factorize. If we take the time to study, we might be able to exploit the block nature of G to compute locally. I just don't really have the time currently.

D.4.1.1 Parameters

- G : [*dict*] The BEM dictionary defined in the .bemmatrix module.

- W : [*tuple*] The LU-factorized parameters returned by .bemmatrix.lu_factor.
- flux : [*dict*] The flux dictionary. If this is None, the dictionary is initialized.

D.4.1.2 Returns

- flux : [*dict*] The flux dictionary updated with the new frequency.

D.4.2 integrate(fluxes, Temps)

Integrate the spectral flux into each object.

Compute the integrated heat

$$H_n = \int_0^\infty \left[\Theta(\omega, T_a) - \Theta(\omega, T_b)\right] \Phi_n \frac{d\omega}{4\pi}$$

into each object due to all other objects at a each edge. Each object must have an associated temperature in the Temps directory. Note that the logic here is for objects embedded in a common background. It is assumed that each label exists for each frequency.

D.4.2.1 Parameters

- fluxes : [*dict*] The flux dictionary to be integrated.
- Temps : [*dict*] A dictionary whose keys are the surfaces used in the flux dictionary and the values are the temperature of the objects in K.

D.4.2.2 Returns

- heat : [*dict*] The heat dictionary generated from the fluxes and Temps.

D.4.3 is_symmetric(fluxes, tolerance=1e-15)

Determine if the flux spectrum is symmetric.

Determine if the flux spectrum is symmetric between two objects. The input fluxes are those returned by the total method. We return a dictionary whose keys are the unique pairs of (INTO, DUE TO) labels and the values are Nx2 boolean NumPy arrays indicating matching frequencies and fluxes. If the reverse key pair is not in the input dictionary, then it is skipped and not included in the output. The optional tolerance is the accuracy to

which we may call the values the same. If all of the values are true, then the reverse key will be removed from the input dictionary.

D.4.3.1 Parameters

- fluxes : [*dict*] A dictionary of the totaled fluxes returned by the .total method.
- tolerance : [*scalar, optional*] Tolerance for calling equal.

D.4.3.2 Returns

- symm : [*dict*] A dictionary whose keys are either (A,B) or (B,A) based on which was found first and the values are Nx2 boolean NumPy arrays indicating matching frequencies and fluxes.

D.4.4 map_to_faces(geometry, heat, fractional=False, swap_labels=False)

Map the heat from the edges to the faces.

We take in a geometry structure and a heat dictionary and map the heat from sorted by edge to the flux through each face. The geometry dictionary is that generated by the geometry submodule and the flux dictionary is a flux at a particular wavelength or the result from the integrate method contained in this module. We return a dictionary similar to the input heat with the flux mapped to the face and not the edges. The values of the flux are the raw values $\mathrm{W\,\mu m^{-2}\,K^{-4}}$.

WARNING: Currently, this method only works with two surfaces. Both surfaces are required to be in the geometry and the heat dictionaries.

D.4.4.1 Parameters

- geometry : [*dict*] A geometry dictionary as defined in the .geometry module.
- heat : [*dict*] A heat dictionary computed for the given geometry.
- fractional : [*boolean, optional*] Return the fractional portion of the flux into the surface. Essentially, normalize by the sum over all the faces. It is not recommended to use this as the normalization is suspect.

- swap_labels : [*boolean, optional*] DEPRECATED: Swap the (INTO, DUE TO) labels. This is for the results for the sphere-spheroid results computed. This should not be a problem with versions > 1.3.15.

D.4.4.2 Returns

- heat : [*dict*] A dictionary very similar to the input heat dictionary except *the values of the nested dictionaries are the flux associated with the faces and not the edges.*

D.4.5 plot(fluxes, R, show=True, legend=True)

Plot the flux spectrum in the given dictionary.

Create a plot of the spectral distribution of the total flux into each object due to the others. The given radius is used to scale the plotting values. The frequencies will be scaled by $R/(2\pi)$ and the flux by $1/(4\pi R^2)$.

D.4.5.1 Parameters

- fluxes : [*dict*] The dictionary returned by the total method.
- R : [*scalar*] The radius used for normalization.
- show : [*boolean, optional*] Show the plot on exit. Default is True.
- legend : [*boolean, optional*] Add a legend to the graph. Default is True.

D.4.5.2 Returns

- fig : [*matplotlib.figure.Figure*] The figure containing the plot.

D.4.6 read(fname)

Parse the given flux file.

This routine parses the given flux file and return a flux dictionary that was written to file. The goal is to reproduced the flux dictionary computed by the compute routine and written to file using the write routine. Lines beginning with the # character are considered comments and ignored. Empty lines are also ignored.

D.4.6.1 Parameters

- fname : [*string*] The file to parse for the flux data.

D.4.6.2 Returns

- flux : [*dict*] A flux dictionary.

D.4.7 total(fluxes)

Get the total flux into each object.

The total flux into each object as a function of frequency is simply the sum over the edges. We restructure the data such that the (INTO, DUE TO) keys become the keys in the returned dictionary and the frequencies are the first column of a NumPy array that are the value. The second column is the total flux. It is assumed that real frequencies are being used.

This method should also work with a well formatted emission output.

D.4.7.1 Parameters

- fluxes : [*dict*] A flux dictionary.

D.4.7.2 Returns

- data : [*dict*] A dictionary whose keys are the (INTO, DUE TO) tuples from the flux dictionary and the values are Nx2 NumPy arrays with the first column the sorted frequencies and the second the total flux through the (INTO) surface due to the (DUE TO) surface.

D.4.8 write(fname, fluxes)

Write the given emission data to the given file.

We append the flux dictionary data to the file. Each line in the file corresponds to a unique frequency and label combination. The label will be the (INTO, DUE TO) names of the interacting objects. The remainder of the line will be the distribution of the flux among the edges of the (INTO) object.

D.4.8.1 Parameters

- fname : [*string*] The file to which to write the flux dictionary.
- fluxes : [*dict*] A flux dictionary

D.5 nanotools.geometry

Tools to load a geometry.

This module defines the *geometry dictionary* for working with a SCUFF-EM geometry in Python, routines for reading and writing the geometry dictionary to file, and a routine to parse a GMSH geometry file.

geometry dictionary A dictionary whose keys are the labels of the surfaces taken from a native SCUFF-EM geometry. The values of the dictionary with keys 'vertices', 'faces by verts', 'faces by edges', and 'edges'. The values of these nested dictionaries are the vertices, faces defined by vertices, faces defined by edges, and the edges defined by vertices respectively.

D.5.1 Example

```
>>> geom = scuffem.analyze_geometry('Test.scuffgeo')
>>> g1 = geom['Label1']
>>> g1['edges'] # The edges defined by the two vertices.
>>> g1['faces by edges'] # The faces defined by the edges.
>>> g1['faces by verts'] # The faces defined by the vertices.
>>> g1['vertices'] # The Cartesian coordinates of the vertices.
>>> plotting.qp_geom(geom) # Displays the mesh
```

D.5.2 read(fname)

Parse the given file and generate the geometry dictionary.

This routine is designed to perform the reverse work of the write function and is very unforgiving about errors. If it manages to catch an error it will return a None value.

D.5.2.1 Parameters

- fname : [*string*] The geometry file generated by the write method.

D.5.2.2 Returns

- geom : [*dict*] The geometry dictionary.

D.5.3 read_gmsh(fname)

Parse a GMSH file and return a dictionary.

We add a routine to parse a GMSH file because I have already copied it around a number of times. We assume that the faces are triangles because that is what they should be for the present purposes. Once we have read in the face and vertex lists, we analyze to determine the edge mapping. The surface is placed in a geometry dictionary under the key 'GMSH'.

D.5.3.1 Parameters

- fname : [*string*] The GMSH geometry file to parse.

D.5.3.2 Returns

- geom : [*dict*] The geometry dictionary.

D.5.4 write(fname, geom)

Write the geometry dictionary to file.

We write the dictionary as text to the file. We begin each object definition with the object label. We then write the vertices, edge definitions, and face definitions. The format is to use the dictionary key followed by a colon followed by the number of elements N. The next N rows are the individual elements (vIx, vIy, vIx), (EI1, EI2), or (FI1, FI2, FI3). Each section is separated by a blank line.

D.5.4.1 Parameters

- fname : [*string*] The name of the file to which to write the geometry.
- geom : [*dict*] The geometry dictionary.

D.6 nanotools.plotting

A collection of tools for plotting surfaces.

D.6.1 qp(F, V, show=True)

Quickly plot a surface defined by a face and vertex list.

Given a list of triangular faces and a vertex list, plot the surface in a 3D axes. The faces are colored blue. The purpose of this is for quick visualization of the geometry.

D.6.1.1 Parameters

- F : [*array_like*] Nx3 NumPy array where each row is the indices in the V array denoting the vertices that define the face.
- V : [*array_like*] Nx3 NumPy array where each row is the Cartesian coordinates (x,y,z) of a vertex.
- show : [*boolean, optional*] Display the figure on exit. Default is True.

D.6.1.2 Returns

- fig : [*matplotlib.figure.Figure*] The figure showing the surface.

D.6.2 qp2(F, V, show=True)

Alternate version of quick patch.

This version directly uses the Poly3DCollection to generate the surface as opposed to the plot_trisurface method. This was derived from the effort to map the flux across the surfaces.

D.6.2.1 Parameters

- F : [*array_like*] Nx3 NumPy array where each row is the indices in the V array denoting the vertices that define the face.
- V : [*array_like*] Nx3 NumPy array where each row is the Cartesian coordinates (x,y,z) of a vertex.
- show : [*boolean, optional*] Display the figure on exit. Default is True.

D.6.2.2 Returns

- fig : [*matplotlib.figure.Figure*] The figure showing the surface.

D.6.3 qp_geom(geometry, axs=None, deg=None, rad=None)

Create a surface plot of the geometry.

Quickly plot the surface arrangement of the system defined in a geometry dictionary. The faces are colored blue to generate a wire frame mesh.

Two parameters, deg and rad, are available to rotate the surfaces outward. These allow for the ability to see the area nearest to the gap.

D.6.3.1 Parameters

- geometry : [*dict*] A geometry dictionary as defined in .geometry.
- axs : [*mpl_toolkits.mplot3d.Axes, optional*] The axes to use for plotting. If None, a new Figure will be created and the Axes returned.
- deg : [*scalar, optional*] The degrees by which to rotate the surface outward. If this is present, rad must be None.
- rad : [*scalar, optional*] The radians by which to rotate the surface outward. If this is present, deg must be None.

D.6.3.2 Returns

- axs : [*mpl_toolkits.mplot3d.Axes3D*] The axes showing the surface.

D.6.4 surface(geometry, flux, axs=None, norm=None, cbar=None, cmap=True, deg=None, rad=None)

Create a surface plot of the flux.

Generate a plot of the flux across the surface of the given geometry. The geometry is that parsed by the geometry module and the flux is the flux mapped by the face.

D.6.4.1 Parameters

- geometry : [*dict*] A geometry dictionary as defined in .geometry.

- flux : [*dict*] The flux dictionary from the .flux.map_to_faces routine. This should be the flux computed for the geometry.
- axs : [*mpl_toolkits.mplot3d.Axes3D, optional*] The axes to use for plotting the surface. If this is None, a new `matplotlib.figure.Figure` is created.
- norm : [*matplotlib.colors.Normalize, optional*] The normalization passed to `axs` as the `norm` keyword argument.
- cbar : [*boolean, optional*] Include the color bar on the axes. Default is True.
- cmap : [*matplotlib.cm*] The color map to use. If None, `gist_heat` is used.
- deg : [*scalar, optional*] The degrees by which to rotate the surface outward. If this is present, rad must be None.
- rad : [*scalar, optional*] The radians by which to rotate the surface outward. If this is present, deg must be None.

D.6.4.2 Returns

- axs : [*mpl_toolkits.mplot3d.Axes3D*] The axes with the plot.

D.7 nanotools.scuffem

The Python side of the interface to LIBSCUFF.

This module works in tandem with the C++ interface to the LIBSCUFF defined in the source directory of the parent project [reid_surface_2011]. If the SCUFF_INTERFACE library has not been built, please go to the root of the project and run

```
$ scons -C src
$ scons -C src install
```

For more details, see the README.txt or the SCons documentation.

This module provides a systematic way to load the LIBSCUFF library and interact with the native data structure. The library is wrapped in the native Python `ctypes` module and all type conversion is handled within the specific routines.

D.7.1 Example

```
>>> import scuffem
>>> scuff = scuffem.load()
>>> f = 'SiCSphere.scuffgeo'
>>> success = scuffem.load_geometry(f)
>>> print(success)
0
>>> scuffem.num_surfaces()
1
>>> scuffem.surface_label(1)
b'TheSphere'
```

D.7.2 Bugs

There is a known issue with data caching in the interface library. The LIBSCUFF library does not properly clear the local storage matrix used in computing a block of the BEM matrix. This becomes a problem when multiple surfaces use the same mesh (sphere-sphere systems). The trick is to simply reload the data structure for every call to the routine to compute a block of the BEM matrix. However, The interface library loads a static copy of the native data structure of LIBSCUFF. The problem with this is that once a geometry has been loaded into memory, you *cannot* change it unless you restart the Python session. To work around this problem and properly compute the blocks of the matrix, you *must* load the geometry into separate processes using the `multiprocessing` module.

D.7.3 References

- [reid_surface_2011] M. T. H. Reid, *Surface current/field fluctuation of electromagnetism* (2011), URL http://homerreid.com/scuff-em.

D.7.4 analyze_geometry(geomfile, check_files=True)

Load the given SCUFF-EM geometry file and analyze the structure.

Load the geometry file and extract the geometry information from the SCUFF-EM data structure. This is then placed into a geometry dictionary as defined in .geometry.

The check_files argument is a flag to scan the geometry file for existence and the existence of required mesh files. If this is False and the appropriate files do not exist, the SCUFF-EM library will call and Abort and bad things will happen. There is no way I can stop this except by checking for the files myself. If you pass False, you are guaranteeing that all of the files exist.

D.7.4.1 Parameters

- geomfile : [*string*] The SCUFF-EM geometry file to analyze.
- check_files : [*boolean, optional*] Check the geometry file before trying to pass it to the SCUFF-EM library. Default is True.

D.7.4.2 Returns

- geom : [*dict*] A geometry dictionary.

D.7.5 compute_block(geomfile, omega, I, J, interior, checked=True)

Compute a block of the boundary element method BEM matrix.

Load the SCUFF-EM geometry file geomfile and compute the (I,J) block of the BEM matrix at wave number omega. If we are computing and diagonal element (I == J), the interior flag indicates if we are to use the interior material properties or not. The checked flag is to indicate that the files have been prescreened by the file_check routine to ensure SCUFF-EM will not call an Abort. If you have not done this already with the file_check routine, set this to False. We return a tuple comprising of the (I, J, interior) inputs appended with the computed block on success or a None value on error.

The logic for this routine is specialized to the case of isolated objects in a common homogeneous background. The computation of a block is independent of the other blocks and may be parallelized.

D.7.5.1 Parameters

- geomfile : [*string*] The SCUFF-EM geometry file.

- omega : [*scalar*] The frequency to use for computations in rad µm^{-1}.
- I : [*scalar*] The index of the first surface to use in calculations.
- J : [*scalar*] The index of the second surface to use in calculations.
- interior : [*boolean*] If I == J, use the interior material for the object.
- checked : [*boolean*] The geometry file has been prescreened to ensure SCUFF-EM will not call an Abort. Default it True.

D.7.5.2 Returns

- data : [*tuple*]
  - data[0] : I
  - data[1] : J
  - data[2] : interior
  - data[3] : The (I,J) block of the full matrix on success and None if there was an error.

D.7.6 file_check(geomfile)

Check for valid files.

Check that the SCUFF-EM file exists and quickly parse and check for the dependent mesh files. This is to ensure the SCUFF-EM will not call an Abort during execution.

D.7.6.1 Parameters

- geomfile : [*string*] The SCUFF-EM file to check.

D.7.6.2 Returns

- good : [*boolean*] The file is valid and will not cause an Abort.

D.7.7 load()

Load the SCUFF-EM library and set the argument types and returns.

Using the `ctypes` module, load the SCUFF-EM library interface. We will define the argument types and the return values. This method allows us to treat the interface as simple class or module. Life is better when we can hide details behind the curtain.

If the interface library is not in the same directory as this module, we raise a runtime error. While I would normally prefer to not raise an error, this qualifies as a critical error and execution should stop. Why would you be accessing this module if you hadn't read the documentation or built the library anyway?

D.8 nanotools.sphere2spheroid

Convert a sphere mesh to a spheroid.

This module contains the routines to compute the equatorial radius and polar distance of a spheroid with surface area equal to a sphere of radius R. When run as a script, take a sphere mesh file (.MSH) and convert it to a spheroid. We will take the eccentricities as integers that are to be divided by 100 to get the proper value

```
10 => 0.10
20 => 0.20
etc.
```

D.8.1 oblate_radii(ecc, R)

Compute oblate spheroid parameters.

Compute the equatorial radius and polar distance of an oblate spheroid with eccentricity ecc and surface area equal to a sphere of radius R.

D.8.1.1 Parameters

- ecc : [*scalar*] The eccentricity of the spheroid.
- R : [*scalar*] The radius of the equal surface area sphere.

D.8.1.2 Returns

- a : [*scalar*] The equatorial radius of the spheroid.
- c : [*scalar*] The polar distance of the spheroid.

D.8.2 prolate_radii(ecc, R)

Compute prolate spheroid parameters.

Compute the equatorial radius and polar distance of an prolate spheroid with eccentricity ecc and surface area equal to a sphere of radius R.

D.8.2.1 Parameters

- ecc : [*scalar*] The eccentricity of the spheroid.
- R : [*scalar*] The radius of the equal surface area sphere.

D.8.2.2 Returns

- a : [*scalar*] The equatorial radius of the spheroid.
- c : [*scalar*] The polar distance of the spheroid.

D.9 nanotools.sphereplots

Tools to generate the plots for the sphere-sphere results.

This module contains the tools to parse a directory for the two spheres interaction data and generating plots. We include a method to generate a heat map of flux versus separation and frequency. We also include the method to generate the figure comparison to that presented by Rodriguez, Reid, and Johnson [rodriguez_fluctuating_2013]. Creating the comparison plot requires that the reference data exists in files named 'bluepts.csv,' 'greenpts.csv,' and 'redpts.csv' in a directory named 'reference' next to this file.

It is assumed that the result files have the naming convention

```
Omegas_Sphere_d######nm_scuffgeo.flux
```

The main point is the third token based on the '_' character. This is assumed to be the separation between the objects in nanometers.

When run as a script, this generates the comparison figure and the heat map presenting the flux as a function of frequency and separation.

D.9.1 References

[rodriguez_fluctuating_2013] A. W. Rodriguez, M. T. H. Reid, and S. G. Johnson, Phys. Rev. B 88, 054305 (2013).

D.9.2 get_reference(refdir=None, reffiles=None)

Load the reference data.

Extract the reference data from the CSV files in the reference directory. The data is returned as a dictionary whose keys are the CSV file names given.

D.9.2.1 Parameters

- refdir : [*string, optional*] The directory to search for the reference data files. The default is a directory named 'reference' in the same directory as this file.
- reffiles : [*list, optional*] A list of the files to load. The files must be in CSV format. The default files are 'redpts.csv', 'bulepts.csv', and 'greenpts.csv'.

D.9.2.2 Returns

- data : [*dict*] A dictionary whose keys are the files listed in reffiles and the values are the data loaded from each file.

D.9.3 heatmap(Phis, R, addboxes=False, addmarks=False)

Create a heat map for the flux.

Generate the heat map for the spectral distribution as a function of separation. The frequencies are scaled by $R/(2\pi)$, the separations by $1/(2R)$ and the flux by $A = 4\pi R^2$.

D.9.3.1 Parameters

- Phis : [*array_like*]
  - Phis[:,0] : Wavenumber k
  - Phis[:,1] : Separation d
  - Phis[:,2] : Flux Φ
- R : [*scalar*] Radius of the spheres.
- addboxes : [*boolean, optional*] Turn the edge colors to cyan. Default is False
- addmarks : [*boolean, optional*] Mark the unique point pairs with a cyan 'x'. Default is False.

D.9.3.2 Returns

- fig : [*matplotlib.figure.Figure*] The figure showing the data.

D.9.4 parse_directory(spheredir, R, T, vsweep=False)

Parse the directory for two spheres data.

Parse the given directory for the spectral flux data. We also go ahead and integrate the total flux in each file as we walk the directory. We will also return the emission data for the separation closest to one radius. This may be parsed later if needed for the plot. The temperature T of the hot object is needed so that we may calculate the integrate flux.

It is assumed that the files contain two spheres with one at T=0 and the other at the given temperature. It is assumed that the files have the naming convention

```
Omegas_Sphere_d######nm_scuffgeo.flux
```

The main point is the third token based on the '_' character. This is assumed to be the separation between the objects in nanometers.

D.9.4.1 Parameters

- spheredir : [*string*] The directory to parse for the flux files.
- R : [*scalar*] The radius of the two spheres.
- T : [*scalar*] The temperature of one sphere in K.
- vsweep : [*boolean, optional*] Use `vsweep` to compute the view factors instead of the semianalytic expression. Default is False.

D.9.4.2 Returns

- Href : [*array_like*]
  - Href[:,0] : Separation d
  - Href[:,1] : Heat transfer H (integrated flux)
  - Href[:,2] : Average view factor with area $A_i F_{ij}$
- Phis : [*array_like*]

  - Phis[:,0] : Frequency k
  - Phis[:,1] : Separation d
  - Phis[:,2] : Spectral Flux Φ

- Emis : [*array_like*] Frequency and emission for $d = R$ (if found)
  - Emis[:,0] : Frequency k
  - Emis[:,1] : Spectral emission Φ

D.9.5 plot(Href, Phis, Emis, refdata, R, T, show=False)

Generate the comparison plot.

Take the computed data (Href, Phis, and Emis) as parsed by parse_dir, reference data (refdata) as parse by get_reference method, radius (R), and temperature (T) and generate the comparison plot for [rodriguez_fluctuating_2013].

WARNING: Keep in mind that many of the values used are hard coded for the R=0.2 and T=300.0 case of gold spheres.

D.9.5.1 Parameters

- Href : [*array_like*] The first return from the parse_directory method.
- Phis : [*array_like*] The second return from the parse_directory method.
- Emis : [*array_like*] The third return from the parse_directory method.
- refdata : [*array_like*] The array returned from the get_reference method.
- R : [*scalar*] The radius of the spheres.
- T : [*scalar*] The temperature of the spheres.
- show : [*boolean, optional*] Show the figure on exit. Default is False.

D.9.5.2 Returns

- fig : [*matplotlib.figure.Figure*] The figure with the plotted data.

D.9.6 print_dollar_sign(fig)

Process all of the text in the figure to print the dollar sign.

We loop over all of the text (that I know about) in the given figure and escape the dollar sign. This is necessary when we want to export as an SVG to be typeset in another document. We also need to modify the tick labels along the axis spines so that they will be bounded by dollar signs.

D.9.6.1 Parameters

- fig : [*matplotlib.figure.Figure*] The figure to process.

D.9.6.2 Returns

- fig : [*matplotlib.figure.Figure*] The figure processed in place.

D.10 nanotools.spheroidplots

Tools to generate plots for the sphere-spheroid results.

DEPRECATED: This module really only contains one useful routine: `parse_directory`, and that will be moved in the future. The routines to generate the heat map and scatter plots have been moved to the `sconstruct` file in the documentation image tree.

This module contains the tools to parse a directory containing data for a sphere and spheroid interaction and generate heat maps. The methods for plotting utilize the two spheres data in order to scale the results. The methods are focused on the equal surface area sphere and spheroid interaction where one object is 'hot' and the other is at T=0 K.

It is assumed that the files in the directory utilize the naming convention

```
Omegas_Sphere_Spheroid_(ob|pr)XXX_dYYYYYYnm_scuffgeo.flux
```

where the XXX is the eccentricity times 100 (flagged by either ob for oblate or pr for prolate) and YYYYYY is the separation in nanometers. The name is tokenized on the '_' character and the fourth and fifth tokens are the critical parts.

When run as a script, this will generate the total heat exchange between the bodies presented as a heat map results as a function of separation and eccentricity

D.10.1 heatmap(data, R, T, Href, addboxes=False, addmarks=False, useF=False)

Create a heat map for the total heat exchange.

Generate the heat map as a function of separation and eccentricity. We integrate the flux over the frequencies with the oscillator energy at temperature T. This method assumes that there are two objects with one 'cold' at 0 K and the other is 'hot' at temperature T. We scale the separations by $1/(2R)$ for plotting.

The heat is scaled based on the value provided in the Href input. If this is a scalar, it is taken to be the black body value and all of the heats are divided by it. This will also trigger the use of a log scale for the color map. If Href is a NumPy array, it must be the integrated reference data, Href, computed by the .sphereplots.parse_directory routine.

D.10.1.1 Parameters

- data : [*array_like*] The data structure returned by parse_directory:
  - data[:,0] : Frequency k (units of wavenumber)
  - data[:,1] : Eccentricity e
  - data[:,2] : Separation d
  - data[:,3] : Flux Φ
- R : [*scalar*] Radius of the equal surface area sphere.
- T : [*scalar*] Temperature of one object in K.
- Href : [*array_like*] The first return value from .sphereplots.parse_directory.
- addboxes : [*boolean, optional*] Turn the edge colors to cyan. Default is False
- addmarks : [*boolean, optional*] Mark the unique point pairs with a cyan 'x'. Default is False.
- useF : [*boolean, optional*] Normalize by the geometric view factor. Default is False.

D.10.1.2 Returns

- fig : [*matplotlib.figure.Figure*] The figure showing the data.
- out : [*array_like*] The X, Y, and Z values plotted in fig.

D.10.2 heatmap_by_frequency_and_eccentricity(data, R, sep, addboxes=False, addmarks=False, logscale=False)

Create the heat map as a function of frequency and eccentricity.

Create a heat map for the spectral distribution of the flux as a function of eccentricity for a particular separation. The default method assumes that the flux data has been scaled by the two spheres data. To plot the raw data scaled by the surface area $4\pi R^2$, set the log scale flag to True. We scale the frequencies by $R/(2\pi)$ for plotting.

The color scale is based on the values in the fourth column of the data. To be consistent across plots, it is best to pass in the full data array.

D.10.2.1 Parameters

- data : [*array_like*]
  - data[:,0] : Frequency k (units of wavenumber)
  - data[:,1] : Eccentricity e
  - data[:,2] : Separation d
  - data[:,3] : Flux /(Flux with e=0) $\Phi/\Phi_{e=0}$
- R : [*scalar*] Radius of the equal surface area sphere.
- sep : [*scalar*] The particular separation to use for creating the heat map.
- addboxes : [*boolean, optional*] Turn the edge colors to cyan. Default is False
- addmarks : [*boolean, optional*] Mark the unique point pairs with a cyan 'x'. Default is False.
- logscale : [*boolean, optional*] Plot assuming the fourth column data[:,3] is normalized by the area $\Phi/(4\pi R^2)$ instead of the sphere result. Essentially, use a log scale for the color bar. Default is False.

D.10.2.2 Returns

- fig : [*matplotlib.figure.Figure*] The figure showing the heat map.

D.10.3 heatmap_by_frequency_and_separation(data, R, ecc, addboxes=False, addmarks=False, logscale=False)

Create the heat map as a function of frequency and separation.

Create a heat map for the spectral distribution of the flux as a function of separation for a particular eccentricity. The default method assumes that the flux data has been scaled

by the two spheres data. To plot the raw data scaled by the surface area $4\pi R^2$, set the log scale flag to True. We scale the frequencies by $R/(2\pi)$ and the separations by $1/(2R)$ for plotting.

The color scale is based on the values in the fourth column of the data. To be consistent across plots, it is best to pass in the full data array.

D.10.3.1 Parameters

- data : [*array_like*]
  - data[:,0] : Frequency k (units of wavenumber)
  - data[:,1] : Eccentricity e
  - data[:,2] : Separation d
  - data[:,3] : Flux /(Flux with e=0) $\Phi/\Phi_{e=0}$
- R : [*scalar*] Radius of the equal surface area sphere.
- ecc : [*scalar*] The particular eccentricity to use for creating the heat map.
- addboxes : [*boolean, optional*] Turn the edge colors to cyan. Default is False
- addmarks : [*boolean, optional*] Mark the unique point pairs with a cyan 'x'. Default is False.
- logscale : [*boolean, optional*] Plot assuming the fourth column data[:,3] is normalized by the area $\Phi/(4\pi R^2)$instead of the sphere result. Essentially, use a log scale for the color bar. Default is False.

D.10.3.2 Returns

- fig : [*matplotlib.figure.Figure*] The figure showing the heat map.

D.10.4 parse_directory(directory, R, vsweep=False)

Parse the directory for Sphere-Spheroid data.

Parse the given directory for the spectral flux data between a sphere and a spheroid. This is simply the raw data. We will return a NumPy array whose columns are the frequency,

eccentricity, separations, and fluxes respectively. To distinguish between oblate and prolate spheroids, we will assign prolate spheroids with a negative value.

It is assumed that the files in the directory utilize the naming convention

```
Omegas_Sphere_Spheroid_(ob|pr)XXX_dYYYYYYnm_scuffgeo.flux
```

where the XXX is the eccentricity times 100 (flagged by either ob for oblate or pr for prolate) and YYYYYY is the separation in nanometers. The name is tokenized on the '_' character and the fourth and fifth tokens are the critical parts.

D.10.4.1 Parameters

- directory : [*string*] Directory to parse for spheroid output files.
- R : [*scalar*] Radius of the equal surface area sphere.
- vsweep : [*boolean, optional*] Use `vsweep` to compute the view factors instead of the semi-analytic expression. Default is False.

D.10.4.2 Returns

- data : [*array_like*]
  - data[:,0] : Frequencies k
  - data[:,1] : Eccentricities e (>0 is oblate, <0 is prolate)
  - data[:,2] : Separations d
  - data[:,3] : Flux Φ
  - data[:,4] : Average view factor with area $A_i F_{ij}$

D.11 nanotools.viewfactors

Tools for computing the view factors.

This module contains the tools to compute the view factors between two objects. It is assumed that the system consists of two convex objects that do not overlap. There are some analytic solutions, but the main routine calls `irma2vs` and `vsweep` from the GTSig tool chain [blakeslee_gtsig_1994]. For that to work, both executables have to be on the

search path. When run as a script, the view factors are computed and printed to standard out.

In a future project, this needs to be broken out of the nanotools package because it is independent of this project.

D.11.1 References

- [blakeslee_gtsig_1994] L. Blakeslee and L. J. Rodriguez, "GTSig manual," tech. rep., Georgia Institute of Technology, Atlanta, GA, Nov. 1994.

D.11.2 get_geometry(geofile, queue)

Call the analyze geometry routine.

This is to isolate the call in a process. Without this, only the first instance of a geometry would be usable in a given Python session.

D.11.2.1 Parameters

- geofile : [*string*] The SCUFF-EM geometry file to read.
- queue : [*multiprocessing.Queue*] The queue to return the geometry dictionary.

D.11.3 irma2vs(facfile)

Run `irma2vs` to create the VIN file.

Run `irma2vs` with the default options to create the input file to `vsweep`.

D.11.3.1 Parameters

- facfile : [*NamedTemporaryFile*] The open readable FAC file.

D.11.3.2 Returns

- vinfile : [*NamedTemporaryFile*] The open readable `vsweep` input file.

D.11.4 main(geomfile)

Compute the view factors and surface areas.

D.11.4.1 Parameters

- geomfile : [*string*] The SCUFF-EM geometry file.

D.11.4.2 Returns

- results : [*array_like*] Array of view factors F_{ij}.
- areas : [*array_like*] Sum of facet areas for each surface.

D.11.5 read_t7(t7file)

Read the T7 file and return the view factors.

Given an open binary file, parse out the T7 information.

D.11.5.1 Parameters

- t7file : [*NamedTemporaryFile*] The open readable T7 file generated by `vsweep`.

D.11.5.2 Returns

- result : [*list*] A list where each entry is [I, J, FIJ] where I and J are the 1 based indices of the surfaces.

D.11.6 sphere_spheroid(R, A, C, d)

Compute the view factor between a sphere and a spheroid.

Compute the geometric view factor between a sphere of radius R and an axially aligned spheroid. The equation for the spheroid in a coordinate system with the origin at the center of the sphere, the equation for the spheroid is

$$\frac{\rho}{A^2} + \frac{(z - R - d - C)^2}{C^2} = 1.$$

We use the formalism presented by Chung and Naraghi to compute the factor [chung_journal_1982]. Currently, we just brute force the result.

D.11.6.1 Parameters

- R : [*scalar*] Sphere radius.

- A : [*scalar*] Spheroid equatorial radius.
- C : [*scalar*] Spheroid polar distance.
- d : [*scalar*] Surface to surface gap.

D.11.6.2 Returns

- F : [*scalar*] $F_{\text{sphere-spheroid}}$

D.11.6.3 References

- [chung_journal_1982] B. T. F. Chung and M. H. N. Naraghi, *Journal of Heat Transfer* **104**, 201 (1982).

D.11.7 vsweep(vinfile)

Run `vsweep`.

Given the input file generated by irma2vs, run `vsweep` with the default inputs.

D.11.7.1 Parameters

- vinfile : [*NamedTemporaryFile*] The input file to `vsweep` generated by irma2vs.

D.11.7.2 Returns

- t7file : [*NamedTemporaryFile*] The open readable T7 file generated by `vsweep`.

D.11.8 write_fac(scuffgeo)

Generate a FAC file from the SCUFF-EM geometry file.

Write a FACet file that is the input for the `irma2vs` program from the GTSig tool chain. The file is written to a named temporary file so that the working directory is not polluted with intermediate data. This file is opened and returned to the caller. It is up to the calling routine to handle closing the file.

D.11.8.1 Parameters

- scuffgeo : [*string*] The SCUFF-EM geometry file.

D.11.8.2 Returns

- facfile : [*NamedTemporaryFile*] The temporary FAC file.
- areas : [*list*] Sum of facet areas for each surface.

D.12 nanoheat

The main script to compute the enhanced near-field energy exchange.

D.12.1 arguments()

Define the command line arguments in a central location.

We define the arguments in a central location so that we may quickly find and edit them. This allows us to reuse the parser multiple times from the batch method.

D.12.2 batch(args)

Run a series of frequency and file combinations.

Create a set of jobs and run them. This will parse an input file of the form

```
---                  ---
| OmegaFile1 geometry1 |
| OmegaFile2 geometry2 |
| OmegaFile3 geometry3 |
|     .          .     |
|     .          .     |
|     .          .     |
---                  ---.
```

These will then be passed to a single run execution of the script with the requested outputs in the argument structure. The output files are created by joining the frequency and geometry file names with a '_' character and replacing all '.' with '_' characters. In short, this method simply calls this script with the single argument requesting the specified outputs. The input structure is taken from the arguments method above and each field is a boolean.

- The input structure (for possible extension):
  - args.inputs : The list if frequency and geometry files
  - args.emis : Write spectral emission
  - args.flux : Write spectral flux
  - args.matrices : Write the BEM matrices to file

WARNING: Writing the matrices to file could take a large amount of disk space.

WARNING: Currently this routine is specialized to serial batch runs on a local machine. It is intended to reincorporate the cluster ability.

D.12.3 convert_geometry(args)

Convert the SCUFF-EM geometry to a geometry dictionary.

Use the tools module to convert the geometry file from the SCUFF-EM format to the native geometry dictionary format used by the tools.

- Input structure:
  - args.geometry : The SCUFF-EM geometry file

D.12.4 single(args)

Compute the results for a single geometry.

Compute the flux through a collection of particles for a series of wavenumbers. For each wavenumber, the boundary element method (BEM) matrix is computed and the requested outputs are computed and written to file. The input is an argument structure parsed by the argparse module. The frequencies are specified in units of angular wavenumbers and a minimum of one is required. The outputs are specified by file indicators. If the field is not None and a name is not specified, the geometry file name with the extension changed to the output name (flux, emis, etc.) will be used.

- Input structure (for possible extension):
  - args.geometry : SCUFF-EM geometry file

- args.Omega : List of wavenumbers (may be complex)
- args.OmegaFile : File containing list of wavenumbers
- args.emis : Write spectral emission
- args.flux : Write spectral flux
- args.matrices : Write the B.E.M. matrices to file
- args.nproc : Number of processes assemble may use
- args.name : Name of the task (for batch run)
- args.overwrite : Overwrite the files (for main)

On return, the default file names will be placed in the appropriate fields in the argument structure if the output was requested. The naming convention for the matrix files is to use the root of the geometry file and append the frequency. '+' and '-' are replaced with 'p' and 'm' respectively. You should not have to run the calculation with the same geometry and wavelength twice so this should be safe. We add 'geometry' and 'omega' as keys to the BEM matrix dictionary and use the pickle module to save the data.

REFERENCES

[1] Abramson, A. R. and Tien, C. L., "Recent Developments in Microscale Thermophysical Engineering," *Microscale Thermophysical Engineering*, vol. 3, no. 4, pp. 229 – 244, 1999. [Online]. Available: http://dx.doi.org/10.1080/108939599199657

[2] Agarwal, G. S., "Quantum electrodynamics in the presence of dielectrics and conductors. I. Electromagnetic-field response functions and black-body fluctuations in finite geometries," *Physical Review A*, vol. 11, no. 1, p. 230, Jan. 1975. [Online]. Available: http://link.aps.org/doi/10.1103/PhysRevA.11.230

[3] Basu, S., Zhang, Z. M., and Fu, C. J., "Review of near-field thermal radiation and its application to energy conversion," *International Journal of Energy Research*, vol. 33, no. 13, pp. 1203–1232, Oct. 2009. [Online]. Available: http://dx.doi.org/10.1002/er.1607

[4] Blakeslee, L. and Rodriguez, L. J., "GTSig Manual," Georgia Institute of Technology, Atlanta, GA, Tech. Rep., Nov. 1994.

[5] Cahill, D. G., Ford, W. K., Goodson, K. E., Mahan, G. D., Majumdar, A., Maris, H. J., Merlin, R., and Phillpot, S. R., "Nanoscale thermal transport," *Journal of Applied Physics*, vol. 93, p. 793, 2003. [Online]. Available: http://dx.doi.org/10.1063/1.1524305

[6] Callen, H. B. and Welton, T. A., "Irreversibility and Generalized Noise," *Physical Review*, vol. 83, no. 1, p. 34, Jul. 1951. [Online]. Available: http://link.aps.org/doi/10.1103/PhysRev.83.34

[7] Carrillo, L. Y. and Bayazitoglu, Y., "Nanosphere near-field radiative heat-exchange analysis," *Journal of Thermophysics and Heat Transfer*, vol. 24, no. 2, pp. 309–315, 2010. [Online]. Available: http://dx.doi.org/10.2514/1.45620

[8] ——, "Nanorod near-field radiative heat exchange analysis," *Journal of Quantitative Spectroscopy and Radiative Transfer*, vol. 112, no. 3, pp. 412–419, Feb. 2011. [Online]. Available: http://dx.doi.org/10.1016/j.jqsrt.2010.10.011

[9] ——, "Sphere Approximation for Nanorod Near-Field Radiative Heat Exchange Analysis," *Nanoscale and Microscale Thermophysical Engineering*, vol. 15, pp. 195–208, Jul. 2011. [Online]. Available: http:/dx.doi.org/10.1080/15567265.2011.597493

[10] Chen, K.-M., "A mathematical formulation of the equivalence principle," *IEEE Transactions on Microwave Theory and Techniques*, vol. 37, no. 10, pp. 1576–1581, 1989.

[11] Chew, W. C., *Waves and fields in inhomogeneous media.* New York :: IEEE Press,, 1995. [Online]. Available: http://ieeexplore.ieee.org/xpl/bkabstractplus.jsp?bkn=5270998

[12] Chung, B. T. F. and Naraghi, M. H. N., "A Simpler Formulation for Radiative View Factors From Spheres to a Class of Axisymmetric Bodies," *Journal of Heat Transfer*, vol. 104, no. 1, pp. 201–204, Feb. 1982. [Online]. Available: http://dx.doi.org/10.1115/1.3245054

[13] Clark, J. A. and Korybalski, M. E., "Algebraic methods for the calculation of radiation exchange in an enclosure," *Wärme - und Stoffübertragung*, vol. 7, no. 1, pp. 31–44, Mar. 1974. [Online]. Available: http://link.springer.com/article/10.1007/BF01438318

[14] Dedkov, G. V. and Kyasov, A. A., "The relativistic theory of fluctuation electromagnetic interactions of moving neutral particles with a flat surface," *Physics of the Solid State*, vol. 45, no. 10, pp. 1815–1828, Oct. 2003. [Online]. Available: http://dx.doi.org/10.1134/1.1620084

[15] ——, "Fluctuation-electromagnetic interaction of a moving neutral particle with a condensed-medium surface: relativistic approach," *Physics of the Solid State*, vol. 51, no. 1, pp. 1–26, Jan. 2009. [Online]. Available: http://dx.doi.org/10.1134/S1063783409010016

[16] ——, "Radiative heat exchange between spherical particles caused by fluctuation electromagnetic field," *Technical Physics Letters*, vol. 36, no. 4, pp. 322–324, May 2010. [Online]. Available: http://dx.doi.org/10.1134/S1063785010040103

[17] ——, "On the radiative heat exchange between spherical particles at small distances," *EPL (Europhysics Letters)*, vol. 93, no. 3, p. 34001, Feb. 2011. [Online]. Available: http://iopscience.iop.org/0295-5075/93/3/34001/

[18] Dedkov, G. and Kyasov, A., "Conservative-dissipative forces and heating mediated by fluctuation electromagnetic field: Two plates in relative nonrelativistic motion," *Surface Science*, vol. 604, no. 5-6, pp. 562–567, Mar. 2010. [Online]. Available: http://www.sciencedirect.com/science/article/pii/S0039602809008036

[19] ——, "Radiative heat exchange of spherical particles with metal and insulator plates," *Surface Science*, vol. 605, no. 3-4, pp. 429–434, Feb. 2011. [Online]. Available: http://dx.doi.org/10.1016/j.susc.2010.11.013

[20] Diem, M., Koschny, T., and Soukoulis, C. M., "Wide-angle perfect absorber/thermal emitter in the terahertz regime," *Physical Review B*, vol. 79, no. 3, p. 033101, Jan. 2009. [Online]. Available: http://link.aps.org/doi/10.1103/PhysRevB.79.033101

[21] Eckhardt, W., "Macroscopic theory of electromagnetic fluctuations and stationary radiative heat transfer," *Physical Review A*, vol. 29, no. 4, pp. 1991–2003, Apr. 1984. [Online]. Available: http://link.aps.org/doi/10.1103/PhysRevA.29.1991

[22] Eichberger, J. I., "Calculation of geometric configuration factors in an enclosure whose boundary is given by an arbitrary polygon in the plane," *Wärme - und Stoffübertragung*, vol. 19, no. 4, pp. 269–271, Dec. 1985. [Online]. Available: http://link.springer.com/article/10.1007/BF01002281

[23] Franklin, J., *Classical Electromagnetism*. Lebanon, Indiana: Addison-Wesley, 2005.

[24] Gebhart, B., "Surface temperature calculations in radiant surroundings of arbitrary complexity—for gray, diffuse radiation," *International Journal of Heat and Mass Transfer*, vol. 3, no. 4, pp. 341–346, Dec. 1961. [Online]. Available: http://www.sciencedirect.com/science/article/pii/0017931061900485

[25] Geuzaine, C. and Remacle, J.-F., "Gmsh: A 3-D finite element mesh generator with built-in pre- and post-processing facilities," *International Journal for Numerical Methods in Engineering*, vol. 79, no. 11, pp. 1309–1331, 2009. [Online]. Available: http://onlinelibrary.wiley.com/doi/10.1002/nme.2579/abstract

[26] Griffiths, D. J., *Introduction to electrodynamics*, 3rd ed. Upper Saddle River, N.J.: Prentice Hall, 1999.

[27] Hargreaves, C., "Anomalous radiative transfer between closely-spaced bodies," *Physics Letters A*, vol. 30, no. 9, pp. 491–492, Dec. 1969. [Online]. Available: http://www.sciencedirect.com/science/article/pii/0375960169902643

[28] Harrington, R. F., *Field computation by moment methods*, ser. IEEE Press series on electromagnetic waves. IEEE Press, 1993. [Online]. Available: http://ieeexplore.ieee.org/servlet/opac?bknumber=5264934

[29] Hottel, H. C. and Sarofim, A. F., *Radiative transfer*, ser. [Mcgraw-hill series in mechanical engineering]. New York: McGraw-Hill, 1967.

[30] Howell, J. R., "A Catalog of Radiation Heat Transfer Configuration Factors," 2010. [Online]. Available: http://www.engr.uky.edu/rtl/Catalog/. Accessed: 2014-02-27

[31] Huth, O., Rüting, F., Biehs, S.-A., and Holthaus, M., "Shape-dependence of near-field heat transfer between a spheroidal nanoparticle and a flat surface," *The European Physical Journal Applied Physics*, vol. 50, p. 10603, Mar. 2010. [Online]. Available: http://dx.doi.org/10.1051/epjap/2010027

[32] Janowicz, M., Reddig, D., and Holthaus, M., "Quantum approach to electromagnetic energy transfer between two dielectric bodies," *Physical Review A*, vol. 68, no. 4, p. 043823, Oct. 2003. [Online]. Available: http://link.aps.org/doi/10.1103/PhysRevA.68.043823

[33] Jones, E., Oliphant, T., Peterson, P. *et al.*, "SciPy: Open source scientific tools for Python," 2001. [Online]. Available: http://www.scipy.org. Accessed: 2013-06-05

[34] Joulain, K., Mulet, J.-P., Marquier, F., Carminati, R., and Greffet, J.-J., "Surface electromagnetic waves thermally excited: Radiative heat transfer, coherence properties and Casimir forces revisited in the near field," *Surface Science Reports*, vol. 57, no. 3-4, pp. 59–112, May 2005. [Online]. Available: http://dx.doi.org/16/j.surfrep.2004.12.002

[35] King, N. S., Knight, M. W., Large, N., Goodman, A. M., Nordlander, P., and Halas, N. J., "Orienting Nanoantennas in Three Dimensions To Control Light Scattering Across a Dielectric Interface," *Nano Letters*, Nov. 2013. [Online]. Available: http://pubs.acs.org/doi/abs/10.1021/nl403199z

[36] Krüger, M., Bimonte, G., Emig, T., and Kardar, M., "Trace formulas for nonequilibrium Casimir interactions, heat radiation, and heat transfer for arbitrary objects," *Physical Review B*, vol. 86, no. 11, p. 115423, Sep. 2012. [Online]. Available: http://link.aps.org/doi/10.1103/PhysRevB.86.115423

[37] Krüger, M., Emig, T., and Kardar, M., "Nonequilibrium Electromagnetic Fluctuations: Heat Transfer and Interactions," *Physical Review Letters*, vol. 106, no. 21, p. 210404, May 2011. [Online]. Available: http://link.aps.org/doi/10.1103/PhysRevLett.106.210404

[38] Kyasov, A. A. and Dedkov, G. V., "Relativistic theory of fluctuating electromagnetic slowing down of neutral spherical particles moving in close vicinity to a flat surface," *Nuclear Instruments and Methods in Physics Research Section B: Beam Interactions with Materials and Atoms*, vol. 195, no. 3-4, pp. 247–258, Oct. 2002. [Online]. Available: http://dx.doi.org/10.1016/S0168-583X(02)00955-2

[39] Landau, L. D., Lifshitz, E. M., and Pitaevskii, L. P., *Statistical physics*, 3rd ed. Oxford: Pergamon Press, 1980.

[40] Lindell, I. V., *Methods for Electromagnetic Field Analysis*, ser. IEEE Press series on electromagnetic waves theory. Piscataway, NJ: IEEE Press, 1992. [Online]. Available: http://ieeexplore.ieee.org/xpl/bkabstractplus.jsp?bkn=5263418

[41] Litvinov, P. and Ziegler, K., "Rigorous derivation of superposition -matrix approach from solution of inhomogeneous wave equation," *Journal of Quantitative Spectroscopy and Radiative Transfer*, vol. 109, no. 1, pp. 74–88, Jan. 2008. [Online]. Available: http://www.sciencedirect.com/science/article/pii/S0022407307001860

[42] Mackowski, D. W. and Mishchenko, M. I., "Prediction of Thermal Emission and Exchange Among Neighboring Wavelength-Sized Spheres," *Journal of Heat Transfer*, vol. 130, no. 11, pp. 112 702–7, Nov. 2008. [Online]. Available: http://heattransfer.asmedigitalcollection.asme.org/article.aspx?articleid=1449366&resultClick=3

[43] Mandl, F., *Statistical physics*, 2nd ed., ser. The Manchester physics series. Chichester: Wiley, 1988.

[44] McCauley, A. P., Reid, M. T. H., Krüger, M., and Johnson, S. G., "Modeling near-field radiative heat transfer from sharp objects using a general three-dimensional numerical scattering technique," *Physical Review B*, vol. 85, no. 16, p. 165104, Apr. 2012. [Online]. Available: http://link.aps.org/doi/10.1103/PhysRevB.85.165104

[45] Messina, R., Tschikin, M., Biehs, S.-A., and Ben-Abdallah, P., "Fluctuation-electrodynamic theory and dynamics of heat transfer in systems of multiple dipoles," *Physical Review B*, vol. 88, no. 10, p. 104307, Sep. 2013. [Online]. Available: http://link.aps.org/doi/10.1103/PhysRevB.88.104307

[46] Mie, G., "Optics of turbid media," *Annalen der Physik*, vol. 25, no. 3, pp. 377–445, Mar. 1908.

[47] Mishchenko, M. I., *Scattering, absorption, and emission of light by small particles*, Travis, L. D. and Lacis, A. A., Eds. Cambridge: Cambridge University Press, 2002.

[48] Naraghi, M. H. N. and Chung, B. T. F., "Radiation Configuration Factors Between Disks and a Class of Axisymmetric Bodies," *Journal of Heat Transfer*, vol. 104, no. 3, pp. 426–431, Aug. 1982. [Online]. Available: http://dx.doi.org/10.1115/1.3245110

[49] Narayanaswamy, A. and Chen, G., "Dyadic Green's functions and electromagnetic local density of states," *Journal of Quantitative Spectroscopy and Radiative Transfer*, vol. 111, no. 12–13, pp. 1877–1884, Aug. 2010. [Online]. Available: http://www.sciencedirect.com/science/article/pii/S0022407309003896

[50] ——, "Thermal near-field radiative transfer between two spheres," *Physical Review B*, vol. 77, no. 7, p. 075125, Feb. 2008. [Online]. Available: http://link.aps.org/doi/10.1103/PhysRevB.77.075125

[51] Narayanaswamy, A., Shen, S., Hu, L., Chen, X., and Chen, G., "Breakdown of the Planck blackbody radiation law at nanoscale gaps," *Applied Physics A*, vol. 96, no. 2, pp. 357–362, May 2009. [Online]. Available: http://www.springerlink.com/content/h1942r8n73348k83/

[52] Otey, C. and Fan, S., "Numerically exact calculation of electromagnetic heat transfer between a dielectric sphere and plate," *Physical Review B*, vol. 84, no. 24, p. 245431, Dec. 2011. [Online]. Available: http://link.aps.org/doi/10.1103/PhysRevB.84.245431

[53] Peterson, B. and Ström, S., "T Matrix for Electromagnetic Scattering from an Arbitrary Number of Scatterers and Representations of E(3)," *Physical Review D*, vol. 8, no. 10, p. 3661, Nov. 1973. [Online]. Available: http://link.aps.org/doi/10.1103/PhysRevD.8.3661

[54] Polder, D. and Van Hove, M., "Theory of Radiative Heat Transfer between Closely Spaced Bodies," *Physical Review B*, vol. 4, no. 10, pp. 3303–3314, Nov. 1971. [Online]. Available: http://link.aps.org/doi/10.1103/PhysRevB.4.3303

[55] Pralle, M. U., Moelders, N., McNeal, M. P., Puscasu, I., Greenwald, A. C., Daly, J. T., Johnson, E. A., George, T., Choi, D. S., El-Kady, I., and Biswas, R., "Photonic crystal enhanced narrow-band infrared emitters," *Applied Physics Letters*, vol. 81, no. 25, pp. 4685–4687, Dec. 2002. [Online]. Available: http://apl.aip.org/resource/1/applab/v81/i25/p4685_s1

[56] Pralle, M. U., McNeal, M. P., Moelders, N., Last, L., Ho, W., Greenwald, A. C., Daly, J. T., Puscasu, I., Johnson, E. A., El-Kady, I., and Biswas, R., "Photonic crystals for narrow-band infrared emission," *Proceedings of SPIE*, vol. 4574, no. 1, pp. 193–200, Feb. 2002. [Online]. Available: http://spiedigitallibrary.org/proceedings/resource/2/psisdg/4574/1/193_1

[57] Prasher, R., "Thermal radiation in dense nano- and microparticulate media," *Journal of Applied Physics*, vol. 102, no. 7, pp. 074 316–074 316–9, Oct. 2007. [Online]. Available: http://jap.aip.org/resource/1/japiau/v102/i7/p074316_s1

[58] Rahi, S. J., Emig, T., Graham, N., Jaffe, R. L., and Kardar, M., "Scattering theory approach to electrodynamic Casimir forces," *Physical Review D*, vol. 80, no. 8, p. 085021, Oct. 2009. [Online]. Available: http://link.aps.org/doi/10.1103/PhysRevD.80.085021

[59] Reid, M. T. H., "Surface Current/Field Formulation of Electromagnetism," Dec. 2011. [Online]. Available: homerreid.com/scuff-em. Accessed: 2013-06-05

[60] Reid, M. T. H. and Johnson, S. G., "Efficient Computation of Power, Force, and Torque in BEM Scattering Calculations," *arXiv:1307.2966 [physics]*, Jul. 2013, arXiv: 1307.2966. [Online]. Available: http://arxiv.org/abs/1307.2966

[61] Rodriguez, A. W., Reid, M. T. H., and Johnson, S. G., "Fluctuating-surface-current formulation of radiative heat transfer: Theory and applications," *Physical Review B*, vol. 88, no. 5, p. 054305, Aug. 2013. [Online]. Available: http://link.aps.org/doi/10.1103/PhysRevB.88.054305

[62] Rother, T., *Electromagnetic wave scattering on nonspherical particles : basic methodology and simulations*. Berlin: Springer, 2009.

[63] Rousseau, E., Siria, A., Jourdan, G., Volz, S., Comin, F., Chevrier, J., and Greffet, J.-J., "Radiative heat transfer at the nanoscale," *Nat Photon*, vol. 3, no. 9, pp. 514–517, 2009. [Online]. Available: http://dx.doi.org/10.1038/nphoton.2009.144

[64] Rytov, S. M., "Theory of electric fluctuations and thermal radiation," Air Force Cambridge Research Labs, Hanscom AFB MA, Tech. Rep. AD0226765, Jul. 1959.

[65] Sasihithlu, K. and Narayanaswamy, A., "Convergence of vector spherical wave expansion method applied to near-field radiative transfer," *Optics Express*, vol. 19, no. S4, pp. A772–A785, Jul. 2011. [Online]. Available: http://dx.doi.org/10.1364/OE.19.00A772

[66] Shen, S., Narayanaswamy, A., and Chen, G., "Surface Phonon Polaritons Mediated Energy Transfer between Nanoscale Gaps," *Nano Lett.*, vol. 9, no. 8, pp. 2909–2913, 2009. [Online]. Available: http://dx.doi.org/10.1021/nl901208v

[67] Shi, C., Soltani, S., and Armani, A. M., "Gold Nanorod Plasmonic Upconversion Microlaser," *Nano Letters*, vol. 13, no. 12, pp. 5827–5831, Dec. 2013. [Online]. Available: http://pubs.acs.org/doi/abs/10.1021/nl4024885

[68] Sparrow, E. M., "A New and Simpler Formulation for Radiative Angle Factors," *Journal of Heat Transfer*, vol. 85, no. 2, pp. 81–87, May 1963. [Online]. Available: http://dx.doi.org/10.1115/1.3686058

[69] Tai, C.-t., *Dyadic green functions in electromagnetic theory*, 2nd ed. Piscataway, NJ: IEEE Press, 1994.

[70] ——, *Generalized vector and dyadic analysis : applied mathematics in field theory*, 2nd ed. Piscataway, NJ: Wiley-IEEE, 1997.

[71] Tsang, L., *Theory of microwave remote sensing*, Kong, J. A. and Shin, R. T., Eds. New York: Wiley, 1985.

[72] Volokitin, A. I. and Persson, B. N. J., "Radiative heat transfer between nanostructures," *Physical Review B*, vol. 63, no. 20, p. 205404, Apr. 2001. [Online]. Available: http://link.aps.org/doi/10.1103/PhysRevB.63.205404

[73] ——, "Near-field radiative heat transfer and noncontact friction," *Reviews of Modern Physics*, vol. 79, no. 4, p. 1291, Oct. 2007. [Online]. Available: http://link.aps.org/doi/10.1103/RevModPhys.79.1291

[74] ——, "Theory of the interaction forces and the radiative heat transfer between moving bodies," *Physical Review B*, vol. 78, no. 15, p. 155437, Oct. 2008. [Online]. Available: http://link.aps.org/doi/10.1103/PhysRevB.78.155437

[75] Walton, G. N., "Calculation of Obstructed View Factors by Adaptive Integration," National Institute of Standards and Technology, Gaithersburg, MD, NIST Interagency/Internal Report (NISTIR) NISTIR 6925, Nov. 2002. [Online]. Available: http://www.nist.gov/manuscript-publication-search.cfm?pub_id=860891

[76] Waterman, P. C., "Symmetry, Unitarity, and Geometry in Electromagnetic Scattering," *Physical Review D*, vol. 3, no. 4, pp. 825–839, Feb. 1971. [Online]. Available: http://link.aps.org/doi/10.1103/PhysRevD.3.825

VITA

Keith F. Prussing was born and raised in the metro Atlanta area. He began his adult life as a music major at Georgia Perimeter College from 2000 to 2006 thinking that he would go on to become a professional musician. During this time, he worked as a salesman for various musical instrument retailers, and became one of the top performing band and orchestra instrument salesmen. After a while, he realized that only one position was available for a professional euphonium player and that job was taken. This meant that a music degree would get him the exact job he already had. Upon reflection, he realized that excelled at physics in high school. And a bit of research revealed that physics was a lucrative job option. So, he set his mind to it and set out to get his doctorate. He transferred his course work to Kennesaw State University in 2006 and, subsequently, to the Georgia Institute of Technology in 2007 where he completed his Bachelor of Science with a major in physics in May 2009. He then turned right around and entered Graduate Studies at the Georgia Institute of Technology in September 2009 while doing research with the Electro-Optical Systems Laboratory of the Georgia Tech Research Institute. Currently, he resides in Doraville, GA, with his lovely wife and their two dogs.